Experiments in Seismometer Azimuth Determination by Comparing the Sensor Signal Outputs with the Signal Output of an Oriented Sensor

By L. Gary Holcomb

Open-File Report 02-183

2002

U.S. DEPARTMENT OF THE INTERIOR
U.S. GEOLOGICAL SURVEY

Albuquerque, New Mexico

1 INTRODUCTION

The problem of orienting horizontal seismometers in the field has persisted throughout the history of seismology. For surface installations in years past, geographic north-south and east-west were usually determined with a compass and the previously known magnetic declination for the site; the sensors were oriented accordingly. In recent years, geographic north-south and east-west can be very accurately determined by using equipment based on the Global Positioning System (GPS). The process becomes somewhat more difficult in underground vaults where compasses and GPS systems become unreliable. In this case, a line whose orientation is known is sometimes extended into the underground chamber using standard surveying methods. If the sensor is installed in a deep borehole, orienting becomes even harder because access to the sensor in the hole is impossible.

Modern borehole technology usually utilizes a keyed holelock which orients the seismometer in a known direction. The orientation of the holelock is usually determined with a gyroscopic tool that is lowered into the hole and into the keyed holelock. This technique has been used successfully for many years throughout the world. However, the gyro tools are relatively fragile and they are frequently damaged in shipment; they are also very expensive to repair. At the Albuquerque Seismological Laboratory (ASL) this problem has recently prompted a search for an alternative cheaper method for orienting borehole sensors.

The use of a horizontal seismometer temporarily installed on the surface whose orientation is known, to determine the unknown orientation of a nearby borehole installed sensor has been proposed by many people throughout the years. As usually depicted, this scheme would involve the rotation of the surface instrument to different azimuths and the comparison of the signal outputs of the two installations; the orientation of the surface instrument at which the two signals are "most alike" would then be assumed to also be the orientation of the borehole instrument. The criteria for determining when the two signals are "most alike" is usually left unspecified by the people proposing the use of this method; apparently it should be obvious to anyone using the method. As far as is known, very little has been written about the potential accuracy of this method for determining the orientation of borehole sensors

The only written material pertaining to this technique, which the author is aware of, is found in Burch (1995). Burch discusses the utilization of the signal from a surface installed horizontal instrument and the signal from one component of the borehole instrument, which are fed to a dual channel oscilloscope. His surface sensor was installed on a mechanical turntable with a graduated azimuthal scale. The turntable was rotated to give the best visible coherence between the two traces on the oscilloscope and the azimuth was read from the turntable scale. He also discussed the use of a dual channel spectrum analyzer to calculate the power spectrum of the two sensor outputs and a HP-85 computer to calculate the coherence between the two outputs. The mechanical table was rotated in one degree steps and the coherence was evaluated at each position. He claims that the azimuth should be resolvable to within one fifth of one degree.

Although simple in concept, this method of orienting a seismometer may be subject to unknown systematic errors. In particular, this method assumes that the input signals to both sensors are identical; this assumption will not hold if the sensors are separated far enough. The author does not know of any quantitative studies of what "far enough" is. This report summarizes the results of both theoretical and experimental studies that are aimed at determining the probable potential accuracy of this orientation method.

This work was started in 1994 and has continued off and on for 7 years as time and other priorities permitted. Therefore, there is a lack of continuity in the experiments and in the documentation because different portions of the work were completed at widely separated times.

2 MATHEMATICAL METHODS FOR DETERMINING THE ORIENTATION

In this report, six different mathematical methods for determining when the output signal from the reference sensor is "most like" the output signal from the borehole sensor will be investigated. These methods range from simply taking the difference between the two signals in the time domain as a function of the relative azimuth between the two sensors to calculating the coherence function between the two sensor outputs in the frequency domain as a function of their relative azimuth. All six methods will be applied to both dummy and real experimental data to assess their accuracy.

There are two ways that the relative azimuth of the surface installation and the borehole sensor can be varied. First, one of the sensor systems can be physically slowly rotated while comparing the outputs of the two systems. At first glance, this method seems to be attractive because of its simplicity but actual experience reveals that it is not as simple as it appears. Horizontal sensors are very sensitive to tilt; this makes it difficult to turn the sensor to different azimuths because the sensor must be releveled each time it is moved. The current azimuth of the rotated sensor must be remeasured each time it turned. Finally, the surface sensor installation must be quiet if its signal output is to be compared with that from the borehole sensor. A temporary shelter of some type may be required for the surface instrument thereby rendering physical access to this instrument difficult.

It is much easier to perform the relative rotation of the two systems with a computer. In this method, both the surface sensor and the borehole sensor are left physically in one place. The digitized signal outputs of the two orthogonal borehole horizontal components are rotated point by point to successive apparent azimuths by a simple coordinate transformation as follows.

$$N_i^{'}(\theta) = -E_i \sin(\theta) + N_i \cos(\theta) \tag{2.1}$$

$$E_i^{'}(\theta) = E_i \cos(\theta) + N_i \sin(\theta) \tag{2.2}$$

Here, the i'th digitized output signal samples N_i and E_i from the two orthogonal borehole sensors are rotated to a new orthogonal cartesian coordinate system N' and E' oriented at an angle θ with respect to the original coordinate system N and E (see Figure 2.1) with Equations 2.1 and 2.2. The angle θ is measured counterclockwise (CCW) from north. The rotation can be performed in either the time domain or the frequency domain. These rotated signals are then compared with the signal K_i from the surface sensor whose orientation is assumed to be known at an angle Δ CCW from north (see Figure 2.3). The angle θ is varied from 0^o to 359^o in small (1^o or less) steps. Five time domain methods for comparing the similarity of the signals after each incremental rotation were tested with comparable results.

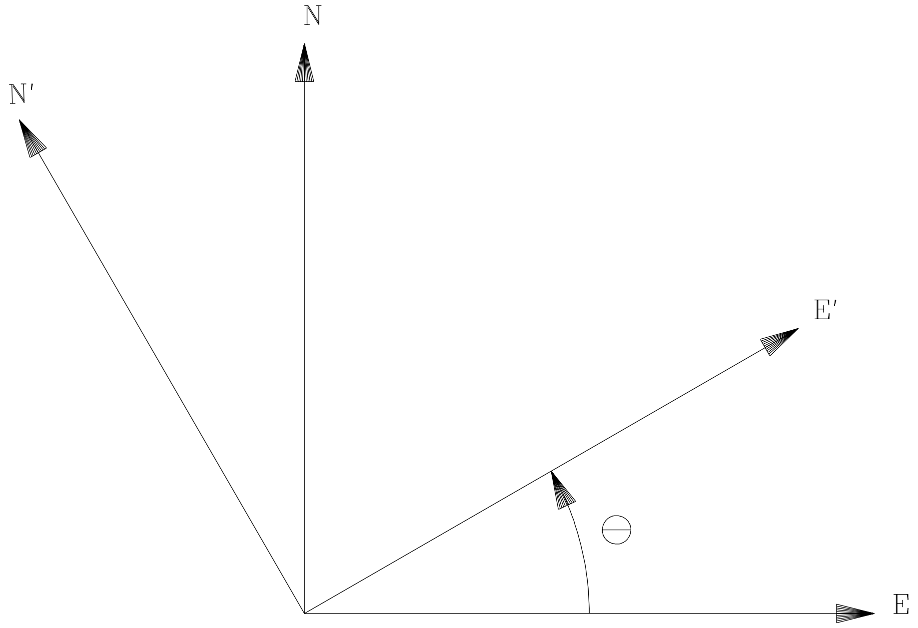

Figure 2.1 Coordinate rotation axes for rotating sensor output signals to arbitrary azimuths.

2.1 THE SIMPLE DIFFERENCE METHOD

The most obvious method of comparing the two signals is to simply subtract the signal output of the known oriented (reference) sensor (K) from one of the unknown oriented (borehole) rotated components (N' or E') and look for a minimum in this difference as a function of the rotation angle θ. This difference is expressed in Equation 2.3 in which the difference has been averaged over M sequential time series data points to increase the accuracy. This equation will be referred to as the simple difference method. If the amplitude and phase response of the two sensors are exactly matched, if both sensor systems are ideally noiseless, if the gains of the two sensors are exactly equal, and if the ground motion input to both sensors is perfectly identical, $D^S(\theta)$ should be exactly equal to zero when the two sensors are perfectly azimuthly aligned and it should reach a maximum value when they are 180^o out of alignment.

$$D^S(\theta) = \tfrac{1}{M}\sum_{i=0}^{M}(N_i'(\theta) - K_i) \tag{2.3}$$

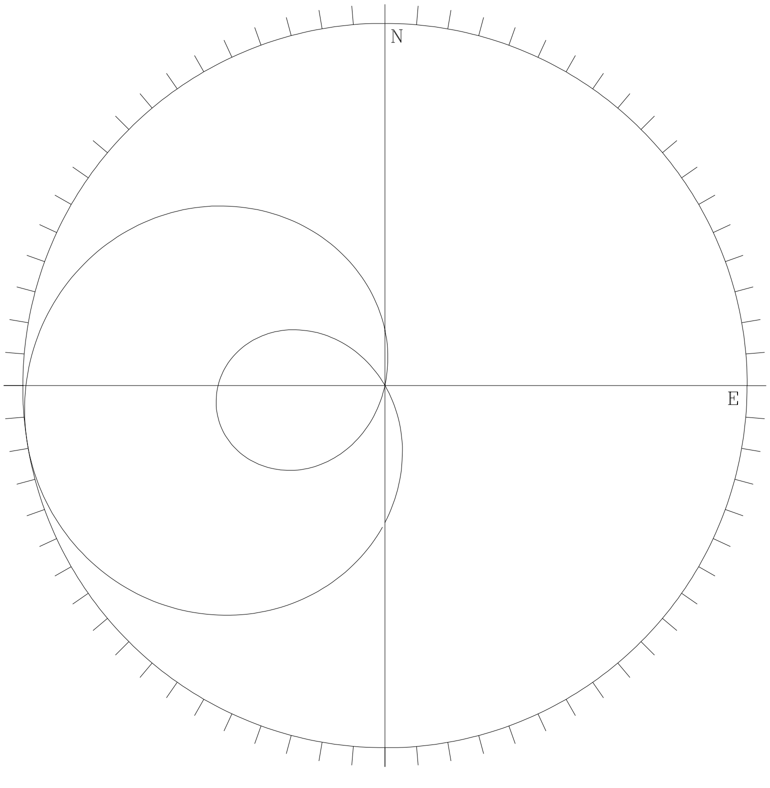

Figure 2.2 Example of simple difference function $(D^S(\theta))$ calculated from real experimental data. The azimuth of the known sensor was 30° CCW from north (N).

These conditions are not likely to occur in a real world experiment. For instance, if the gains of the two sensors are not exactly equal, the difference should not go to exactly zero when the sensors are aligned. Figure 2.2 illustrates the typical azimuthal dependence of $D^S(\theta)$ obtained from actual experimental data. In this figure, θ is measured counterclockwise from N in degrees and $D^S(\theta)$ forms the second coordinate of a polar coordinate pair. The difference error, $D^S(\theta)$, in Figure 2.2 closely resembles a Lemacon curve in which $D^S(\theta)$ becomes negative for $-40^o < \theta < 30^o$. This may occur because the gains of sensor K and sensor N are not exactly equal. The fact that the curve in Figure 2.2 crosses zero twice raises questions about how to interpret the azimuth of the unknown sensor. The azimuth of the known sensor which generated the data in Figure 2.2 was 30^o counterclockwise from the north component of the borehole instrument. Note that the minimum in the simple difference plot does not correspond to this known azimuth; instead, it seems to indicate an azimuth of about 80^o clockwise from the borehole north. Analysis of a simple model of the situation should clarify the picture.

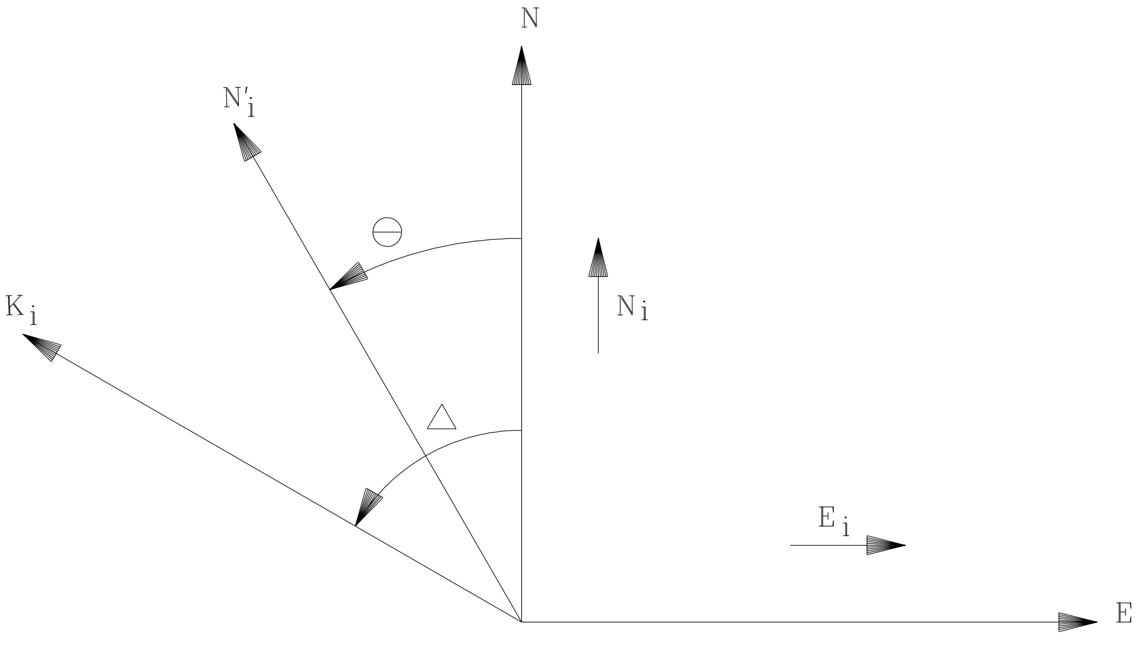

Figure 2.3 Definition of symbols for modeling the behavior of the simple difference equation.

Let the known sensor system be positioned at Δ degrees counterclockwise from the north component of the borehole sensor system as depicted in Figure 2.3. Let N_i denote the instantaneous acceleration of the earth's surface in the direction parallel to the north component of the borehole instrument at time "i" and E_i denote the instantaneous acceleration of the earth's surface in the direction parallel to the east component of the borehole instrument at the same time. If we assume that the borehole sensor is "ideal" (that is, it has no internal noise), and that the response of the sensor system is flat, the i'th sample of the north channel output of the borehole instrument can be expressed as

$$S_{N_i} = G_n N_i \tag{2.4}$$

and likewise the i'th sample of the east channel output can be expressed as

$$S_{E_i} = G_N E_i \tag{2.5}$$

where G_N and G_E are the gains of the north and east channels respectively. The rotated north component of the borehole instrument $N^{'}$ in Figure 2.3) is given by (see Figure 2.1 and Equation 2.2)

$$N_i^{'}(\theta) = -S_{E_i}\sin(\theta) + S_{N_i}\cos(\theta) \tag{2.6}$$

or substituting for S_{E_i} and S_{N_i} yields

$$N_i^{'} = -G_E E_i \sin(\theta) + G_N N_i \cos(\theta) \tag{2.7}$$

If the known sensor is also "ideal", the output of the known sensor may be expressed in terms of ground acceleration parallel to the N-S and E-W components of the borehole instrument is

$$K_i = -G_K E_i \sin(\Delta) + G_K N_i \cos(\Delta) \tag{2.8}$$

where G_K is the gain of the known sensor. The i'th sample of the simple difference is (from Equation 2.3)

$$D_i^S(\theta) = N_i^{'}(\theta) - K_i \tag{2.9}$$

Substituting for $N_i^{'}(\theta)$ and K_i from equations 2.7 and 2.8 respectively, $D_i^S(\theta)$ becomes

$$D_i^S(\theta) = E_i(G_K\sin(\Delta) - G_E\sin(\theta)) + N_i(G_N\cos(\theta) - G_K\cos(\Delta)) \tag{2.10}$$

This expression can be simplified if we note that the acceleration along the N and E directions of the coordinate system will be approximately equal ($N_i = E_i = A_i$).

$$D_i^S(\theta) = A_i((G_K\sin(\Delta) - G_E\sin(\theta)) + (G_N\cos(\theta) - G_K\cos(\Delta))) \tag{2.11}$$

In a real world situation, the gains of the three sensor systems will also probably be approximately equal ($G_E = G_N = G_K = G$). If these conditions are met the simple difference expression becomes

$$D_i^S = GA_i(\sin(\Delta) - \sin(\theta) + \cos(\theta) - \cos(\Delta)) \tag{2.12}$$

Since we have assumed that the amplitude and phase response of the two sensors are exactly matched, that both sensor systems are perfectly noiseless, that all of the gains are equal, and that the ground motion input to both sensors is identical, the simple difference function must equal zero if the rotated borehole north component is aligned with the azimuth of the known sensor

$$\sin(\Delta) - \sin(\theta) + \cos(\theta) - \cos(\Delta) = 0 \tag{2.13}$$

Obviously, this expression is true if $\theta = \Delta$. Unfortunately, this equation also has another root as can be verified in Figure 2.4 in which $D_i^S(\theta)$ (Equation 2.12) is plotted as the radius in a normalized polar coordinate system with θ being measured CCW from the borehole north (N) direction for a fixed known azimuth of 30^o ($\Delta = 30^o$) in Figure 2.4. In Figure 2.4, small arrows have been added the curve to indicate the direction that the curve is traced out as the angle θ increases counterclockwise. The other root lies at $\theta = 240^o$ as the reader can verify; the azimuths of the two roots are plotted in Figure 2.5.

An example of the application of the simple difference equation to real data is shown in Figure 2.6; the azimuth of the known sensor was 30^o. Note that one of the roots shown in Figure 2.6 does lie at 30^o as it should but the second root does not equal 240^o. This discrepancy will be discussed later in Section 4.

Figure 2.4 Normalized plot of simple difference equation (Equation 2.10) if $N_i = E_i$, $G_K = G_E = G_N$, and $\Delta = 30°$

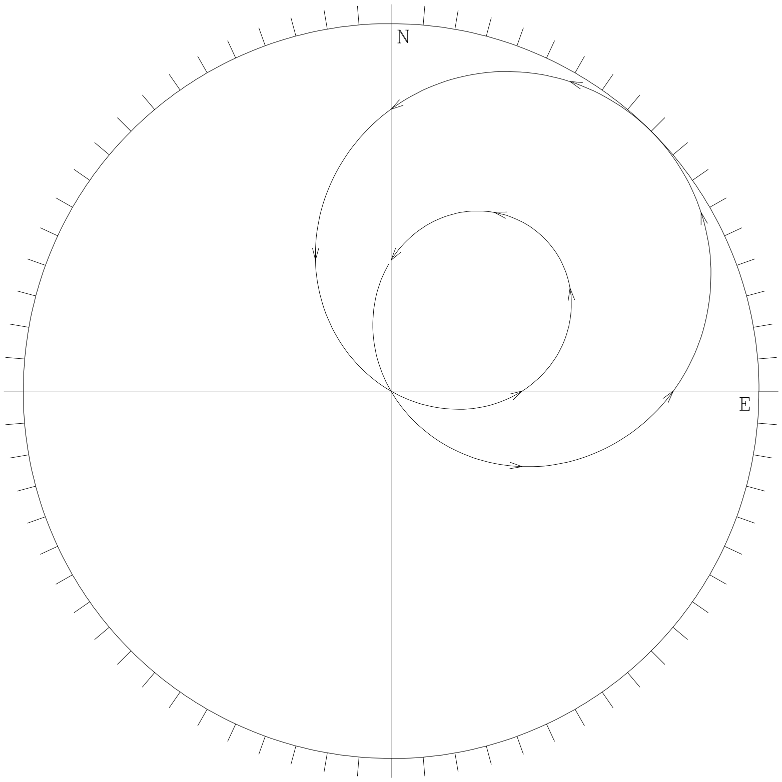

Figure 2.5 Roots of simple difference equation (Equation 2.13) if $\Delta = 30°$.

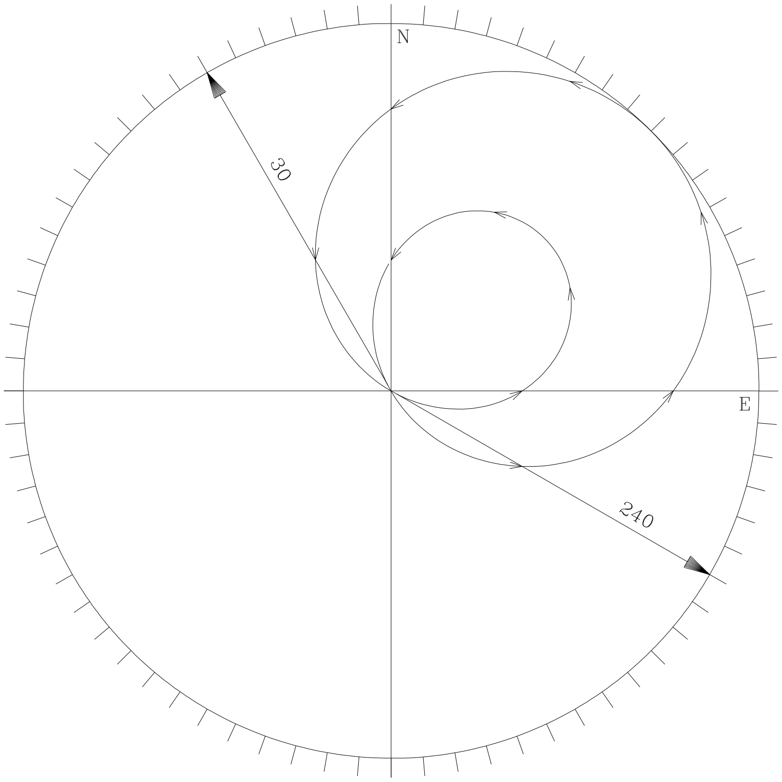

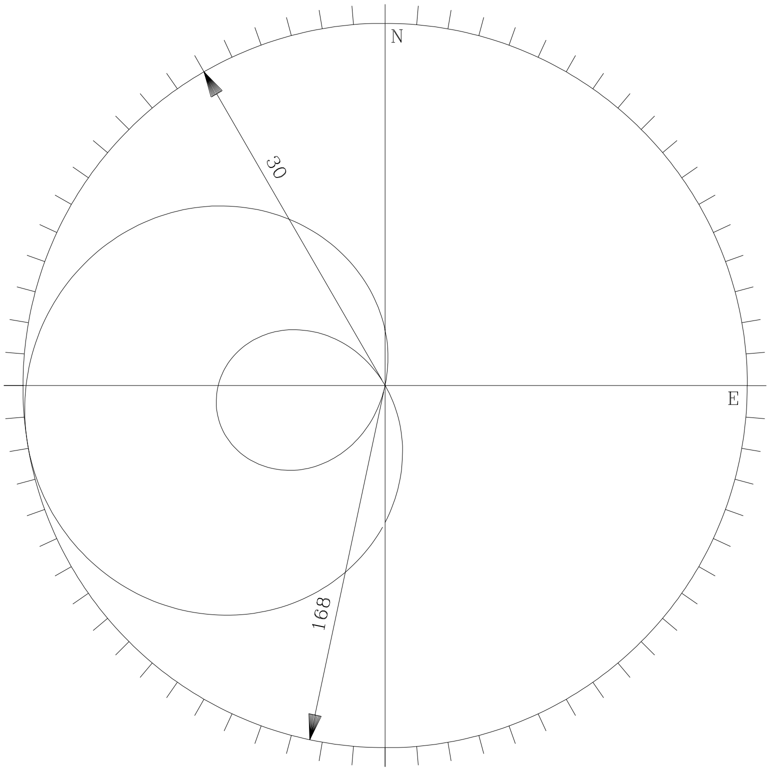

Figure 2.6 Real data simple difference azimuths. The known azimuth of the reference sensor was $\Delta = 30^\circ$.

2.2 THE ABSOLUTE DIFFERENCE METHOD

A logical modification to Equation 2.3 would be to minimize the absolute difference error between the signals as a function of θ as expressed in Equation 2.14. This equation will be referred to as the absolute difference method. The equation never becomes negative although it may be equal to zero if the signal outputs of the perfectly aligned sensors are identical.

$$D^{A}(\theta)=\tfrac{1}{M}\sum_{i=0}^{M}\left|N_{i}^{'}(\theta)=K_{i}\right| \qquad (2.14)$$

As was the case for the simple difference equation, the absolute difference equation also has two roots which can be shown as follows. The i'th sample of the absolute difference is

$$D_{i}^{A}(\theta)=\left|N_{i}^{'}(\theta)-K_{i}\right| \qquad (2.15)$$

Substituting for $N_{i}^{'}(\theta)$ and K_{i} from equations 2.7 and 2.8 respectively, $D_{i}^{A}(\theta)$ becomes

$$D_{i}^{A}(\theta)=\left|E_{i}(G_{K}\sin(\Delta)-G_{E}\sin(\theta)+N_{i}(G_{N}\cos(\theta)-G_{K}\cos(\Delta)\right| \qquad (2.16)$$

Letting $(G_{E}=G_{N}=G_{K}=G)$ and $(N_{i}=E_{i}=A_{i})$ yields

$$D_{i}^{A}(\theta)=GA_{i}\,|\sin(\Delta)-\sin(\theta)+\cos(\theta)-\cos(\Delta)| \qquad (2.17)$$

A normalized plot of the absolute difference function of Equation 2.17 for a known azimuth of 30° is shown in Figure 2.7. Note the similarity to Figure 2.4; the large lobe of Figure 2.4 is mirrored by the absolute value in Equation 2.14 to yield Figure 2.7 from Figure 2.4. If the rotated borehole north is aligned with the known sensor the signal output of the two sensors should be identical and the absolute difference function should equal 0.

$$|\sin(\Delta)-\sin(\theta)+\cos(\Delta)|=0 \qquad (2.18)$$

if $\Delta=30^{\circ}$, the roots of this equation are the same as were the roots of the simple difference equation (Equation 2.13): they are plotted in Figure 2.8.

Figure 2.7 Normalized plot of the absolute difference equation (Equation 2.17) if $\Delta = 30°$.

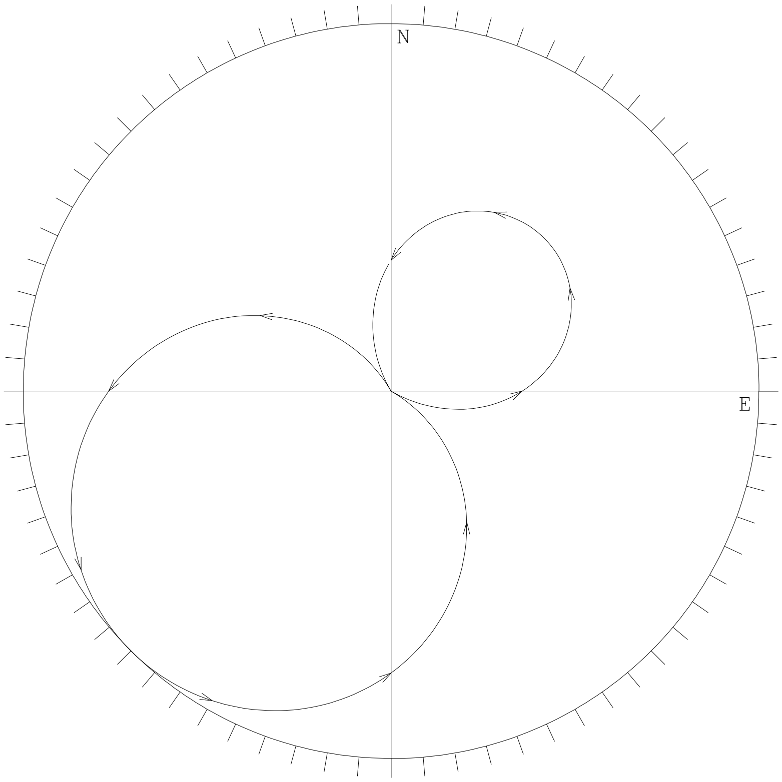

Figure 2.8 Roots of the absolute difference equation (Equation 2.16) if $G_K = G_E = G_N$ and $N_i = E_i$ and $\Delta = 30°$

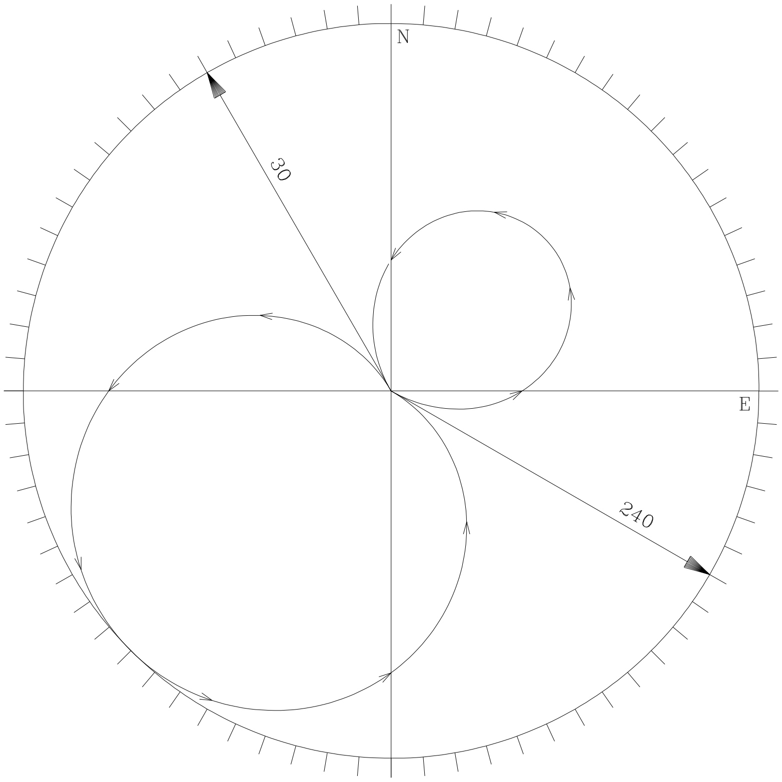

2.3 THE SIMPLE RATIO METHOD

Another relatively simple method for comparing the signals is to form a ratio of the two signals as in Equation 2.19. This expression will be referred to as the simple ratio method. If the amplitude and phase response of the two sensors are exactly matched, if the gains of the sensors are equal, and if the ground motion input to both sensors is identical, this expression should be equal to one when the two sensors are aligned (or -1 if they are 180° misaligned).

$$R^S(\theta) = \frac{1}{M}\sum_{i=1}^{M}\frac{N_i^{'}(\theta)}{K_i} \tag{2.19}$$

Substituting for $N_i(\theta)$ and K_i from Equations 2.7 and 2.8 respectively, the ith sample of the simple ratio becomes

$$R_i^S(\theta) = \frac{-G_E E_i \sin(\theta) + G_n N_i \cos(\theta)}{-G_k E_i \sin(\Delta) + G_k N_i \cos(\Delta)} \tag{2.20}$$

Once again, the gains of the three sensor systems will probably be approximately equal $(G_E = G_N = G_K = G)$ and the acceleration along the N and E directions of the coordinate system will be approximately equal $(N_i = E_i = A_i)$. If these conditions are met, the simple ratio expression becomes.

$$R_i^S(\theta) = \frac{-\sin(\theta) + \cos(\theta)}{-\sin(\Delta) + \cos(\Delta)} \tag{2.21}$$

A normalized plot of Equation 2.21 for $\Delta = 30°$ is shown in Figure 2.9. Note that the function in this figure is double valued (the curve is traversed twice as θ ranges from $0°$ to $360°$) in a polar coordinate plot because ratios separated by $180°$ are equal in amplitude but opposite in sign. Since all of the gains are equal and both ground accelerations are equal, the simple ratio function should equal one if the rotated borehole component is aligned with azimuth of the known sensor.

$$\frac{-\sin(\theta) + \cos(\theta)}{-\sin(\Delta) + \cos(\Delta)} = 1 \tag{2.22}$$

As in the simple difference case, this expression is obviously true if $\theta = \Delta$. However, there is another root which is not so obvious. Figure 2.9 contains a plot of Equation 2.21 but the roots (the point at which Equation 2.22 is equal to 1) are not apparent because the function is double valued - that is the circle in the figure is traversed twice as θ goes from $0°$ to $360°$.

Figure 2.9 Normalized plot of the simple ratio equation (Equation 2.21) if $\Delta = 30°$

.

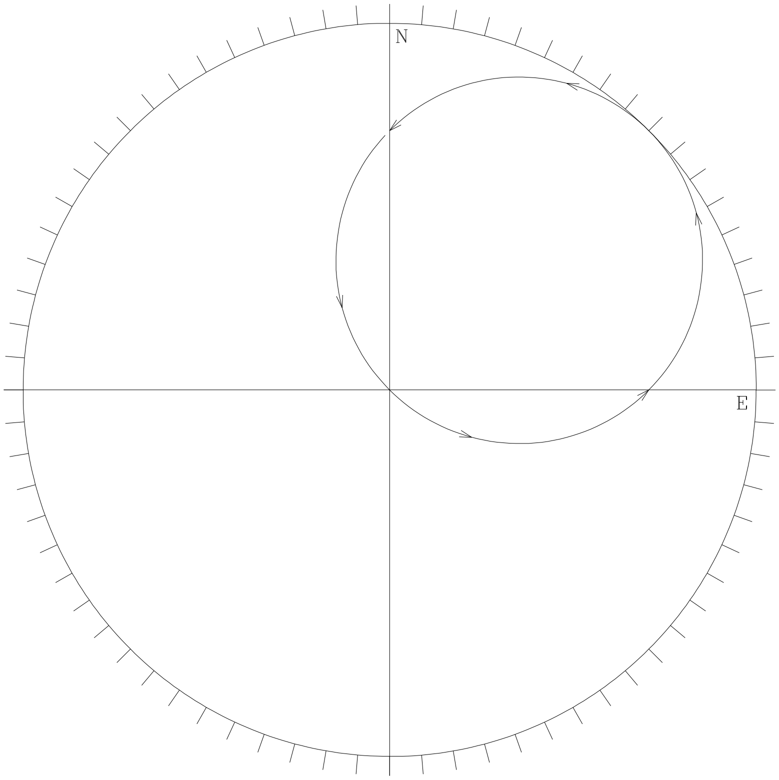

This ambiguity can be removed by subtracting 1 from $R_i^S(\theta)$ to yield

$$R_i^S(\theta) - 1 = \frac{-\sin(\theta) + \cos(\theta)}{-\sin(\Delta) + \cos(\Delta)} - 1 \tag{2.23}$$

A normalized plot of this simple ratio minus one function is shown in Figure 2.10. Note that this function appears to be identical to the simple difference function plotted in Figure 2.4. In fact normalized plots of Equations 2.12 and 2.23 are identical; the two equations differ only by a scalar constant because Equation 2.23 may be written as

$$R_i^S(\theta) - 1 = \frac{-\sin(\theta) + \cos(\theta) + \sin(\Delta) - \cos(\Delta)}{-\sin(\Delta) + \cos(\Delta)} = \frac{D_i^S(\theta)}{-\sin(\Delta) + \cos(\Delta)} \tag{2.24}$$

Thus the simple difference expression (Equation 2.12) divided by the scalar constant $-\sin(\Delta) + \cos(\Delta)$ is equal to the simple ratio minus one expression. If the rotated borehole north component and the known sensor are aligned, the simple ratio minus one expression of Equation 2.23 must equal to zero

$$\frac{-\sin(\theta)+\cos(\theta)}{-siun(\Delta)+\cos(\Delta)}-1=0 \tag{2.24}$$

If $\Delta = 30°$, the roots to Equation 2.25 are shown in Figure 2.11.

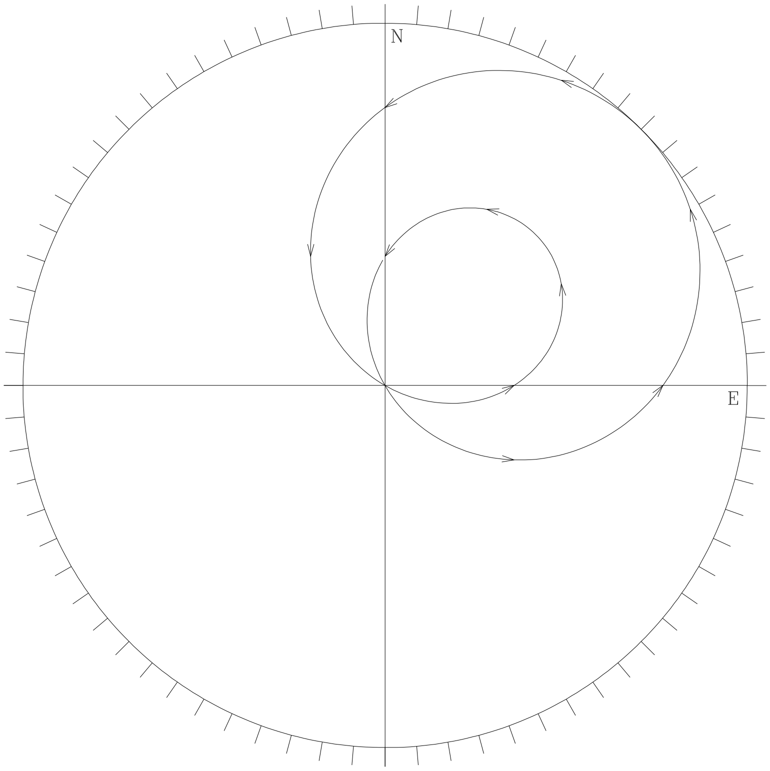

Figure 2.10. Normalized plot of the simple ratio minus one expression (equation 2.23).

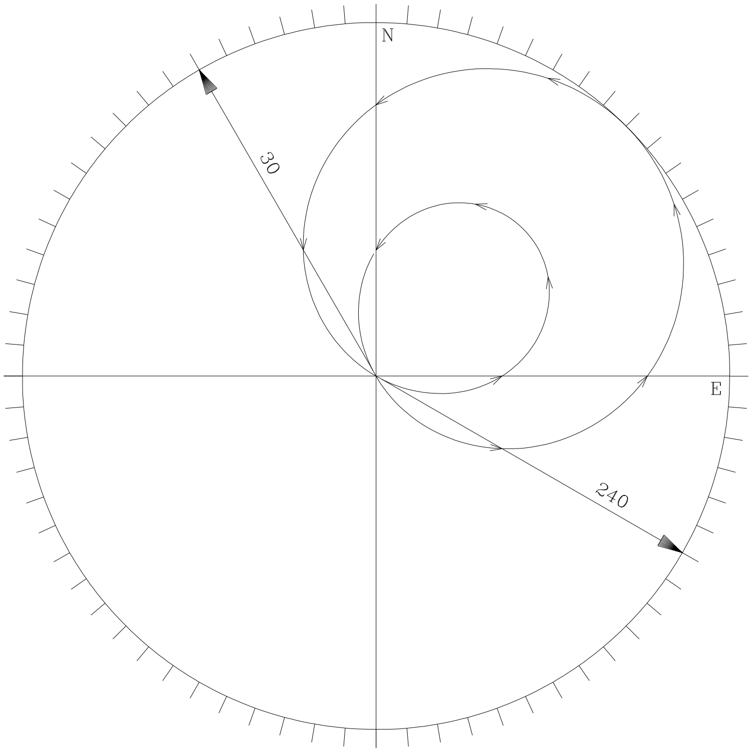

Figure 2.11. Roots of the simple ratio minus one expression (Equation 2.24).

2.4 THE ABSOLUTE RATIO METHOD

Another method of determining the azimuth is to calculate the absolute ratio of the rotated borehole north component signal to the known sensor output similar to the absolute difference equation (Equation 2.14). This ratio is expressed in Equation 2.25 and will be referred to as the absolute ratio method. This ratio should equal 1 if the amplitude and phase response of the two sensors are exactly matched, if the gains of the sensors are equal, if the ground motion input to both sensors is identical, if the sensors are noise free and if they are perfectly aligned.

$$R^{R}(\theta) = \frac{1}{M}\sum_{i=1}^{M}\left|\frac{N_i^{'}(\theta)}{K_i}\right| \tag{2.25}$$

Substituting for $N_i^{'}(\theta)$ and K_i from Equations 2.7 and 2.8 respectively

$$R_i^{A}(\theta) = \left|\frac{-G_E E_i \sin(\theta) + G_N N_i \cos(\theta)}{-G_K E_i \sin(\Delta) + G_K N_i \cos(\Delta)}\right| \tag{2.26}$$

letting $(G_E = G_N = G_K = G)$ and $(N_i = E_i = A_i)$

$$R_i^{A}(\theta) = \left|\frac{-\sin(\theta) + \cos(\theta)}{-\sin(\Delta) + \cos(\Delta)}\right| \tag{2.27}$$

A normalized plot of this equation is shown in Figure 2.12. Since all of the gains are equal and both ground accelerations are equal, the signal outputs of the two sensors should be equal and the absolute ratio function should equal one if the rotated borehole component is aligned with the azimuth of the known sensor.

$$R_i^{A}(\theta) = \left|\frac{-\sin(\theta) + \cos(\theta)}{-\sin(\Delta) + \cos(\Delta)}\right| = 1 \tag{2.28}$$

The roots of Equation 2.29 are not readily apparent in Figure 2.12 but if 1 is subtracted from both sides as

$$R_i^{A}(\theta) - 1 = \left|\frac{-\sin(\theta) + \cos(\theta)}{-\sin(\Delta) + \cos(\Delta)}\right| - 1 = 0 \tag{2.29}$$

Figure 2.12 becomes the curve portrayed in Figure 2.13. Now the roots at $R_i^{A}(\theta) - 1 = 0$ are more readily visualized. There are four roots whose values are shown in Figure 2.14.

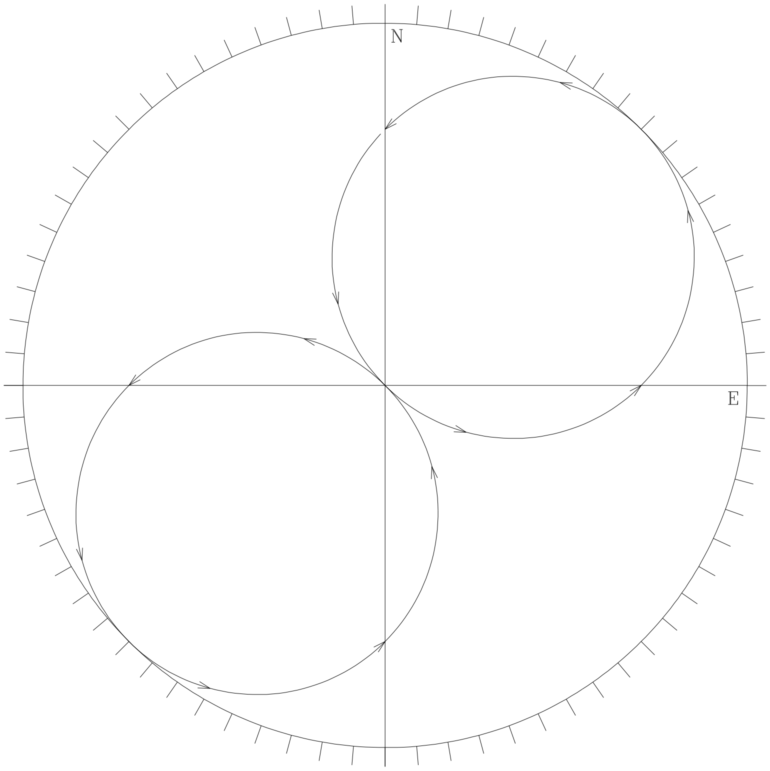

Figure 2.12 Normalized plot of the absolute ratio equation (Equation 2.28) if $N_i = E_i$, $G_K = G_E = G_N$, and $\Delta = 30°$.

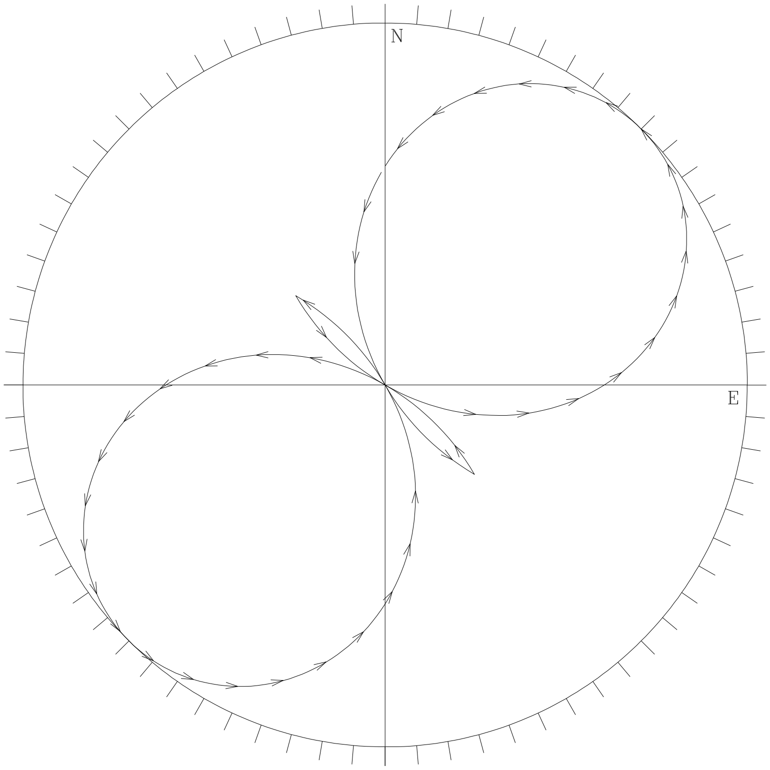

Figure 2.13 Normalized plot of the absolute ratio minus one equation (Equation 2.30) if $G_K = G_E = G_N$ and $N_i = E_i$ and $\Delta = 30°$.

Figure 2.14 Roots of the absolute ration minus one equation (Equation 2.27) if $G_K = G_E = G_N$ and $N_i = E_i$.

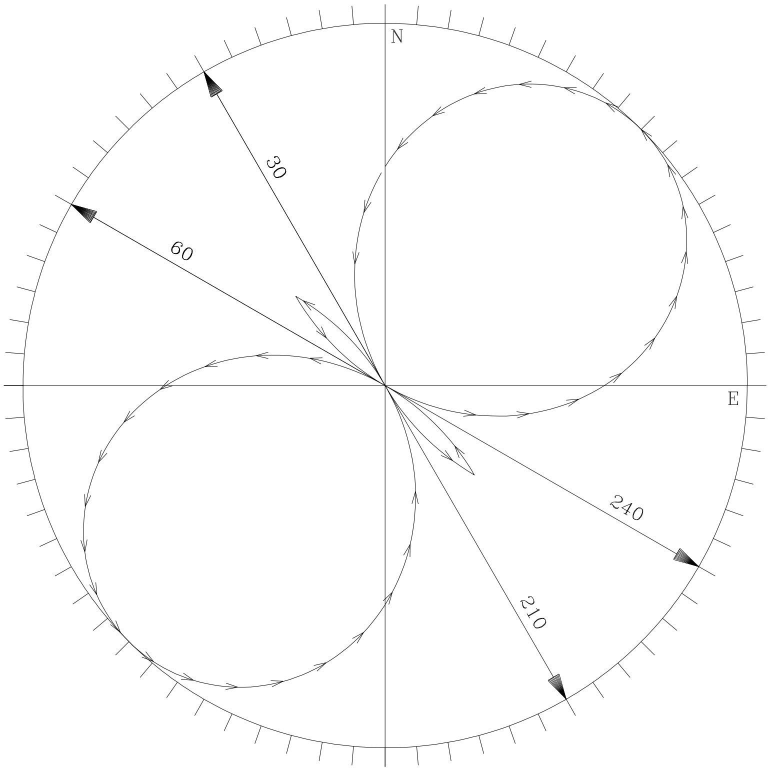

2.5 THE CORRELATION METHOD

Finally, the similarity of the sensor outputs can be quantified with the linear correlation coefficient between the x and y components that is expressed as

$$r = \frac{\sum_{i=1}^{M} (x_i - \overline{x})(y_i - \overline{y})}{\sqrt{\sum_{i=1}^{M} (x_i - \overline{x})^2} \sqrt{\sum_{i=1}^{M} (y_i - \overline{y})^2}} \qquad (2.30)$$

where x and y is the notation from Press et al, 1986. In the notation used in this paper (see Figure 2.3), this equation becomes

$$r = \frac{\sum_{i=1}^{M} (N_o^{'} - \overline{N}^{'})(K_i - \overline{K})}{\sqrt{\sum_{i=1}^{M} (N_i^{'} - \overline{N}^{'})^2} \sqrt{\sum_{i=1}^{M} (K_i - \overline{K})^2}} \qquad (2.30)$$

Noting that $N^{'}$ is a function of θ, the equation becomes

$$r(\theta) = \frac{\sum_{i=1}^{M} (N_i^{'}(\theta) - \overline{N}^{'}(\theta))(K_i - \overline{K})}{\sqrt{\sum_{i=1}^{M} (N_i^{'}(\theta) - \overline{N}^{'}(\theta))^2} \sqrt{\sum_{i=1}^{M} (K_i - \overline{K})^2}} \qquad (2.31)$$

where $\overline{N}(\theta)$ is the mean of the N_i's and $\overline{K}$ is the mean of the K_i's (see Press et al 1986). The correlation coefficient should reach a maximum when the rotated component $N^{'}$ becomes parallel to the azimuth of the unknown component K. The functional dependence of Equation 2.32 on θ as calculated from dummy data for a known sensor orientation of $\Delta = 30°$ is shown in Figure 2.15; the curve in the figure is actually double because the negative valued correlation values directly overlay the positive values in a polar plot. The arrow in Figure 2.16 is drawn in the direction in which $r(\theta)$ reaches a maximum.

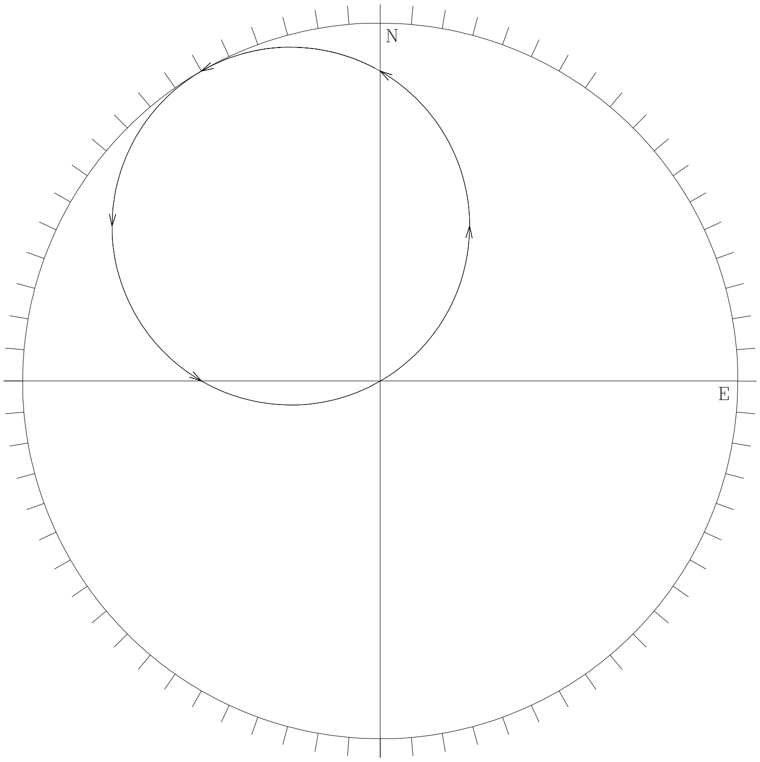

Figure 2.15 Normalized plot of the correlation coefficient as calculated for dummy data for a know sensor orientation of $\Delta = 30°$.

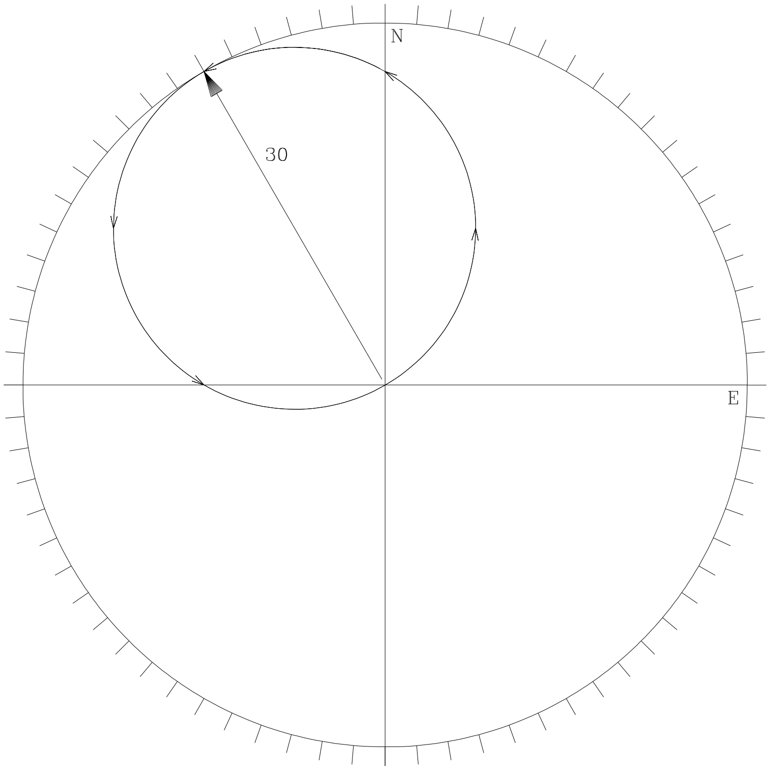

Figure 2.16 Normalized plot of the correlation coefficient as calculated from dummy data for a known sensor orientation of $\Delta = 30°$

2.6 THE COHERENCE METHOD

All five of the azimuth estimation methods discussed so far are time domain procedures. Another candidate for consideration for calculating the azimuth is the frequency domain coherence function as defined by (see Bendat and Piersol, 1986)

$$\gamma_{xy}^2(f) = \frac{\left|G_{xy}(f)\right|^2}{G_x(f)G_y(f)} \tag{2.32}$$

where $\gamma_{xy}^2(f)$ is referred to as the coherence between channels x and y, $G\ (f)$ is the power spectral density function for channel x, $G_y(f)$ is the power spectral density function for channel y, and $G_{xy}(f)$ is the cross-spectral density function between channels x and y.

The x and y channel designations are Bendat and Piersol notation; in terms of the notation used in the current paper (see Figure 2.3), the coherence becomes

$$\gamma_{KN'}^2 = \frac{\left|G_{KN'}(f)\right|^2}{G_K(f)G_{N'}(f)} \tag{2.33}$$

where x and y have been replaced by K and N'. Note that for the current azimuth determination effort, the cross spectral density between K and N' will be a function of θ and the power spectral density of channel N' will also be a function of θ. Therefore, $\gamma_{KN'}^2$ will also be a function of θ as

$$\gamma_{KN'}^2(f,\theta) = \frac{\left|G_{KN'}(f,\theta)\right|^2}{G_K(f)G_{N'}(f,\theta)} \tag{2.34}$$

Figure 2.16 contains a normalized (maximum $\gamma_{KN'}^2(f,\theta)=1$) plot of $\gamma_{KN'}^2(f,\theta)$ as calculated from real data generated by an orthogonal pair of CMG-3NSN sensors located near (a separation of less than 3 feet) the unknown sensor which was oriented 30° CCW from north. Alignment of the horizontal components in the two sensors is indicated by a maximum in the coherence function. The data in Figure 2.16 indicates that the coherence function reaches two equal maximums as the horizontal data is rotated. The rotated azimuths for which the coherence reached a maximum are shown by the two arrows in Figure 2.17. Note that the coherence function cannot resolve whether the two sensors are lined up or misaligned by 180°. The reason is because all phase information is lost in the coherence function; it is calculated by simply taking the ratio of power spectral density functions and the PSD out of a given sensor is the same regardless of the polarity with which it is connected. Therefore, the coherence function alone cannot resolve the azimuth of the borehole sensor system.

Figure 2.15 Example of a plot of the coherence function as generated from real data. The known azimuth was 30° CCW from north.

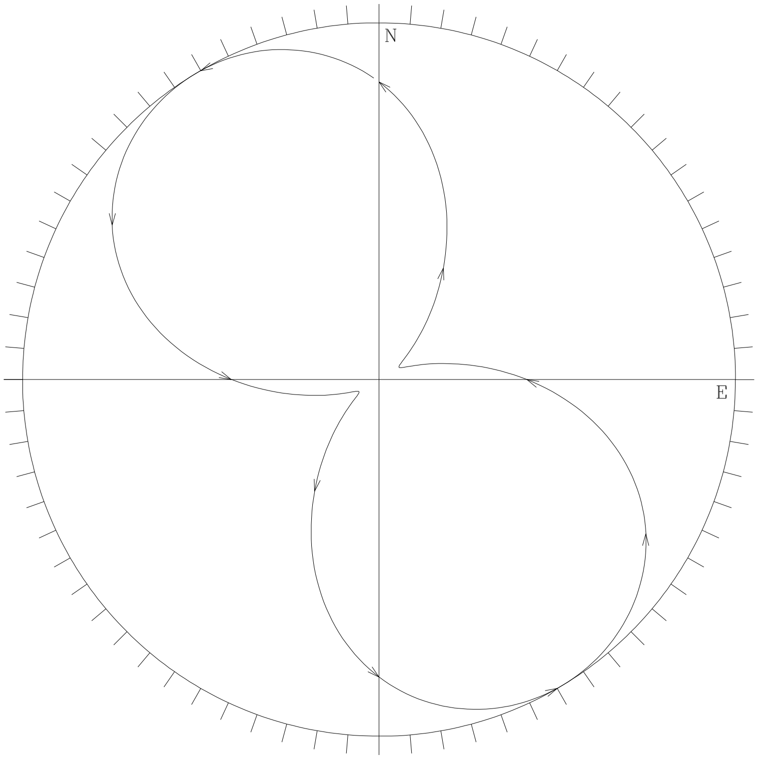

Figure 2.16 Example of a plot of the coherence function as generated from real data with the estimated roots plotted. The known azimuth was 30° CCW from north.

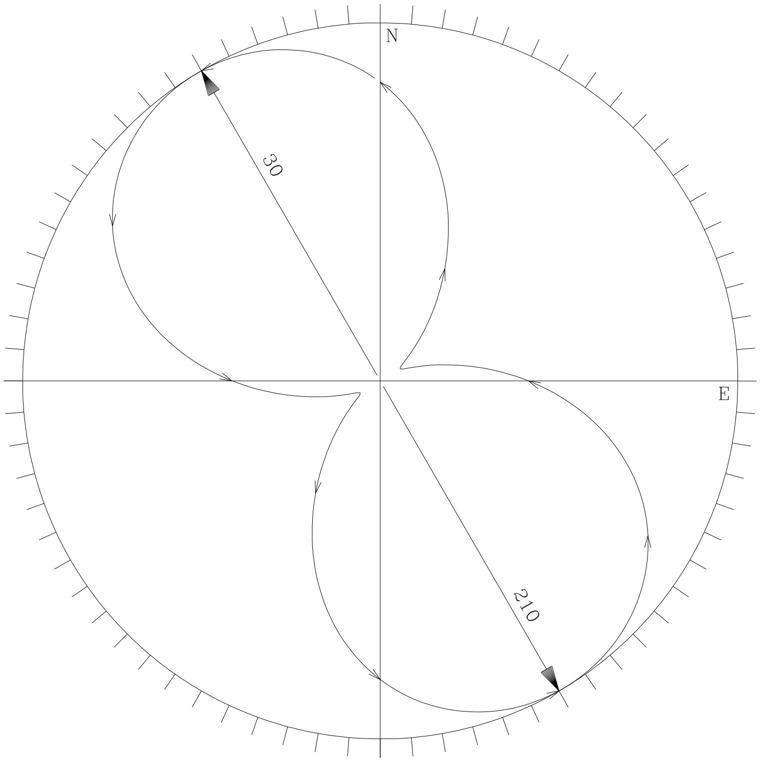

3 GAIN ERRORS

So far in this report, the analysis has been confined to the special case in which the gains of the three sensors are equal ($G_k = G_e = G_N$) and the acceleration in the N and E directions are equal ($N_i = E_i$). If the gains are not equal errors arise in the calculated azimuths; the magnitude of these errors can be estimated as follows.

If $N_i = E_i = A_i$ the simple difference equation (Equation 2.10) can be written as

$$D_i^S(\theta) = A_i(G_N \cos(\theta) - G_E \sin(\theta) + G_K(\sin(\Delta) - \cos(\Delta))) \tag{3. 1}$$

The azimuths θ for which this expression is equal to zero will depend on the relative sizes of the gains of the three sensors. If the gains of the individual sensors are not considered when analyzing real data, errors will arise in the derived azimuths. The magnitude of these errors can be studied by holding the gain of two of the sensors constant while allowing the third gain to vary. The results of this procedure for the simple difference expression of Equation 3.1 are shown in Figure 3.1. The data in the figure was calculated by holding the gain of two of the sensors constant at 1.0 and allowing the gain of the third sensor to vary from 0.8 to 1.2. This procedure was performed three times to generate the three curves in the figure.

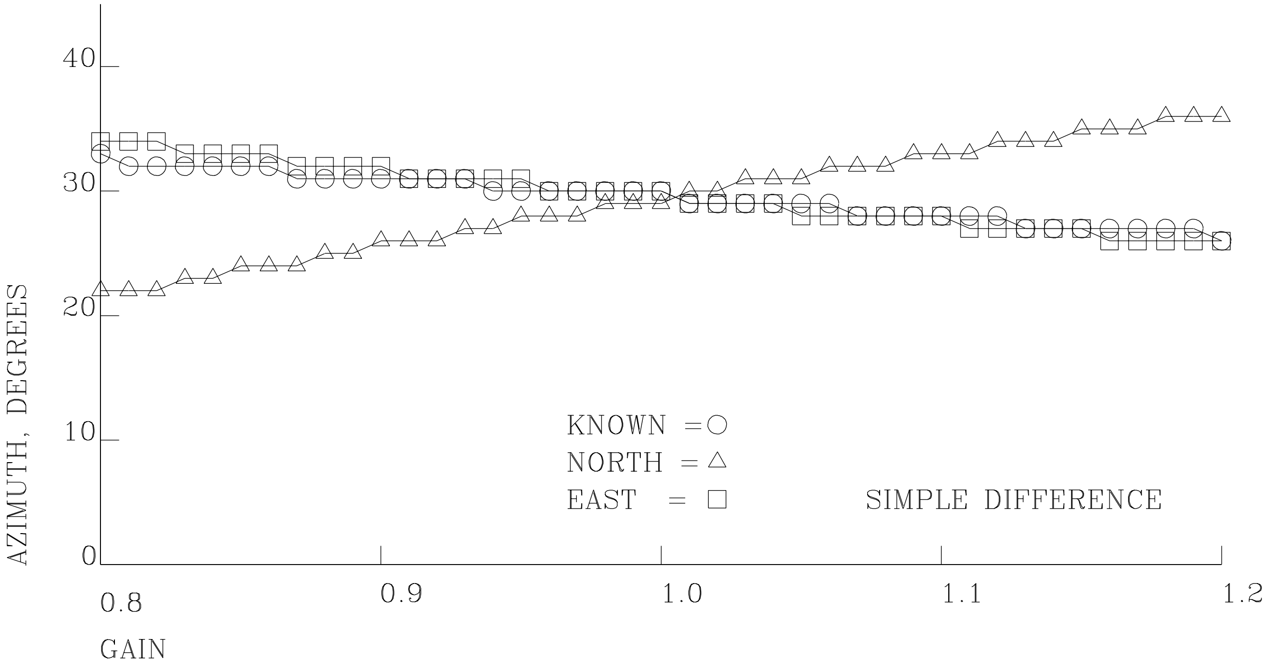

Figure 3. 1 Calculated azimuths produced by varying one gain at a time with the other two gains equal to 1 for the simple difference method of Equation 3.1 with $N_i = E_i$. The known azimuth was $30°$.

As the figure indicates, significant errors occur in the calculated azimuth if the gain of a sensor departs very far from 1.0. For greatest accuracy, the gains of the sensors should be either be closely matched or unequal gains should be compensated for in the data analysis process.

If $N_i = E_i = A_i$, the absolute difference equation (Equation 2.16) becomes

$$D_i^S(\theta) = A_i \left| G_N \cos(\theta) - G_E \sin(\theta) + G_K (\sin(\Delta) - \cos(\Delta)) \right| \tag{3. 2}$$

As in the simple difference case, the azimuths θ for which this expression is a minimum will depend on the relative sizes of the gains of the three sensors. The errors generated by varying the three gains from 0.8 to 1.2 one at a time are shown in Figure 3.2.

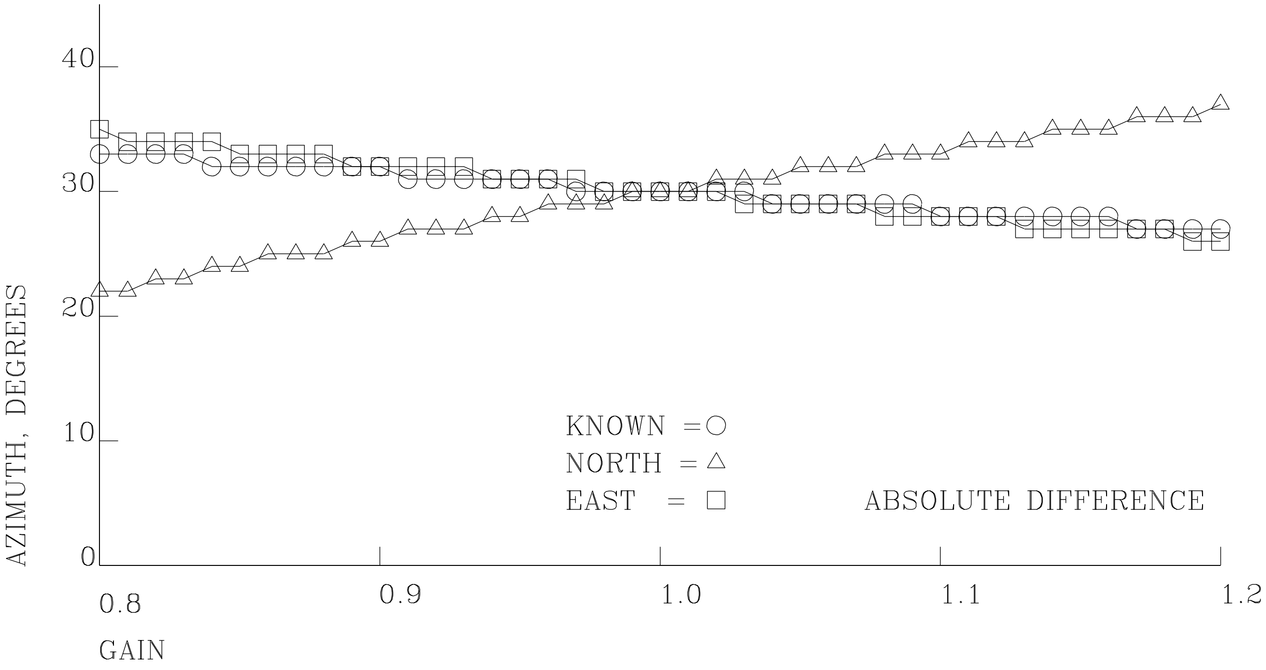

Figure 3. 2 Calculated azimuths produced by varying one gain at a time with the other two gains equal to 1 for the absolute difference method of Equation 3.2 with $N_i = E_i$. The known azimuth was $30°$.

The azimuth errors for the absolute difference equation are exactly the same as for the simple difference equation. Error calculation results for the simple ratio minus one equation are in Figure 3.3. Here the potential error for a given gain mismatch is greater than in the two previous cases. Finally, Figure 3.4 presents the error analysis for the absolute ratio minus 1 equation. These results indicate that significant errors may occur in calculated azimuths if the calculations do not correct for gain differences regardless of the azimuth calculation method.

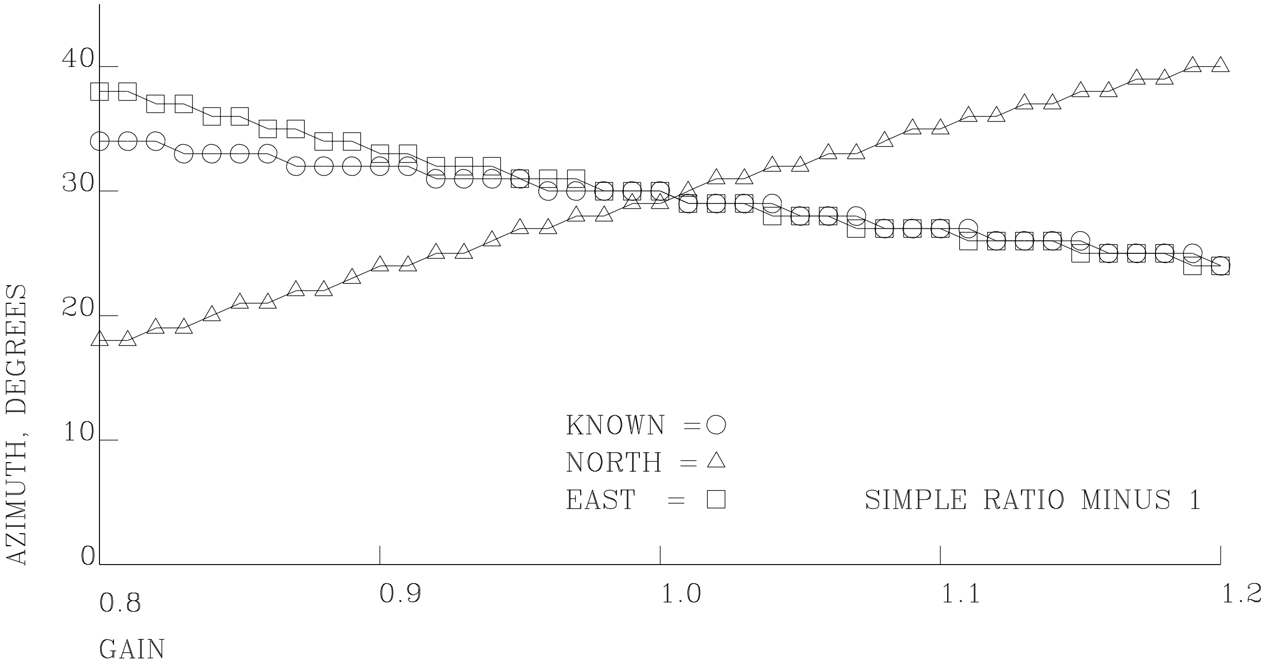

Figure 3. 3 Calculated azimuths produced by varying one gain at a time with the other two gains equal to 1 for the simple ratio minus 1 method of with $N_i = E_i$. The known azimuth was 30°.

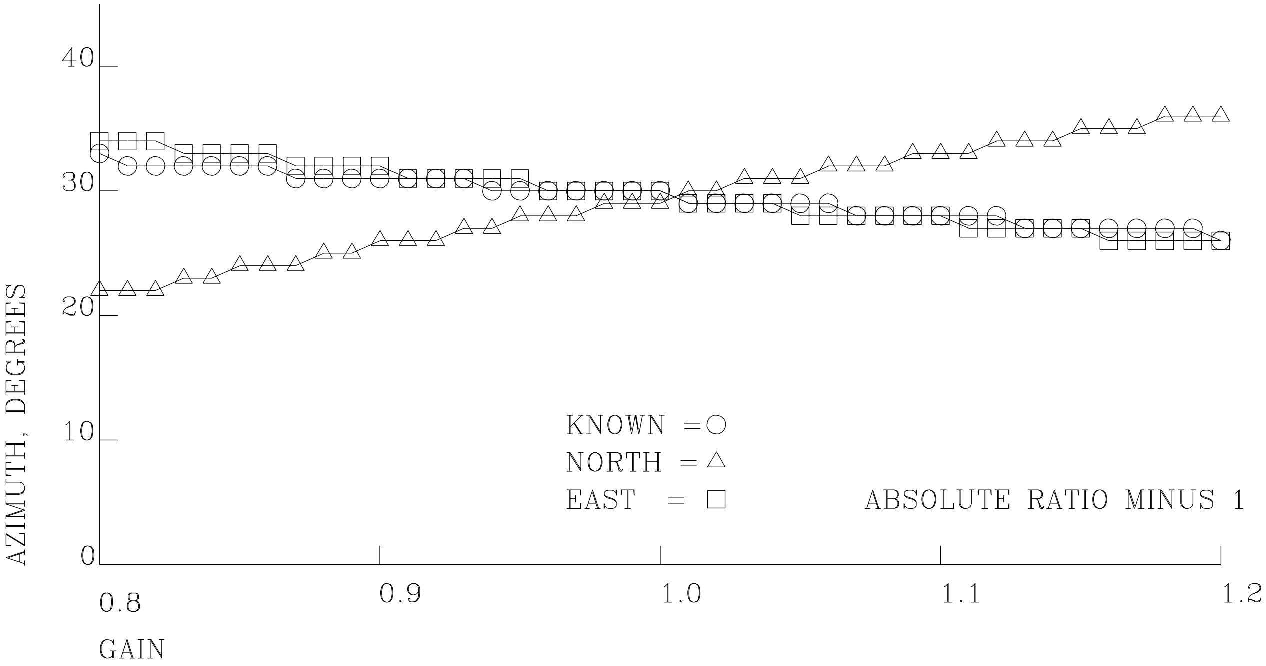

4 TIME DOMAIN AZIMUTH CALCULATIONS USING DUMMY DATA

It should be informative to illustrate how the various methods for calculating the azimuth perform on dummy data. Dummy data was generated by using Equations 2.1 and 2.2 to rotate the outputs of the original borehole components (N and E in Figure 2.1) to a known azimuth with respect to their original positions $N^{'}$ and $E^{'}$ in Figure 2.1). The rotated north component samples $N_i^{'}(\theta)$ in Equation 2.1 were then treated as the output of the known sensor at Δ_1 counterclockwise from the borehole north sensor and the rotated east component samples $E_i^{'}(\theta)$ were treated as the output of a second known sensor at Δ_2 counterclockwise from the borehole north sensor.

The results obtained by applying all five time domain azimuth calculation methods to this dummy data are shown in Figures 4.1 through 4.12. Figures 4.1, 4.2, and 4.3 contain the azimuths calculated from three sequential 3600 point time sequences (M=3600 in Equations 2.3, 2.14, 2.19, 2.25, and 2.31) without correcting for the individual gains of the sensors for an unknown azimuth of $30°$. Inspection of the three figures indicates that all five methods successfully calculate the unknown azimuth but there are some details which may not be obvious. Note that all three results for the simple difference calculation (upper left corner in all three figures) contain two roots, one at exactly the unknown azimuth of $30°$ in all three figures and the second at three different azimuths ($340°$ in Figure 4.1, $122°$ in Figure 4.2, and $153°$ in Figure 4.3). The variation in the azimuth of the second root may seem strange but, as was the case for the simplified case in Section 2.1; the variation be explained as follows.

From equation 2.8, the i'th sample of the output of the first known sensor can be written as

$$K_i = -G_E E_i \sin(\Delta) + G_N N_i \cos(\Delta) \tag{4.1}$$

where G_K in Equation 2.8 has been replaced with the gains of the north and east components of the borehole sensor G_N and G_E because the known current signal was generated by rotating the borehole outputs. The ith sample of the simple difference expression (Equation 2.10) becomes

$$D_i^S(\theta) = E_i(G_E \sin(\Delta) - G_E \sin(\theta)) \_ N_i(G_N \cos(\theta) - G_N \cos(\Delta)) \tag{4.2}$$

Regrouping terms yields

$$D_i^S(\theta) = E_i G_E (\sin(\Delta) - \sin(\theta) + N_i G_N (\cos(\theta) - \cos(\Delta) \tag{4.3}$$

If the sensors are aligned in space, this expression is equal to zero

$$E_i G_E (\sin(\Delta) - \sin(\theta)) + N_i G_N (\cos(\theta) - \cos(\Delta)) = 0 \tag{4.4}$$

Obviously, $D_i^S(\theta)$ equals zero if $\theta = \Delta$; this root will always be equal to Δ. There will also be another root depending on the relative magnitudes of $G_N, G_E, N_i,$ and E_i. The azimuth corresponding to this root will vary from sample to sample as the amplitudes of N_i and E_i change with respect to one another Thus the azimuth corresponding to the second root of Equation 4.4 will be a function of the relative amplitudes of N_i and E_i and it will in all probability be different for each time segment of data. This explains why the second azimuths in the simple difference portion of Figures 4.1, 4.2, and 4.3 are drastically different from one another.

The absolute difference azimuths shown in the upper right corner of Figures 4.1, 4.2, and 4.3 as calculated with Equation 4.5 which was derived from Equation 2.16 are more well behaved than the simple difference azimuths. The absolute difference never crosses zero; it is either equal to zero or it reaches a minimum. There is only one azimuth for which this is true for each segment and it is exactly at $30°$ CCW from north in all three figures just as it should be and $D_i^A(\theta)$ approaches zero in all three figures just as it should.

$$D_i^A(\theta) = \left| E_i G_E(\sin(\Delta) - \sin(\theta) + N_i G_N(\cos(\theta) - \cos(\Delta)) \right| \tag{4.5}$$

The simple ratio minus 1 azimuths (middle left) in Figures 4.1, 4.2, and 4.3 are double valued as were the simple difference azimuths. One of them is equal to $30°$ in all three figures whereas the second one is $119°$ in Figure 4.1, $19°$ in Figure 4.2, and $11°$ in Figure 4.3. The lack of uniqueness of the second azimuth may be explained by substituting G_E and G_N for G_K in Equation 2.20 to obtain

$$R_i^S - 1 = \frac{-G_E E_i \sin(\theta) + G_N N_i \cos(\theta)}{-G_E E_i \sin(\Delta) + G_N N_i \cos(\Delta)} - 1 \tag{4.6}$$

If the sensors are aligned in space, this expression must be equal to zero or

$$G_E E_i(\sin(\Delta) - \sin(\theta)) + G_N N_i(\cos(\theta) - \cos(\Delta)) = 0 \tag{4.7}$$

Once again, this expression is obviously true if $\theta = \Delta$. There will also be another root depending on the relative values of G_N, G_E, N_i, and E_i. Therefore, the second azimuth in the dummy simple ratio minus 1 azimuths will vary depending on the relative amplitude of the earth motion.

At this point, the astute reader may note that the simple difference plots obtained from dummy data in the upper left corners of Figures 4.1, 4.2, and 4.3 are not the same as the simple ratio minus 1 plots in the middle left of the same figures as might be expected based on the results the theoretical derivation of the simple ratio minus 1 expressions in Section 2.3. Despite considerable thought and investigation of this discrepancy, the reason for the apparent disagreement between the mathematical model and the real world has not been discovered. The problem persists for all of the real data results presented in this report.

The absolute ratio azimuths (middle right side of page) in Figures 4.1, 4.2, and 4.3 behave much like the absolute difference azimuths; they reach a minimum but in this case there are two azimuths for which the absolute ratio reaches a minimum. Therefore, the absolute ratio method (Equation 4.8) for determining the orientation of unknown sensors is not capable of uniquely resolving an unknown azimuth.

$$R_i^A = \left| \frac{-G_E E_i \sin(\theta) + G_N N_i \cos(\theta)}{-G_E E_i \sin(\Delta) + G_N N_i \cos(\Delta)} \right| \tag{4.8}$$

Finally, the results of determining the unknown azimuth using the correlation coefficient of Equation 2.33 are show in the lower left corners of Figures 4.1, 4.2, and 4.3. All three of the azimuths are at $30°$ CCW from north as they should be.

The results obtained by applying all five time domain azimuth calculation methods to a second known azimuth are shown in Figures 4.4, 4.5, and 4.6. In this case the known azimuth was $300°$ and the azimuths were not corrected for sensor gain. All five azimuth calculation methods successfully determined the $300°$ azimuth to within a degree. Once again there is a wide variation in the second azimuth obtained by the simple difference and simple ratio minus one methods.

The next six figures (Figures 4.8 through 4.13) contain the results of reapplying the five azimuth estimation methods to the same set of data as in Figures 4.2 thorough 4.7 but this time the analysis includes a correction for the gains of the individual sensors. Correcting for the sensor gain should improve the overall accuracy of the azimuth estimate. For this dummy data example, the uncorrected azimuths were already very accurate so little improvement is evident when the gain correction was added. However, the detailed shape of some of the azimuthal plots does change rather drastically and the value of the second azimuth calculated by the simple difference and simple ratio minus one methods change significantly when the gain correction is added.

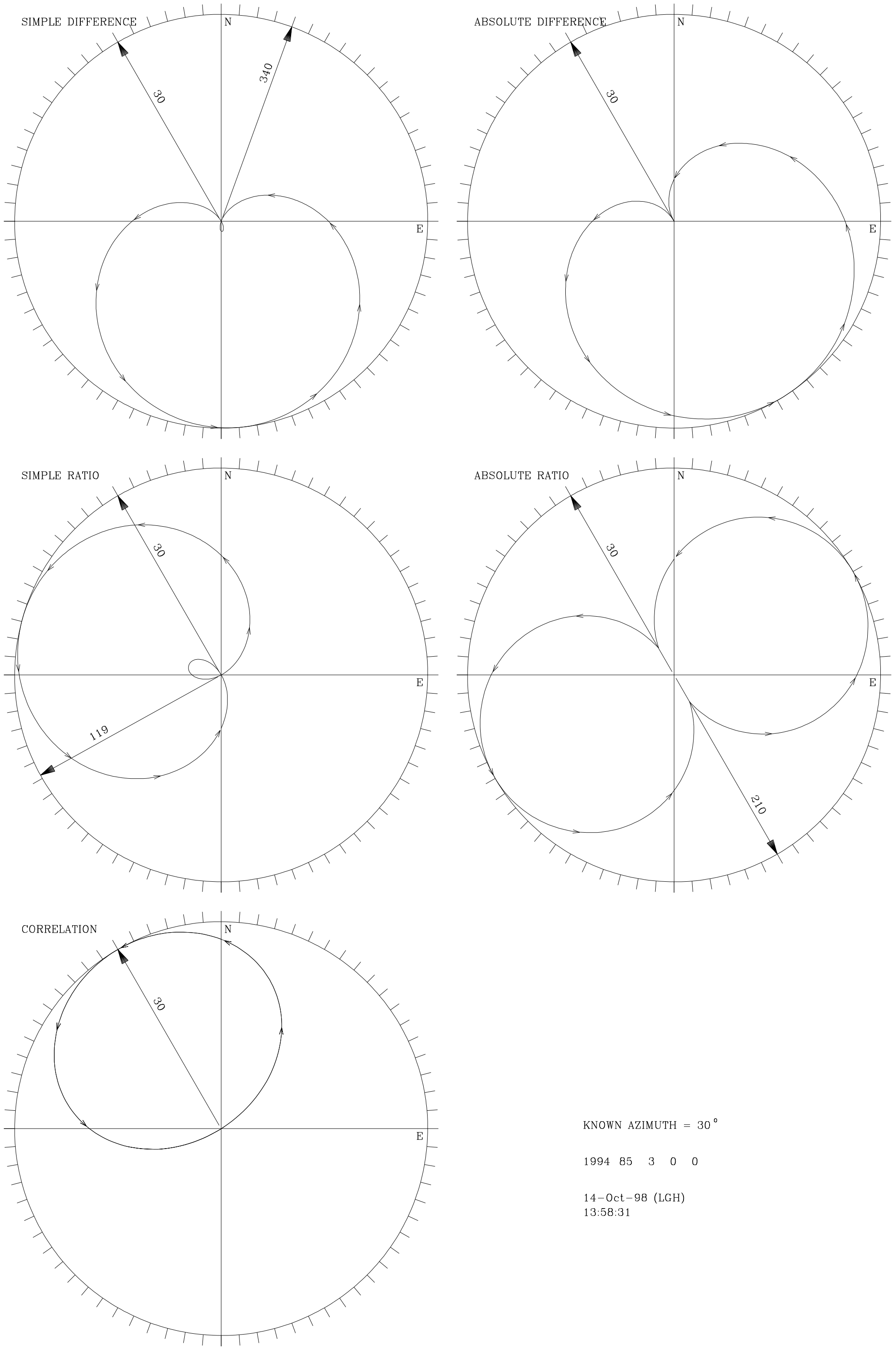

Figure 4. 1 Azimuth function plots generated from uncorrected gain artificial data as calculated from Equations 2.3, 2.14, 2.19, 2.26 and 2.33. The known azimuth was 30° CCW from north.

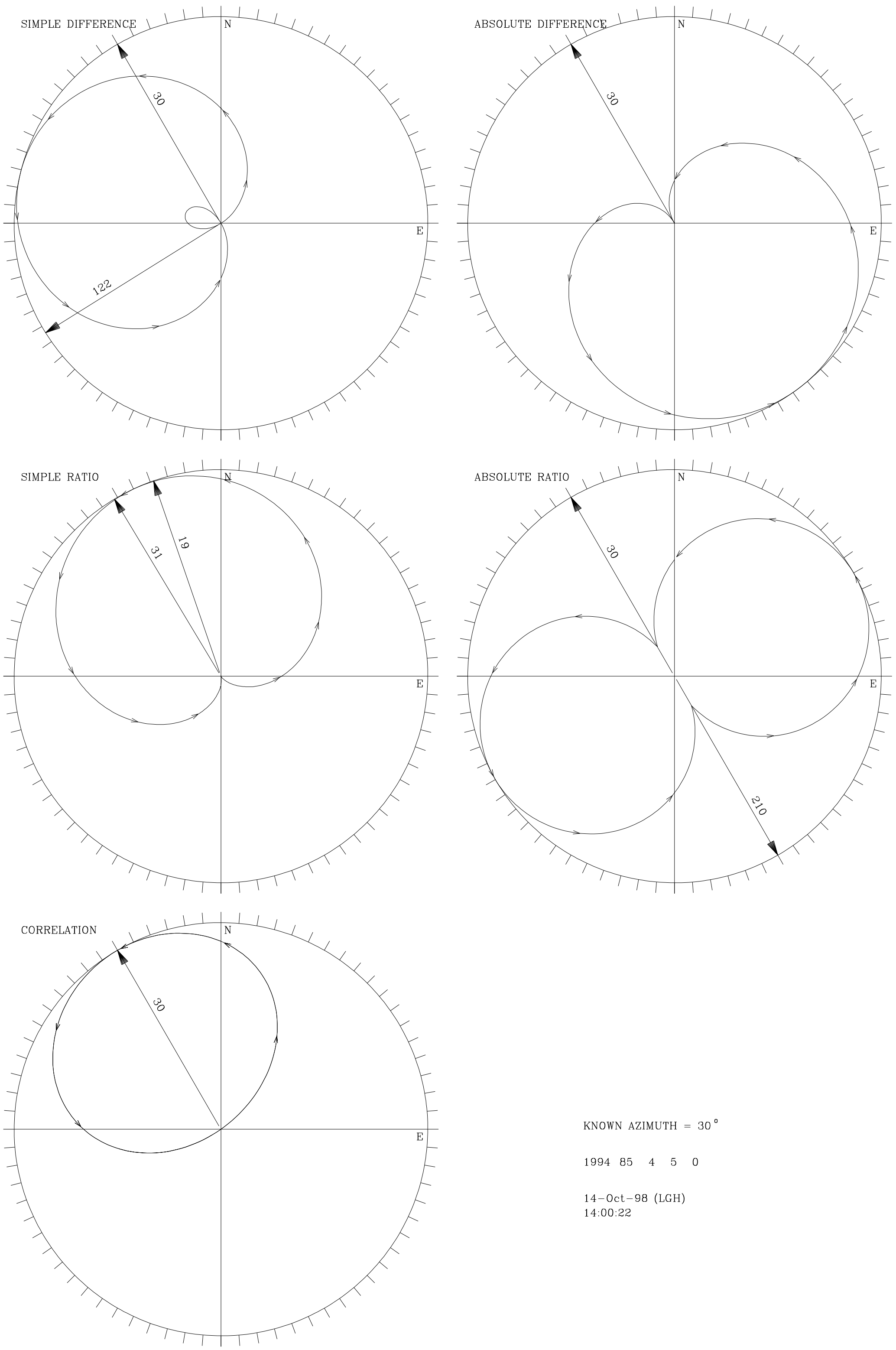
SIMPLE DIFFERENCE

ABSOLUTE DIFFERENCE

SIMPLE RATIO

ABSOLUTE RATIO

CORRELATION

KNOWN AZIMUTH = 30°

1994 85 4 5 0

14-Oct-98 (LGH)
14:00:22

Figure 4. 2 Azimuth function plots generated from uncorrected gain artificial data as calculated from equations 2.3, 2.14, 2.19, 2.26, and 2.33. The known azimuth was 30° CCW from north.

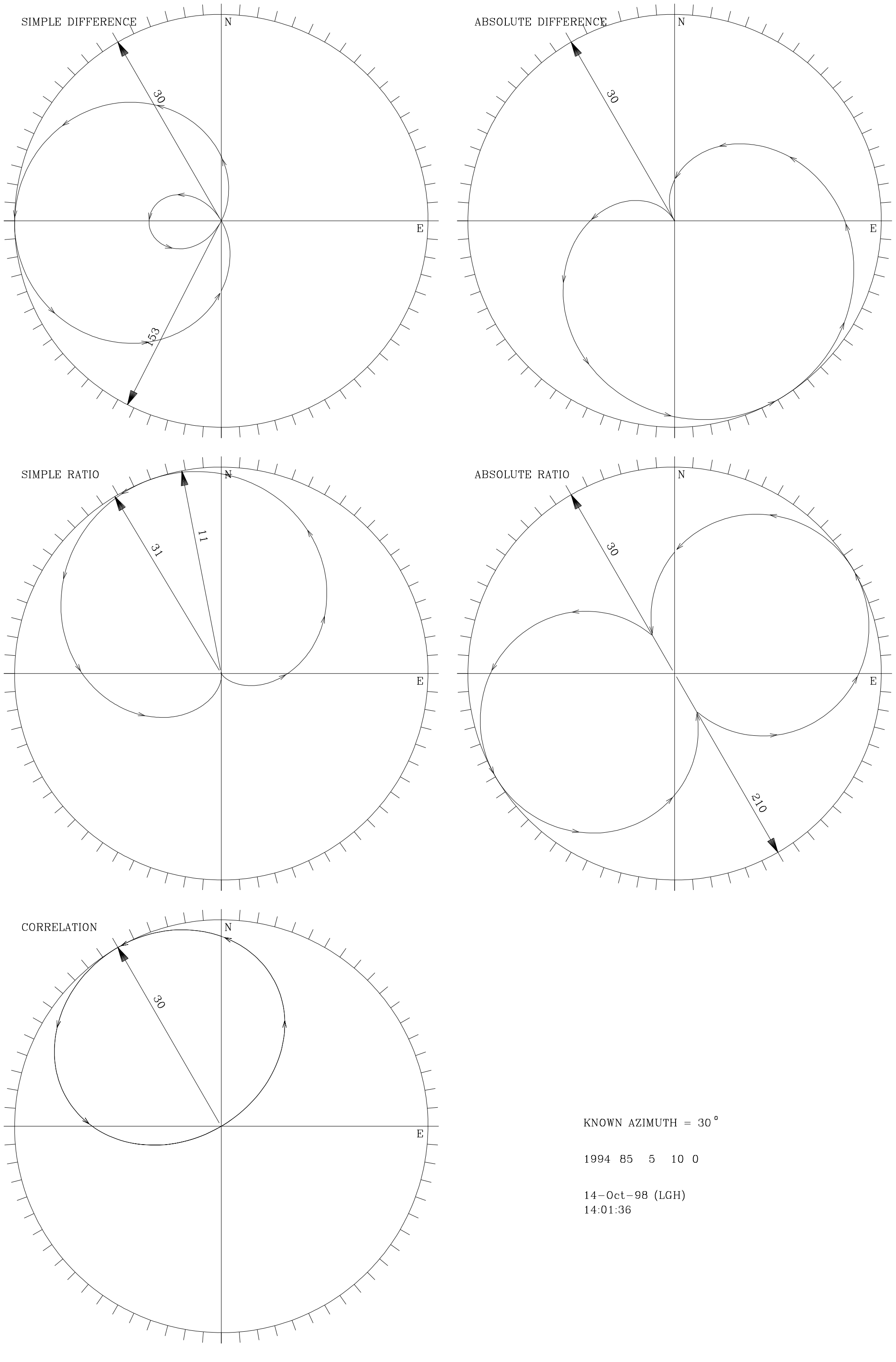

Figure 4. 3 Azimuth function plots generated from uncorrected gain artificial data as calculated from equations 2.3, 2.14, 2.19, 2.26, and 2.33. The known azimuth was 30° CCW from north.

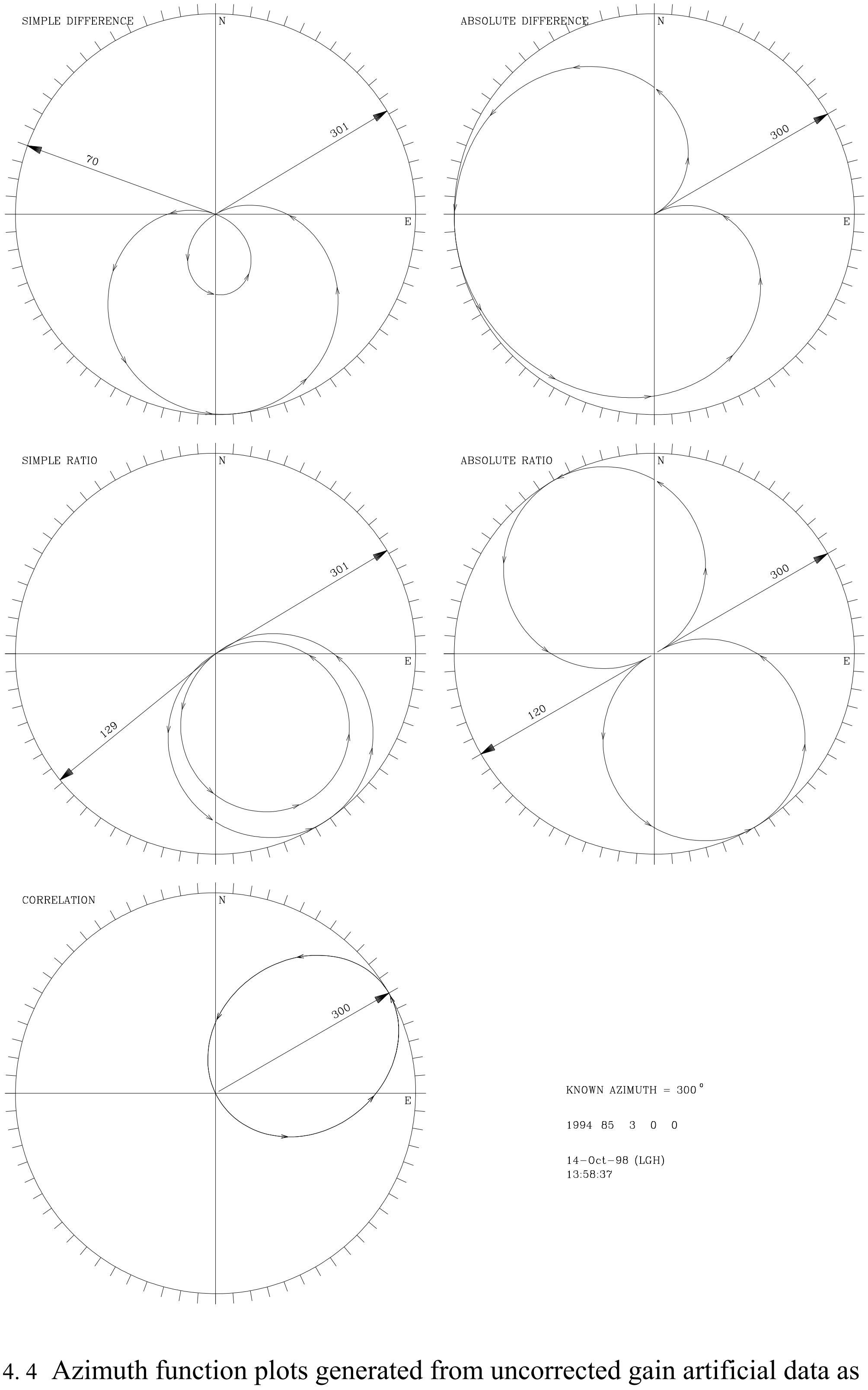

Figure 4. 4 Azimuth function plots generated from uncorrected gain artificial data as calculated from equations 2.3, 2.14, 2.19, 2.26, and 2.33. The known azimuth was 300° CCW from north.

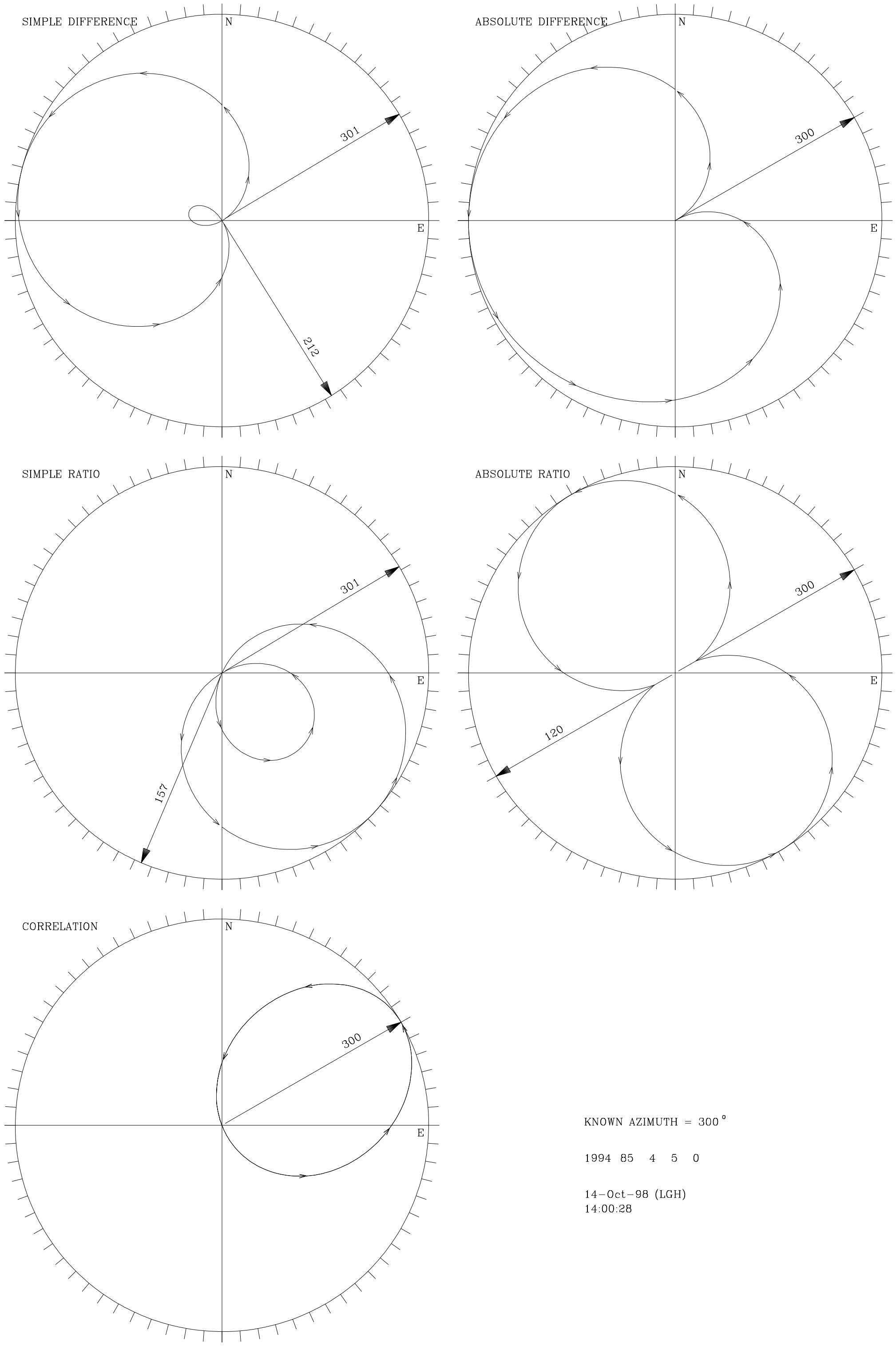

KNOWN AZIMUTH = 300°

1994 85 4 5 0

14-Oct-98 (LGH)
14:00:28

Figure 4. 5 Azimuth function plots generated from uncorrected gain artificial data as calculated from equations 2.3, 2.14, 2.19, 2.26, and 2.33. The known azimuth was 300° CCW from north.

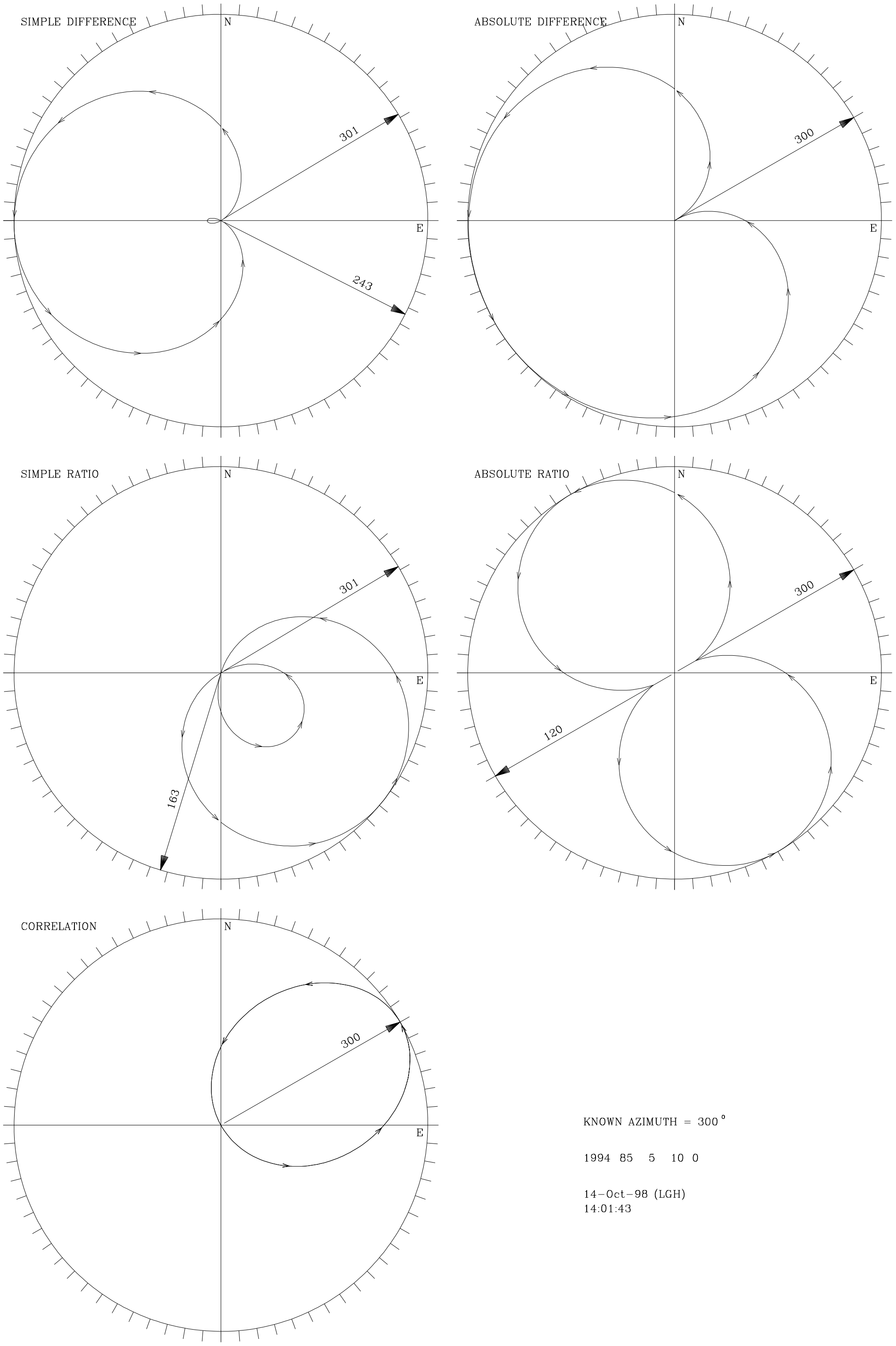

KNOWN AZIMUTH = 300°

1994 85 5 10 0

14-Oct-98 (LGH)
14:01:43

Figure 4. 6 Azimuth function plots generated from uncorrected gain artificial data as calculated from equations 2.3, 2.14, 2.19, 2.26, and 2.33. The known azimuth was 300° CCW from north.

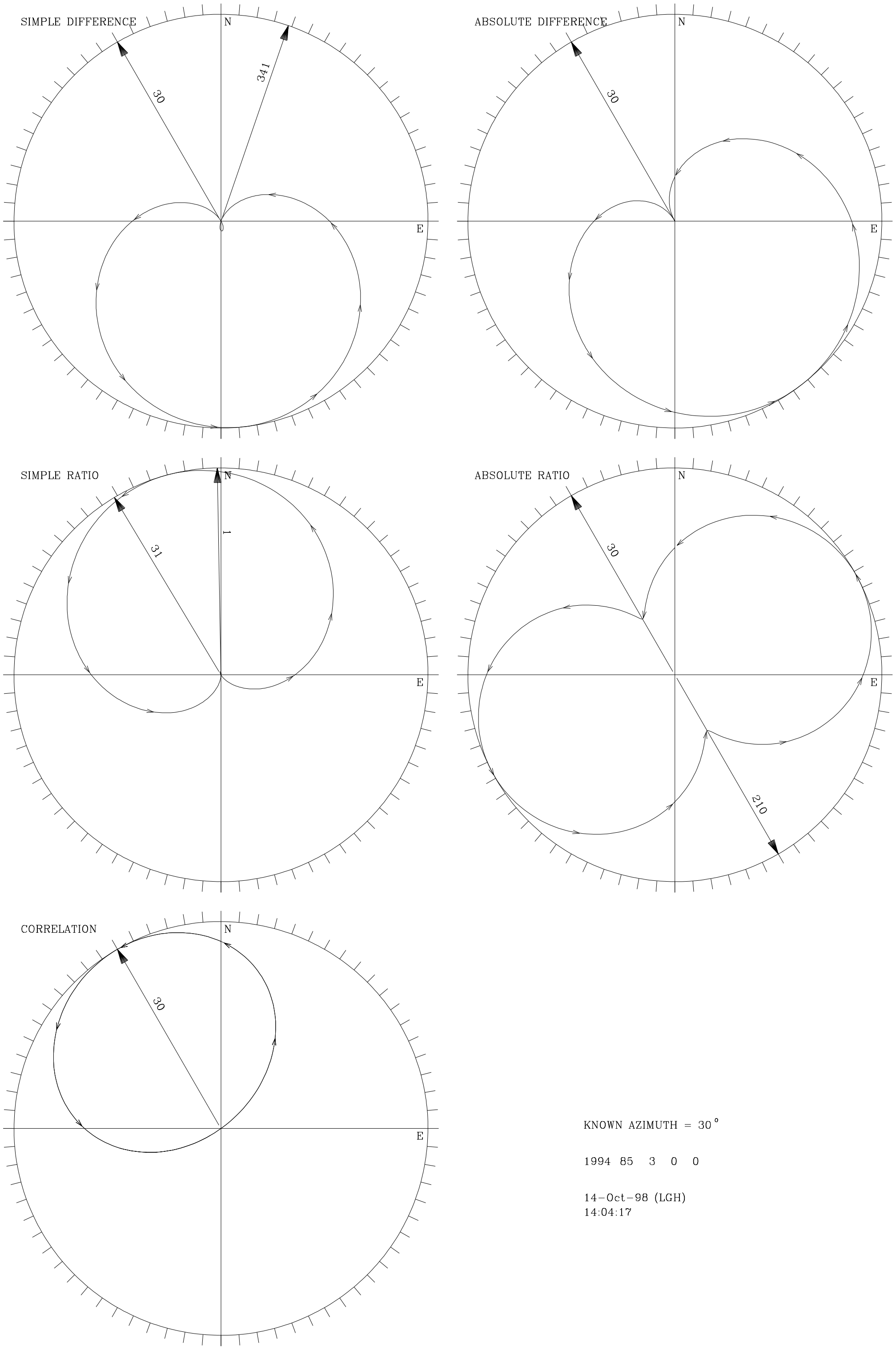

Figure 4. 7 Azimuth function plots generated from corrected gain artificial data as calculated from equations 2.3, 2.14, 2.19, 2.26, and 2.33. The known azimuth was 30° CCW from north.

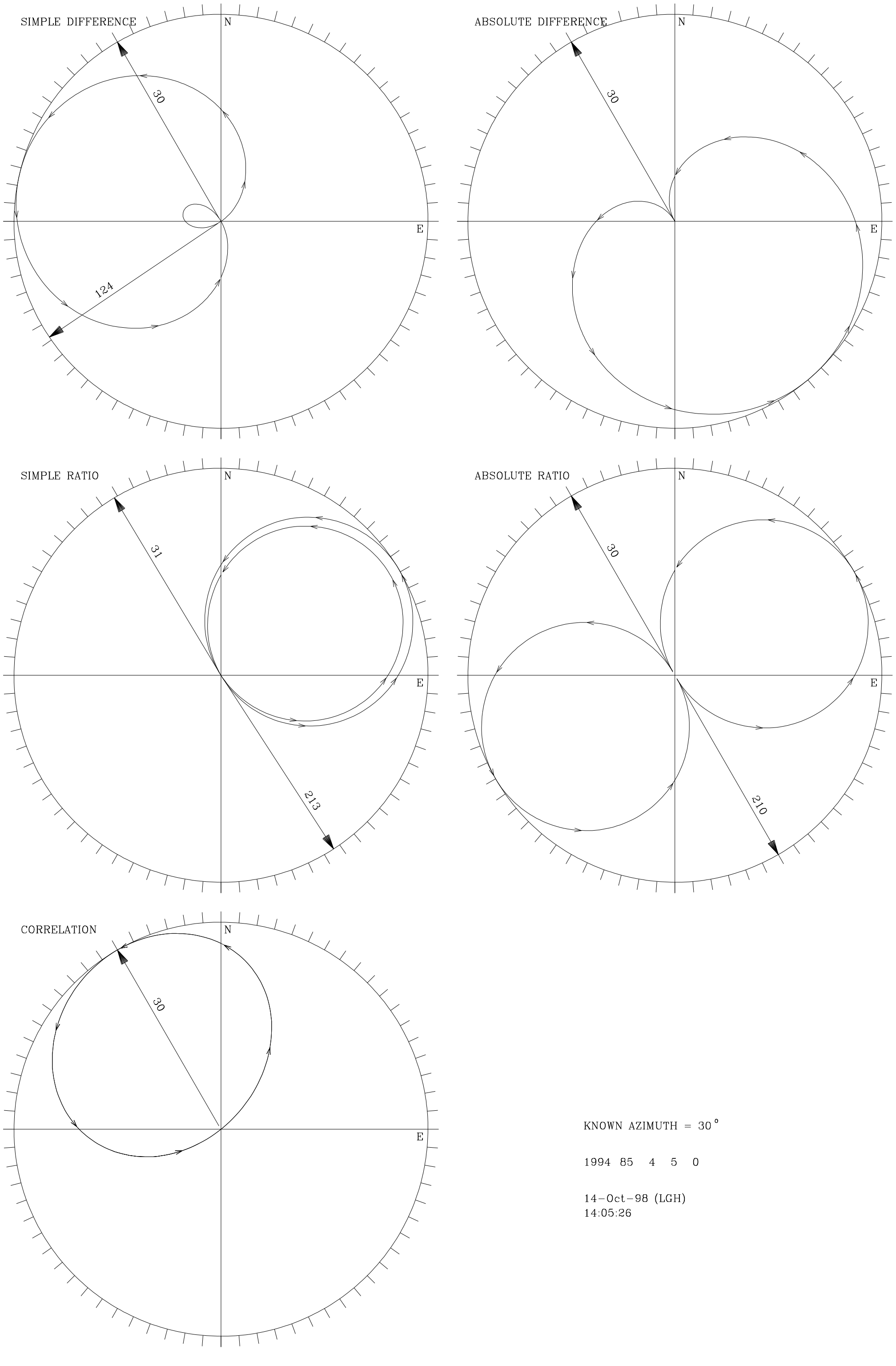

Figure 4. 8 Azimuth function plots generated from corrected gain artificial data as calculated from equations 2.3, 2.14, 2.19, 2.26, and 2.33. The known azimuth was 30° CCW from north.

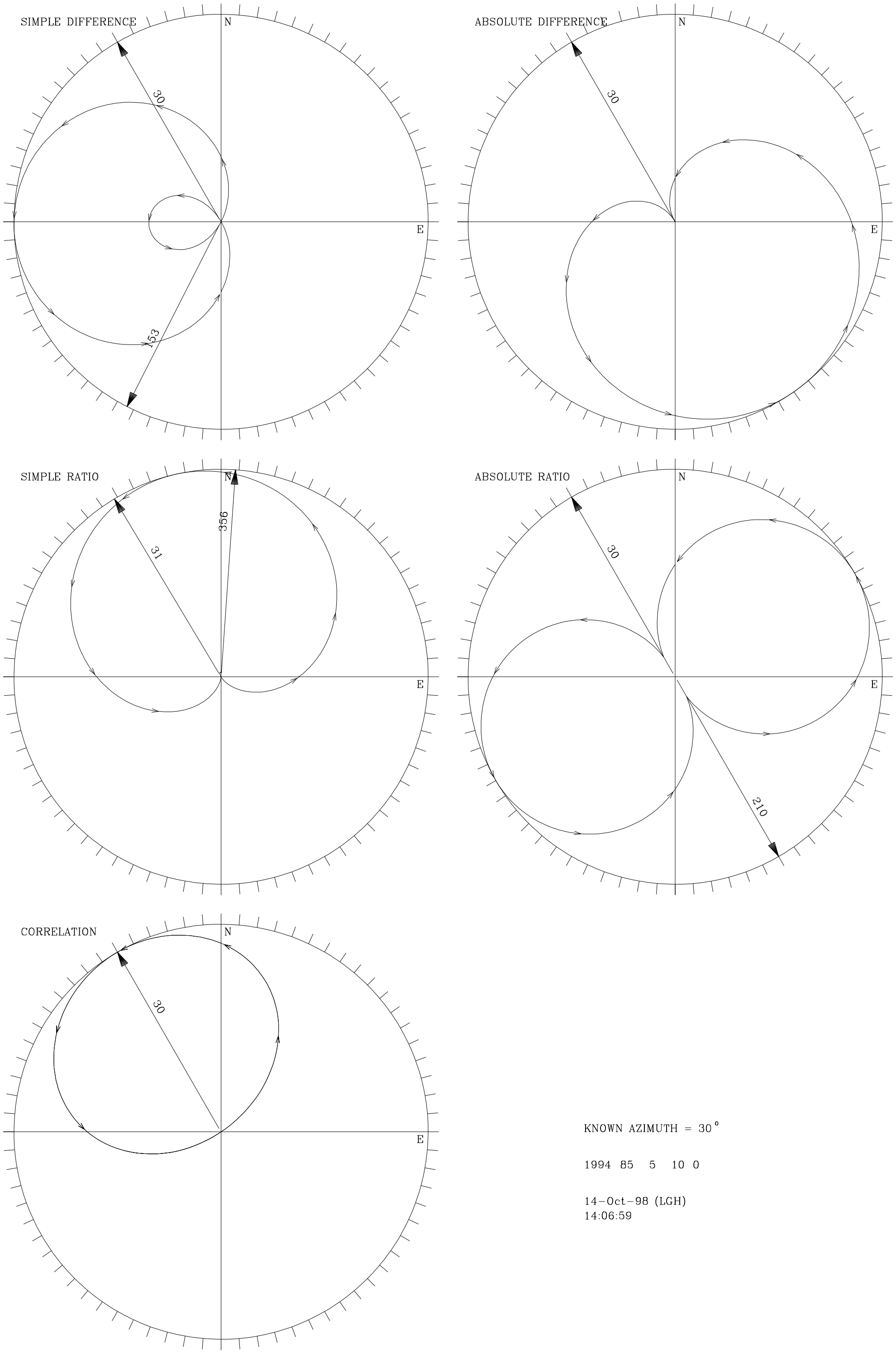

Figure 4. 9 Azimuth function plots generated from corrected gain artificial data as calculated from equations 2.3, 2.14, 2.19, 2.26, and 2.33. The known azimuth was 30° CCW from north.

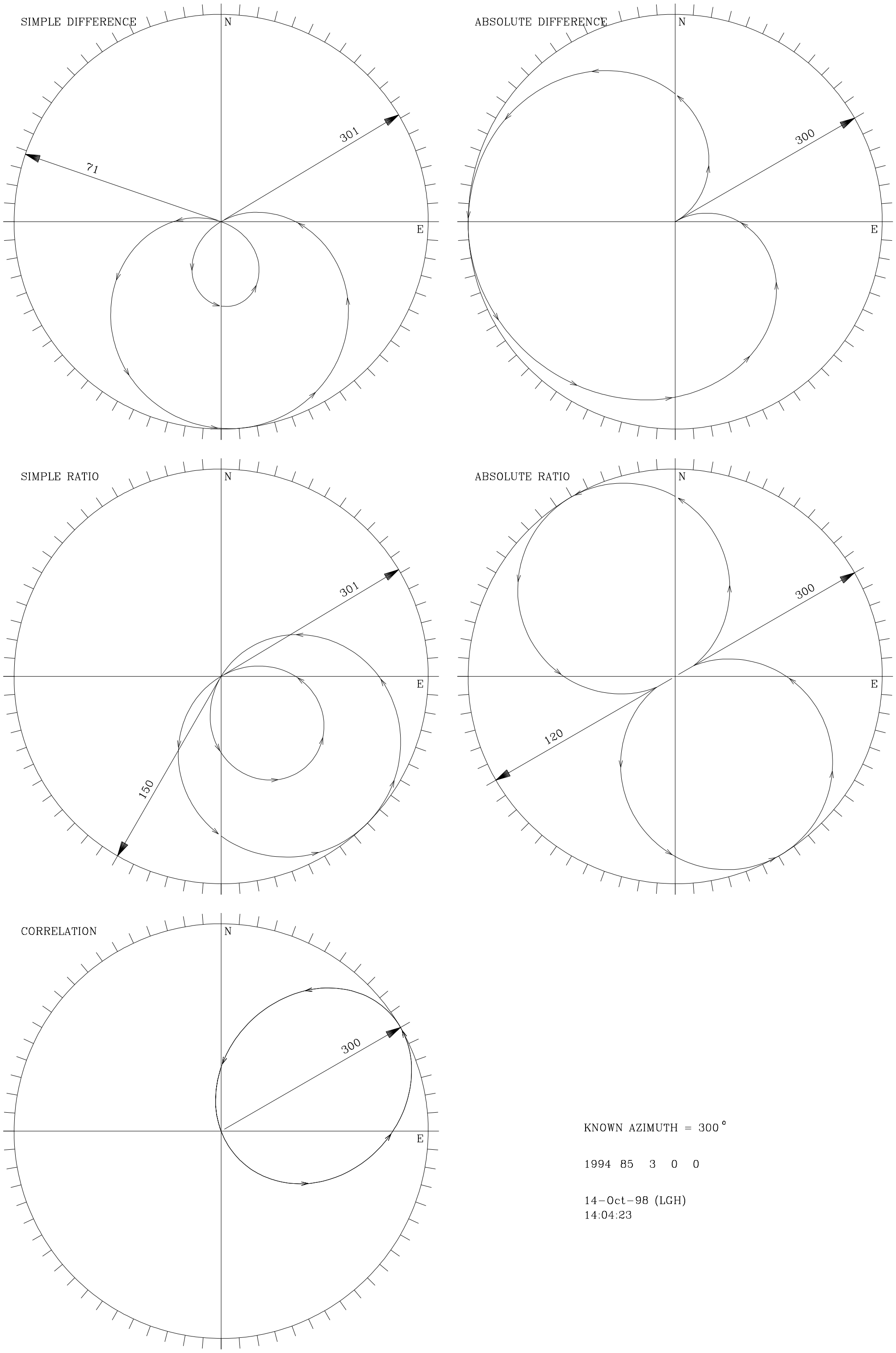

Figure 4. 10 Azimuth function plots generated from corrected gain artificial data as calculated from equations 2.3, 2.14, 2.19, 2.26, and 2.33. The known azimuth was 300° CCW from north.

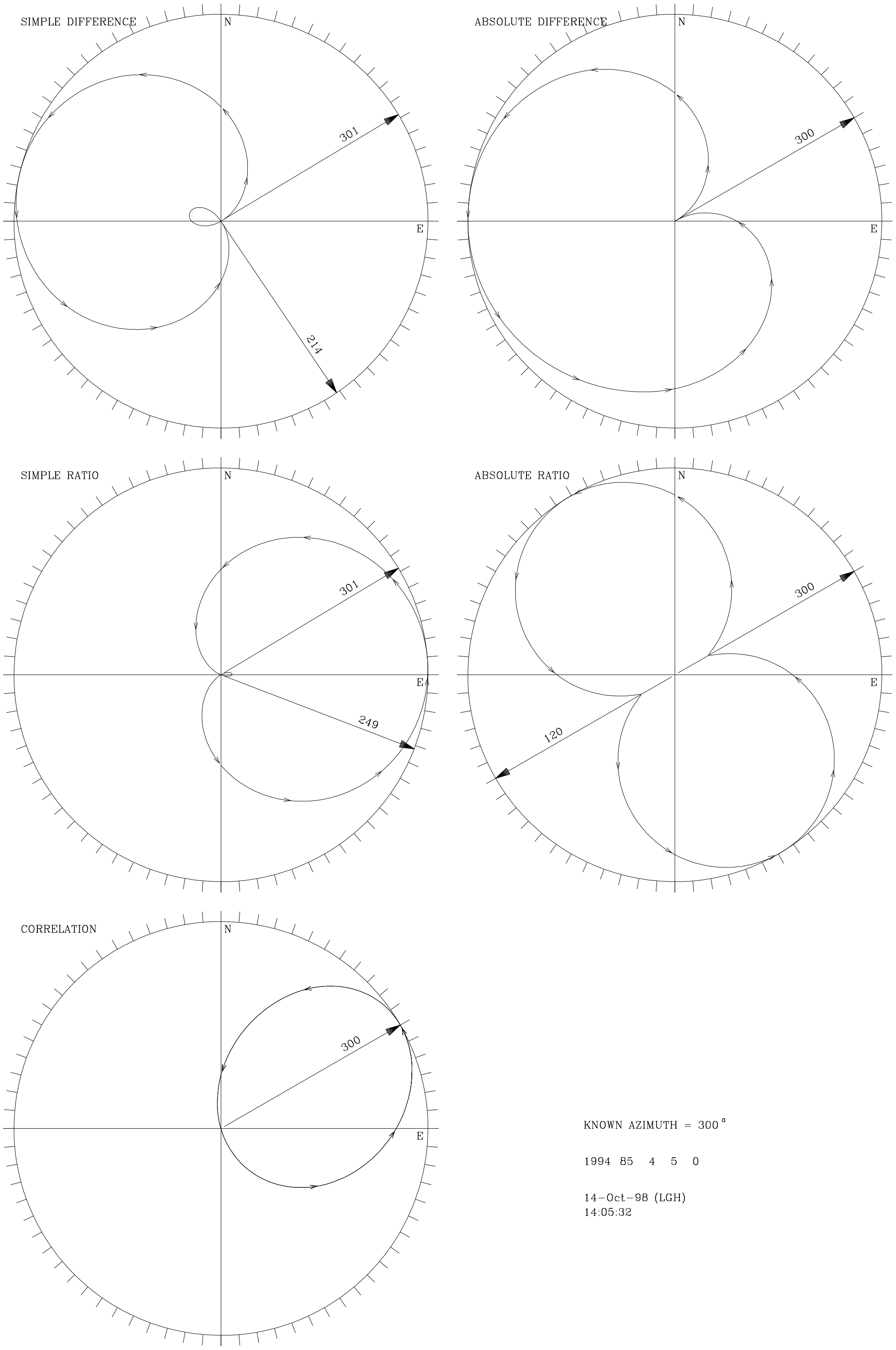

Figure 4. 11 Azimuth function plots generated from corrected gain artificial data as calculated from equations 2.3, 2.14, 2.19, 2.26, and 2.33. The known azimuth was 300° CCW from north.

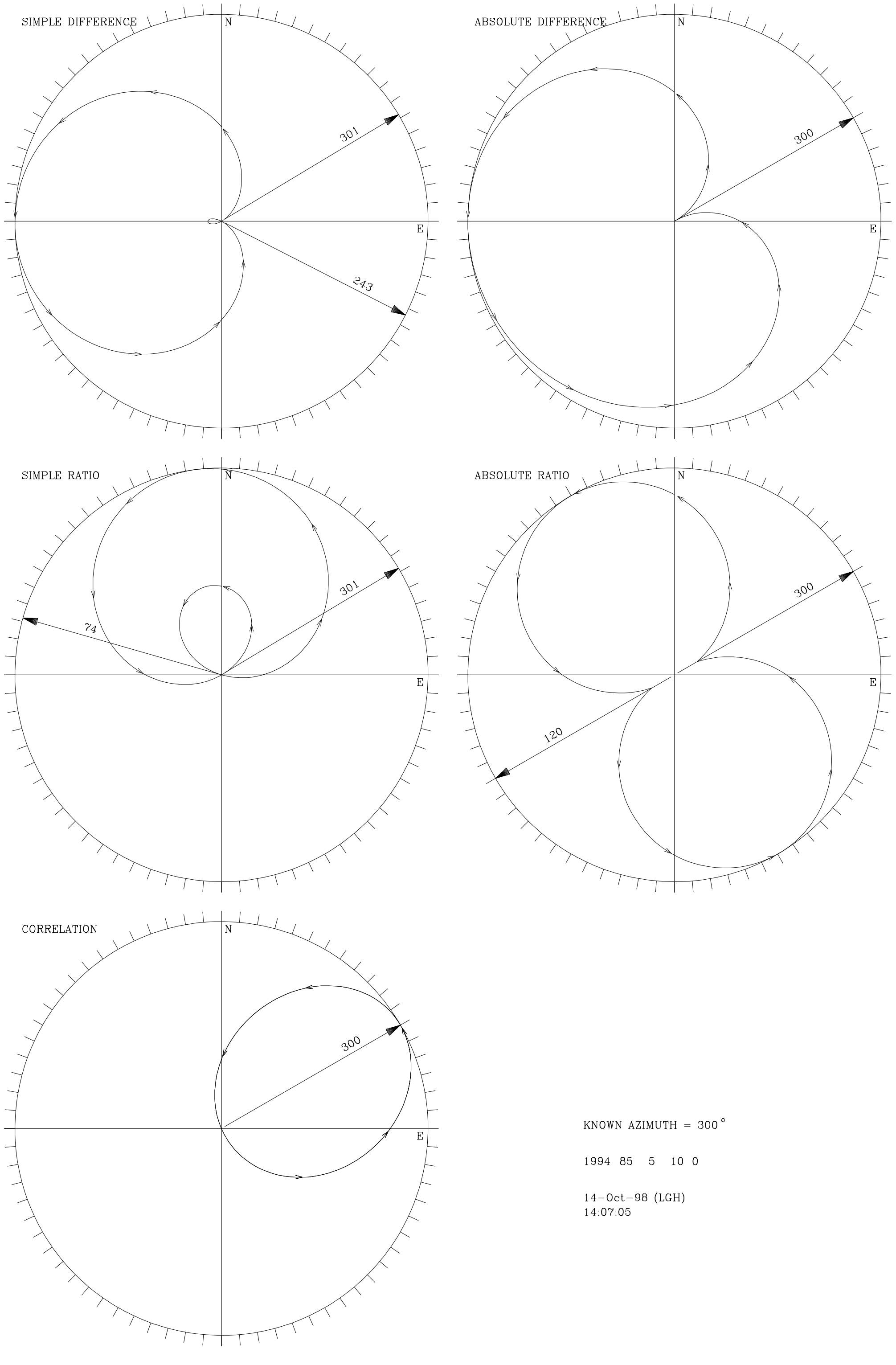

Figure 4. 12 Azimuth function plots generated from corrected gain artificial data as calculated from equations 2.3, 2.14, 2.19, 2.26, and 2.33. The known azimuth was 30^{o} CCW from north.

FIGURE → FIGURE	SIMPLE DIFF	ABS DIFF	SIMPLE RATION MINUS ONE	ABS RATIO	CORR	TRUE AZIMUTH
3.2 → 3.8	30 → 30	30 → 30	30 → 31	30 → 30	30 → 30	30
3.3 → 3.9	30 → 30	30 → 30	30 → 31	30 → 30	30 → 30	30
3.4 → 3.10	30 → 30	30 → 30	30 → 31	30 → 30	30 → 30	30
3.5 → 3.11	301 → 301	300 → 300	301 → 301	300 → 300	300 → 300	300
3.6 → 3.12	301 → 301	300 → 300	301 → 301	300 → 300	300 → 300	300
3.7 → 3.13	301 → 301	300 → 300	301 → 301	300 → 300	300 → 300	300

Table 4. 1 Changes in calculated dummy data azimuths created by correcting the time series data with the individual channel gains. Numbers to the left of the → symbol were derived from uncorrected gain processing; numbers to the right of the → symbol were derived from corrected gain processing.

Table 4. 1 summarizes the results of applying a gain correction to the processing of the dummy data. The figure numbers in the left had column denote uncorrected data figure numbers on the left side of the → symbol and corresponding corrected data figure numbers on the right side of the →. Figure 4.1 indicates that there is no difference between uncorrected processing and corrected processing when applied to dummy data.

5 TIME DOMAIN AZIMUTH CALCULATIONS USING REAL DATA

The first step in evaluating the performance of the five time domain azimuth calculation procedures was to design an experiment to provide data for which the "unknown" azimuths were actually known. Four Guralp Systems CMG-3NSN horizontal seismometers were installed in the ASL underground vault; a vault installation was chosen for the initial experimental configuration because in this situation, the orientation of both the "unknown orientation" sensors and the "known orientation" sensors could be visually verified thereby providing a check on the accuracy of the azimuth determination procedures. All four sensors were oriented with respect to a string stretched in an arbitrary direction across the floor of the vault. Two of the sensors (sensors N and E in Figure 5.1) were oriented orthogonally with respect to one another in simulated borehole "unknown" N-S and E-W directions. These two sensors represent the orthogonal pair of horizontal sensors contained in the borehole sensor whose orientation is to be determined. The remaining two sensors (sensors K_1 and K_2 in Figure 5.1) were sequentially installed at several known angles with respect to the string. These two sensors taken one at a time represent the surface installed (reference) instrument whose orientation is known. The object of this experiment is to determine how precisely data from the two orthogonal borehole sensors and data from the surface sensor can be used to determine the "unknown" relative position of the orthogonal borehole components with respect to the known surface instruments.

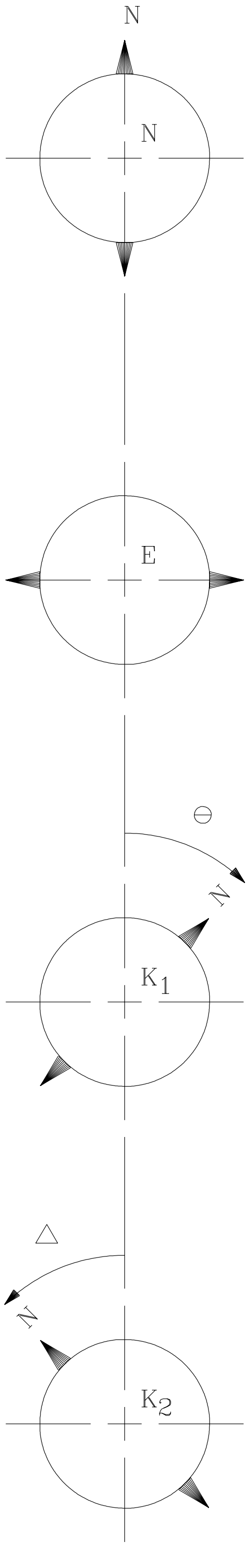

Figure 5.1 The physical orientation of sensors N, E, K_1 and K_2. The drawing depicts Guralp CMG-3NSN horizontal sensors; the N marking on each sensor indicates the sensor marking to be pointed north or east for correct polarity conventions.

The known orientation sensors (sensors K_1 and K_2) were not physically moved to attempt to line them up with one of the borehole horizontals during the experiment. Instead, time series data was recorded from the outputs of all four sensors and the orientation of the two orthogonal borehole horizontals was rotated in the computer to obtain a best match between their outputs and the output of the known orientation sensors (the horizontal that would be installed on the surface in a real world situation).

This experiment requires a source of high level ground motion to assure that a common signal appears at the input to all sensors and to assure that this input signal dominates any sensor system noise. The six second microseism peak provides a natural source of continuous relatively high level signal. Therefore, all of the data processed in this experiment was digitally bandpass filtered prior to subsequent processing. The passband extended from 4 to 10 seconds.

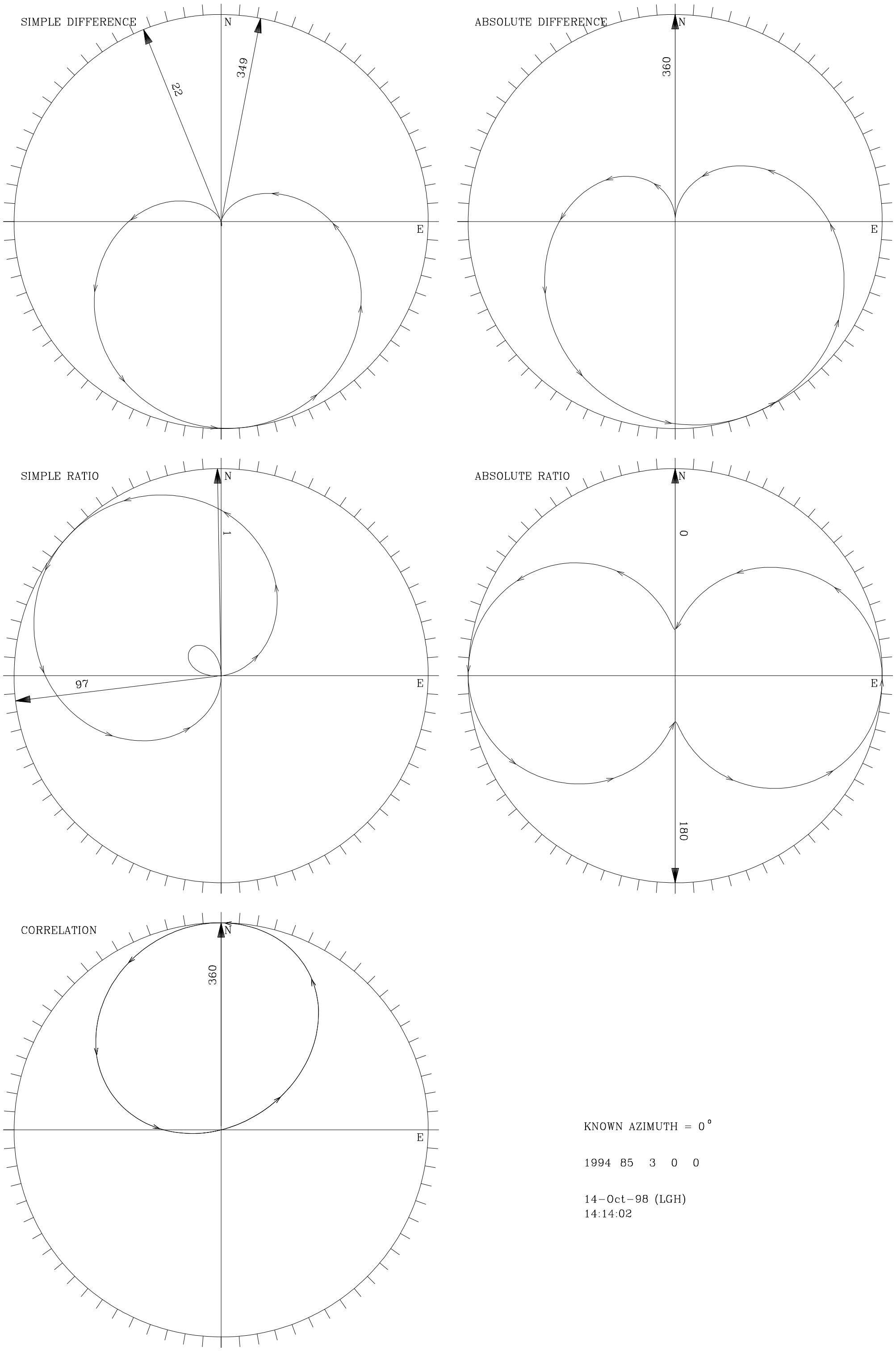

Figure 5.2 Azimuth function plots generated from uncorrected gain real data as calculated from Equations 2.3, 2.14, 2.19, 2.25, and 2.31. The known azimuth was 0° CCW from north.

Typical results of processing real time domain data without correcting for the system gains are illustrated in Figures 5.2, 5.3, and 5.4 in which the "unknown sensor" was known to be oriented at 0° and in Figures 5.5, 5.6, and 5.7 in which the "unknown sensor" was known to be oriented at 30°. Note that in some cases the calculated azimuth differs by a large amount from the known true azimuth.

Applying the correction for individual channel gains yields the results shown in Figures 5.8,5.9, and 5.10 for the 0° "unknown" azimuth, and the results in Figures 5.11, 5.12, and 5.13 for the 30° "unknown" azimuth. Note that applying the channel gain correction significantly improves the overall calculated azimuths.

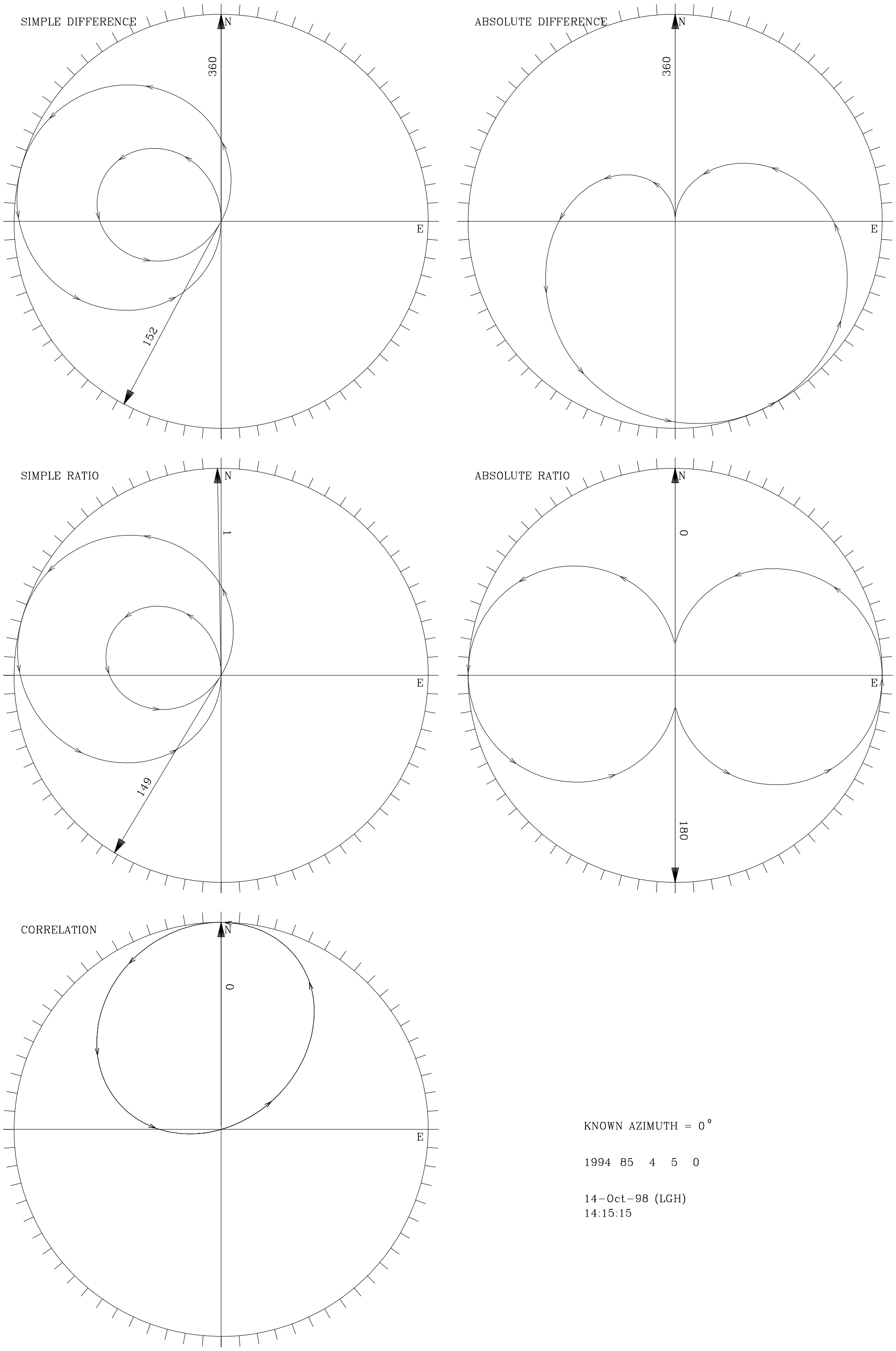

Figure 5.3 Azimuth function plots generated from uncorrected gain real data as calculated from Equations 2.3, 2.14, 2.19, 2.25, and 2.31. The known azimuth was 0° CCW from north.

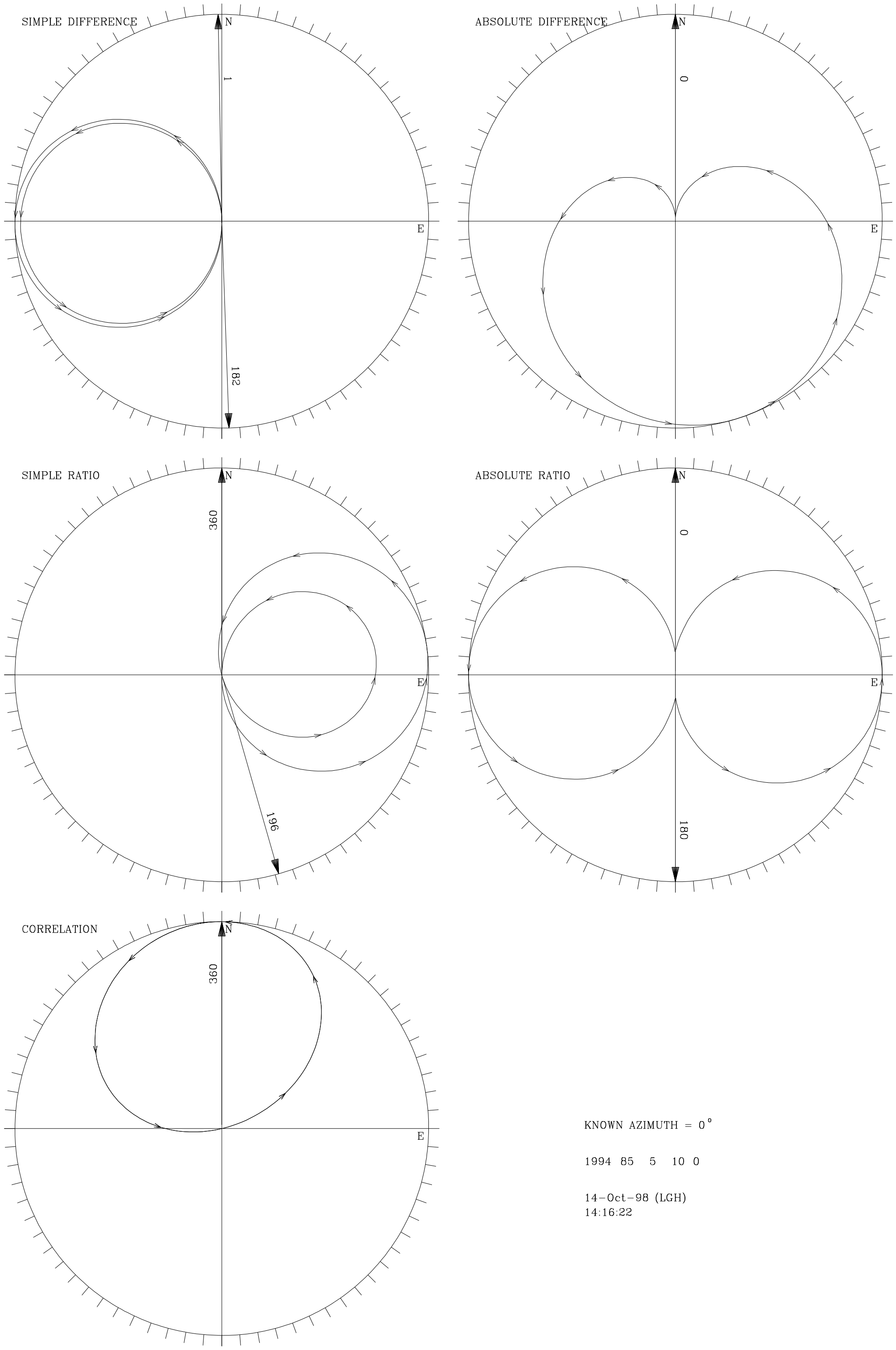

Figure 5.4 Azimuth function plots generated from uncorrected gain real data as calculated from Equations 2.3, 2.14, 2.19, 2.25, and 2.31. The known azimuth was 0° CCW from north.

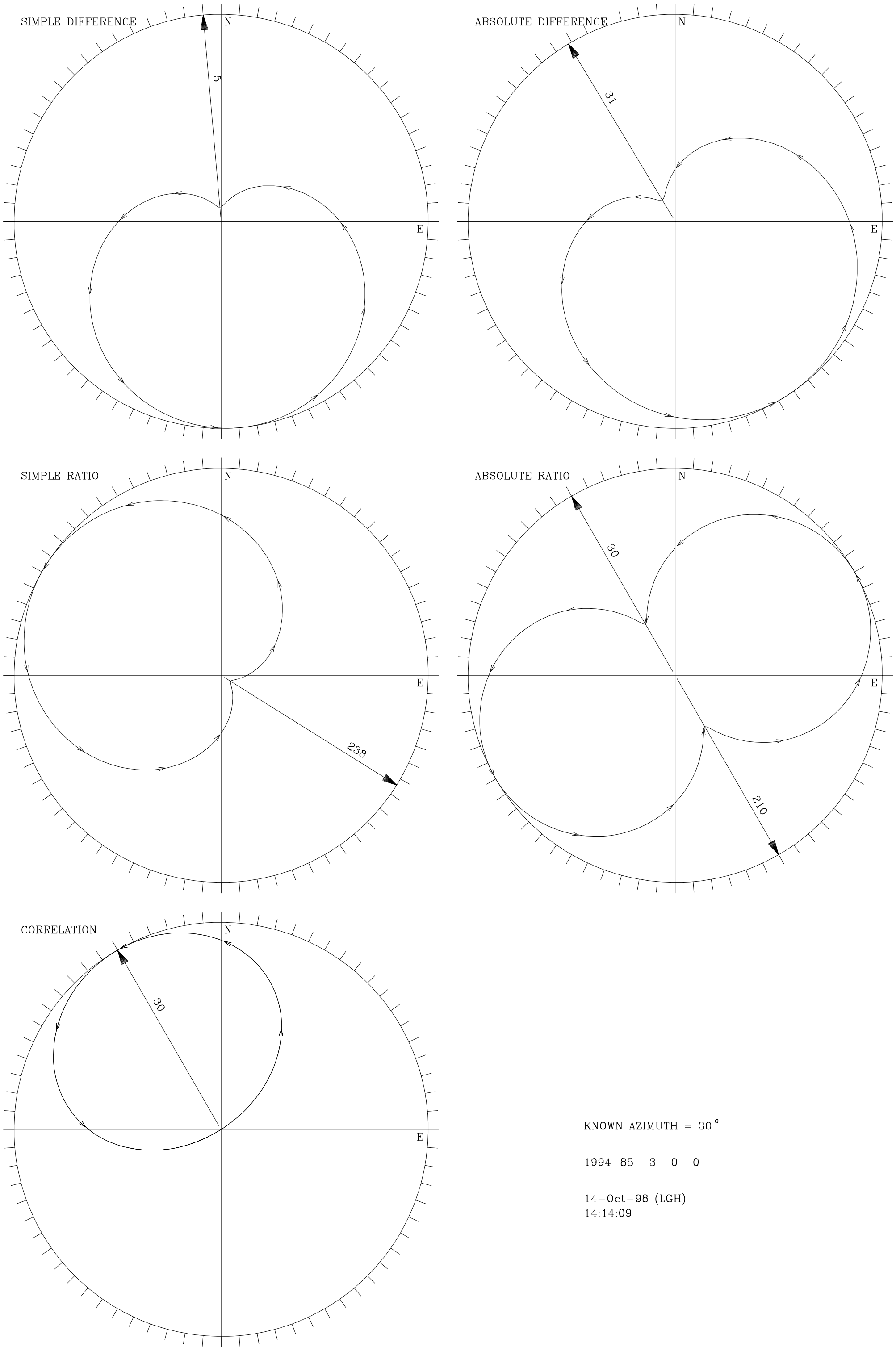

Figure 5.5 Azimuth function plots generated from uncorrected gain real data as calculated from Equations 2.3, 2.14, 2.19, 2.25, and 2.35. The known azimuth was 30° CCW from north.

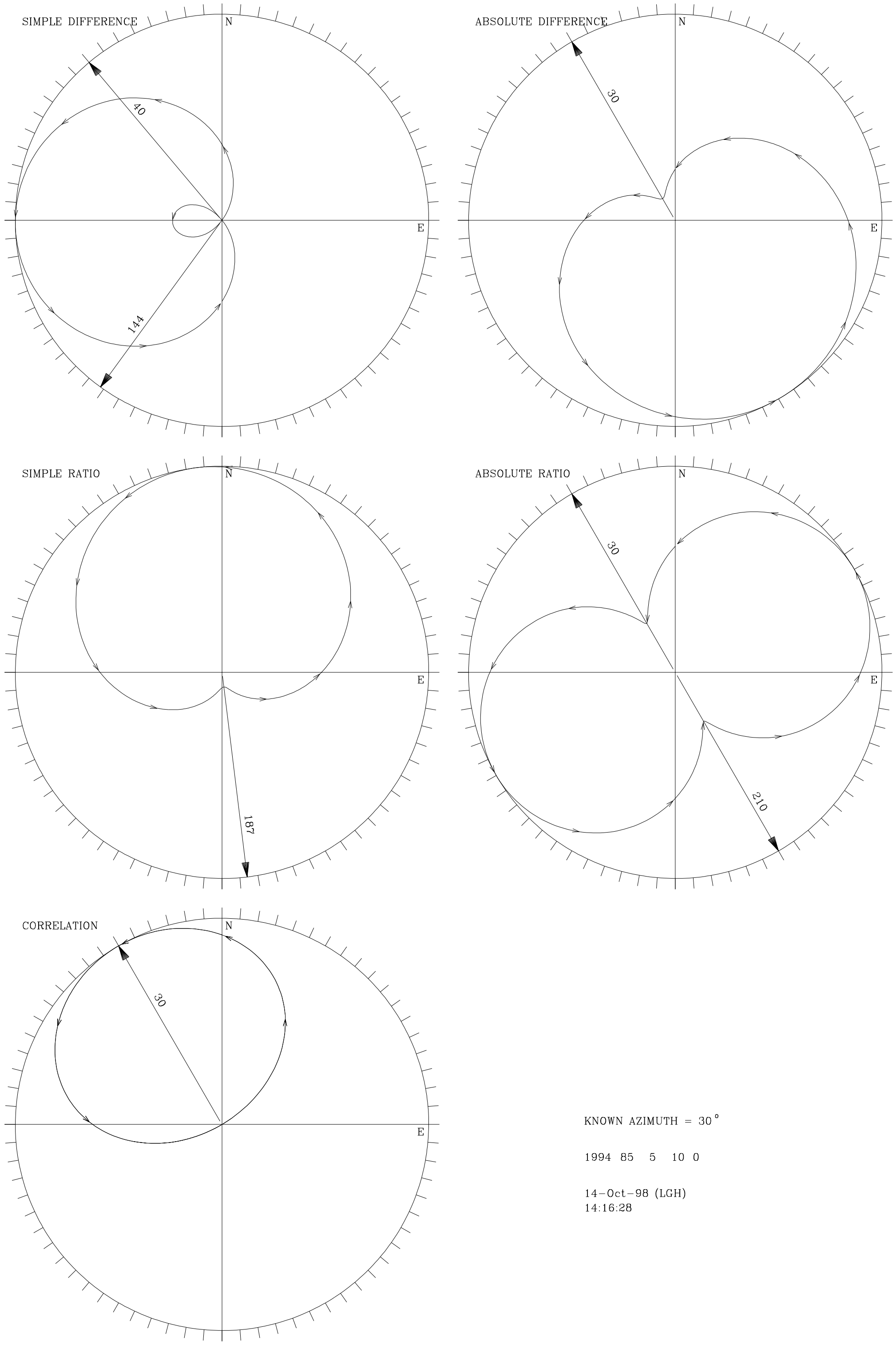

KNOWN AZIMUTH = 30°

1994 85 5 10 0

14-Oct-98 (LGH)
14:16:28

Figure 5.6 Azimuth function plots generated from uncorrected gain real data as calculated from Equations 2.3, 2.14, 2.19, 2.25, and 2.31. The known azimuth was 30° CCW from north.

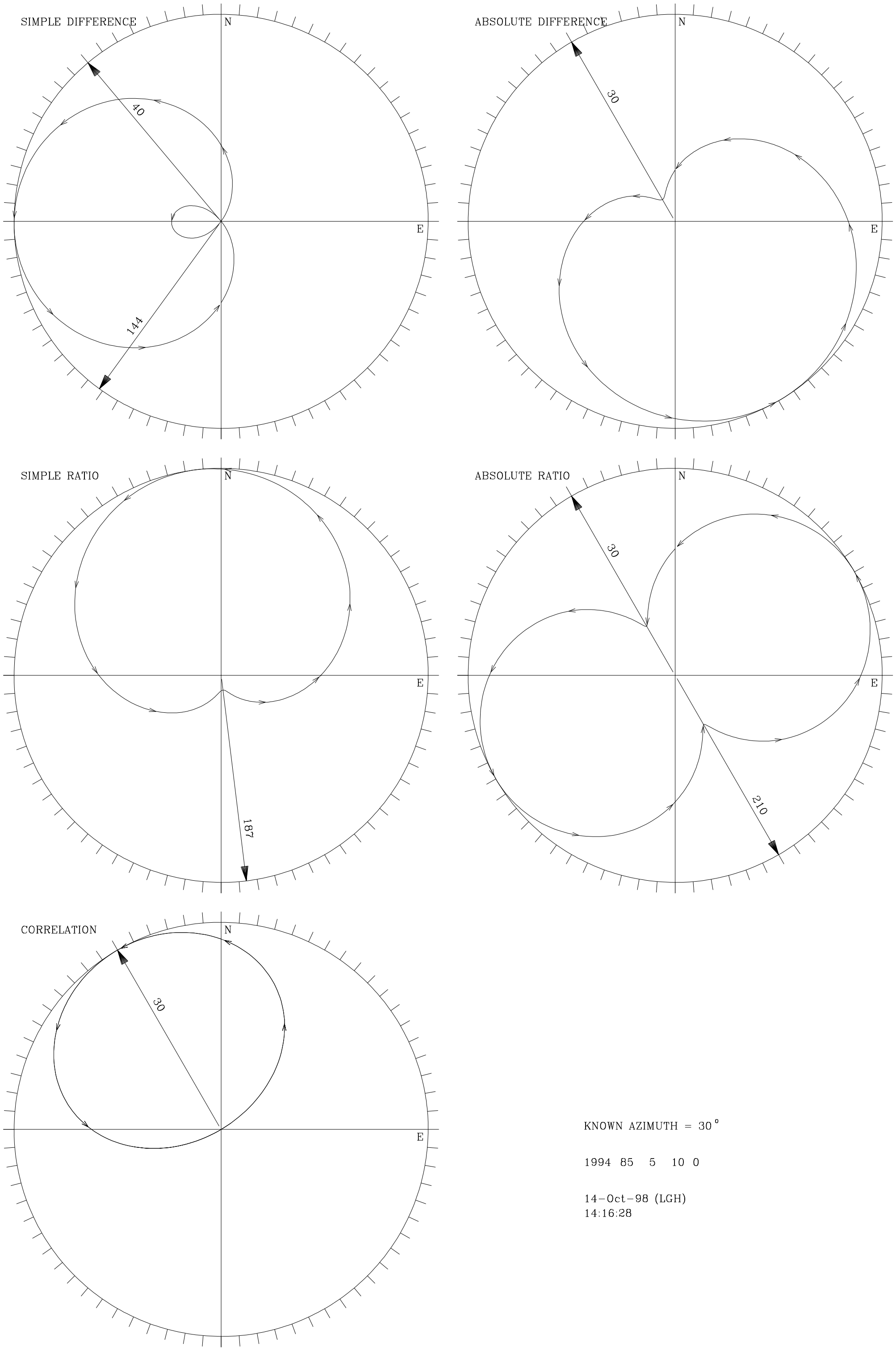

Figure 5.7 Azimuth function plots generated from uncorrected gain real data as calculated from Equations 2.3, 2.14, 2.19, 2.25, and 2.31. The known azimuth was 30° CCW from north.

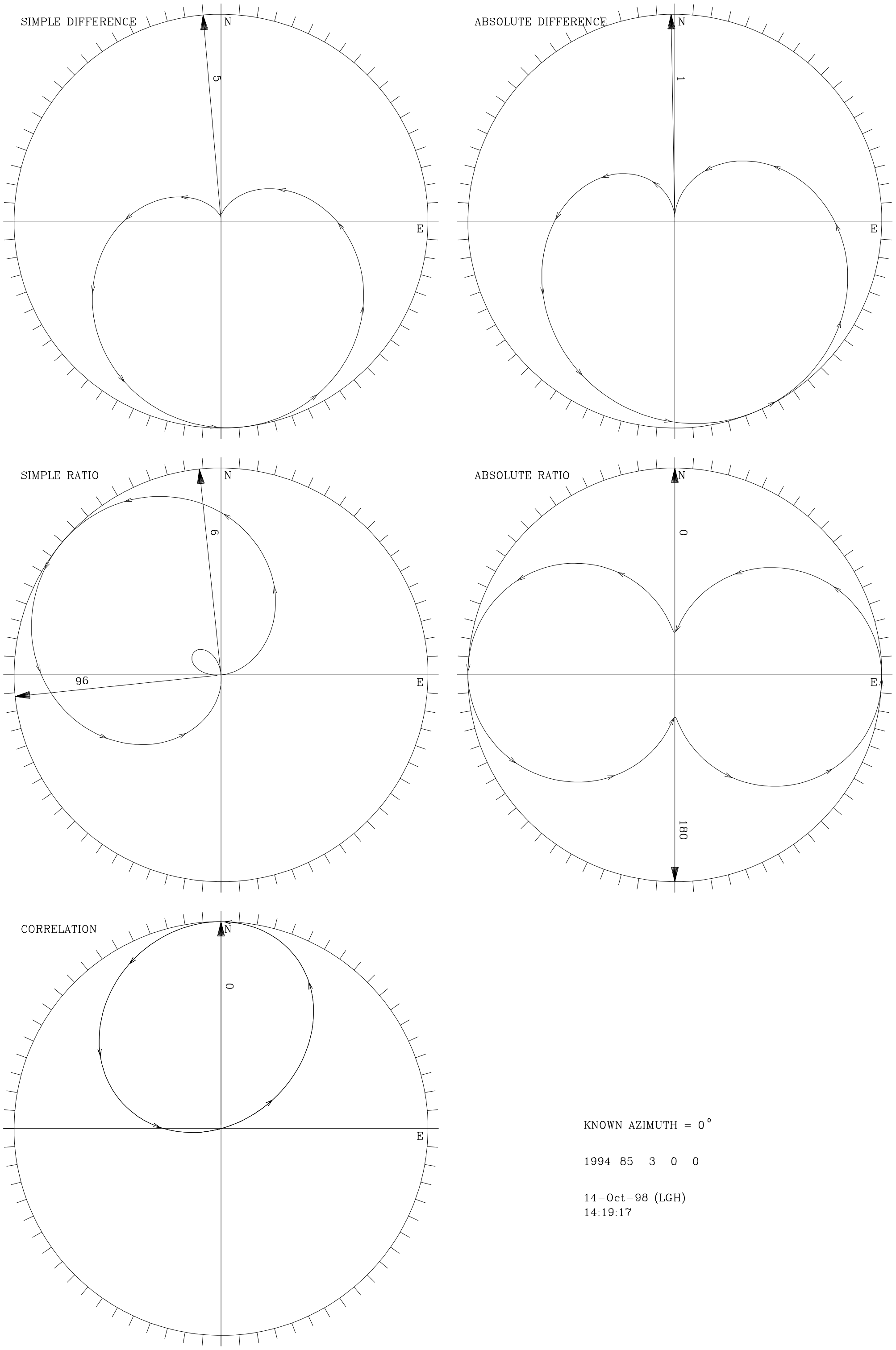

Figure 5.8 Azimuth function plots generated from corrected gain real data as calculated from Equations 2.3, 2.14, 2.19, 2.25, and 2.31. The known azimuth was 0° CCW from north.

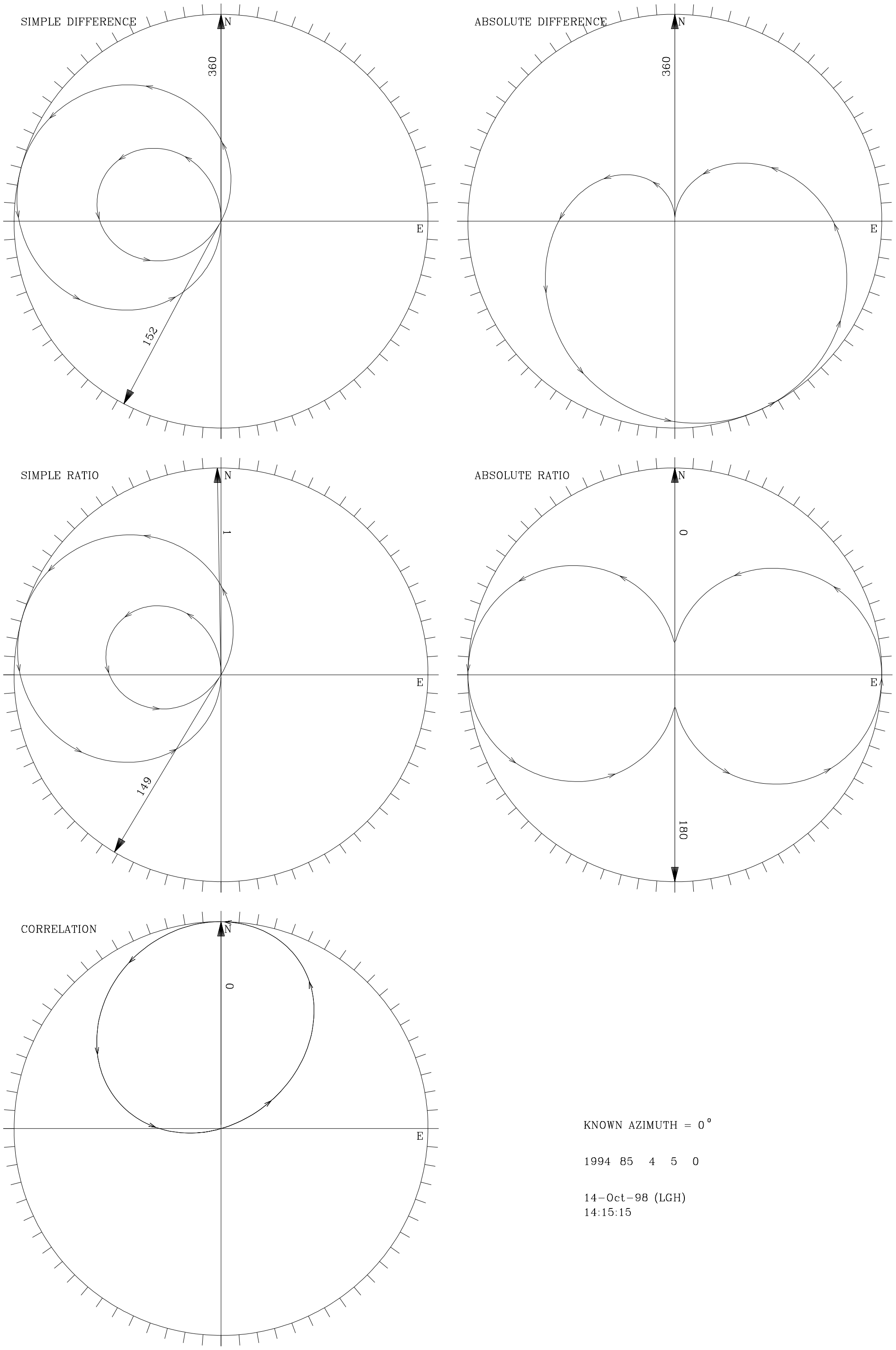

Figure 5.9 Azimuth function plots generated from corrected gain real data as calculated from Equations 2.3, 2.14, 2.19, 2.25, and 2.31. The known azimuth was 0° CCW from north.

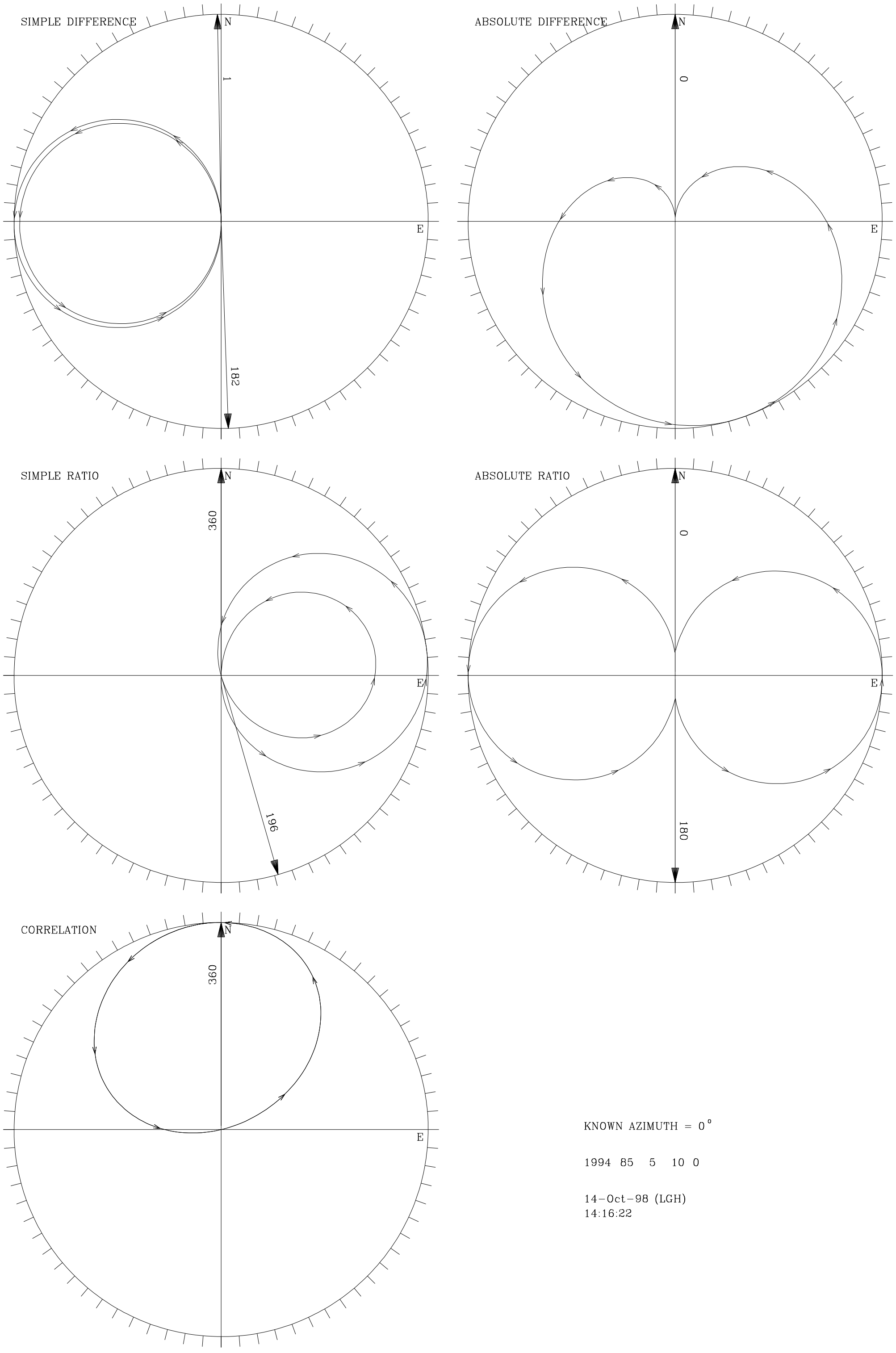

KNOWN AZIMUTH = 0°

1994 85 5 10 0

14-Oct-98 (LGH)
14:16:22

Figure 5.10 Azimuth function plots generated from corrected gain real data as calculated from Equations 2.3, 2.14, 2.19, 2.25, and 2.31. The known azimuth was 0° CCW from north.

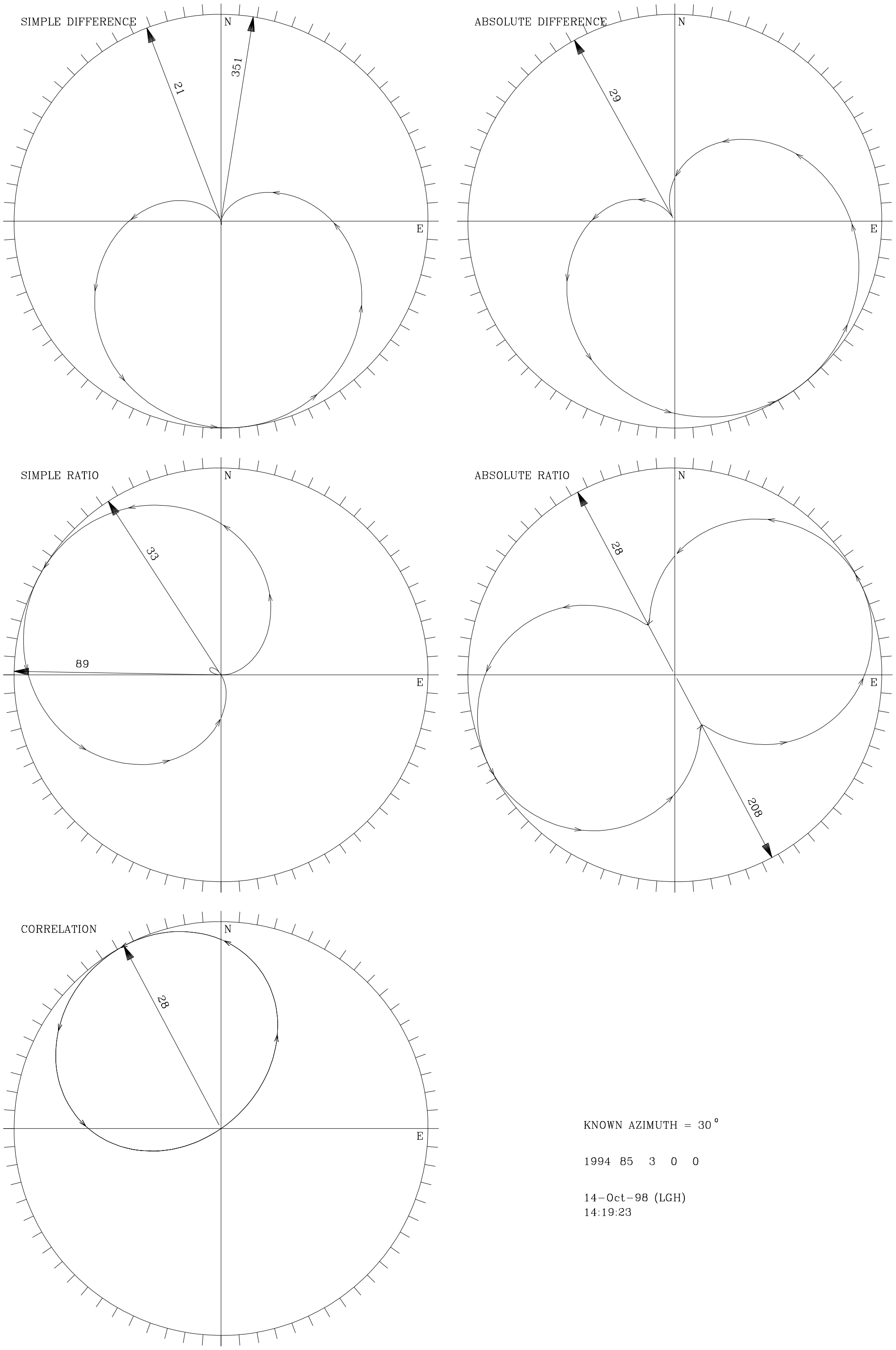

Figure 5.11 Azimuth function plots generated from corrected gain real data as calculated from Equations 2.3, 2.14, 2.19, 2.25, and 2.31. The known azimuth was 30° CCW from north.

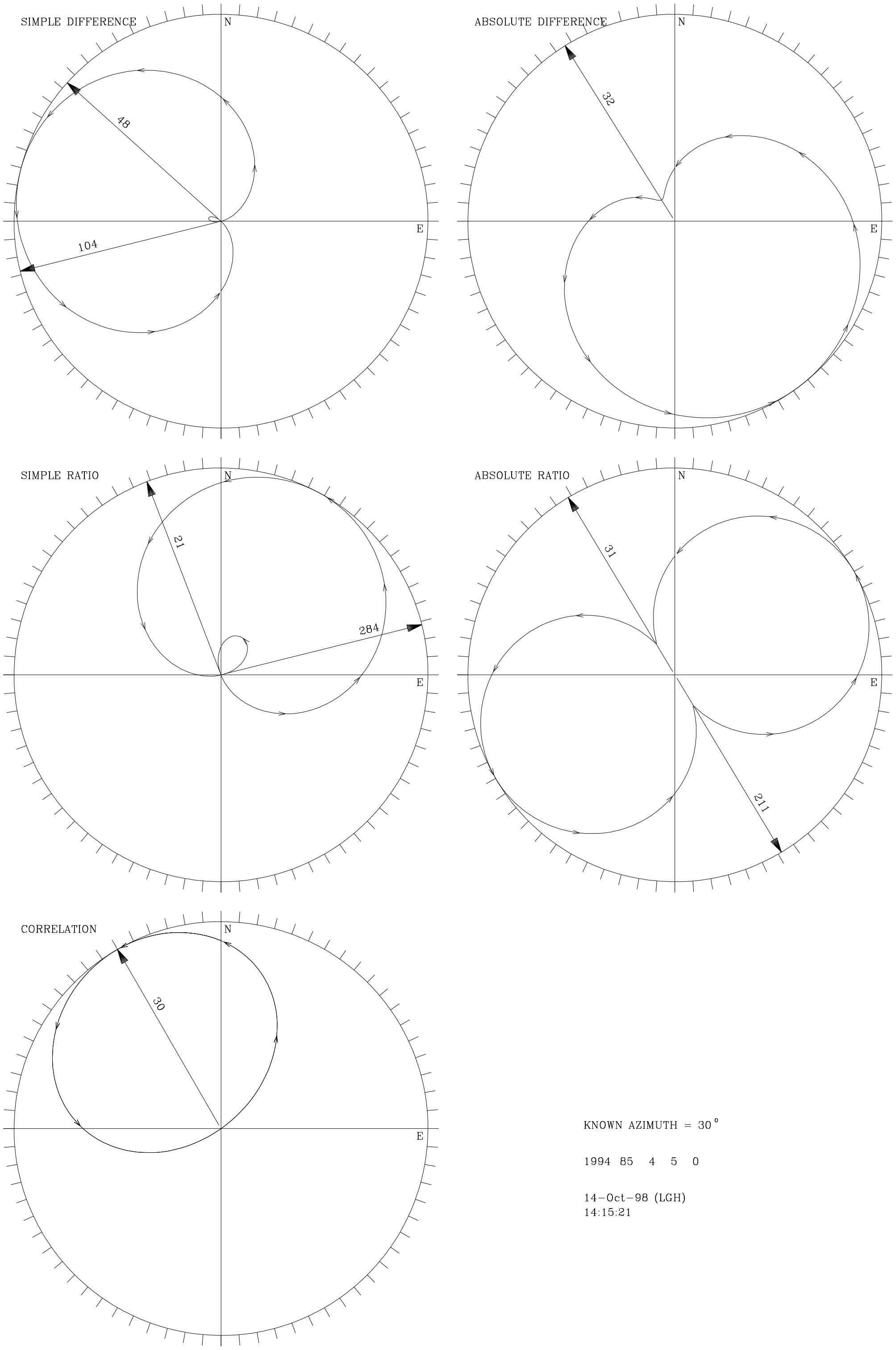

Figure 5.12 Azimuth function plots generated from corrected gain real data as calculated from Equations 2.3, 2.14, 2.19, 2.25, and 2.31. The known azimuth was 30° CCW from north.

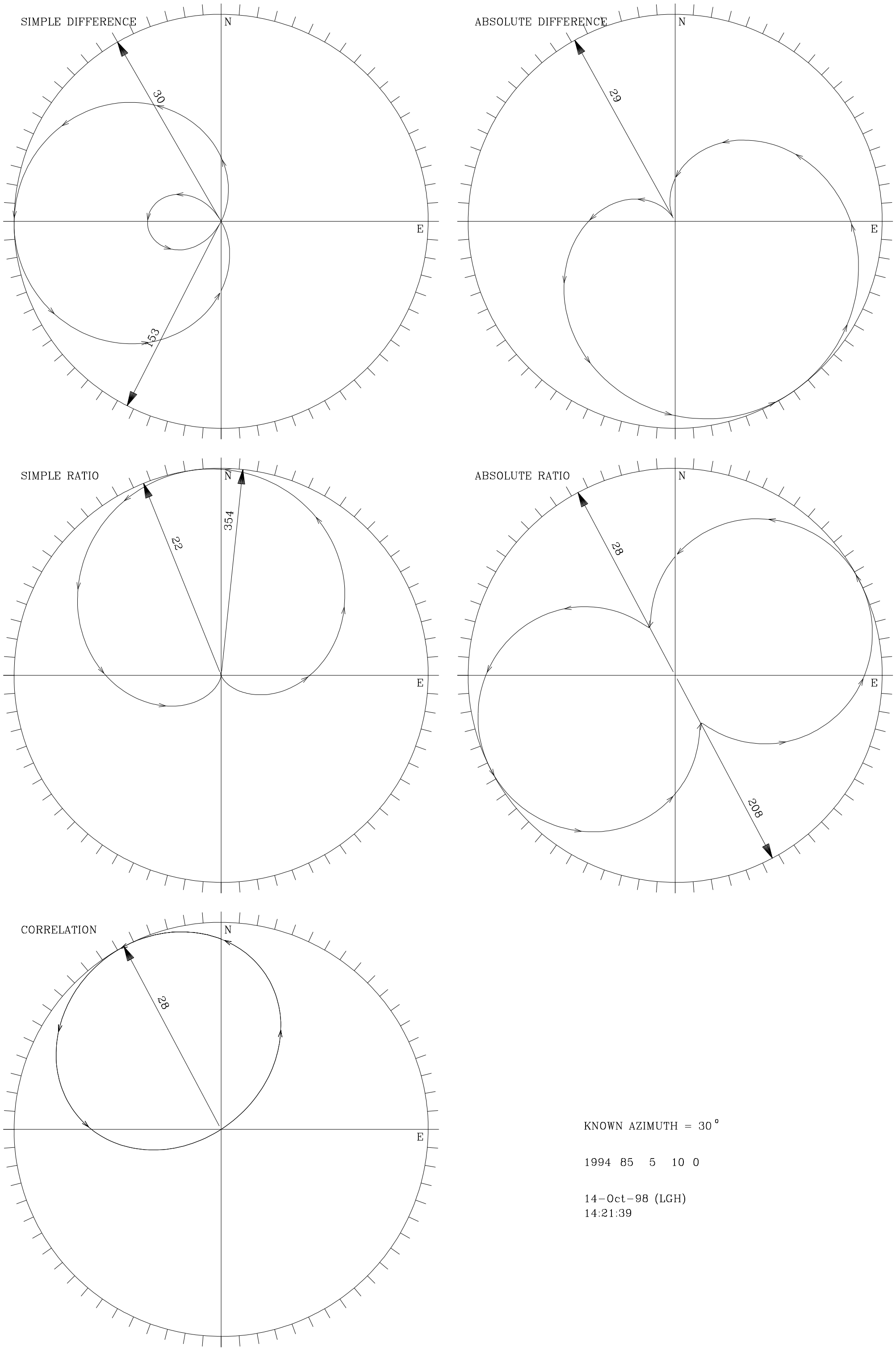

Figure 5.13 Azimuth function plots generated from corrected gain real data as calculated from Equations 2.3, 2.14, 2.19, 2.25, and 2.31. The known azimuth was 30° CCW from north.

FIGURE → FIGURE	SIMPLE DIFF	ABS DIFF	SIMPLE RATIO MINUS ONE	ABS RATIO	CORR	TRUE AZIMUTH
4.2 → 4.8	22 → 5	0 → 1	1 → 6	0 → 0	0 → 0	0
4.3 → 4.9	0 → 2	0 → 1	1 → 2	0 → 0	0 → 0	0
4.4 → 4.10	1 → 1	0 → 1	0 → 359	0 → 0	0 → 0	0
4.5 → 4.11	5 → 21	31 → 29	238 → 33	30 → 28	30 → 28	0
4.6 → 4.12	48 → 31	32 → 29	21 → 28	31 → 29	30 → 28	0
4.7 → 4.13	40 → 30	30 → 29	187 → 22	30 → 28	30 → 28	0

Table 5. 1 Changes in calculated real data azimuths created by correcting the real time series data with the individual channel gains. Numbers to the left of the → symbol were derived from uncorrected gain processing; numbers to the right of the → symbol were derived from corrected gain processing.

Histograms summarizing the results of many (250) time domain azimuth calculations for dummy data are shown in Figures 5.14 through 5.21. Each of these histograms contain 360 bins; each bin is 1° wide. The uncorrected gain results shown in Figures 5.14 ("unknown" azimuth = 30°) and 5.15 ("unknown" azimuth = 300°) are exactly what one should expect based on the models presented in Section 2. There is a definite concentration of azimuth estimates near 30° in Figure 5.14 and another at 300° in Figure 5.15. Note there are what appear to be a very small number of apparently random azimuths scattered throughout the 0° to 360° range in the histograms for the simple difference and the simple ratio minus 1 histogram plots. These azimuths may be hard to discern on the plot because they appear to be merely a slight thickening along the x-axis. Actually, there are 250 of these scattered azimuths; there is one for every azimuth at or near to 30° in Figure 5.14 and at or near 300° in Figure 5.15. These scattered azimuths arise from the second root of Equations 2.13 and 2.25 which depends on the relative channel gains and the relative ground motion amplitudes for the particular segment of data being processed.

Histograms of the results of reprocessing the same data set while correcting for individual channel gains are shown in Figures 5.16 and 5.17 . There is little change from the results in the previous two figures in which channel gain was not considered.

The results of processing 250 sequential segments of real data without gain corrections are shown in Figures 5.18 and 5.19. There is much more scatter in the calculated azimuths from real data because real data is noisy. The ground motion inputs to the individual sensor modules are not necessarily equal and there is sensor mechanical plus electronic noise; all of these can decrease the accuracy of the calculations. There is a fairly tight cluster of calculated azimuths for all five methods near the "known" unknown azimuth of 0° in Figure 5.18. There is considerably more scatter in calculated azimuths near the "known" unknown azimuth of 30° in Figure 5.19. The scatter is so bad that the true azimuth derived by the simple difference and simple ratio minus one methods is rather in doubt.

However, correcting the individual channel gain significantly improves the results as the histogram in Figure 5.21 illustrates. This histogram was constructed by processing the same data set as was the histogram in Figure 5.19; the only change was adding individual channel gain correction to the data in Figure 5.21. The peaks in the histogram calculated azimuths derived from the simple difference method and from the simple ratio minus one method are much more distinct with gain correction than without.

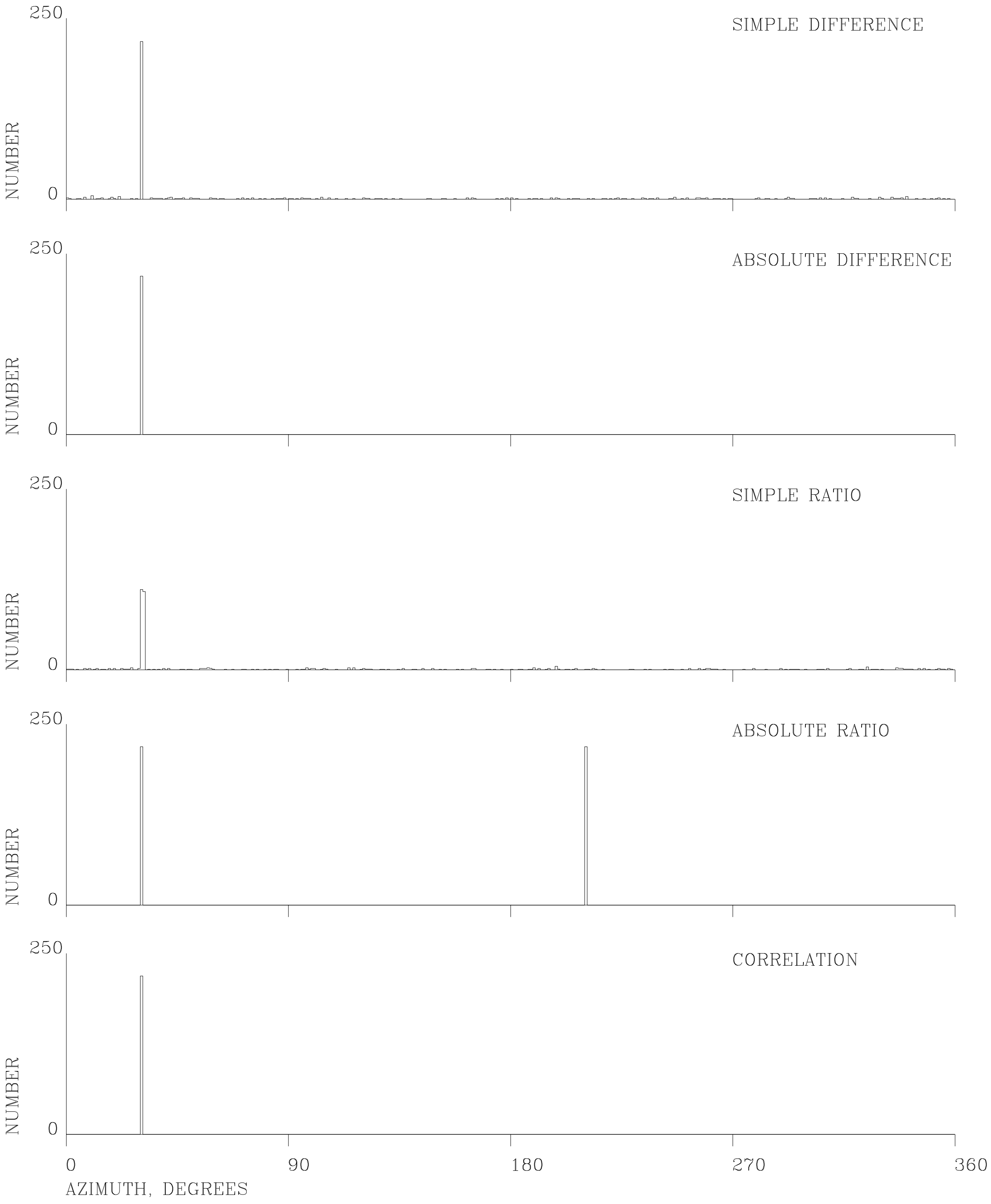

Figure 5.14 Histograms of the azimuths derived from uncorrected gain dummy data as calculated from Equations 2.3, 2.14, 2.19, 2.25, and 2.31. The known azimuth was 30° CCW from north.

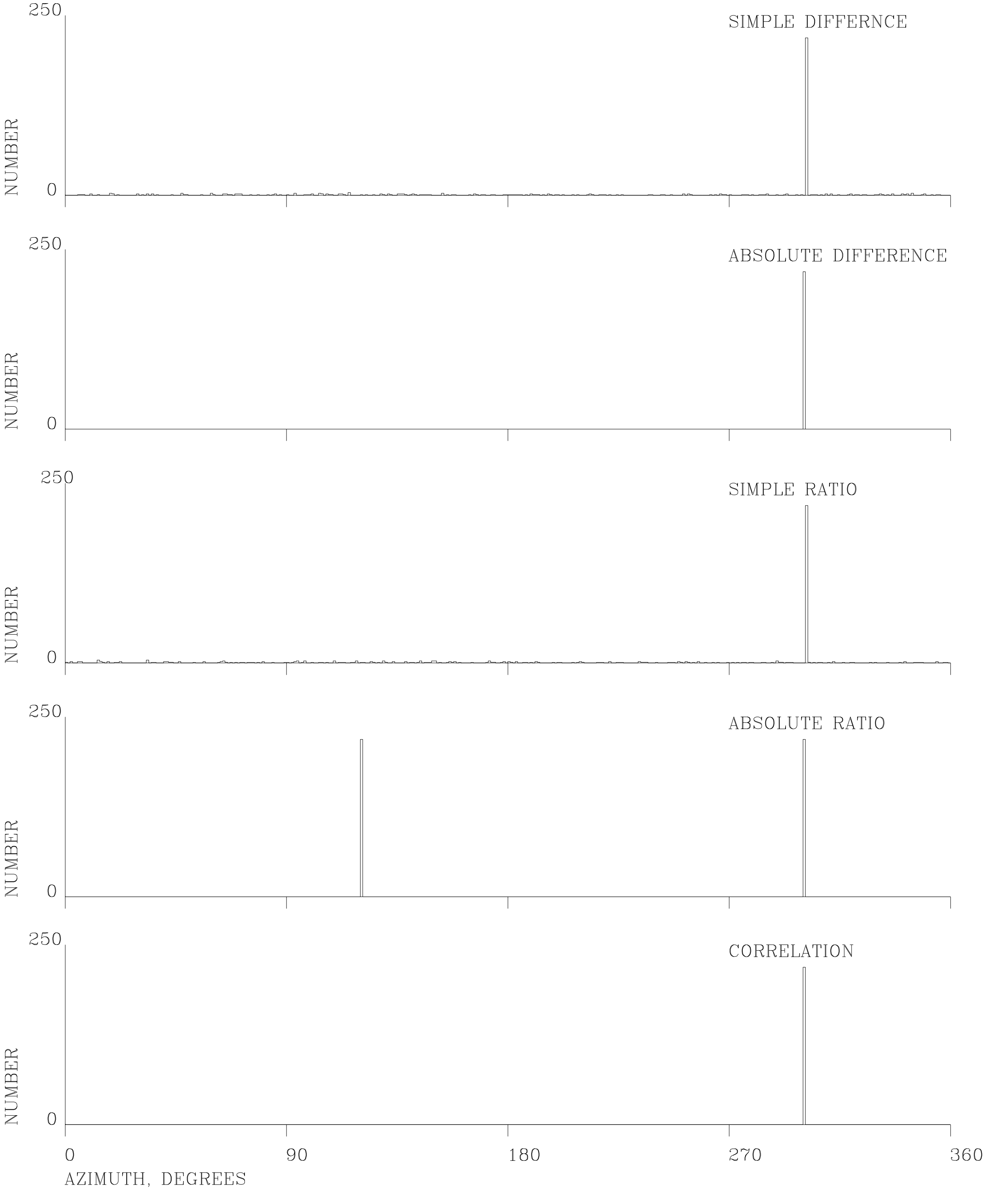

Figure 5.15 Histograms of the azimuths derived from uncorrected gain dummy data as calculated from Equations 2.3, 2.14, 2.19, 2.25, and 2.31. The known azimuth was 300° CCW from north.

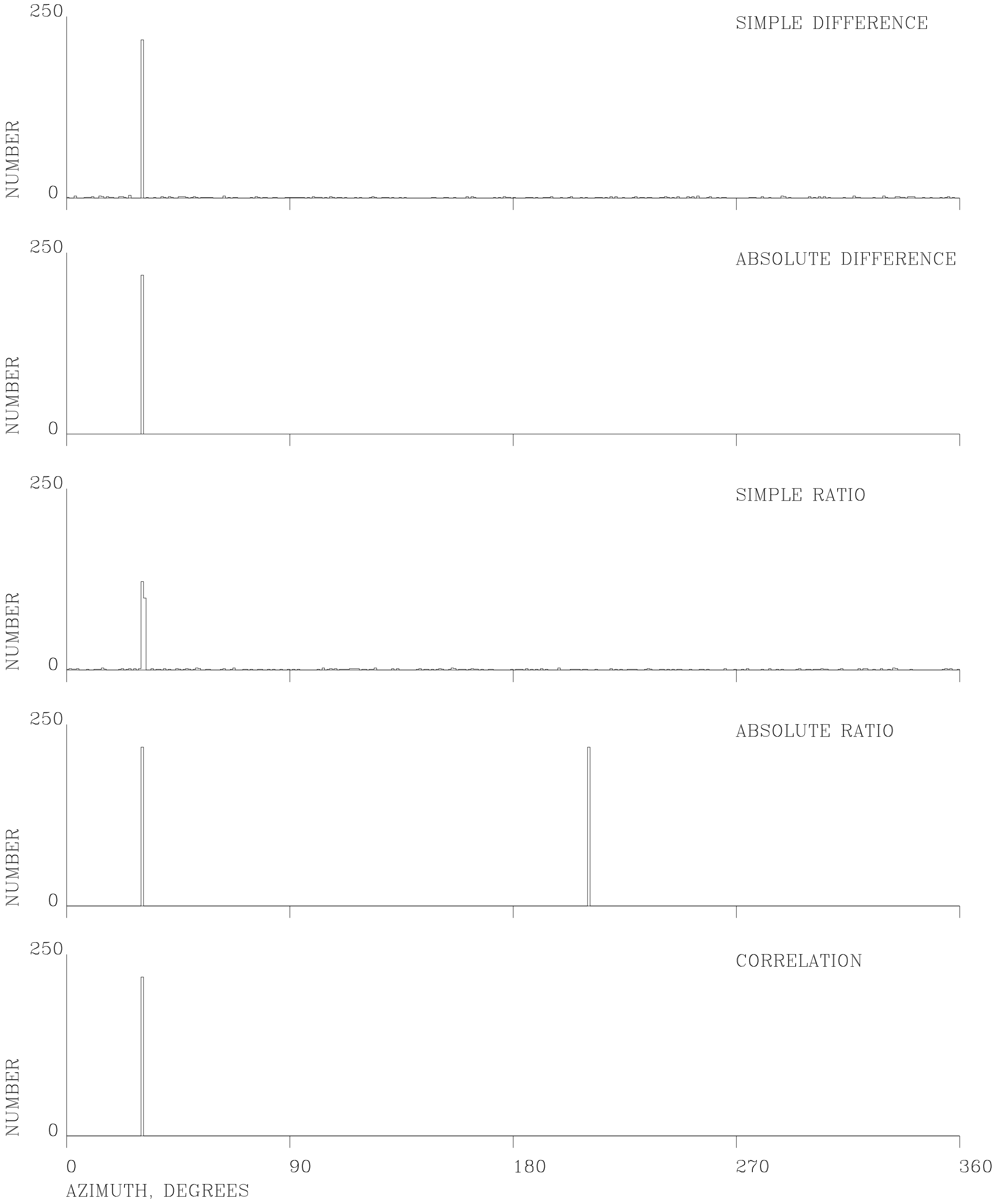

Figure 5.16 Histograms of the azimuths derived from corrected gain dummy data as calculated from Equations 2.3, 2.14, 2.19, 2.25, and 2.31. The known azimuth was 30° CCW from north.

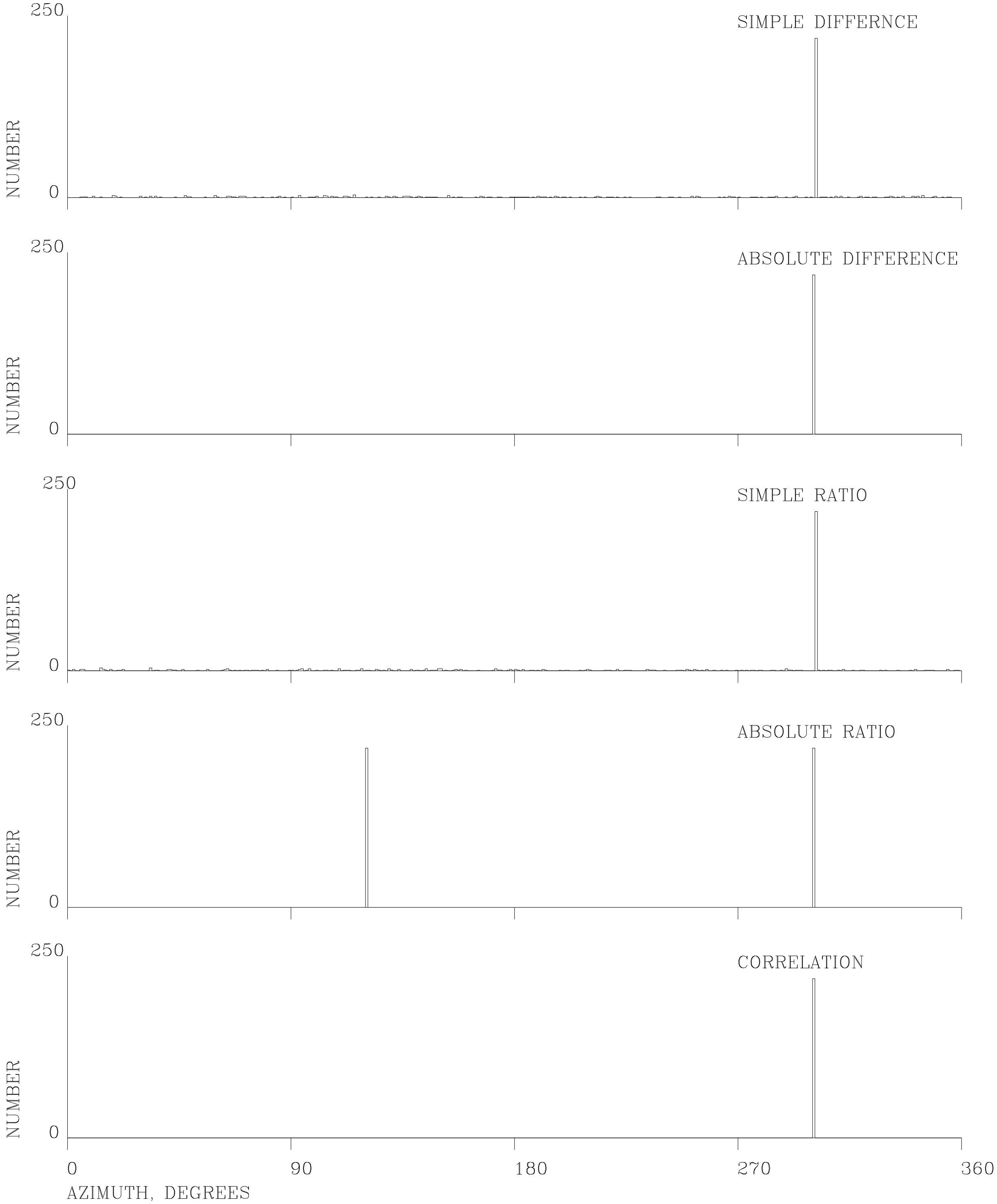

Figure 5.17 Histograms of the azimuths derived from corrected gain dummy data as calculated from Equations 2.3, 2.14, 2.19, 2.25, and 2.31. The known azimuth was 300° CCW from north.

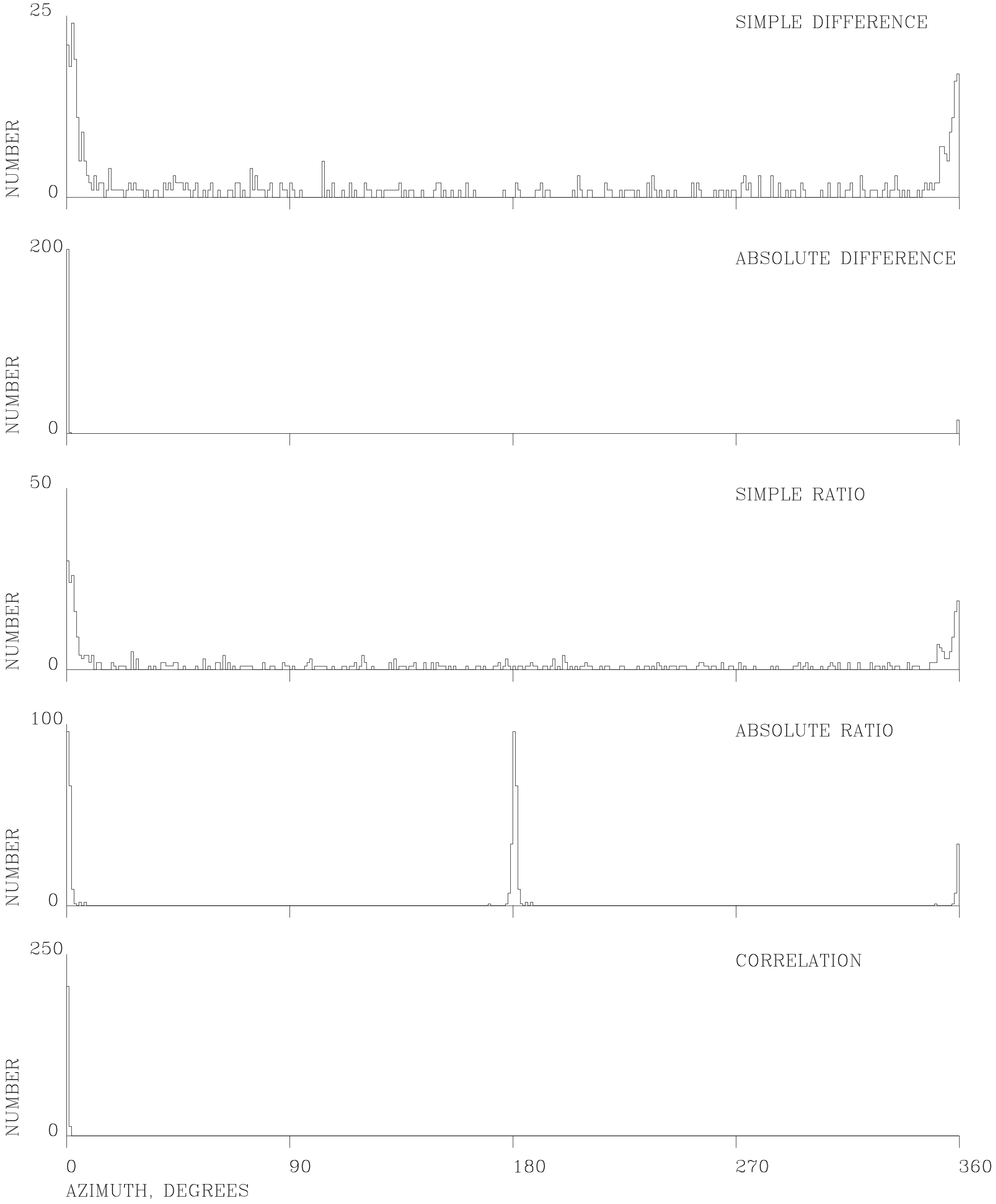

Figure 5. 18 Histograms of the azimuths derived from uncorrected gain real data as calculated from Equations 2.3, 2.14, 2.19, 2.25, and 2.31. The known azimuth was 0° CCW from north.

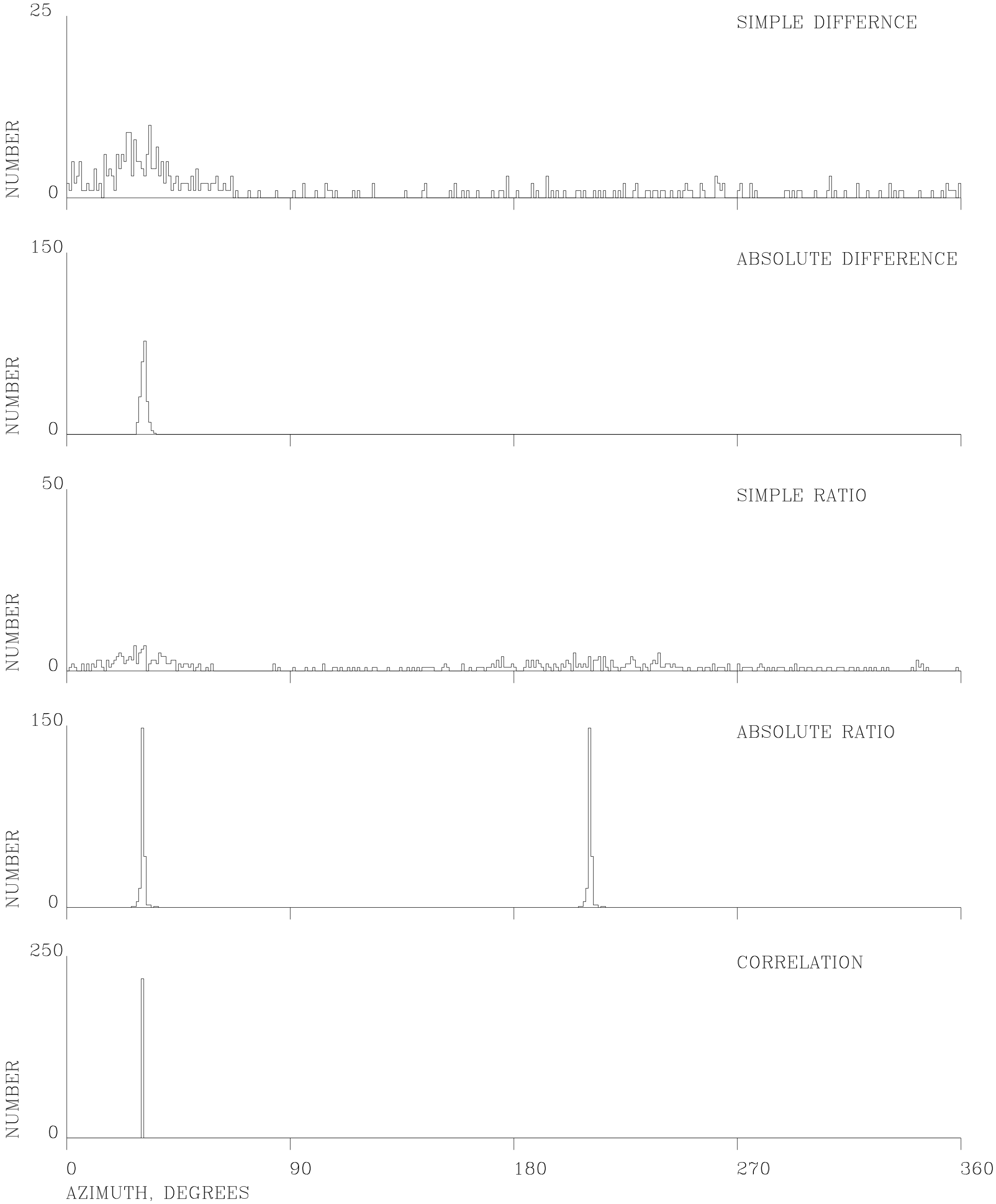

Figure 5.19 Histograms of the azimuths derived from uncorrected gain real data as calculated from Equations 2.3, 2.14, 2.19, 2.25, and 2.31. The known azimuth was 30° CCW from north.

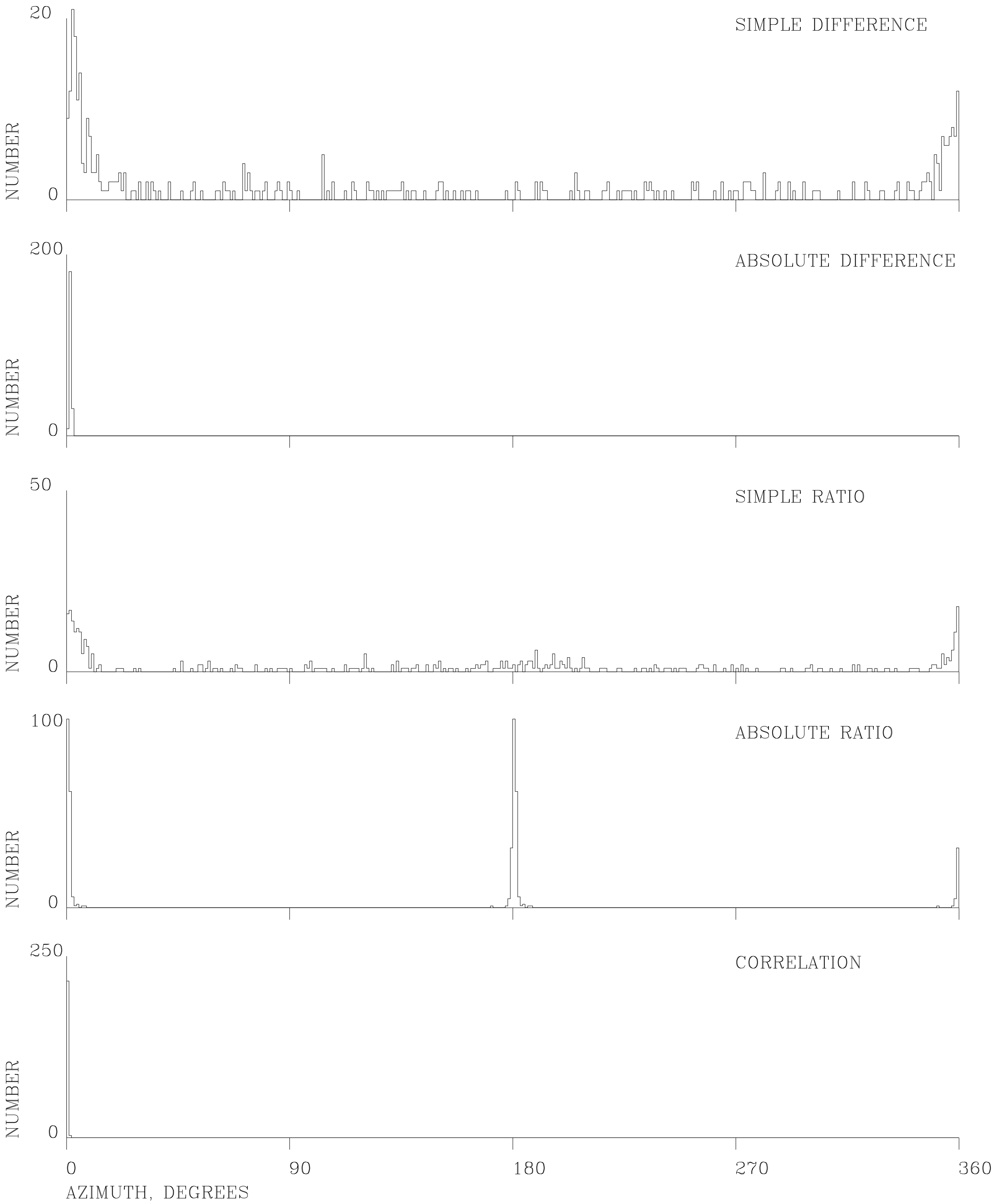

Figure 5.20 Histograms of the azimuths derived from corrected gain real data as calculated from Equations 2.3, 2.14, 2.19, 2.25, and 2.31. The known azimuth was 0° CCW from north.

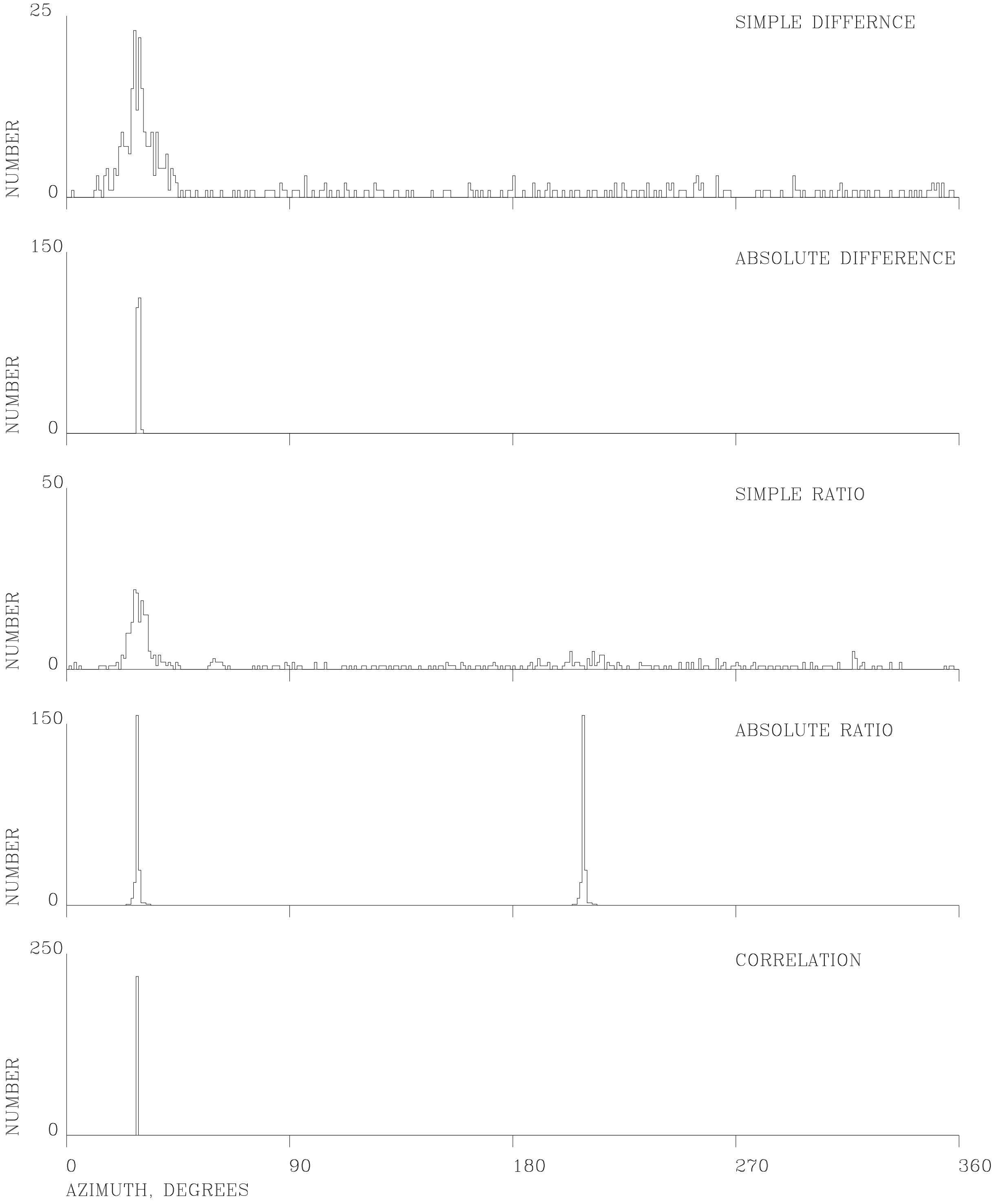

Figure 5.21 Histograms of the azimuths derived from corrected gain real data as calculated from Equations 2.3, 2.14, 2.19, 2.25, and 2.31. The known azimuth was 30° CCW from north.

6 FREQUENCY DOMAIN AZIMUTH DETERMINATION

In this section, the performance of the coherence function that was first discussed in Section 2.6 is illustrated by using the coherence function to reprocess the same set of data as was processed by the time domain methods that were presented in Sections 4 and 5.

First the coherence function is used to estimate the azimuths of the dummy computer generated data created as described in the first paragraph of Section 3. This data was programmed to simulate borehole sensor orientations of 30° and 300° CCW from the reference sensor. The results produced by a coherence based azimuth criteria are shown in Figure 6.1. Note that as should be expected, the coherence approach produces two possible azimuth estimates for each known orientation because the coherence analysis does not retain phase information; it is a purely power based method. Inspection of the figure indicates that for the 30° dummy data, the vast majority of the azimuth coherence derived estimates are at exactly 30° or 210° as they should be. There a few estimates that lie ±1° from each of the major histogram bins but not many.

Applying the coherence method to real data that was recorded from sensors installed in the ASL vault and were physically oriented as closely as possible to 0° and 30° CCW from the reference sensor yields the results shown in Figure 6.2. Here again the vast majority of the estimates are exactly what one would expect with a few of the 0° estimates being 1° higher than they should be. This may be due to the fact that the sensor may have actually been oriented at slightly more than 0° with respect to the reference sensor.

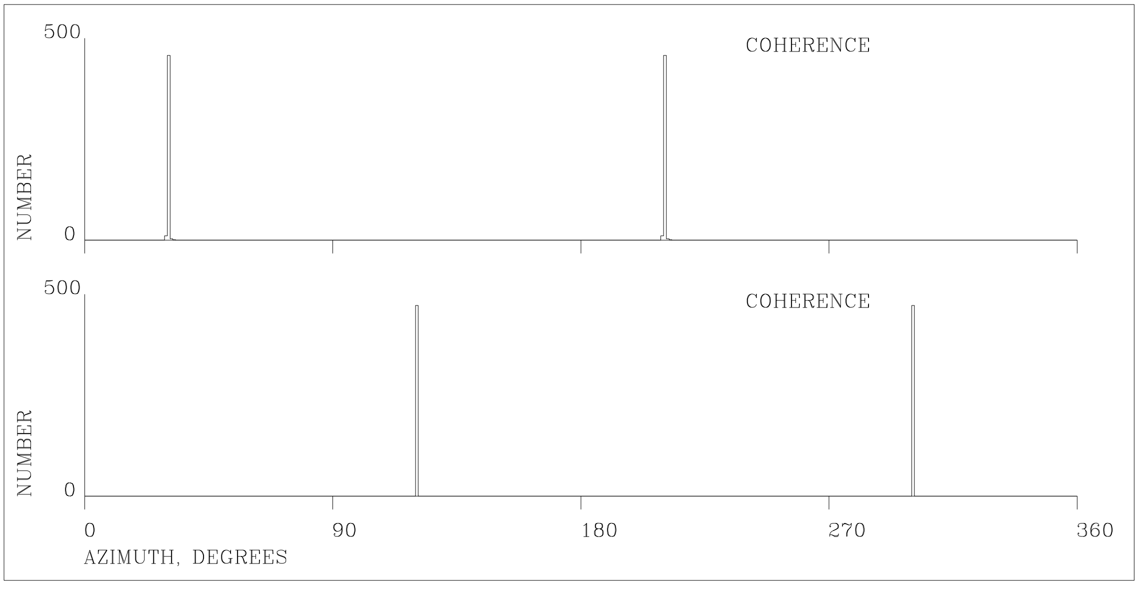

Figure 6.1 Histograms of coherence derived azimuths of dummy data. The known azimuths in the upper set of data was 30° and in the lower set of data was 300° CCW from north.

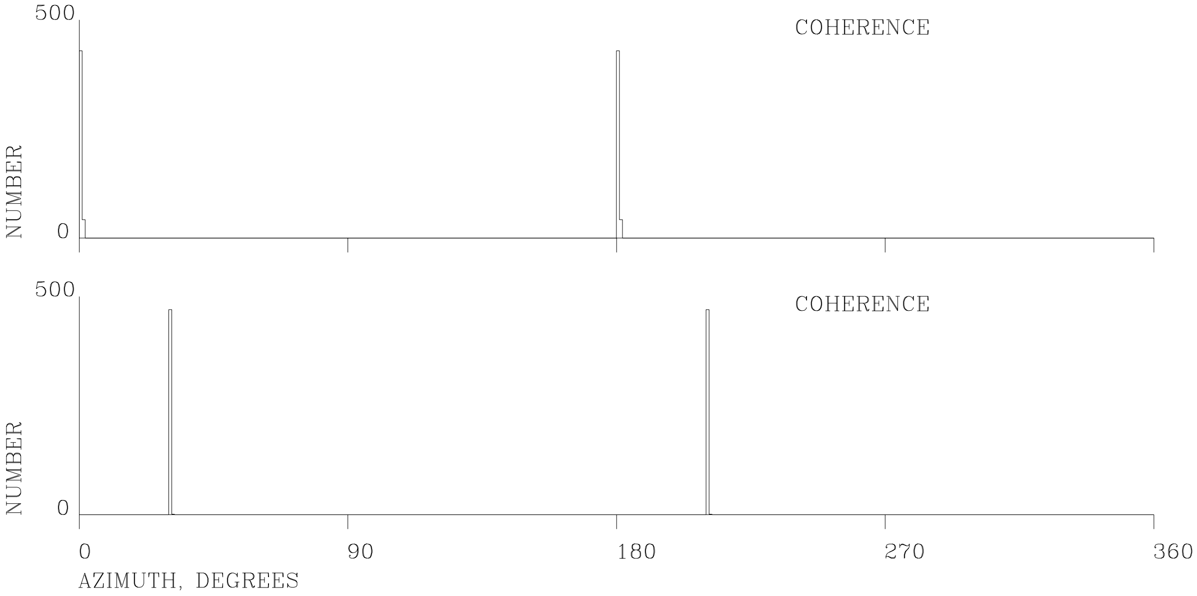

Figure 6.2 Histograms of coherence derived azimuths of real data. The known azimuths in the upper set of data was 0° and in the lower set of data was 30° CCW from north.

7 APPLICATION OF THE COHERENCE FUNCTION METHOD TO BOREHOLE INSTALLATIONS

An experiment was assembled on the ANMO borehole pad to gather data for testing the accuracy of using the coherence function as a criterion for determining the unknown azimuth of a sensor system installed in a borehole. Figure 7.1 is a drawing of the physical positions of the four systems involved in the experiment. System "ANMO" was the standard ANMO KS-36000I borehole system installed in a borehole at a depth of 100 meters. It's orientation was known because the holelock in this borehole was oriented years ago using a gyroscopic orientation tool. System "ALQX" was a GTSN KS-54000 installed in a borehole at a depth of 100 meters. It's orientation was unknown even though it was installed on a Teledyne holelock because the orientation of the holelock was never determined. System "SAND" is a KS-54000 installed in a borehole at a depth of approximately 20 feet; this system was installed by setting the KS-54000 (the probe was removed and replaced by an end cap) on the bottom of the hole and pouring playground sand into the hole up to the top of the sensor package. Its orientation was unknown. System "SURF" was a three component set of Guralp CMG-3NSN sensors installed on the surface on the concrete borehole pad. The orientation of the two horizontal components was carefully determined using a local landmark which is known to be due north. This system will be referred to as “SURFACE” in the rest of this section.

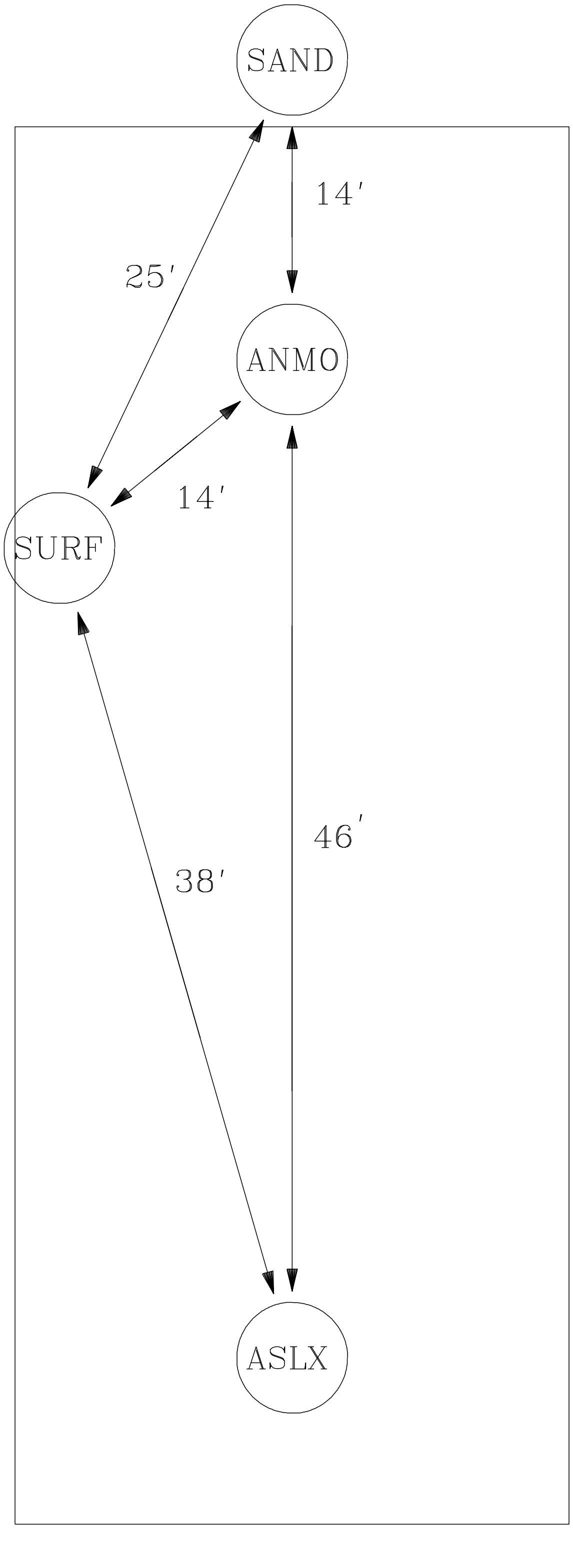

Figure 7. 1 Relative locations of the four sensor systems on the ANMO borehole pad.

Figure 7.2 contains a definition of the coordinate axis to be used to determine relative azimuths using the coherence function. The upper coordinates in the figure denote the orthogonal horizontal components of the sensor system which is to be rotated (system 1) and the lower coordinates denote the orthogonal horizontal components of the stationary sensor system (system 2). The angles in the figures are defined to be measured counterclockwise looking down on the sensor systems. The angle θ is the coordinate rotation angle; ϕ denotes the relative azimuth of the unknown orientation system. This is the angle to be determined.

Briefly, the process for determining this angle is as follows. Time series data from components N_1 and E_1 and at least one of the components N_2 or E_2 are recorded over a considerable time period; a lengthy time series is desirable because surface noise generated by local environmental conditions will contaminate the data from the surface system (one of these systems is assumed to be installed on the surface in a real borehole orientation situation). In addition, recently installed seismic systems tend to be noisy; this is true for both surface and borehole installations. Recording over a long period of time particularly at night will increase the chances that the recording will include time periods during which both systems are quiet.

The four recorded horizontal time series (N_1 and E_1 from system 1, and N_2, and E_2 from system 2, see Figure 7.1) are then broken up into convenient length segments for coherence processing. Segments consisting of 3600 data points (1 hour of data at one sample per second) with a 50% overlap were extracted from each channel and passed through a 4 to 10 second bandpass digital filter to isolate the 6 second microseisms. Each segment was then subdivided into 13 shorter subsegments with 256 points each and each subsegment was Fast Fourier Transformed (FFT). The transform values contained in the 6 FFT bins corresponding to periods between 6 and 7 seconds from each of the 13 segments were stored for use in the coherence determined azimuth calculations.

Coordinate rotation of system 1 was performed in the frequency domain using Equations 7.1 and 7.2, where N_i and E_i (see also Figure 7.1) are the complex valued FFT's of the unrotated north and east system 1 subsegments respectively, and $N_i^{'}(\theta)$ and $E_i^{'}(\theta)$ are the complex valued FFT's of the rotated north and east system 1 subsegments respectively. Rotating in the frequency domain saves considerable computing time because the data does not need to be retransformed for each rotation.

After rotation, the power spectral density (PSD) functions for all four channels were calculated for all 13 subsegments, and the cross spectral density (XPSD) functions between components $N_1^{'}$ and N_2, $N_1^{'}$ and E_2, $E_1^{'}$ and N_2, and $E_1^{'}$ and E_2 for each subsegment were also evaluated. The PSD's and XPSD's were smoothed by segment averaging over the 13 subsegments. These smoothed PSD and XPSD estimates were then used to calculate the coherence at the 6 FFT bin periods between 6 and 7 seconds. Finally, the 6 individual bin coherence estimates were averaged to yield an overall coherence estimate for each rotation angle under consideration. The rotated sensor was turned throughout $360°$ in $1°$ steps.

An example of the functional dependence of the coherence as the rotated sensor turns as obtained from experimental data is shown as the solid line in Figure 7.3. A plot of the theoretical $\cos^2(\theta)$ is also shown in the figure as the hollow circle curve. The departure of the experimental data from the theoretical curve is not currently understood.

Figure 7.4 contains four polar coordinate plots of the same type of experimental data as that in Figure 7.3. A coherence of one plots on the radius of the circles in the figure; the coherence in all four plots in the figure reaches values nearly equal to one. The relative azimuth is indicated by tic marks on the circle in $5°$ increments. The data in the upper left plot was derived from the coherence between the two north components of two sensor systems which were known to be nearly aligned. The coherence data indicates a $2°$ or a $182°$ angle between the two north components; if the first system north points north, then the second system north points either nearly north or south. The upper right plot contains the coherence between the rotated north component of the first system and the fixed east component of the second system. In this case, the coherence peaks for first system north component counterclockwise rotations of $92°$ and $272°$. This means that if the first system north points north, the second system east points either nearly east or west. This is what one should expect because the north and east components are $90°$ apart. The lower left plot is the coherence between the first system east component and the second system north component. It peaks after the first system east has been rotated counterclockwise $92°$ and $272°$. This rotation agrees with the data from the two north rotations; that is, if the first system east points east, then the second system north points nearly north or south. Finally the lower right plot is the coherence obtained by rotating the first system east into the second system east. The indication is that if the first system east points east, then the second system east points either nearly east or west.

Unfortunately, as can be seen from the figures, the coherence azimuth function does not yield a unique solution to the unknown azimuth; the coherence reaches a maximum value both when the two sensors are aligned and when they point in opposite directions. Although the correlation function does not yield precise azimuth estimates between sensors with different phase responses, it is good enough to be used to indicate which of the two γ^2 maximums corresponds to the true alignment direction instead of $180°$ out.

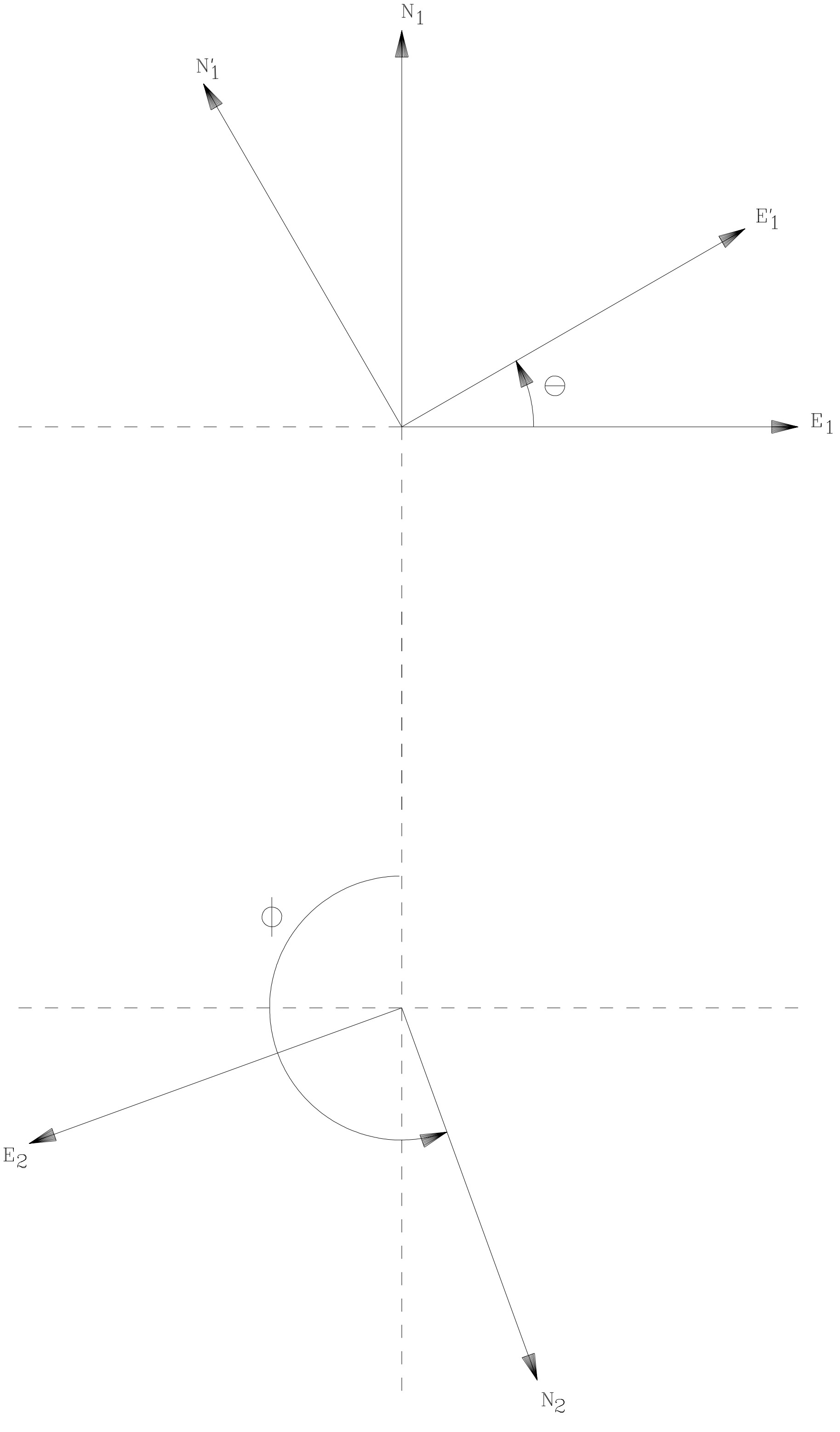

Figure 7. 2 Definition of the coordinate systems utilized to determine relative azimuths using the coherence function.

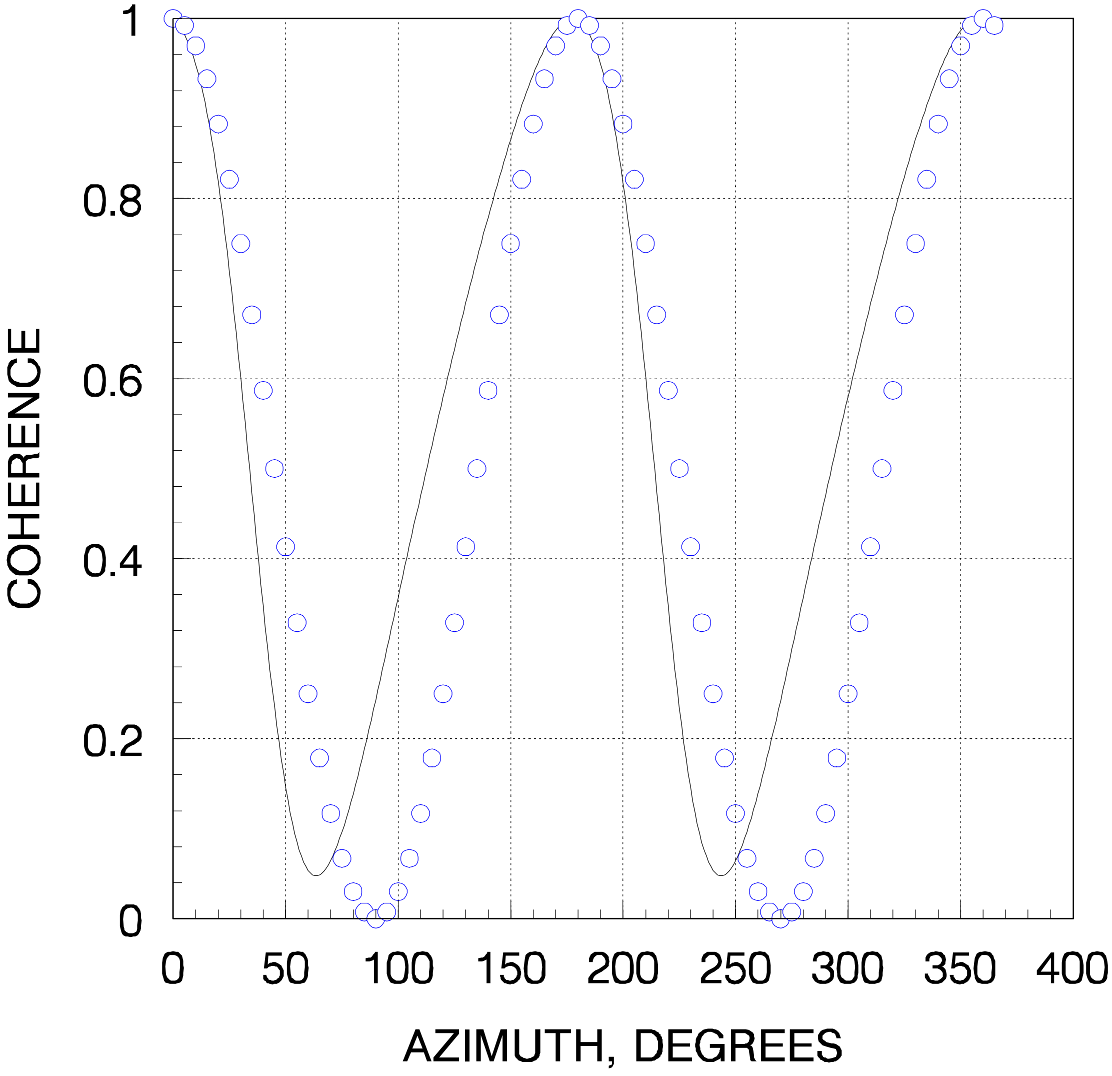

Figure 7. 3 Example of the degree of fit of experimentally determined coherence values (the solid curve) to a theoretical $\cos^2(\theta)$ function (the circles) .

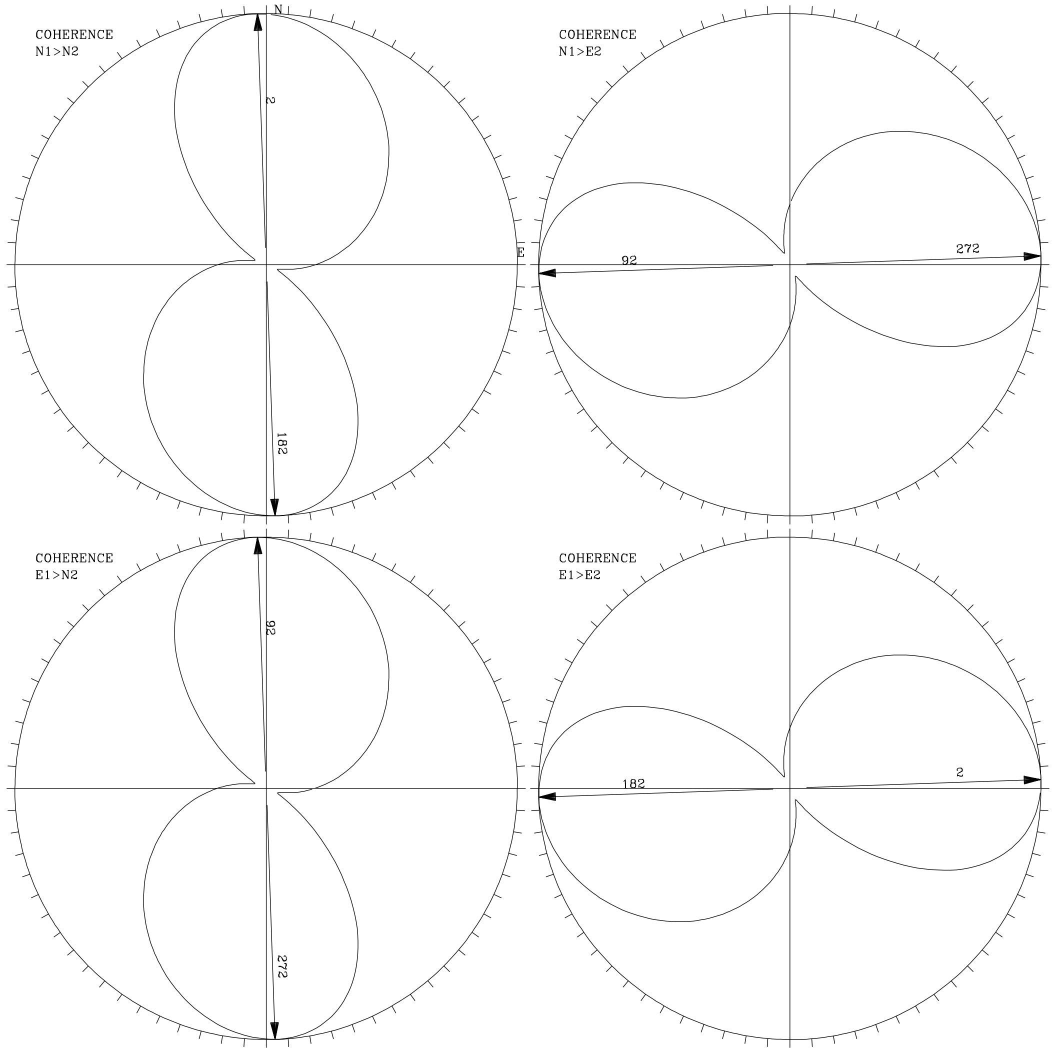

Figure 7. 4 Polar plots of the azimuthal dependence of the coherence between different components of real data.

Nearly 5 days of data was gathered from the experimental configuration shown in Figure 7.1 from ANMO, and the SURFACE systems and was analyzed as described above. Figures 7.5 and 7.6 illustrate the calculated coherence values obtained by rotating sensor system ANMO into system SURFACE throughout the 5 day period. Unfortunately, the coherence between the rotated ANMO components and the stationary SURFACE components is rather low during most of the recording period. The reason for the low coherence values throughout most of the recording period is noise which occurs in the surface data due to wind, temperature changes, instrument settling processes etc.. However, coherence was reasonably high during some of the time thereby raising hopes that reasonable estimates of the relative azimuths of the two systems could be made.

Figure 7.7 summarizes the 222 azimuth estimates obtained by calculating the coherence between the rotated ANMO north component and the fixed SURFACE north component when plotted against the maximum value of the coherence and Figure 7.8 contains the same data obtained from rotating the ANMO north component into the SURFACE east component. The two sensor systems were believed to be oriented in the same direction because ANMO was installed in a holelock which had been oriented several years ago with a gyro probe tool, and the SURFACE north had been oriented north as closely as possible. Note the wide spread in azimuth estimates for low coherence values (γ^2 less than 0.1). There is a better grouping of azimuth estimates for coherence values between 0.1 and 0.6, and the azimuth estimates center about two definite angles near $0°$ and $180°$ for γ^2 above 0.65 in Figure 7.7. This is the expected result for the two north components because the two sensor systems are believed to be aligned and the coherence function is double valued as mentioned previously. The data in Figure 7.8 for the ANMO north rotated into the SURFACE east is similar with the higher coherence (γ^2 greater than about 0.65) azimuth estimates grouping near $90°$ and $270°$. Remember that the rotated component is turned counterclockwise looking down on the system. Therefore, the ANMO north component should come into opposition with the SURFACE east component after turning $90°$ and into alignment after turning $270°$.

Figure 7.9 presents azimuth estimates obtained by calculating the correlation function between the ANMO north and the fixed SURFACE north component and Figure 7.10 contains the same data obtained from rotating the ANMO north component into the SURFACE east component. Although not as tightly grouped as the coherence azimuth's, these estimates are sufficient to resolve the $180°$ ambiguity in the coherence data. Figure 7.9 indicates that the smaller angle coherence azimuths in Figure 7.7 are the azimuths for alignment of the two north components and Figure 7.10 indicates that the larger angle coherence azimuths in Figure 7.8 are the azimuths for alignment of the two east components. Thus, the combined coherence and correlation data indicates that the two sensor systems are quite closely but not exactly aligned.

Table 7.1 summarizes all of the azimuth estimates obtained by rotating both of the ANMO horizontals into both of the SURFACE horizontals. Although only the relative azimuth plots for the rotation of the ANMO north into the SURFACE north and south are shown in Figures 7.13 through 7.16, there are a total of four possible rotations for these two component systems. These are the rotation of the ANMO north into the SURFACE north and east, and the rotation of the ANMO east into the SURFACE north and east. These four rotations are specified in column one of the table in which the symbol ">" denotes "rotated into". Angles in the table are referenced to the original position of the component being rotated - that is the first component listed before the ">" symbol. This means that the zero azimuth reference for the rotated north component is not the same as the zero azimuth reference for the east component. The azimuth angles in the table are the angles though which the rotated component must be turned to reach a maximum in the coherence or correlation function from the original position of that component. In Table 7.1 and the tables that follow, "COH 1 MEAN" is the mean value of the smaller coherence derived azimuth estimates and "COH 2 MEAN" is the mean value of the larger coherence derived azimuth estimates for each of the four possible rotations. "COH NUM" is the number of azimuth estimates used to calculate each mean coherence value. "COR MEAN" is the mean value of the correlation derived azimuth estimates over "COR NUM" azimuth estimates. The columns subheaded "STAN DEV" contain the standard deviations of the indicated mean values. The bold numbers in the table are the resolved ambiguity coherence derived mean azimuth estimates selected by the correlation function.

The average of all of the 65 smaller angle azimuth estimates corresponding to coherence estimates greater than 0.65 derived from rotating the ANMO north into the SURFACE north in Figure 7.7 is 3.78° (see line one of Table 7.1). If the ANMO north is assumed to be absolutely correctly oriented true north, this data indicates that the SURFACE north is oriented 3.78° counterclockwise from true north. The average of the 49 larger azimuth estimates corresponding to coherence estimates greater than 0.65 derived from rotating the ANMO north into the SURFACE east in Figure 7.9 is 272.33° (see line two of Table 7.1). If the ANMO north is assumed to be absolutely correctly oriented true north, this data indicates that the SURFACE east is oriented at 272.33 counterclockwise from true north. These azimuths are shown in Figure 7.17

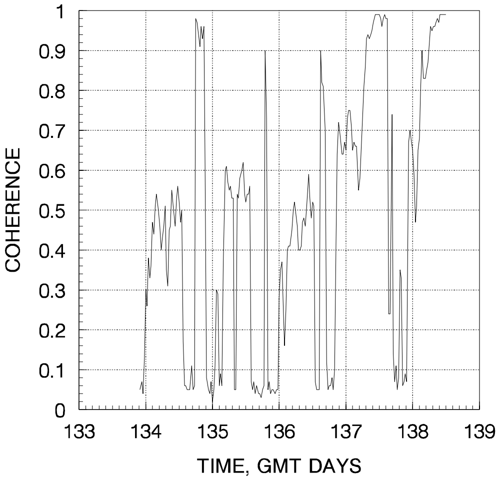

Figure 7. 5 Maximum coherence between the rotated ANMO north and the fixed SURFACE north component.

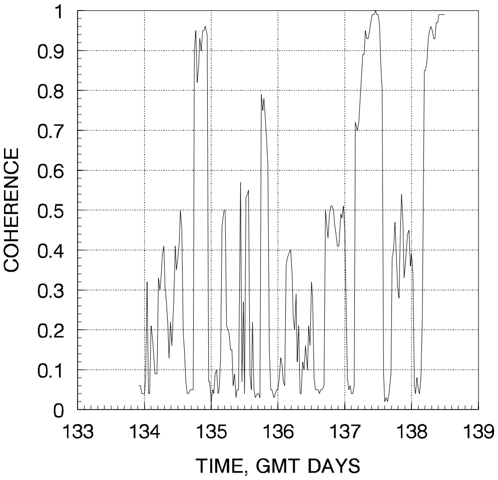

Figure 7. 6 Maximum coherence between the rotated ANMO north and the fixed SURFACE east component.

NOTE: The horizontal axes in Figures 7.7, 7.8, and 7.10 are mislabeled. All three axes should be labeled “AZIMUTH, DEGREES”.

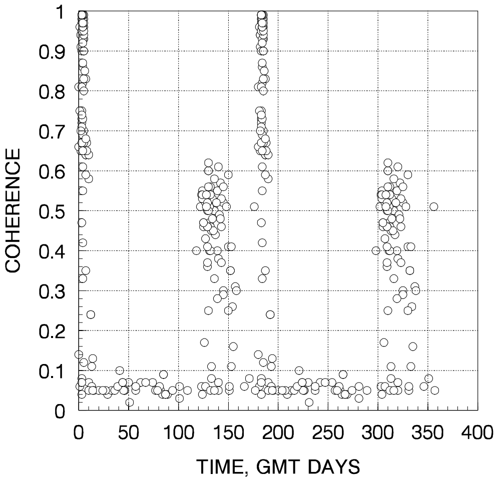

Figure 7. 7 Azimuth estimates as determined by the maximum in the coherence between the rotated ANMO north and the fixed SURFACE north component. The true azimuth between the two components was supposed to be 0°. See NOTE above.

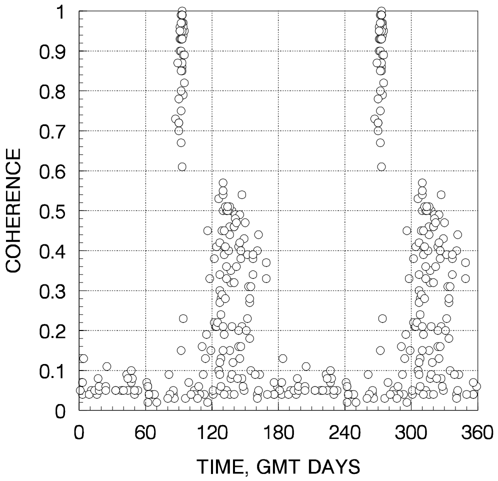

Figure 7. 8 Azimuth estimates as determined by the maximum in the coherence between the rotated ANMO north and the fixed SURFACE east component. The true azimuth between the two components was supposed to be 270°. See NOTE above.

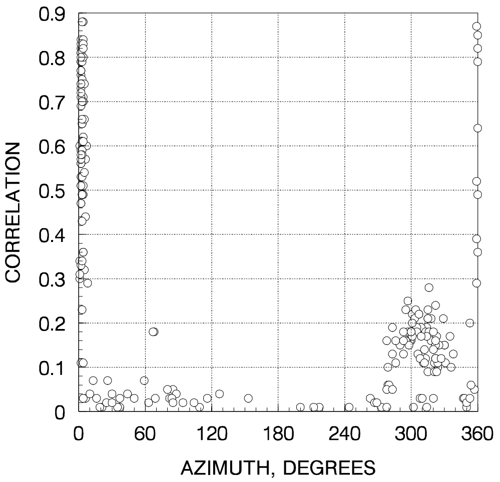

Figure 7. 9 Azimuth estimates as determined by the maximum in the correlation between the rotated ANMO north and the fixed SURFACE north component. The true azimuth between the two components was supposed to be 0°.

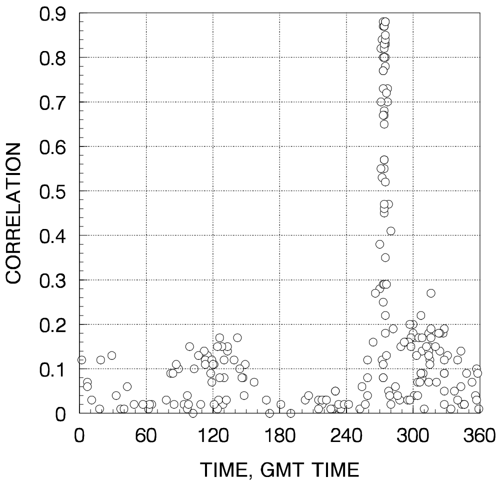

Figure 7. 10 Azimuth estimates as determined by the maximum in the correlation between the rotated ANMO north and the fixed SURFACE east component. The true azimuth between the two components was supposed to be 270°. See NOTE above.

The relative orientation data in Figures 7.5 through 7.10 was obtained by rotating sensor system ANMO. The same data should result if the two systems are interchanged, that is, if the SURFACE system is rotated. Figures 7.11 and 7.12 are plots of the maximum coherence as a function of time for the same data set with the SURFACE system rotated. Although there are differences, these results are quite similar to the previous case. Greater changes are evident in the estimated azimuths of Figures 7.13 and 7.14; there is greater scatter in the estimates corresponding to higher coherence estimates. This is probably due to the fact that the SURFACE system is noisier than ANMO. The process of rotating quiet ANMO data into noisy SURFACE data has a greater probability of finding quiet segments in the SURFACE data than does rotating noisy SURFACE data into quiet ANMO data because rotating SURFACE data mixes the noise from two noisy horizontals in performing the rotation. There is therefore less chance that this mix will result in a quiet rotated component.

The correlation data in Figure 7.15 indicates that the coherence azimuth data near 0° in Figure 7.13 is the true alignment data; similarly the correlation data in Figure 7.16 shows that the coherence azimuth data near 270° in Figure 7.14 is the aligned data. The average of all 71 azimuths corresponding to coherence estimates greater than 0.65 in Figure 7.13 is 352.68 and the average for the 56 data points whose coherence values are greater than 0.65 in Figure 7.14 is 272.09° (see Table 7.6. These results indicate that the ANMO north and east are only 80.59° apart. This is improbable because the manufacturer probably constructed the instrument to a greater precision than this. The discrepancy is probably due to the noise in the surface sensors and the mixing of the noise from both the north and the east components in the rotation process.

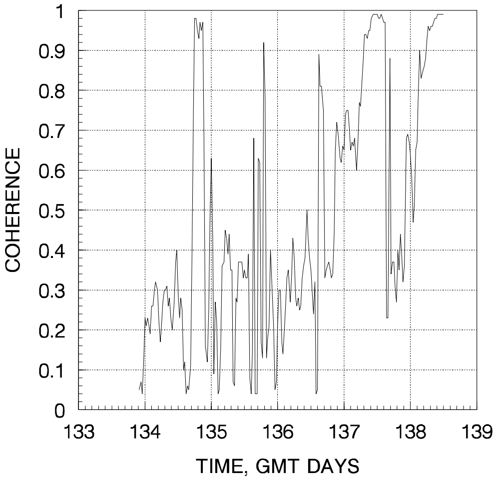

Figure 7. 11 Maximum coherence between the rotated SURFACE north component and the fixed ANMO north component.

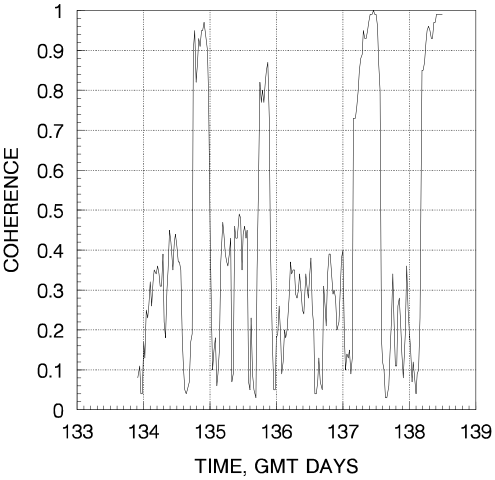

Figure 7. 12 Maximum coherence between the rotated SURFACE north component and the fixed ANMO east component.

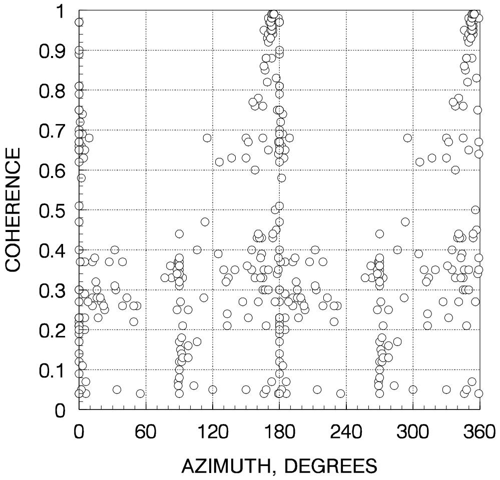

Figure 7. 13 Azimuth estimates as determined by the maximum in the coherence between the rotated SURFACE north component and the fixed ANMO north component. The true azimuth between the two components was supposed to be 0°.

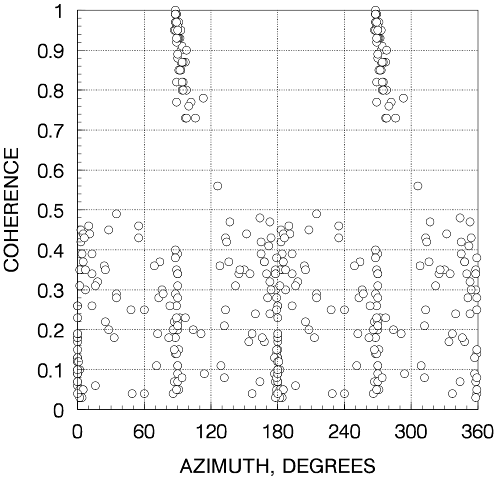

Figure 7. 14 Azimuth estimates as determined by the maximum in the coherence between the rotated SURFACE north component and the fixed ANMO east component. the true azimuth between the two components was supposed to be 270°.

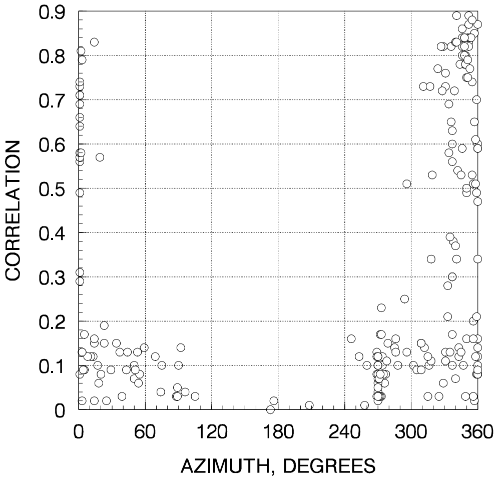

Figure 7. 15 Azimuth estimates as determined by the maximum in the correlation function between the rotated SURFACE north component and the fixed ANMO north. The true azimuth between the two components was supposed to be 0°.

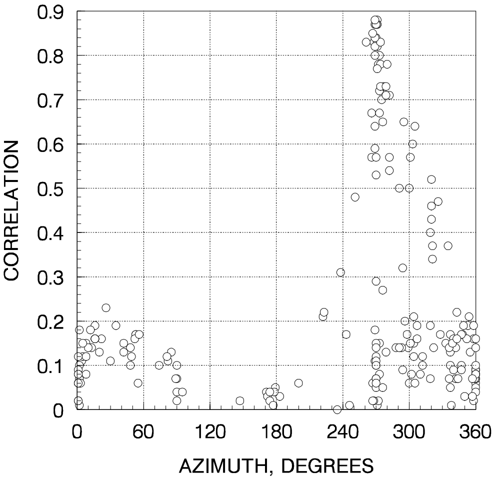

Figure 7. 16 Azimuth estimates as determined by the maximum in the correlation function between the rotated SURFACE north component and the fixed ANMO east. The true azimuth between the two components was supposed to be 270°.

	COH 1 MEAN	COH 1 STAN DEV	COH 2 MEAN	COH 2 STAN DEV	COH NUM	COR MEAN	COR STAN DEV	COR NUM
$N_{anmo} > N_{surf}$	**3.78**	1.44	183.78	1.44	65	2.55	1.29	42
$N_{anmo} > E_{surf}$	92.33	1.55	**272.33**	1.55	49	274.03	1.40	31
$E_{anmo} > N_{surf}$	**93.78**	1.44	273.78	1.44	49	92.5	1.31	42
$E_{anmo} > E_{surf}$	**2.33**	1.55	182.33	1.55	49	4.10	1.27	31

Table 7. 1 Azimuth estimate results obtained by rotating the horizontal components of ANMO into the horizontal components of the SURFACE system. All angles are in degrees clockwise from north looking down on the sensor systems.

	COH 1 MEAN	COH 1 STAN DEV	COH 2 MEAN	COH 2 STAN DEV	COH NUM	COR MEAN	COR STAN DEV	COR NUM
$N_{surf} \rightarrow N_{anmo}$	172.68	9.86	**352.68**	9.86	71	346.85	12.62	47
$N_{surf} \rightarrow E_{anmo}$	92.09	4.91	**272.09**	4.91	56	271.80	4.29	30
$E_{surf} \rightarrow N_{anmo}$	**82.68**	9.86	262.68	9.86	56	77.04	12.53	48
$E_{surf} \rightarrow E_{anmo}$	182.09	4.91	**362.09**	4.91	56	362.10	4.23	30

Table 7. 2 Azimuth estimate results obtained by rotating the horizontal components of SURFACE into the horizontal components of the ANMO system. All angles are in degrees clockwise from north looking down on the sensor systems.

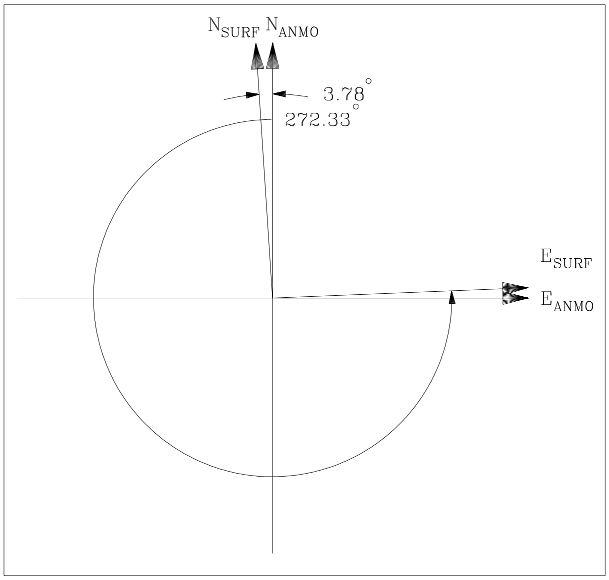

Figure 7. 17 Relative AZIMUTHS Obtained by rotating ANMO into the SURFACE sensors. ANMO is assumed to be oriented exactly north-south.

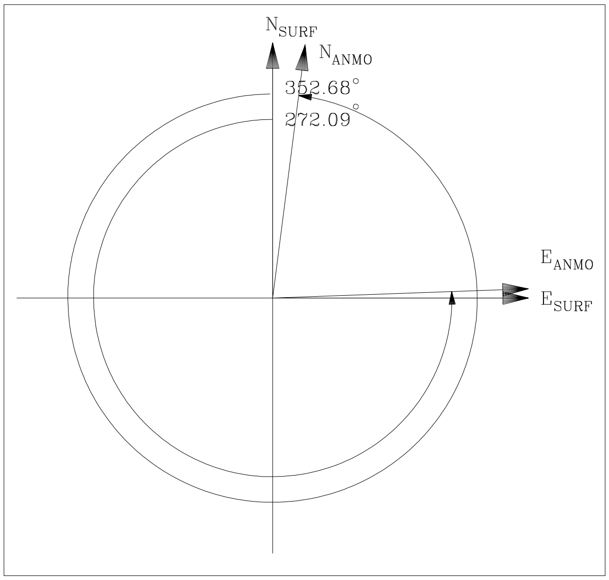

Figure 7. 18 Relative azimuths obtained by rotating the SURFACE sensors into ANMO. The SURFACE system is assumed to be oriented exactly north-south.

There is a dramatic difference in the results of relative azimuth estimates between the ANMO sensor and the SAND system compared with the results of the ANMO to SURFACE estimates. The maximum coherence estimates shown in Figures 7.19 and 7.20 are the coherence values obtained by rotating the ANMO north into the SAND north and east respectively; all γ^2 values appear to plot at one in the two figures. The coherence estimates were greater than 0.995 for all 215 azimuth estimates. The increase in coherence cannot be attributed to horizontal separation because the SAND system was separate horizontally from ANMO by the same distance as was the SURFACE SYSTEM (see Figure 7.1). There was a slight difference of about 20 feet in vertical separation of the SURFACE and the SAND systems (0 meters deep for the SURFACE system, about 6 meters deep for the SAND system), ANMO was vertically separate considerably more (100 meters deep for the ANMO system). The increase in coherence is due to the fact that the SURFACE system is quite noisy; it had been installed recently and, despite the fact that it was covered with a protective box, it was exposed to various environmental influences.

The high coherence estimates lead to highly repeatable relative azimuth estimates as Figures 7.21 and 7.22 illustrate. The 215 double valued azimuth estimates obtained by rotating the ANMO north component into the fixed SAND north plot as two dots in Figure 7.21: the same is true for the ANMO north component rotated into the fixed SAND east in Figure 7.22. In fact, all of the 215 estimates obtained by rotating the ANMO north into the SAND north are within 1° of one another. The same is true for the remaining three possible rotations. The correlation derived azimuth estimates are also highly repeatable as shown in Figures 7.23 and 7.24. Table 7.3 summarizes the results of rotating the ANMO horizontals into the SAND horizontals and Figure 7.25 graphically depicts their relative orientations. The two systems were oriented almost 180° apart.

Rotating the SAND system into the ANMO system yielded tightly grouped azimuth estimates just like those obtained by the reverse rotation. Graphical plots of these results will not be presented, but Table 7.4 numerically summarizes the results and Figure 7.26 graphically depicts the relative positions of the two systems as calculated by rotating the SAND system into ANMO. Once again the analysis indicates that the two system azimuths' are nearly 180° apart. Comparing Figure 7.26 with Figure 7.25 yields excellent agreement in the relative positions of the two systems; the relative position of the east components is the same in both figures (178°), and the relative positions of the north components disagree by only 0.02°. Ideally the sum of the ANMO north into SAND north relative azimuth plus the SAND north into ANMO north relative azimuth should equal 360°; the same relationship for the east components. From Figures 7.25 and 7.26, the experimental sum of the two north angles is 360.11° and the sum for the east components is exactly 360°. This is excellent agreement with theory which leads to the conclusion that the relative azimuths are known to within a degree or so.

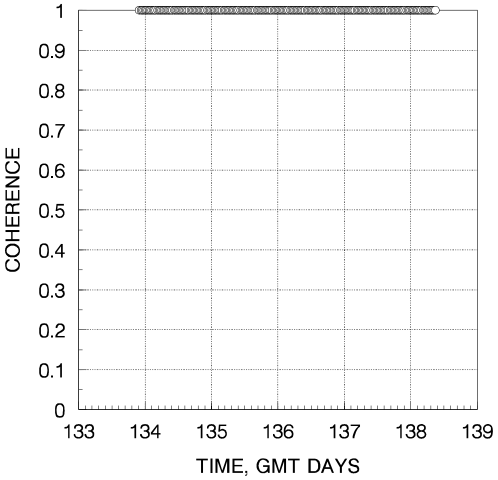

Figure 7. 19 Maximum coherence between the rotated ANMO north component and the fixed SAND north component.

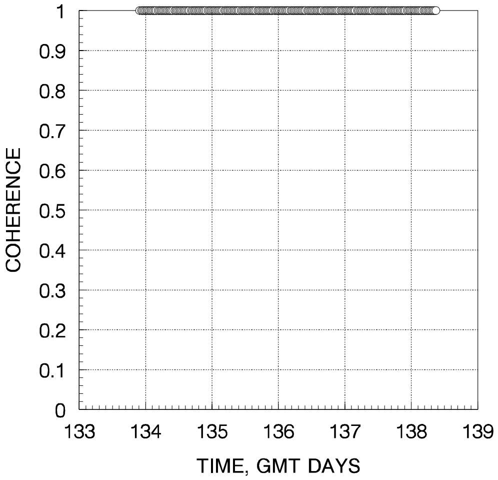

Figure 7. 20 Maximum coherence between the rotated ANMO north component and the fixed SAND east component.

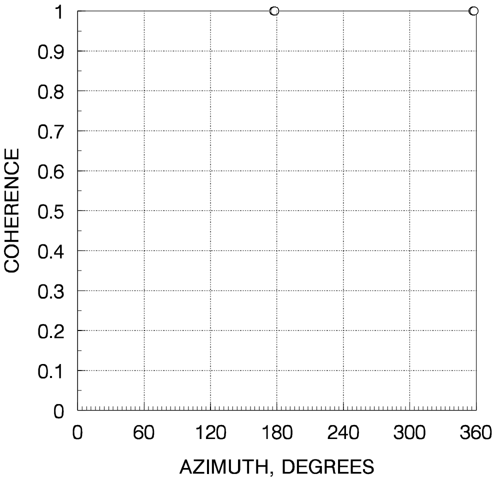

Figure 7. 21 Azimuth estimates as determined by the maximum in the coherence function between the rotated ANMO north component and the fixed SAND north.

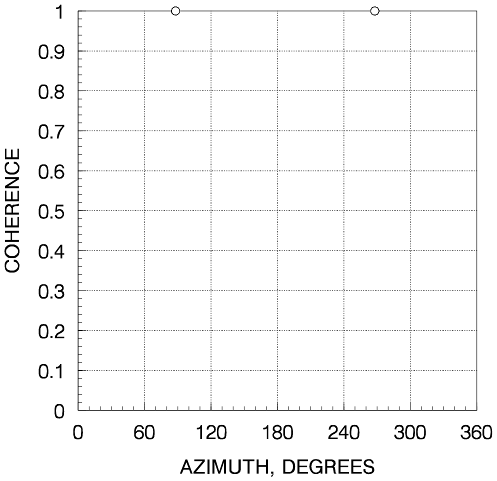

Figure 7. 22 Azimuth estimates as determined by the maximum in the coherence function between the rotated ANMO north component and the fixed SAND east.

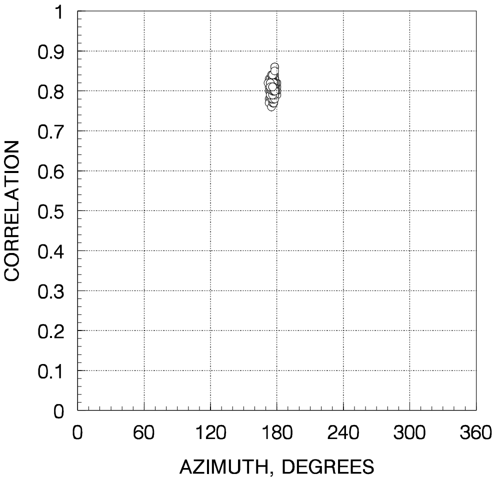

Figure 7. 23 Azimuth estimates as determined by the maximum in the correlation function between the rotated ANMO north component and the fixed SAND north.

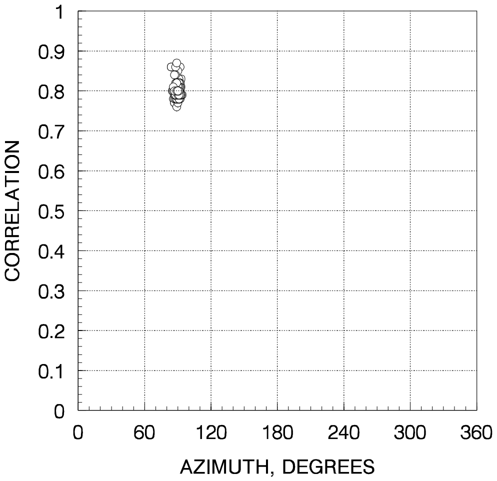

Figure 7. 24 Azimuth estimates as determined by the maximum in the correlation function between the rotated ANMO north component and the fixed SAND east.

	COH 1 MEAN	COH 1 STAN DEV	COH 2 MEAN	COH 2 STAN DEV	COH NUM	COR MEAN	COR STAN DEV	COR NUM
N_{anmo} → N_{sand}	**177.46**	0.50	357.46	0.50	215	176.47	1.49	215
N_{anmo} → E_{sand}	**88.00**	0.00	268.00	0.00	215	89.70	1.67	215
E_{anmo} → N_{sand}	87.46	0.50	**267.46**	0.50	215	266.47	1.49	215
E_{anmo} → E_{sand}	**178.00**	0.00	358.00	0.00	215	179.70	1.67	215

Table 7. 3 Azimuth estimate results obtained by rotating the horizontal components of ANMO into the horizontal components of the SAND system. All angles are in degrees clockwise from north looking down on the sensor systems.

	COH 1 MEAN	COH 1 STAN DEV	COH 2 MEAN	COH 2 STAN DEV	COH NUM	COR MEAN	COR STAN DEV	COR NUM
N_{sand} → N_{anmo}	2.65	0.48	**182.65**	0.48	197	181.17	1.51	198
N_{sand} → E_{anmo}	**92.00**	0.00	272.00	0.00	197	93.01	1.53	198
E_{sand} → N_{anmo}	92.65	0.48	**272.66**	0.47	197	271.17	1.51	198
E_{sand} → E_{anmo}	2.00	0.00	**182.00**	0.00	197	183.01	1.53	198

Table 7. 4 Azimuth estimate results obtained by rotating the horizontal components of SAND into the horizontal components of the ANMO system. All angles are in degrees clockwise from north looking down on the sensor systems.

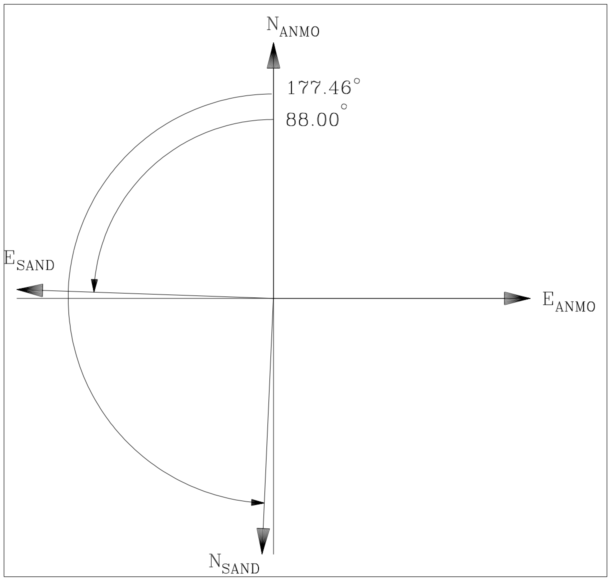

Figure 7. 25 Relative azimuths obtained by rotating ANMO into the SAND sensor system. ANMO is assumed to be oriented exactly north-south.

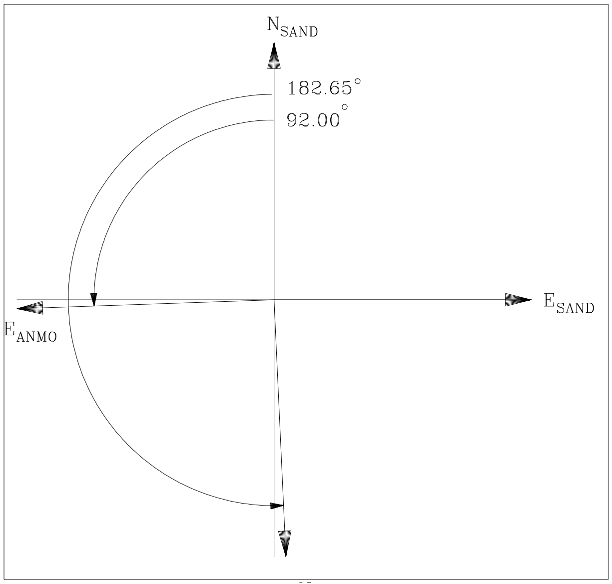

Figure 7. 26 Relative azimuths obtained by rotating the SAND sensor system into ANMO. The SAND system is assumed to be oriented exactly north-south.

The final azimuth relationship in this SURFACE - ANMO – SAND experiment is the relative position of the SAND and SURFACE systems. Figures 7.27 and 7.28 contain plots of the azimuth estimates obtained by rotating the SAND north into the fixed SURFACE north and east respectively and Figures 7.29 and 7.30 present the corresponding correlation data. The results of interchanging the two systems are shown in Figures 7.31 through 7.32. Note the greater scatter in the azimuth estimates the latter figures when the SURFACE system components are rotated particularly for the correlation azimuth estimates. Table 7.5 and Figure 7.35 summarize the results obtained by rotating the SAND system into the fixed SURFACE system and Table 7.6 and Figure 7.36 do the same for the interchange of the two systems. Note that the standard deviation of the azimuth estimates are considerably higher when the SURFACE system is rotated (Table 7.6) than when the SAND system is rotated (Table 7.5). Once again surface noise is the probable explanation.

The relative positions of the norths of the three systems should add up to 360°. Assume that the SURFACE system is oriented true north-south. Rotating ANMO north into the SURFACE north indicates that ANMO north is 3.78° (Table 7.1 or Figure 7.17) clockwise from the SURFACE north. Therefore, it points at 356.22° azimuth. Rotating the SAND north into ANMO north yields a relative azimuth of 182.65° (Table 7.4 or Figure 7.26) clockwise from ANMO. SAND north points at 173.57° azimuth. Rotating the SAND north into the SURFACE north indicates that the SAND north is 186.44° clockwise from the SURFACE north or at 173.56° azimuth. Only 0.01° error!

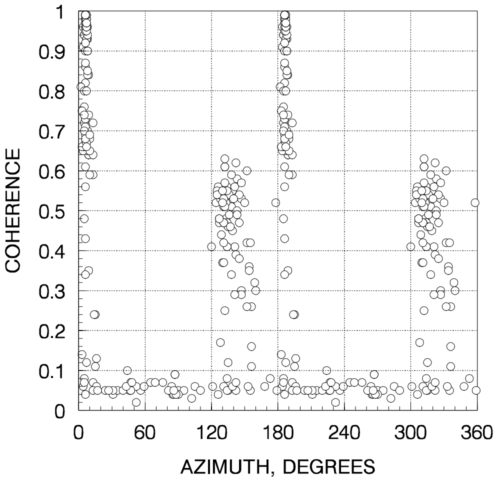

Figure 7. 27 Azimuth estimates as determined by the maximum in the coherence function between the rotated SAND north and the fixed SURFACE north.

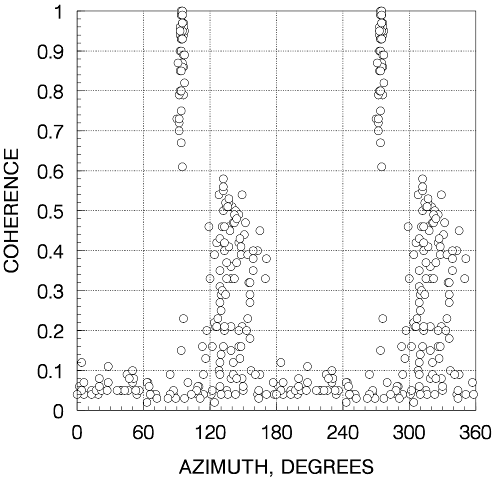

Figure 7. 28 Azimuth estimates as determined by the maximum in the coherence function between the rotated SAND north and the fixed SURFACE east.

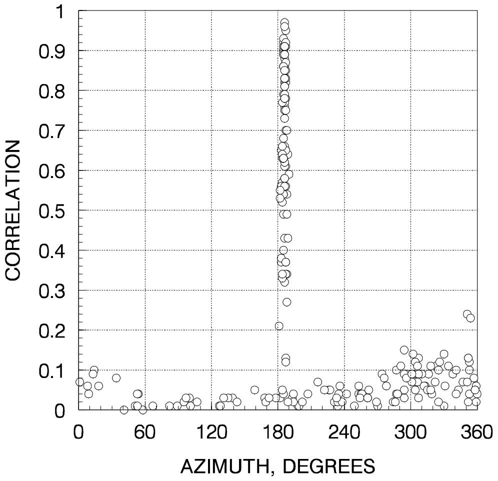

Figure 7. 29 Azimuth estimates as detrmined by the maximum in the correlation function between the rotated SAND north and the fixed SURFACE north.

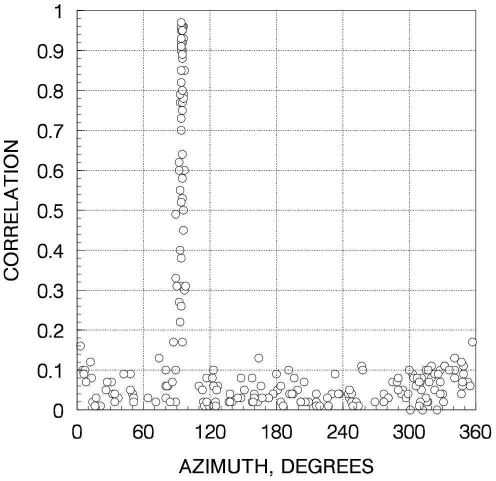

Figure 7. 30 Azimuth estimates as determined by the maximum in the correlation function between the rotated SAND north and the fixed SURFACE east.

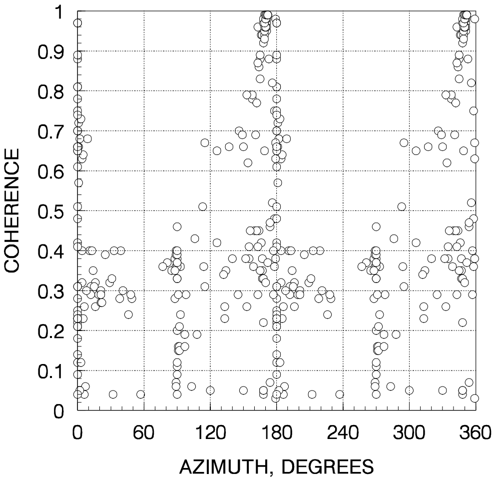

Figure 7. 31 Azimuth estimates as determined by the maximum in the coherence function between the rotated SURFACE north and the fixed SAND north.

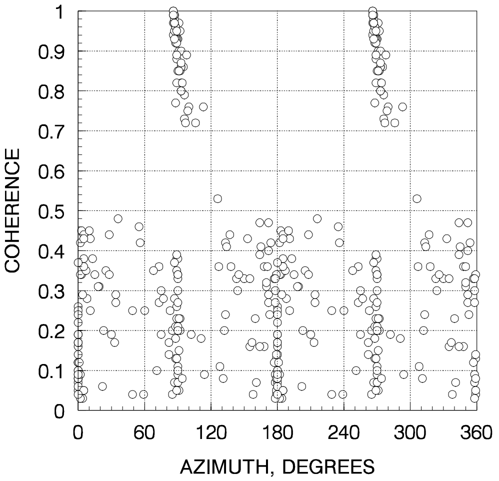

Figure 7. 32 Azimuth estimates as determined by the maximum in the coherence function between the rotated SURFACE north and the fixed SAND east.

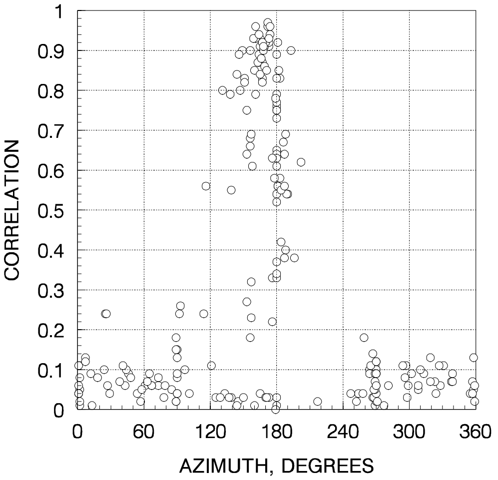

Figure 7. 33 Azimuth estimates as determined by the maximum in the correlation function between the rotated SURFACE north and the fixed SAND north.

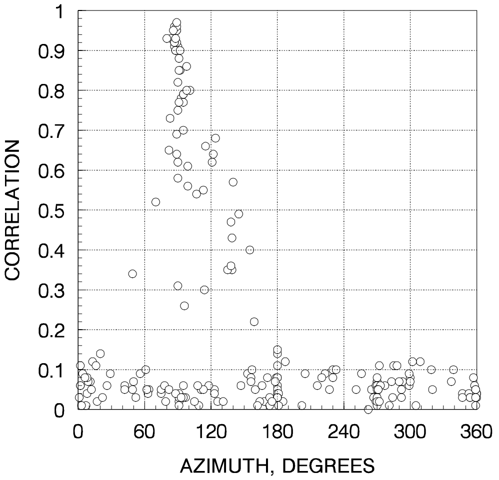

Figure 7. 34 Azimuth estimates as determined by the maximum in the correlation function between the rotated SURFACE and the fixed SAND east.

	COH 1 MEAN	COH 1 STAN DEV	COH 2 MEAN	COH 2 STAN DEV	COH NUM	COR MEAN	COR STAN DEV	COR NUM
$N_{sand} \rightarrow N_{surf}$	6.44	1.65	**186.44**	1.65	68	185.94	0.84	47
$N_{sand} \rightarrow E_{surf}$	**94.31**	1.49	274.31	1.49	51	94.66	0.90	32
$E_{sand} \rightarrow N_{surf}$	96.44	1.65	**276.44**	1.65	51	275.94	0.84	47
$E_{sand} \rightarrow E_{surf}$	4.31	1.49	**184.31**	1.49	51	184.66	0.90	32

Table 7. 5 Azimuth estimate results obtained by rotating the horizontal components of SAND into the horizontal components of the SURFACE system. All angles are in degrees clockwise from north looking down on the sensor systems.

	COH 1 MEAN	COH 1 STAN DEV	COH 2 MEAN	COH 2 STAN DEV	COH NUM	COR MEAN	COR STAN DEV	COR NUM
$N_{surf} \rightarrow N_{sand}$	**169.93**	11.26	349.93	11.26	73	166.72	12.46	53
$N_{surf} \rightarrow E_{sand}$	**90.84**	5.14	270.84	5.14	56	89.91	89.91	33
$E_{surf} \rightarrow N_{sand}$	79.93	11.26	**259.93**	11.26	56	256.72	256.72	53
$E_{surf} \rightarrow E_{sand}$	**180.84**	5.14	360.84	5.14	56	179.91	179.91	33

Table 7. 6 Azimuth estimate results obtained by rotating the horizontal components of SURFACE into the horizontal components of the SAND system. All angles are in degrees clockwise from north looking down on the sensor systems.

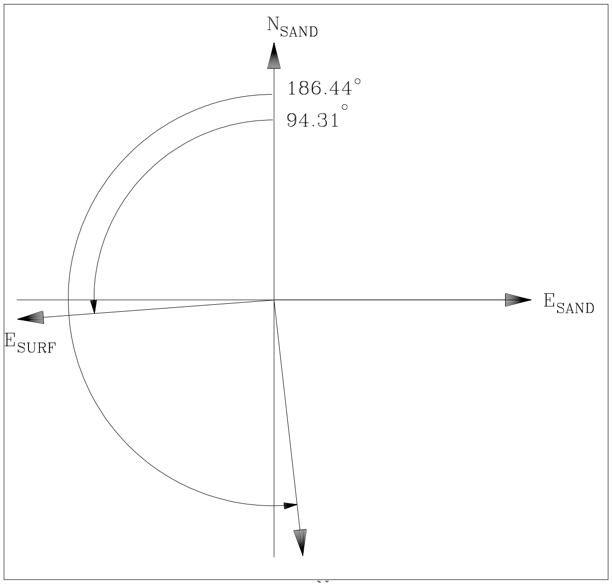

Figure 7. 35 Relative azimuths obtained by rotating the SAND system into the SURFACE system. The SAND sensors are assumed to be oriented exactly north-south.

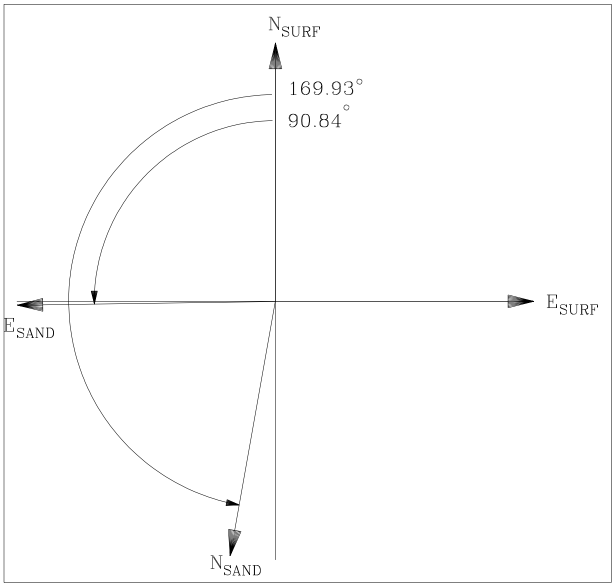

Figure 7. 36 Relative azimuths obtained by rotating the SURFACE system into the SAND system. The SURFACE system is assumed to be oriented exactly north-south.

In July of 1994, a blind experiment was conducted in which the data analysis personnel (Gary Holcomb) did not know the orientation of the target instrument which was installed by Juan Nieto in the ASLX borehole (see Figure 7.1). The experimental layout consisted of ANMO, a BOREHOLE system installed in the ASLX borehole at a depth of 90 feet, and a single component CMG-3NSN sensor oriented north on the surface. This surface sensor had been removed after the earlier experiment and reinstalled for the current experiment. Data from the SAND system was not recorded in this experiment. In the first configuration, the azimuth ring on the CMG-3NSN BOREHOLE system was set to zero; it was installed in a hole lock whose orientation was unknown to anyone. Approximately 16 hours of data as then recorded on days 200 and 201 from all three systems. Then the CMG-3NSN BOREHOLE system was pulled and the azimuth ring was turned a known (to Juan Nieto) azimuth and the system was reinstalled in the borehole. Approximately 20 hours of data was recorded on days 202 and 203 from this configuration.

The results of processing the data from days 200 and 201 (CMG-3NSN BOREHOLE azimuth ring set at 0°) for relative azimuths are presented in Tables 7.7 and 7.8 and Figures 7.37 through 7.38. The azimuth estimates in Table 7.7 and the relative azimuths shown in Figure 7.37, which were obtained by rotating ANMO into the CMG-3NSN BOREHOLE system, indicate that there were 25.86° between the north components of these two systems. The azimuth estimates in Table 7.8 and the relative azimuths shown in Figure 7.38, which were obtained by rotating the CMG-3NSN BOREHOLE system into ANMO, indicate that there were 26.07° between the north components of these two systems. This is excellent agreement between the two methods of determining the relative azimuth's. The average of these two results indicates that the ANMO north azimuth is 25.97° counterclockwise looking down on the two systems from the CMG-3NSN BOREHOLE north azimuth during the initial installation of the CMG-3NSN BOREHOLE system.

Table 7.9 contains the results of relative azimuth calculations between ANMO and the CMG-3NSN SURFACE NORTH sensor; ANMO is positioned 2.31° clockwise from the CMG-3NSN SURFACE NORTH sensor. Rotating the CMG-3NSN BOREHOLE sensor into the CMG-3NSN SURFACE NORTH sensor yields a relative azimuth of 28.18° clockwise from the CMG-3NSN SURFACE NORTH. The combination of these two results yields a relative azimuth between ANMO and the CMG-3NSN BOREHOLE system of 25.87°. This azimuth agrees quite well with the 25.97° estimate obtained by rotating the two borehole sensor systems into one another.

The relative azimuths obtained from the data recorded on days 202 and 203 after the azimuth ring was reset to 120° are shown in Tables 7.11 and 7.12 and Figures 7.39 and 7.40. Rotating ANMO into the CMG-3NSN BOREHOLE yields 14.03° between the two norths and rotating the CMG-3NSN BOREHOLE into ANMO yields 15.11°. Crudely averaging these two results, ANMO north is now about 14.5° clockwise looking down on the two systems from the CMG-3NSN BOREHOLE north.

The results of rotating the days 202 and 203 data from ANMO into the CMG-3NSN SURFACE NORTH are shown in Table 7.13 and Figure 7.43. The data indicates that the ANMO north is 2.32° clockwise from the CMG-3NSN SURFACE NORTH. Since neither ANMO nor the CMG-3NSN SURFACE NORTH have been physically moved, these results should agree with the azimuths obtained from the days 200 and 203 data. They do, the disagreement is only 0.01°! Rotating the CMG-3NSN BOREHOLE into the CMG-3NSN SURFACE NORTH days 202 and 203 data yields the relative azimuth estimates shown in Table 7.14 and Figure 7.44. The CMG-3NSN BOREHOLE north is oriented 15.05° counterclockwise from the CMG-3NSN SURFACE NORTH. Combining these two results yields a relative azimuth between the ANMO north and the CMG-3NSN BOREHOLE north of 15.05° which agrees quite well with the 14.50° result obtained by rotating the two borehole sensors into one another above.

Combining the results of rotating the ANMO north into the CMG-3NSN BOREHOLE north before changing the setting of the azimuth ring (Figure 7.40) with the azimuth estimates obtained by the same rotation after the change of the azimuth ring (Figure 7.42) indicates that the azimuth ring was changed 41.68° clockwise between the recording of the two sets of data. This result does not even approximate the 120° change mechanically set in the azimuth ring between the acquisition of the two sets of data. Alas, oh me, oh my, oh why?

The probable explanation lies in the mechanical design of the Guralp holelock. First of all, the Guralp system relies on two separate sets of small setscrews and a threaded bolt with a locking nut to maintain the position of the probe key with respect to the azimuth ring. All three of these connections appear to be potential sources of error because they could unknowingly slip.

However, the installation crew did not observe any slipping during the borehole pad installations. Second, the Guralp design attempts to achieve a potential 180° rotation of the inserted sensor in 2 inches or less of vertical travel whereas the Teledyne Geotech designed KS holelock allows approximately 10 inches of vertical travel to achieve the same rotation. The slope of the Guralp design is therefore much less and the torque it can generate is correspondingly less. If there is enough resistance to turning the package when the probe key encounters the bishop hat, the Guralp sensor may not rotate into alignment with the keyway in the holelock. It is probable that this is what happened during this experiment.

	COH 1 MEAN	COH 1 STAN DEV	COH 2 MEAN	COH 2 STAN DEV	COH NUM	COR MEAN	COR STAN DEV	COR NUM
$N_{anmo} \rightarrow N_{bore}$	154,14	2.12	**334.14**	2.12	28	333.02	1.43	30
$N_{anmo} \rightarrow E_{bore}$	66.03	0.32	**246.03**	0.32	30	245.97	0.61	30
$E_{anmo} \rightarrow N_{bore}$	**64.14**	2.12	244.14	2.12	30	63.03	1.43	30
$E_{anmo} \rightarrow E_{bore}$	156.03	2.12	**336.03**	0.32	30	335.97	0.61	30

Table 7. 7 Azimuth estimate results obtained by rotating the horizontal components of ANMO into the horizontal components of the CMG-3NSN BOREHOLE system. This data was recorded on days 200 - 201 with the azimuth ring set to 0^{o}. All angles are in degrees clockwise from north looking down on the sensor systems.

	COH 1 MEAN	COH 1 STAN DEV	COH 2 MEAN	COH 2 STAN DEV	COH NUM	COR MEAN	COR STAN DEV	COR NUM
$N_{bore} \rightarrow N_{anmo}$	**26.07**	1.176	206.07	1.76	28	29.60	5.55	30
$N_{bore} \rightarrow E_{anmo}$	112.83	2.59	**292.83**	2.59	30	290.73	3.67	30
$E_{bore} \rightarrow N_{anmo}$	**116.07**	11.76	296.07	1.76	30	119.60	5.55	30
$E_{bore} \rightarrow E_{anmo}$	**22.83**	2.59	202.83	2.59	30	20.73	3.67	30

Table 7. 8 Azimuth estimate results obtained by rotating the horizontal components of CMG-3NSN BOREHOLE into the horizontal components of the ANMO system. This data was recorded on days 200 - 201 with the azimuth ring set to 0°. All angles are in degrees clockwise from north looking down on the sensor systems.

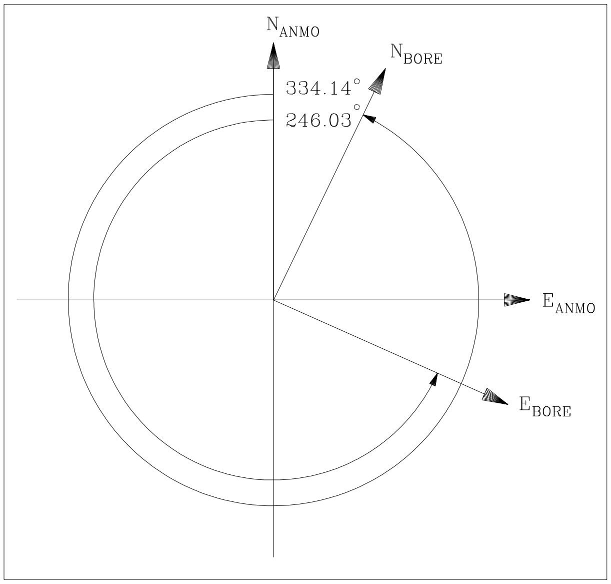

Figure 7. 37 Relative azimuths obtained by rotating ANMO into the BOREHOLE system. The BOREHOLE azimuth ring was set to *o*° in the holelock whose orientation was unknown. The ANMO sensors are assumed to be oriented exactly north-south.

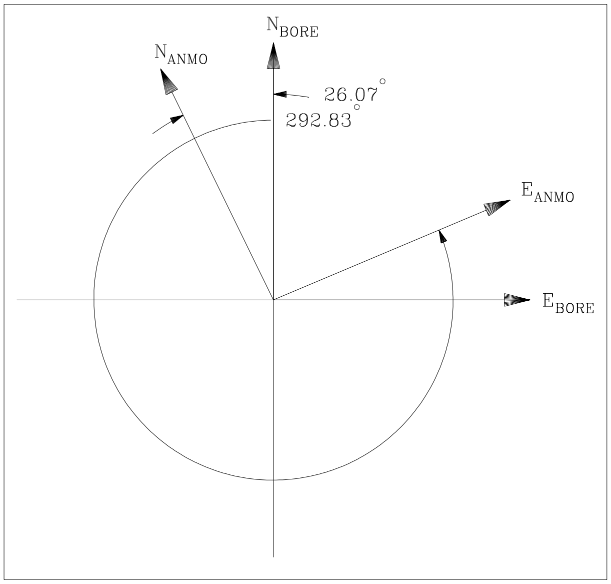

Figure 7. 38 Relative azimuths obtained by rotating the BOREHOLE system into ANMO. The BOREHOLE azimuth ring was set to 0° in the holelock whose oreientation was unknown. The BOREHOLE system is assumed to be oriented exactly north-south.

	COH 1 MEAN	COH 1 STAN DEV	COH 2 MEAN	COH 2 STAN DEV	COH NUM	COR MEAN	COR STAN DEV	COR NUM
N_{anmo} → N_{north}	**2.31**	2.69	182.31	2.69	13	3.50	0.71	2
E_{anmo} → N_{north}	92.31	2.69	**272.31**	2.69	13	93.50	0.71	2

Table 7. 9 Azimuth estimate results obtained by rotating the horizontal components of ANMO into the horizontal components of the CMG-3NSN SURFACE NORTH system. This data was recorded on days 200 - 201 with the azimuth ring set to 0°. All angles are in degrees clockwise from north looking down on the sensor systems.

	COH 1 MEAN	COH 1 STAN DEV	COH 2 MEAN	COH 2 NUM	COH NUM	COR MEAN	COR STAN DEV	COR NUM
N_{bore} → N_{north}	**28.18**	1.72	208.18	1.72	11	27.50	0.71	2
E_{bore} → N_{north}	118.18	1.72	**298.18**	1.72	11	117.50	0.71	2

Table 7. 10 Azimuth estimate results obtained by rotating the horizontal components of CMG-3NSN BOREHOLE into the horizontal components of the CMG-3NSN SURFACE NORTH system. This data was recorded on days 200 – 201 with the azimuth ring set to 0°. All angles are in degrees clockwise from north looking down on the sensor systems.

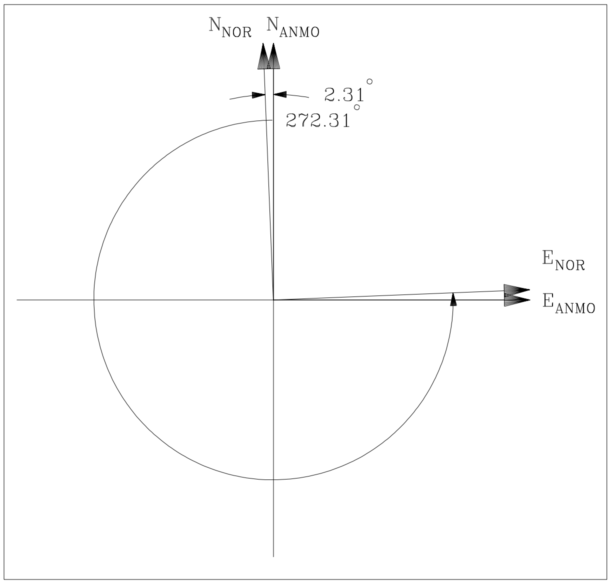

Figure 7. 39 Relative azimuths obtained by rotating ANMO into the SURFACE north sensor. ANMO is assumed to be oriented exactly north-south.

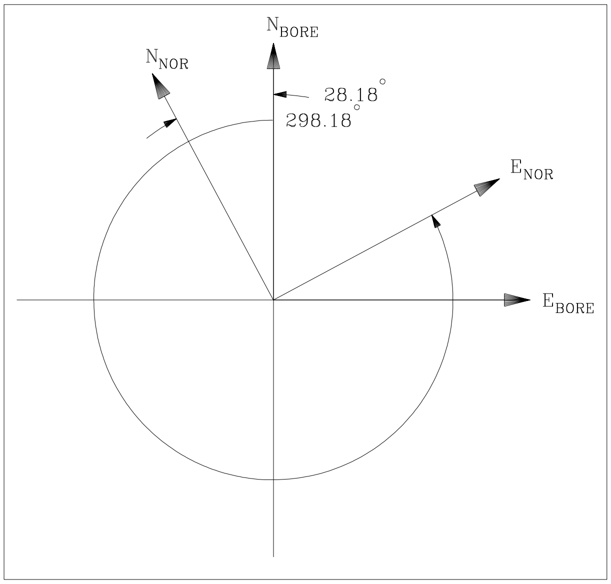

Figure 7. 40 Relative azimuths obtained by rotating the BOREHOLE system into the SURFACE north sensor. The BOREHOLE azimuth ring was set to 0° in the holelock whose orientation was unknown. The BOREHOLE system is assumed to be oriented exactly north-south.

	COH 1 MEAN	COH 1 STAN DEV	COH 2 MEAN	COH 2 STAN DEV	COH NUM	COR MEAN	COR STAN DEV	COR NUM
N_{anmo} → N_{bore}	**14.03**	0.70	194.03	0.7	36	14.25	1.16	36
N_{anmo} → E_{bore}	102.92	0.60	**282.92**	0.6	36	282.89	1.12	36
E_{anmo} → N_{bore}	**104.03**	0.70	284.03	0.7	36	104.25	1.16	36
E_{anmo} > E_{bore}	**12.92**	0.70	192.92	0.6	36	12.89	1.13	36

Table 7. 11 Azimuth estimate results obtained by rotating the horizontal components of ANMO into the horizontal components of the CMT-3NSN BOREHOLE system. This data was recorded on days 202 - 203 with the azimuth ring set to 120°. All angles are in degrees clockwise from north looking down on the sensor systems.

	COH 1 MEAN	COH 1 STAN DEV	COH 2 MEAN	COH 2 STAN DEV	COH NUM	COR MEAN	COR STAN DEV	COR NUM
N_{bore} → N_{anmo}	164.89	2.41	**344.89**	2.41	36	344.19	3.54	36
N_{bore} → E_{anmo}	78.56	2.76	**258.56**	2.76	36	258.97	3.93	36
E_{bore} → N_{anmo}	**74.89**	2.41	254.89	2.41	36	74.19	3.54	36
E_{bore} → E_{anmo}	168.56	2.76	**348.56**	3.76	36	349.00	4.01	36

Table 7. 12 Azimuth estimate results obtained by rotating the horizontal components of CMG-3NSN BOREHOLE into the horizontal components of the ANMO system. This data was recorded on days 202 - 203 with the azimuth ring set to 120°. All angles are in degrees clockwise from north looking down on the sensor systems.

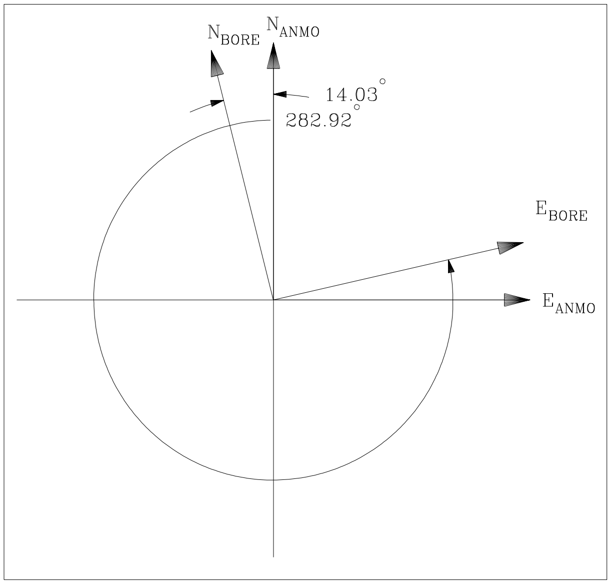

Figure 7. 41 Relative azimuths obtained by rotating ANMO into the BOREHOLE system. The BOREHOLE azimuth ring was set to 120° in a holelock whose orientation was unknown. The ANMO sensors are assumed to be oriented exactly north-south.

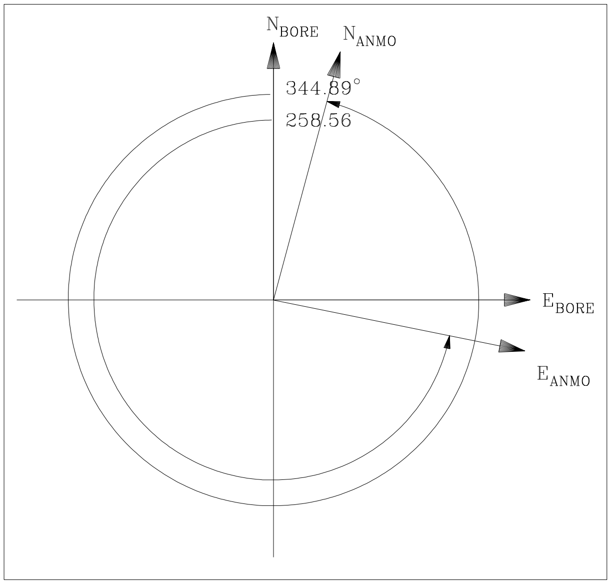

Figure 7. 42 Relative azimuths obtained by rotating the BOREHOLE system into ANMO. The BOREHOLE azimuth ring was set to 120° in a holelock whose orientation was unknown. The ANMO sensors are assumed to be oriented exactly north-south.

	COH 1 MEAN	COH 1 STAN DEV	COH 2 MEAN	COH 2 STAN DEV	COH NUM	COR MEAN	COR STAN DEV	COR NUM
N_{anmo} → N_{north}	**2.32**	1.25	182.32	1.25	22	2.63	1.38	19
E_{anmo} → N_{north}	**92.32**	1.25	272.32	1.25	22	92.53	1.47	19

Table 7. 13 Azimuth estimate results obtained by rotating the horizontal components of ANMO into the horizontal components of the CMG-3NSN SURFACE NORTH system. This data was recorded on days 202 - 203 with the azimuth ring set to 120°. All angles are in degrees clockwise from north looking down on the sensor systems.

	COH 1 MEAN	COH 1 STAN DEV	COH 2 MEAN	COH 2 STAN DEV	COH NUM	COR MEAN	COR STAN DEV	COR NUM
$N_{bore} \rightarrow N_{north}$	168.27	1.32	**348.27**	1.32	22	348.25	0.79	20
$E_{bore} \rightarrow N_{north}$	**78.27**	1.32	258.27	1.32	22	78.25	0.79	20

Table 7. 14 Azimuth estimate results obtained by rotating the horizontal components of CMG-3NSN BOREHOLE into the horizontal components of the CMG-3NSN SURFACE NORTH system. This data was recorded on days 202 – 203 with the azimuth ring set to 120°. All angles are in degrees clockwise from north looking down on the sensor systems.

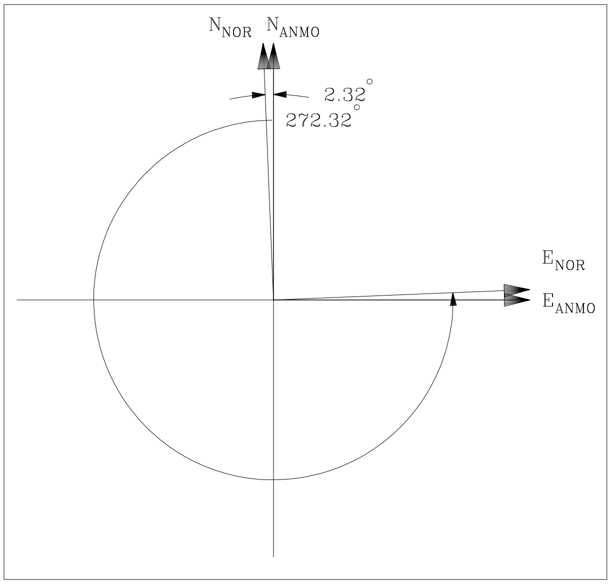

Figure 7. 43 Relative azimuths obtained by rotating ANMO into the SURFACE north sensor. ANMO is assumed to be oriented exactly north-south.

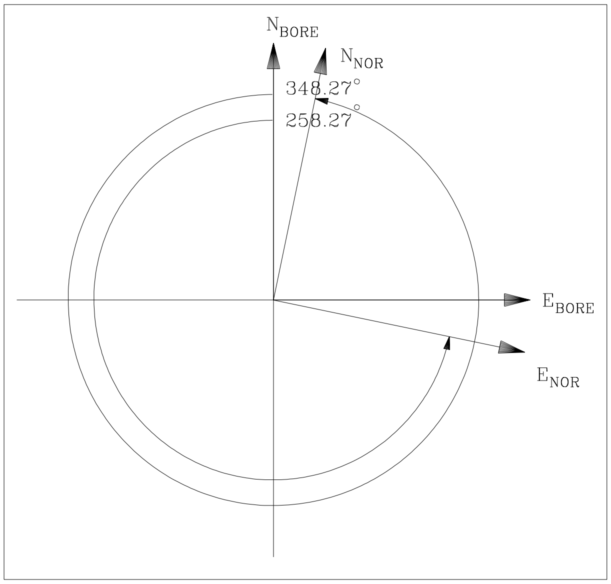

Figure 7. 44 Relative azimuths obtained by rotating the BOREHOLE system into the SURFACE north sensor. The BOREHOLE azimuth ring was set to 120° in a holelock whose orientation was unknown. The BOREHOLE system is assumed to be oriented exactly north-south.

8 THE ASL POSTHOLE AZIMUTH EXPERIMENT

During the spring of 1998, an experiment was assembled at ASL to investigate the relative performance of a KS-54000 sensor in a shallow posthole and another KS-54000 deployed at a much greater depth. The data gathered in this experiment is also quite useful for studying the precision of the coherence method for determining the relative azimuths of the sensors.

The physical layout of the experiment is shown in Figure 8.1. There were four sensors involved in the test as follows. The ANMO Teledyne KS-54000 that was deployed in sand at a 500 foot depth served as the deep sensor system (ANMO in Figure 8.1). Another Teledyne KS-54000 was installed in another borehole in sand at a shallow depth (bottom of the seismometer was at 20 feet below the surface all in alluvium) as the "posthole" sensor (POST in Figure 8.1). The ANMO CMG-3TB installed at 293 feet in sand in a third borehole provided high frequency data to supplement the deep KS-54000 at high frequencies (HIGH in Figure 8.1). Finally, a Guralp CMG-3T was installed in a shallow concrete pit (approximately 5 feet deep) (PIT in Figure 8.1). The orientations of the newly installed KS-54000 in the posthole (POST) and the Guralp CMG-3TB (HIGH) were unknown at the beginning of the experiment. The orientation of the ANMO KS-54000 had been determined about a year previously using the coherence method. The Guralp CMG-3T installed in the concrete pit was carefully oriented north south using recently surveyed north south marks on the sides of the pit. At the surface the horizontal separation distances between the four sensors were quite small as shown in Figure 8.1. At depth, the horizontal separation distances probably depart from the distances in Figure 8.1 because the boreholes are not exactly vertical. The vertical separation distances were significantly greater than the horizontal separation distances because of the differences in the depth of burial which range from 15 feet of vertical distance between PIT and POST to 495 feet between PIT and ANMO.

The signals from the three supposedly orthogonal components of all four of the sensors were recorded for about 30 days thereby providing an abundance of data from which to calculate various orientations. The experimental setup proved to be surprisingly quiet for the duration of the experiment thereby providing usable orientation data throughout the time period. Even the relatively shallow pit installation was quiet enough to permit the use of most of the PIT data; however, data containing noise from vehicle activity in the immediate vicinity of the pit was manually edited from the results.

With four sensor systems, each one of which contains two sets of horizontal components, there are six sets of relative azimuths which may be calculated (see Figure 8.36 for a visual illustration). For each pair of sensors (here the sensors are denoted sensor A and sensor B), four azimuths were calculated as follows. First, the north component of sensor A was rotated to align it with the north component of sensor B to calculate the number of degrees the north component of sensor A is positioned clockwise (looking down the borehole) from the north component of sensor B. In the tables that follow, the data corresponding to this operation is denoted by notation of the form A N > B N. Next, the north component of sensor B was rotated to align it with the north component of sensor A to calculate the number of degrees the north component of sensor B is positioned (clockwise looking down the borehole) from the north component of sensor A. Data corresponding to this operation is denoted by notation of the form B N > A N. Note that, if the technique is perfect, the sum of these two calculations should equal 360 degrees; therefore, we should get an estimate of the accuracy of the azimuth calculation process from these two sets of data. These two azimuth estimates establish the relative positions of the north components of the two sensors. In the ideal world the east components of both sensor systems would be 90.0 degrees clockwise from their corresponding north components. However, this possibility is not likely in the real world because of the inexact tolerances of the mechanical parts. Therefore, the relative position of the east component of sensor A was calculated by rotating the north component of sensor A to align it with the east component of sensor B to calculate the number of degrees the north component of sensor A is clockwise looking down the borehole from the east component of sensor B. This operation is denoted as A N > B E below. Finally, the relative position of the east component of sensor B was calculated by rotating the north component of sensor B to align it with the east component of sensor A to calculate the number of degrees the north component of sensor B is positioned clockwise (looking down the borehole) from the east component of sensor A. This calculation is labeled as B N > A E in the figures which follow. A typical example of the four angles calculated is shown in Figure 8.2.

The data were analyzed as follows. First, the time series were divided into 10000 second long sequential segments. Each of these segments was then subdivided into ten 1000 second long segments and the linear correlation coefficient between two components at a time was calculated as a function of azimuth to find the azimuth for which the correlation was a maximum. Then each of the 10000 second segments was resubdivided into 39 sequential subsegments of 256 seconds length and the Fast Fourier Transform was computed for each of these segments. These transforms were converted to power spectra and cross power spectra and the spectra were smoothed by segment averaging; the coherence function was then calculated as a function of azimuth from these smoothed spectral density functions.

As discussed earlier in this report, since the coherence function is defined solely in terms of frequency domain power spectral density functions, it can not discriminate between the data produced by perfectly aligned sensors and the signals from two components which are 180° out of alignment. The time domain defined linear correlation coefficient can tell the difference between these two conditions; however, the correlation coefficient derived azimuths are not as precise as the coherence calculated azimuths. Therefore, the correlation coefficient azimuth data is used to resolve the 180° ambiguity in the coherence azimuths and the coherence derived data is used to determine the best estimate of the true azimuth.

The data from this experiment provides an excellent opportunity to study the repeatability of azimuth estimates as calculated from many separate time series segments while maintaining a constant physical experimental configuration. A total of 191 sets of coherence derived azimuths were calculated for comparison with one another. The results are presented in the tables which follow; the average azimuth, the average deviation, the standard deviation, the minimum azimuth, the maximum azimuth, and the angle spanned by the minimum and maximum are all shown in the tables.

It is significant to note that essentially all of the data recorded during an approximately 22 day time span were included in the analysis. The time span was not continuous due to the loss of data caused by tape drive failure on one of the data recording systems. It was necessary to manually edit out the following 27 segments due to the reasons indicated.

1998,099,13;35:00 Vehicle activity near the PIT
1998,099,16:21:40 Recentering of the PIT sensor
1998,104,13: 1:40 People in the PIT
1998,104,15:48:20 People in the PIT
1998,105,16:48:30 Unknown
1998,105,19:35:00 Unknown
1998,106,16:48:20 Unknown
1998,111,19:23:20 Trigonometry fold over in software
1998,112,13:06:40 Vehicle activity near the PIT
1998,114,12:20:00 Vehicle activity near the PIT
1998,114,15:06:40 Vehicle activity near the PIT
1998,115,18:53:20 Trigonometry fold over in software
1998,116,14:20:00 Unknown
1998,117,13:53:20 Vehicle activity near the PIT
1998,118,13:53:20 Vehicle activity near the PIT
1998,120,14:06:40 Vehicle activity near the PIT
1998,120,16:53:20 Vehicle activity near the PIT
1998,120,19:40:00 Vehicle activity near the PIT
1998,121,15:06:40 Vehicle activity near the PIT
1998,123,08:46:40 Vehicle activity near the PIT
1998,123,11:33:20 Vehicle activity near the PIT
1998,123,14:20:00 Vehicle activity near the PIT
1998,123,17:06:40 Vehicle activity near the PIT
1998,127,16:40:00 Vehicle activity near the PIT
1998,127,19:26:40 Vehicle activity near the PIT
1998,128,12:06:40 Vehicle activity near the PIT
1998,128,17:40:00 Vehicle activity near the PIT

The four data segments labeled "Unknown" appear to be true outliers. The azimuths calculated from these four segments departed drastically from the other azimuths for reasons that are certainly not understood.

All of the remaining data were included in the analysis regardless of day-night time periods or time periods during which the wind was blowing quite severely. Wind speeds reached a maximum of 53 miles per hour during the 13 day span of the data with one period of time during which the wind speed averaged 23 miles per hour over a 2.77 hour segment.

The model for the analysis of the relative azimuths assumes that the individual horizontal components within each three component sensor package are absolutely orthogonal. If this is not true (it will not be true for most real world sensor systems), the rotation algorithm that is used to rotate components in the computer will not produce undistorted signals at the outputs of the rotated sensors.

Since the model for the mathematical analysis of the data also assumes that the ground motion input to both sensor systems is identical, the precision of the azimuth measurement technique should degrade if this assumption is not valid. Sensor systems installed at the surface tend to be noisier than sensors installed at depth because of the influence of the wind and pressure variations at the surface. This noise input to the sensor at the surface violates the assumption of identical ground motion input to both sensor systems and degrades the precision of the analysis. To illustrate this effect, the discussion of the test results from the current experiment will be presented in order of shallow to greater depth of installation.

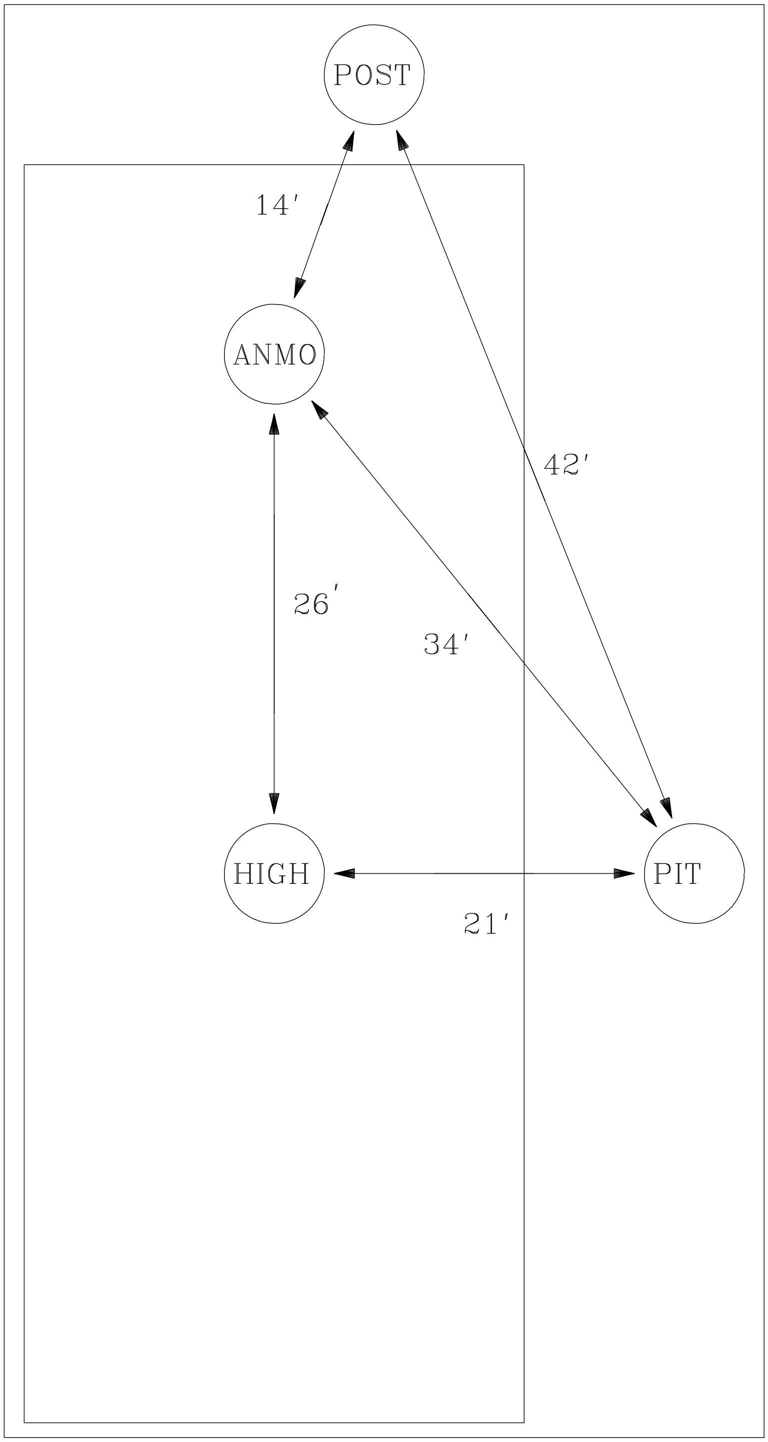

Figure 8.1 Physical surface horizontal separation distances between sensor systems for the post hole experiment. Horizontal separation distances at depth may be different due to the lack of perfect hole verticality. Depths of the installations are as follows: PIT = 5 feet, POST = 20 feet, HIGH = 293 feet, ANMO = 500 feet.

8.1 PIT-POST

The PIT and POST pair of sensors should be the noisiest combination of sensors because they are installed at shallower depths (5 feet for the PIT and 20 feet for the POST).

	AVE ANGLE	AVE DEV	STD DEV	MIN ANGLE	MAX ANGLE	SPAN ANGLE
PIT N → POST N	112.28	0.58	1.14	106.	132.	26.
POST N → PIT N	248.83	0.36	0.57	244.	253.	9.
PIT N → POST E	21.34	0.69	1.29	2.	26.	24.
POST N → PIT E	157.55	0.64	1.01	152.	173.	21.

Table 8.1 Tabulation of the statistics of 1900 linear correlation measured angles in degrees between the PIT and POST horizontal components.

The statistics of the correlation measured relative azimuth estimates between the horizontal components of the PIT and POST sensors are tabulated in Table 8.1. The standard deviation of all of the correlation derived angles are all less than 1.4° but the span of the azimuths extends up to ±13°. The large span renders single segment correlation estimates of the azimuth highly suspect; they could be off by 13° or so.

	AVE COR	AVE DEV	STD DEV	MIN COR	MAX COR	SPAN COR
PIT N → POST N	0.9915	0.0092	0.0212	0.6449	0.9998	0.3549
POST N → PIT N	0.9907	0.0090	0.0198	0.6903	0.9999	0.3096
PIT N → POST E	0.9895	0.0103	0.0224	0.7191	0.9998	0.2807
POST N → PIT E	0.9903	0.0105	0.0238	0.6631	0.9998	0.3367

Table 8.2 Tabulation of the statistics of the measured linear correlation values between the PIT and POST horizontal components.

In general, the averages of linear correlation coefficients in Table 8.2 are quite high but note the large span between the maximum and minimum coefficients. This indicates that both the PIT and POST sensor systems become quite quiet at times and they also become rather noisy at other times. This is typical of wind generated noise in shallow systems.

	AVE ANGLE	AVE DEV	STD DEV	MIN ANGLE	MAX ANGLE	SPAN ANGLE
PIT N → POST N	112.18	0.17	0.33	111.0	114.3	3.3
POST N → PIT N	248.90	0.12	0.23	247.3	250.5	3.2
PIT N → POST E	21.42	0.15	0.30	18.5	21.9	3.4
POST N → PIT E	157.50	0.09	0.17	156.5	158.4	1.9

Table 8.3 Tabulation of the statistics of 190 coherence measured relative angles in degrees between the PIT and POST horizontal components.

The relative positions of the horizontal components of PIT and POST sensors as determined from coherence based azimuth calculations are shown in Figure 8.3 and a summary of the statistical analysis of the azimuth calculations between these two sensors is contained in Table 8.4. The average value of 190 coherence estimated azimuths between the north components indicates that the PIT north is $112.18°$ clockwise from the POST north. The standard deviation of derived angles in this estimate is $0.33°$ and the span between the lowest and highest azimuth is $3.3°$. Therefore, based on this set of measurements, the relative azimuth between the two north components is $122.18° \pm 0.33°$. This a fairly precise measurement of the relative positions of the two components; it is certainly precise enough for most seismic measurements. However, note that if only one azimuth had been estimated, the span between the lowest and highest estimated azimuth indicates that the answer might have deviated as much as $1.7°$ or so from the average value above depending on which segment of data is chosen for analysis. The precisions in measuring the remaining three azimuths shown in Table 8.3 are all slightly better than that for the angle between the two north components but they are approximately the same magnitude.

It is interesting to note that the average azimuth estimates derived from the correlation function in Table 8.1 compare rather favorably with the average azimuth estimates derived with the coherence function in Table 8.3. Despite the significantly larger standard deviation of the correlation measured azimuths and the much larger span of the correlation measured azimuths, the average of the correlation azimuths is quite close to the average of the coherence derived azimuths.

	AVE COH	AVE DEV	STD DEV	MIN COH	MAX COH	SPAN COH
PIT N → POST N	0.9951	0.0065	0.0140	0.8685	1.000	0.1315
POST N → PIT N	0.9951	0.0057	0.0132	0.8713	0.9999	0.1286
PIT N → POST E	0.9940	0.0066	0.0153	0.8407	0.9998	0.1591
PSOT N → PIT E	0.9944	0.0073	0.0159	0.8443	0.9999	0.1556

Table 8.4 Tabulation of the statistics of the measured maximum coherence values between the rotated PIT and POST horizontal components.

The statistics of the spread of the maximum coherence values calculated between the rotated horizontal components of the PIT and POST horizontals are shown in Table 8.4. As was the case for the correlation coefficient values in Table 8.2, the coherence values in Table 8.4 reach quite high values at times. The value 1.0000 in this table is probably the result of Fortran roundup in formatted output. The true value is more probably something like 0.99996 or so. This is still very high coherence between two separate sensor systems. It is the highest coherence measured between any of the systems during this test. One might think that the coherence between the two deeply buried sensors (ANMO and HIGH) would be higher. This was not the case and it may be due to the fact that the PIT and POST sensors were physically closer together (46 feet apart) than were the ANMO and HIGH sensors (209 feet apart). The slight lack of coherence at depth may be a measure of the decay of signal coherence with separation distance.

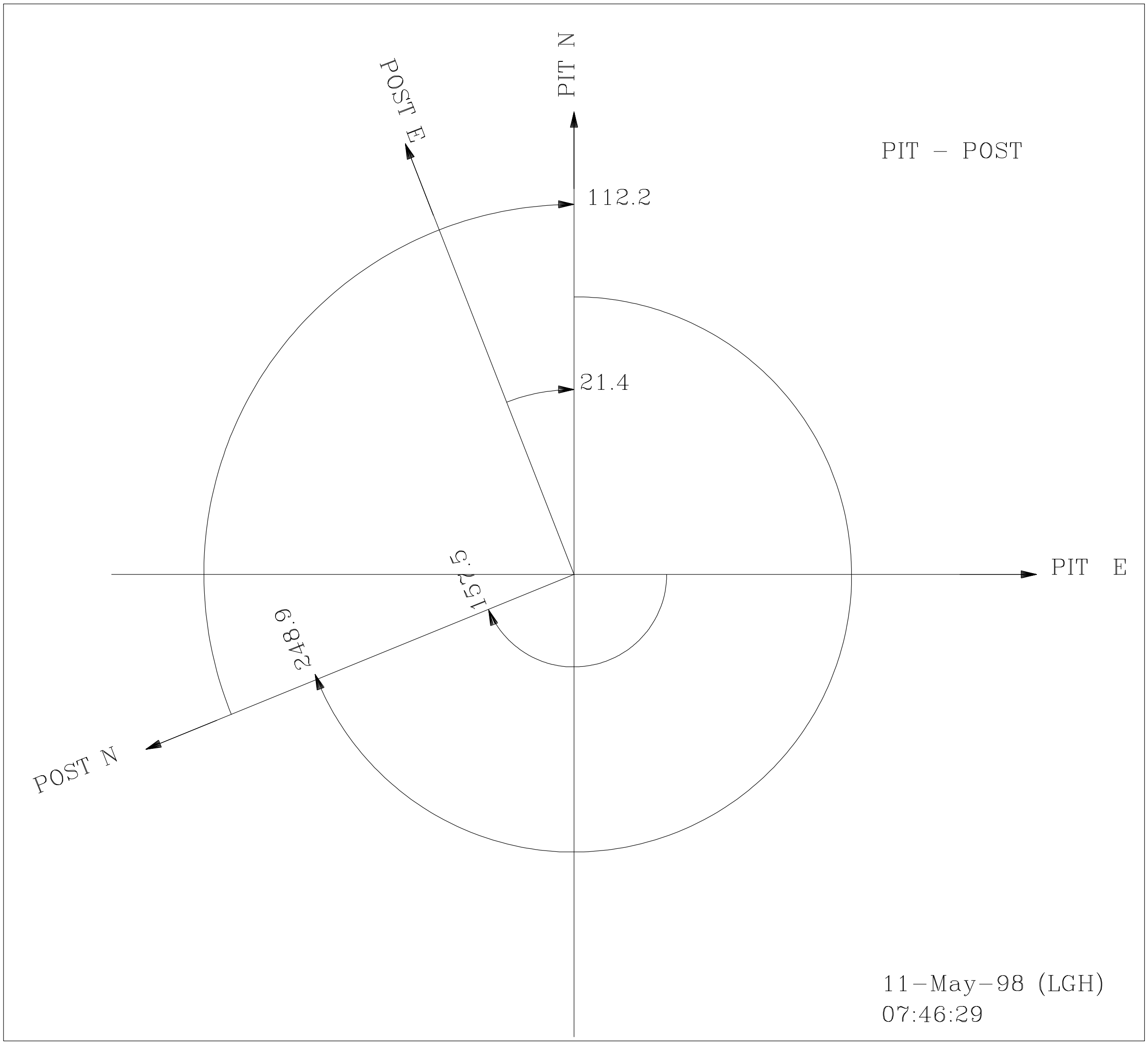

Figure 8.2 Average of the coherence calculated azimuths between the horizontal components of the CMG-3T installed in the pit (PIT) and the KS-54000 at 20 feet in the posthole (POST)

8.2 PIT-HIGH

	AVE ANGLE	AVE DEV	STD DEV	MIN ANGLE	MAX ANGLE	SPAN ANGLE
PIT N → HIGH N	72.48	2.76	3.46	61.	84.	23.
HIGH N → PIT N	287.74	2.80	3.52	273.	300.	27.
PIT N → HIGH E	339.82	3.19	4.06	325.	354.	29.
HIGH N → PIT E	200.31	3.15	3.99	188.	214.	26.

Table 8.5 Tabulation of the statistics of 1900 correlation measured angles in degrees between the PIT and HIGH horizontal components.

The statistics for the correlation derived relative azimuths between the PIT and HIGH sensor components are in Table 8.5. In reality, the standard deviation and span for this set of data are higher than for the PIT and POST azimuths in Table 8.1. One would expect them to be smaller because the HIGH sensor should be quieter than the POST sensor because it is considerably deeper.

	AVE COR	AVE DEV	STD DEV	MIN COR	MAX COR	SPAN COR
PIT N → HIGH N	0.7923	0.0329	0.0421	0.4979	0.9681	0.4703
HIGH N → PIT N	0.8055	0.0358	0.0430	0.5671	0.9608	0.3937
PIT N → HIGH E	0.8118	0.0334	0.0408	0.5701	0.9612	0.3911
HIGH N → PIT E	0.8002	0.0316	0.0406	0.5111	0.9690	0.4579

Table 8.6 Tabulation of the statistics of the measured correlation values between the PIT and HIGH horizontal components.

Likewise, the average correlation for the four azimuths in Table 8.6 PIT-HIGH sensors are considerably below the averages in Table 8.2 for the PIT-POST sensors.

	AVE ANGLE	AVE DEV	STD DEV	MIN ANGLE	MAX ANGLE	SPAN ANGLE
PIT N → HIGH N	72.72	0.14	0.20	72.2	73.8	1.6
HIGH N → PIT N	289.67	0.14	0.22	286.3	288.9	2.6
PIT N → HIGH E	341.47	0.17	0.30	339.8	343.4	3.6
HIGH N → PIT E	198.11	0.14	0.20	197.0	198.7	1.7

Table 8.7 Tabulation of the statistics of 190 coherence measured angles in degrees between the PIT and HIGH horizontal components.

The average of the coherence derived relative azimuths of the horizontal components of the PIT and HIGH are shown in Figure 8.7 and the statistics derived from these azimuths are in Table 8.8. Overall, the precision of the measurements is slightly better than it was for the PIT POST azimuths but the improvement is not large. Overall, the precision of the estimates is well within $0.3°$ and the average of the spans is less than $3°$.

	AVE COH	AVE DEV	STD DEV	MIN COH	MAX COH	SPAN COH
PIT N → HIGH N	0.9939	0.0071	0.0134	0.9146	0.9995	0.0849
HIGH N → PIT N	0.9940	0.0059	0.0137	0.8673	0.9992	0.1319
PIT N → HIGH E	0.9948	0.0056	0.0128	0.8809	0.9995	0.1186
HIGH N → PIT E	0.9946	0.0066	0.0125	0.9203	0.9997	0.0794

Table 8.8 Tabulation of the statistics of the measured coherence values between the PIT and HIGH horizontal components.

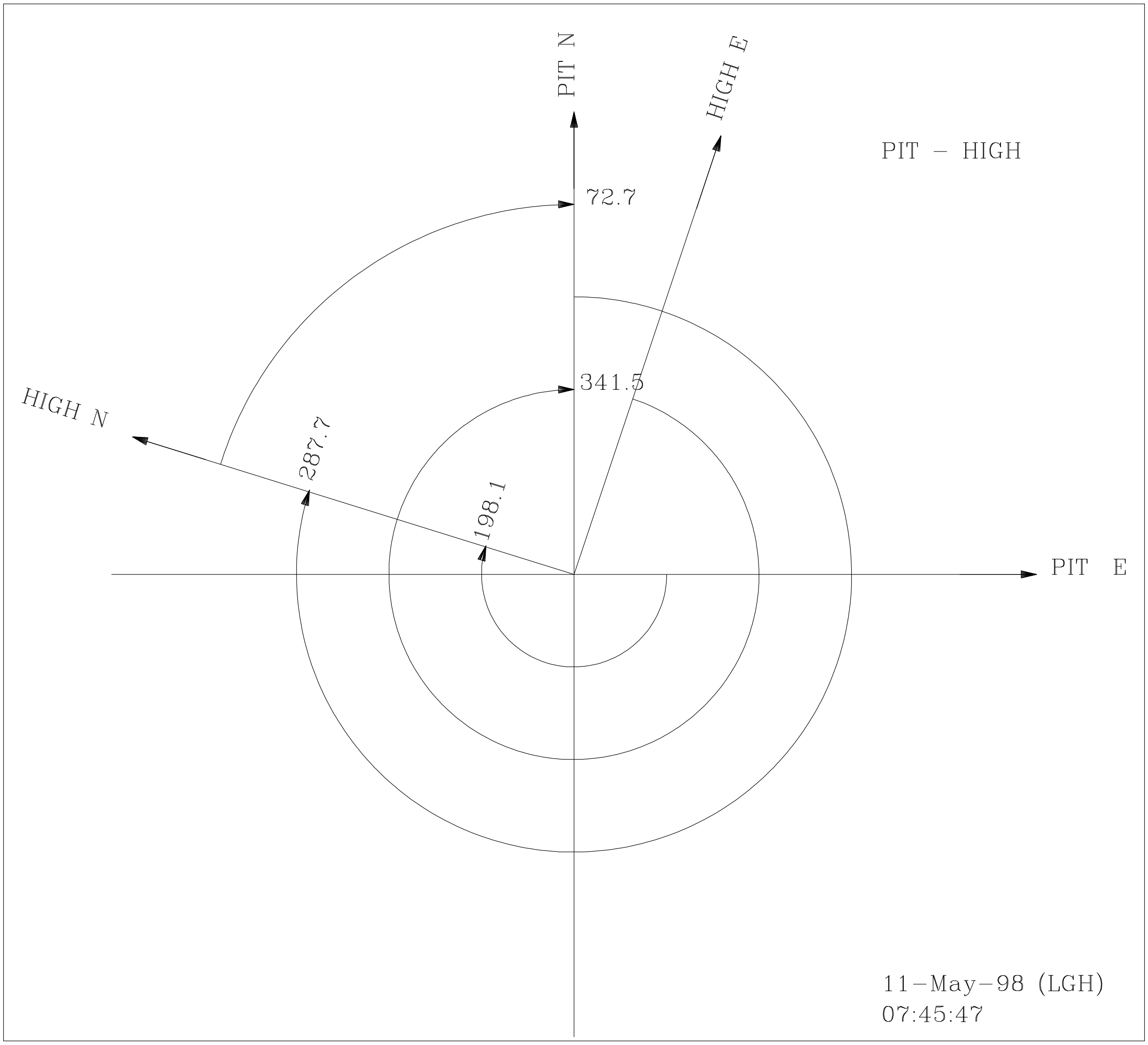

Figure 8.3 Average of the coherence calculated azimuths between the horizontal components of the CMG-3T installed in the pit (PIT) and the CMG-3TB at 293 feet in the borehole (HIGH).

8.3 PIT-ANMO

	AVE ANGLE	AVE DEV	STD DEV	MIN ANGLE	MAX ANGLE	SPAN ANGLE
PIT N → ANMO N	77.40	2.64	3.31	67.	88.	21.
ANMO N → PIT N	283.95	2.75	3.48	270.	296.	26.
PIT N → ANMO E	345.08	2.88	3.67	332.	358.	26.
ANMO N → PIT E	193.88	2.77	3.52	183.	206.	23.

Table 8.9 Tabulation of the statistics of 1900 correlation measured angles in degrees between the PIT and ANMO horizontal components.

The correlation calculated relative azimuth angles between the horizontal components of the PIT and ANMO sensors are shown in Table 8.9 and the linear correlation coefficient statistics are in Table 8.10.

	AVE COR	AVE DEV	STD DEV	MIN COR	MAX COR	SPAN COR
PIT N → ANMO N	0.8142	0.0279	0.0373	0.5074	0.9668	0.4594
ANMO N → PIT N	0.8266	0.0310	0.0378	0.5822	0.9626	0.3804
PIT N → ANMO E	0.8302	0.0292	0.0361	0.5822	0.9629	0.3807
ANMO N → PIT E	0.8189	0.0269	0.0362	0.5153	0.9673	0.4520

Table 8.10 Tabulation of the statistics of the measured correlation values between the PIT and ANMO horizontal components.

	AVE ANGLE	AVE DEV	STD DEV	MIN ANGLE	MAX ANGLE	SPAN ANGLE
PIT N → ANMO N	77.84	0.19	0.26	77.3	79.2	1.9
ANMO N → PIT N	283.69	0.16	0.25	282.3	285.0	2.7
PIT N → ANMO E	346.55	0.19	0.31	344.9	348.2	3.3
ANMO N → PIT E	191.98	0.17	0.23	190.9	192.5	1.6

Table 8.11 Tabulation of the statistics of 190 coherence measured angles in degrees between the PIT and ANMO horizontal components.

Table 8.11 contains the statistics of the results for the relative coherence derived azimuths between the components of the PIT sensor and the ANMO sensor. Figure 8.4 displays the average azimuth data from Table 8.11 for easier visualization of the relative positions of the two sensor systems. The average of 190 coherence derived azimuths indicates that the PIT north component is 77.84° clockwise looking down the borehole from the ANMO north. The standard deviation of this estimate is 0.26° and the total angular spread of all of the estimates was 1.9°. Therefore, the precision of the measurement is probably within ±0.26° of the average of 77.84°. The precision for the remaining three azimuths is slightly less but still quite high.

	AVE COH	AVE DEV	STD DEV	MIN COH	MAX COH	SPAN COH
PIT N → ANMO N	0.9932	0.0070	0.0132	0.9254	0.9990	0.0836
ANMO N → PIT N	0.9941	0.0059	0.0137	0.8668	0.9991	0.1323
PIT N → ANMO E	0.9947	0.0056	0.0230	0.8786	0.9995	0.1209
ANMO N → PIT E	0.9939	0.0066	0.0066	0.9193	0.9993	0.0800

Table 8.12 Tabulation of the statistics of the measured coherence values between the PIT and ANMO horizontal components.

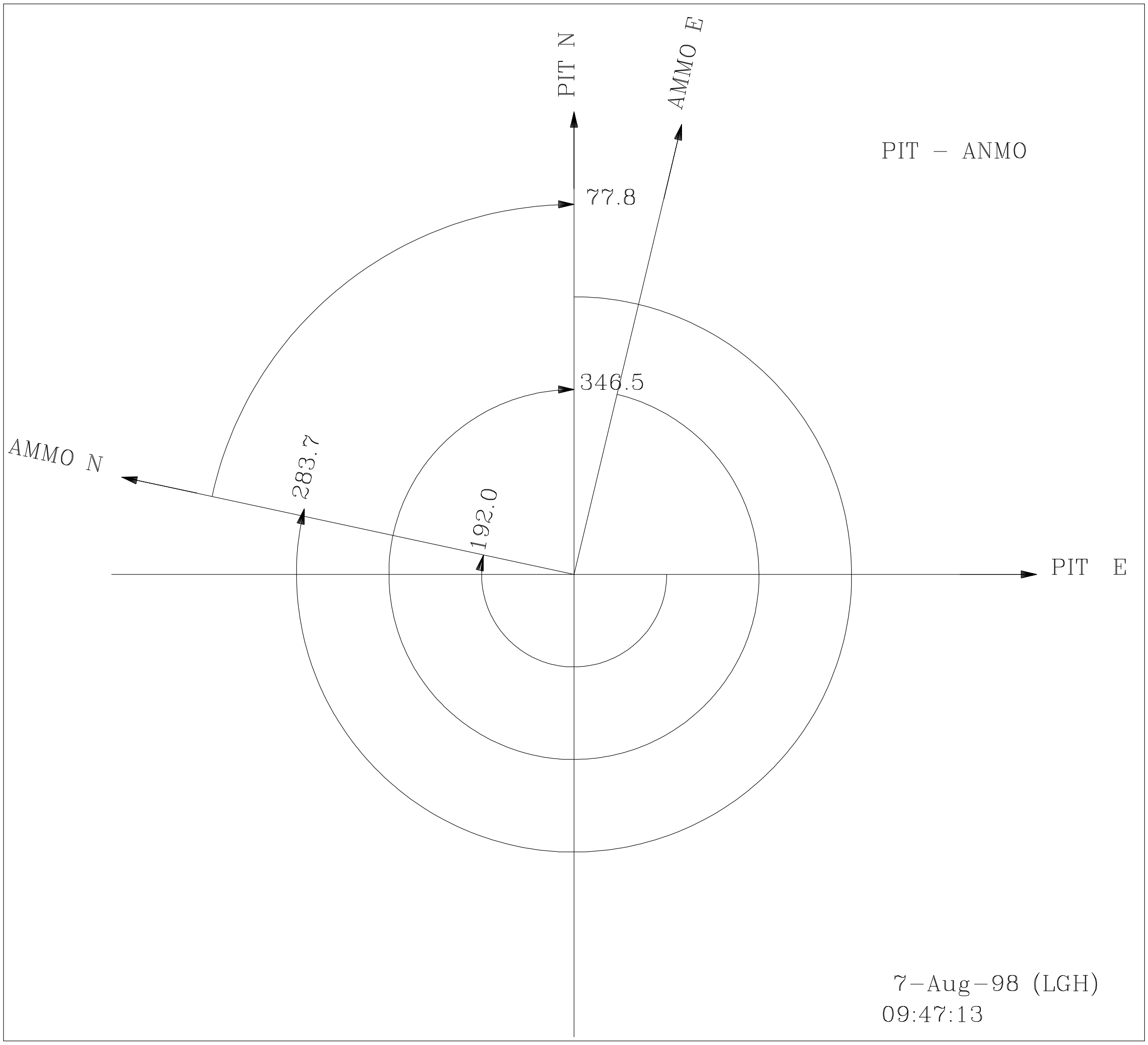

Figure 8.4 Average of the coherence calculated azimuths between the horizontal components of the CMG-3T installed in the pit (PIT) and the KS-54000 at installed at 500 feet in the deep borehole (ANMO).

8.4 HIGH-POST

	AVE ANGLE	AVE DEV	STD DEV	MIN ANGLE	MAX ANGLE	SPAN ANGLE
HIGH N → POST N	43.39	3.68	4.70	30.	59.	29.
POST N → HIGH N	319.90	2.94	3.70	308.	332.	24.
HIGH N → POST E	308.69	2.79	3.53	290.	321.	31.
POST N → HIGH E	228.06	3.53	4.51	211.	245.	34.

Table 8.13 Tabulation of the statistics of 1900 correlation measured angles in degrees between the HIGH and POST horizontal components.

The statistics for the correlation derived azimuth estimates in Table 8.13 for the HIGH and POST sensors are quite similar to those for the previous three pairs of data all of which included data from the PIT sensor. In particular the standard deviation figures in Table 8.13 for the HIGH-POST combination are more than twice the corresponding data in Table 8.1 for the PIT-POST pair. This result is somewhat surprising because the POST sensor is about 15 feet deeper than the PIT sensor and thereby should be quieter. There is currently no explanation for this result.

	AVE COR	AVE DEV	STD DEV	MIN COR	MAX COR	SPAN COR
HIGH N → POST N	0.7905	0.0301	0.0363	0.6945	0.9657	0.2712
POST N → HIGH N	0.7742	0.0346	0.0411	0.6718	0.9662	0.2944
HIGH N → POST E	0.7708	0.0390	0.0457	0.6556	0.9615	0.3059
POST N → HIGH E	0.7883	0.0338	0.0403	0.6703	0.9590	0.2887

Table 8.14 Tabulation of the statistics of the measured correlation values between the HIGH and POST horizontal components.

	AVE ANGLE	AVE DEV	STD DEV	MIN ANGLE	MAX ANGLE	SPAN ANGLE
HIGH N → POST N	41.05	0.08	0.10	40.9	41.3	0.4
POST N → HIGH N	320.14	0.09	0.10	319.9	320.4	0.5
HIGH N → POST E	308.37	0.08	0.08	308.1	308.5	0.4
POST N → HIGH E	230.45	0.09	0.10	230.2	230.7	0.5

Table 8.15 Tabulation of the statistics of 190 coherence measured angles in degrees between the HIGH and POST horizontal components.

The results of calculating the coherence derived relative azimuths between the horizontal components of the POST and HIGH sensors are contained in Table 8.15 and shown in Figure 8.5. Here we see a large improvement in the precision of the angle estimates over the precision exhibited in the three cases discussed previously. All three of the earlier cases calculated relative azimuths between the PIT sensor and the other three sensors. The shallow sensor in the current calculation is about 15 feet deeper than the PIT sensor; therefore, it should be quieter than the PIT sensor. As indicated in Table 8.15, the precision of all four average azimuth estimates is approximately $\pm 0.1^\circ$ and the span between the lowest and highest of the 190 estimates is only approximately 0.5° for all four of the measured angles. The improvement in precision is probably due to much lower noise levels in the POST sensor than in the PIT sensor due to differences in the depth of burial of the two sensors. This illustrates the importance of taking precautions to assure that the reference sensor installed at or near the earth's surface is as quiet as possible.

	AVE COH	AVE DEV	STD DEV	MIN COH	MAX COH	SPAN COH
HIGH N → POST N	0.9996	0.0001	0.0002	0.9978	0.9998	0.0020
POST N → HIGH N	0.9996	0.0001	0.0003	0.9969	0.9997	0.0028
HIGH N → POST E	0.9995	0.0001	0.0002	0.9983	0.9996	0.0013
POST N → HIGH E	0.9996	0.0001	0.0001	0.9989	0.9997	0.0008

Table 8.16 Tabulation of the statistics of the measured coherence values between the HIGH and POST horizontal components.

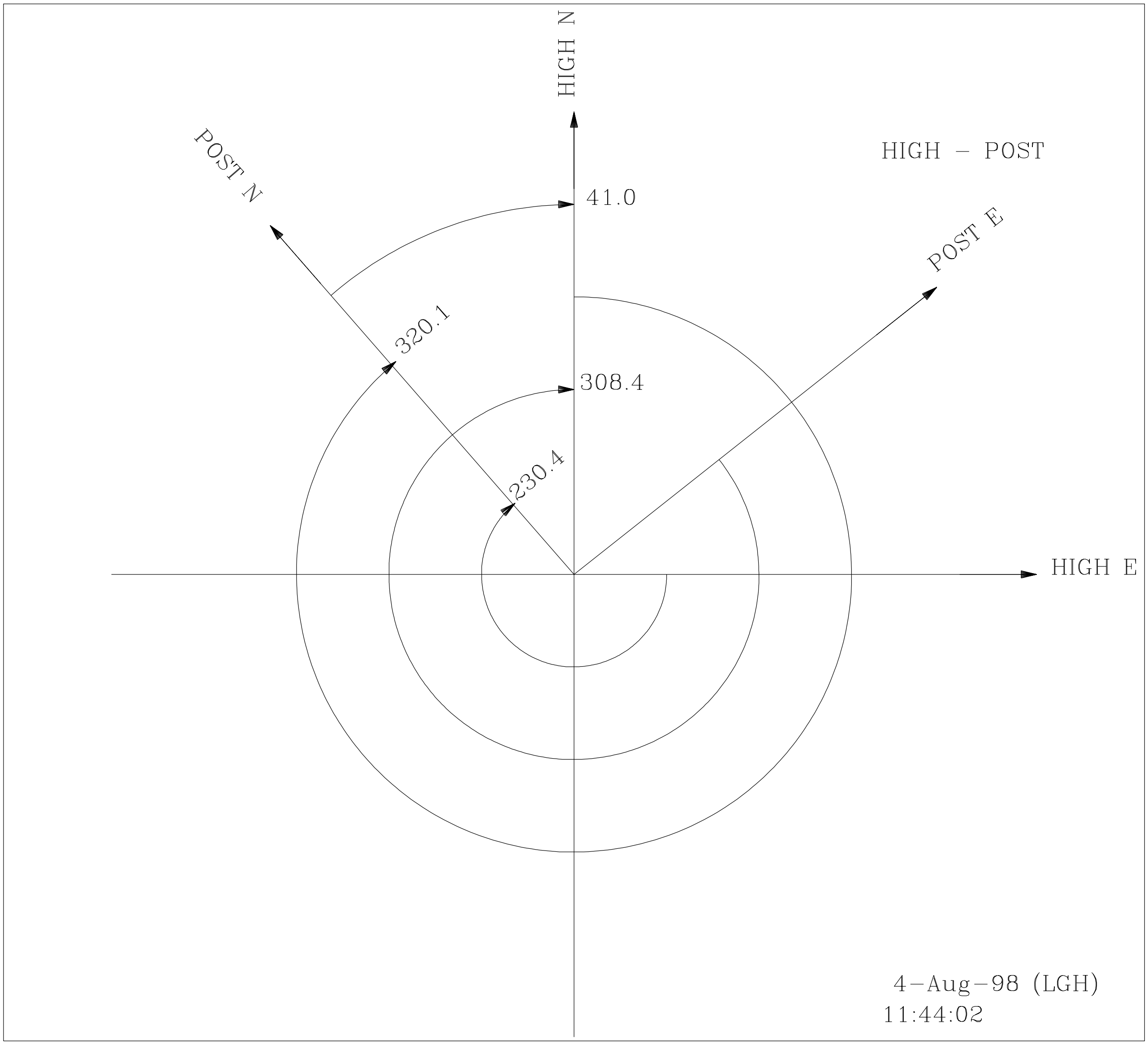

Figure 8.5 Average of the coherence calculated azimuths between the horizontal components of the CMG-3TB at 293 feet in a borehole (HIGH) and the KS-54000 at 20 feet in the posthole (POST).

8.5 POST-ANMO

	AVE ANGLE	AVE DEV	STD DEV	MIN ANGLE	MAX ANGLE	SPAN ANGLE
POST N → ANMO N	324.71	2.82	3.54	313.	336.	23.
ANMO N → POST N	36.23	3.42	4.38	24.	42.	28.
POST N → ANMO E	233.45	3.22	4.09	219.	250.	31.
ANMO N → POST E	305.69	2.63	3.31	288.	317.	29.

Table 8.17 Tabulation of the statistics of 1900 correlation measured angles in degrees between the POST and ANMO horizontal components.

	AVE COR	AVE DEV	STD DEV	MIN COR	MAX COR	SPAN COR
POST N → ANMO N	0.7980	0.0287	0.0344	0.7142	0.9649	0.2507
ANMO N → POST N	0.8093	0.0248	0.0302	0.7315	0.9645	0.2330
POST N → ANMO E	0.8075	0.0294	0.0351	0.6868	0.9609	0.2741
ANMO N → PSOT E	0.7953	0.0342	0.0400	0.6789	0.9621	0.2832

Table 8.18 Tabulation of the statistics of the measured correlation values between the POST and ANMO horizontal components.

	AVE ANGLE	AVE DEV	STD DEV	MIN ANGLE	MAX ANGLE	SPAN ANGLE
POST N → ANMO N	325.21	0.14	324.8	324.8	325.8	1.0
ANMO N → POST N	33.98	0.11	33.7	33.7	34.2	0.6
POST N → ANMO E	235.55	0.12	235.1	235.1	235.9	0.8
ANMO N → POST E	305.28	0.11	304.9	304.9	305.6	0.7

Table 8.19 Tabulation of the statistics of 190 coherence measured angles in degrees between the POST and ANMO horizontal components.

Even though the ANMO sensor is deeper than the HIGH sensor, the precision of azimuth estimation between the POST and ANMO sensors contained in Table 8.19 and shown in Figure 8.6 is slightly lower than it was for the POST and HIGH combination discussed in the previous section. The spans in the calculated azimuths are also slightly larger for the

POST ANMO combination. The reason for this somewhat surprising result is not clear but it may be that the AMMO sensor (a KS -54000) itself is slightly noisier in the 6 second band than is the HIGH sensor (CMG-3TB). Despite this fact, the precision of the relative azimuth estimates is impressively high; the standard deviation of all four estimates is in the $0.13°$ to $0.17°$ range and the span of the estimates ranges from $0.6°$ to $0.8°$.

	AVE COH	AVE DEV	STD DEV	MIN COH	MAX COH	SPAN COH
POST N → ANMO N	0.9990	0.0002	0.0003	0.9966	0.9993	0.0027
ANMO N → POST N	0.9993	0.0001	0.0002	0.9976	0.9997	0.0021
POST N → ANMO E	0.9994	0.0001	0.0001	0.9987	0.9997	0.0010
ANMO N → POST E	0.9991	0.0001	0.0002	0.9980	0.9994	0.0014

Table 8.20 Tabulation of the statistics of the measured coherence values between the POST and ANMO horizontal components.

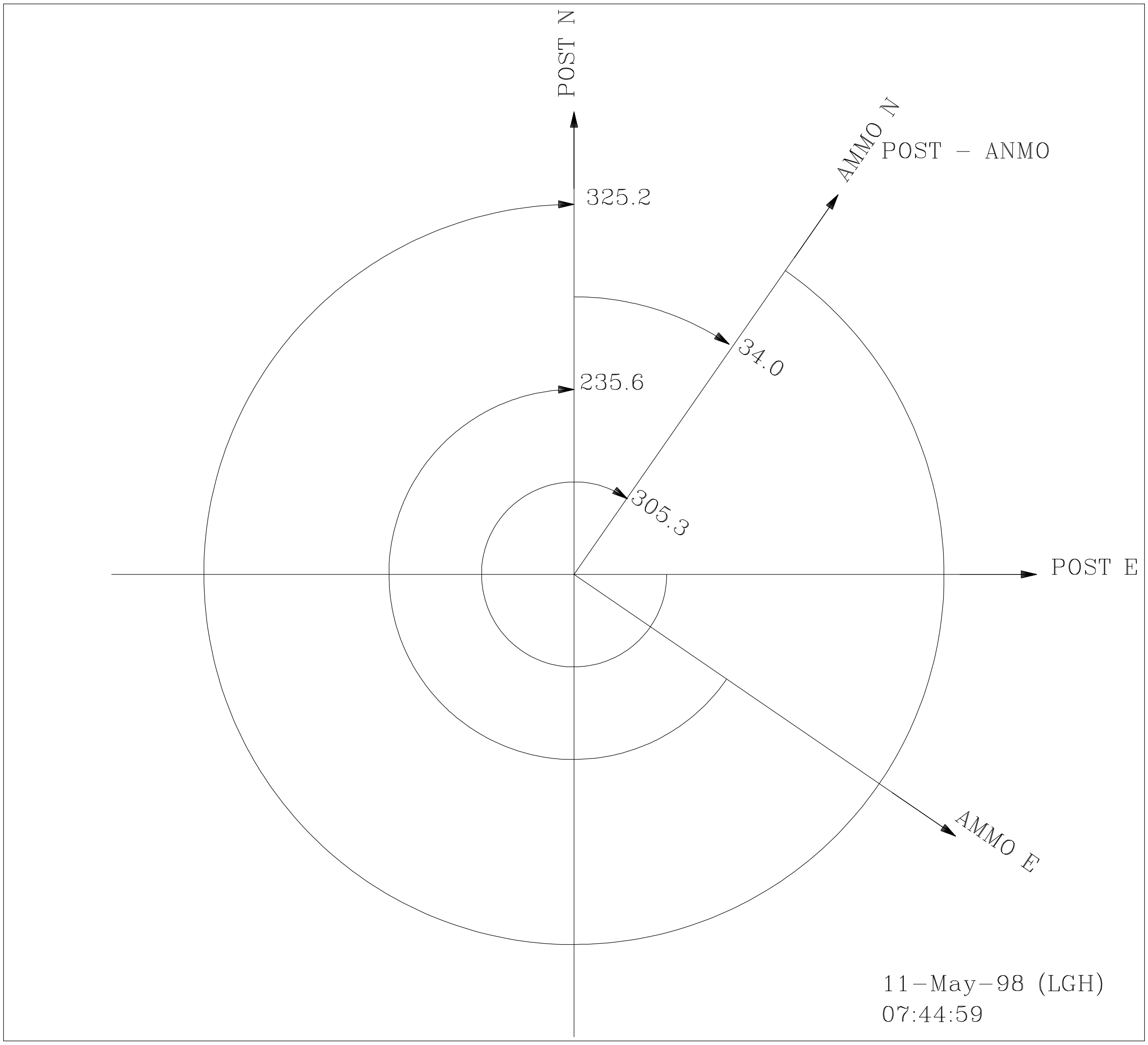

Figure 8.6 Average of the coherence calculated azimuths between the horizontal components of the KS54000 at 20 feet in the posthole (POST) and the KS-54000 at 500 feet in the deep borehole (ANMO)

8.6 ANMO-HIGH

	AVE ANGLE	AVE DEV	STD DEV	MIN ANGLE	MAX ANGLE	SPAN ANGLE
ANMO N → HIGH N	355.04	0.08	0.20	354.	356.	2.
HIGH N → ANMO N	5.17	0.29	0.39	4.	6.	2.
ANMO N → HIGH E	264.84	0.27	0.37	264.	266.	2.
HIGHN → ANMOE	274.99	0.03	0.13	274.	276.	2.

Table 8.21 Tabulation of the statistics of 1900 correlation measured angles in degrees between the ANMO and HIGH horizontal components.

	AVE COR	AVE DEV	STD DEV	MIN COR	MAX COR	SPAN COR
ANMO N → HIGH N	0.9991	0.0002	0.0003	0.9983	0.9999	0.0016
HIGH N → ANMO N	0.9991	0.0002	0.0003	0.9983	0.9999	0.0016
ANMO N → HIGH E	0.9992	0.0003	0.0003	0.9983	0.9999	0.0015
HIGH N → ANMO E	0.9992	0.0003	0.0003	0.9983	0.9999	0.0016

Table 8.22 Tabulation of the statistics of the measured correlation values between the ANMO and HIGH horizontal components.

	AVE ANGLE	AVE DEV	STD DEV	MIN ANGLE	MAX ANGLE	SPAN ANGLE
ANMO N → HIGH N	355.06	0.06	0.07	354.7	355.2	0.5
HIGH N → ANMO N	5.29	0.05	0.08	5.1	5.7	0.6
ANMO N → HIGH E	264.78	0.06	0.07	264.6	265.0	0.4
HIGH N → ANMO E	274.86	0.06	0.07	274.6	275.0	0.4

Table 8.23 Tabulation of the statistics of 190 coherence measured angles in degrees between the ANMO and HIGH horizontal components.

Finally, the relative coherence derived azimuth estimates between ANMO and HIGH are shown in Table 8.23 and Figure 8.7. The precision of these measurements is truly remarkable; the standard deviation of all 190 angles for all four relative azimuths are all $0.08°$ or less and the span between the minimum and maximum estimated azimuths are all $0.6°$ or less. The reason for the high precision is probably due to the fact that both sensors were deployed rather deep (HIGH was 290 feet deep and ANMO was 500 feet deep) which should significantly reduce or eliminate the effects of extraneous surface noise. This set of data is proof that if the influence of noise is reduced to low enough levels, the precision of this type of measurement can be quite high and well within the needs of seismology.

The coherence statistics calculated from the ANMO-HIGH data are shown in Table 8.24. The average deviation and standard deviation are not zero as shown in the table; more places were simply not printed out in the data processing. The remarkable feature of this table is the consistency of the coherence data. There was very little variation in the coherence (only a span of 0.0002) segment after segment for a period of over 22 days throughout night and day, wind and calm, event and no event etc.. If varying levels of incoherent noise are present in the six second band at these depths it is not detectable with the coherence function.

	AVE COH	AVE DEV	STD DEV	MIN COH	MAX COH	SPAN COH
ANMO N → HIGH N	0.9997	0.0000	0.0000	0.9996	0.9998	0.0002
HIGH N → ANMO N	0.9997	0.0000	0.0000	0.9996	0.9998	0.0002
ANMO N → HIGH E	0.9998	0.0000	0.0000	0.9997	0.9999	0.0002
HIGH N → ANMO E	0.9998	0.0000	0.0000	0.9997	0.9999	0.0002

Table 8.24 Tabulation of the statistics of the measured coherence values between the ANMO and HIGH horizontal components.

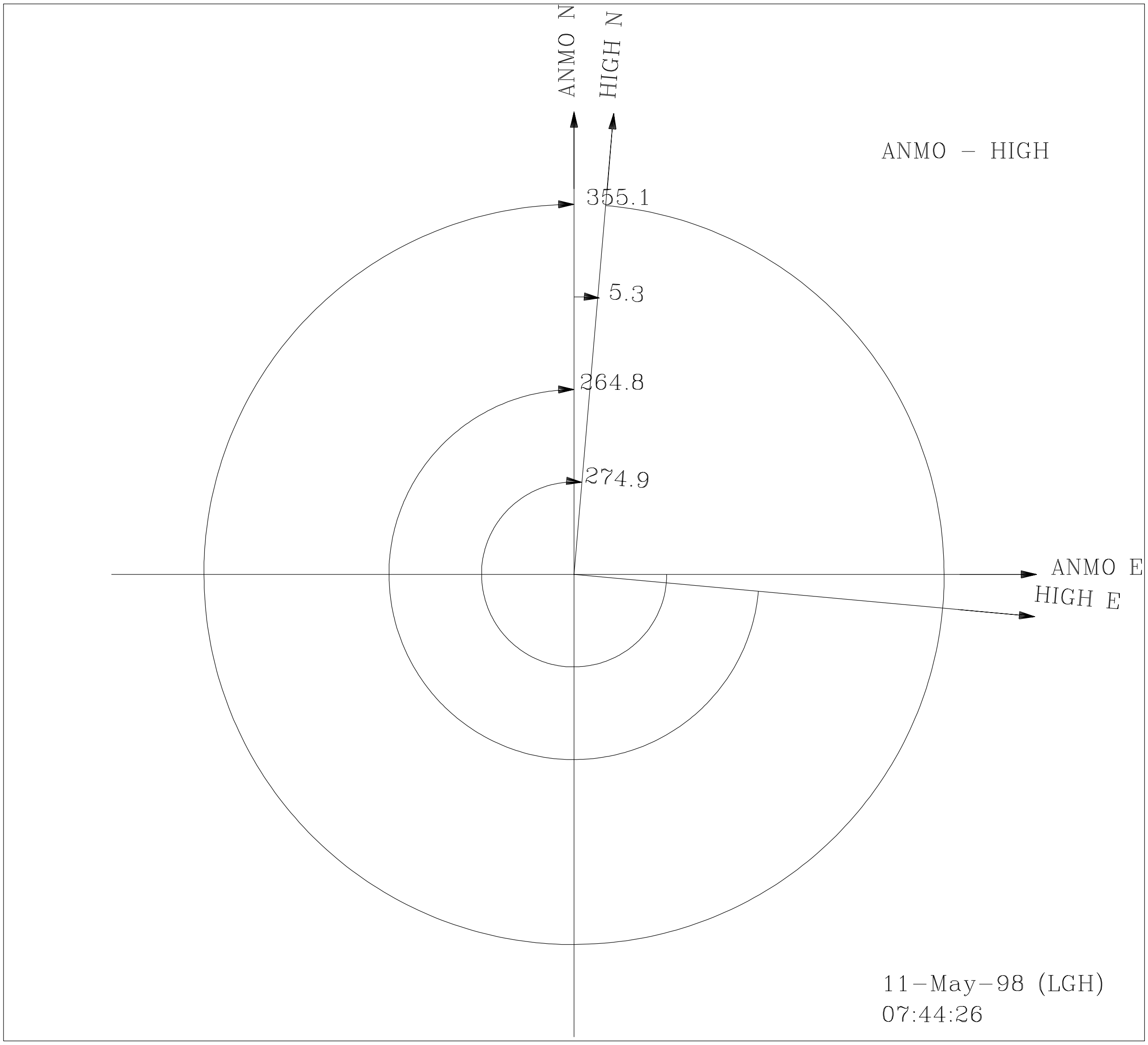

Figure 8.7 Average of the coherence calculated azimuths between the horizontal components of the KS-54000 at 500 feet in the deep borehole (ANMO) and the CMG-3TB at 293 feet in a borehole (HIGH).

8.7 TIME DEPENDENCE OF MEASURED PARAMETERS

The time dependence of the measured parameters is important because they should provide a guide to determining how long data must be recorded in order to achieve a certain degree of precision in the final azimuth estimates. In particular, one would hope that the average values of the various relative azimuths will converge to a stable value in a fairly short time. This would minimize system down time while recording data for azimuth determining purposes and it would decrease installation costs by shortening the time spent on site by the installation team.

Figures 8.8 through 8.31 each contain time plots of the calculated coherence, the coherence derived relative azimuth, the average coherence derived azimuth, the average deviation of the coherence derived relative azimuth, and the standard deviation of the coherence derived relative azimuth.

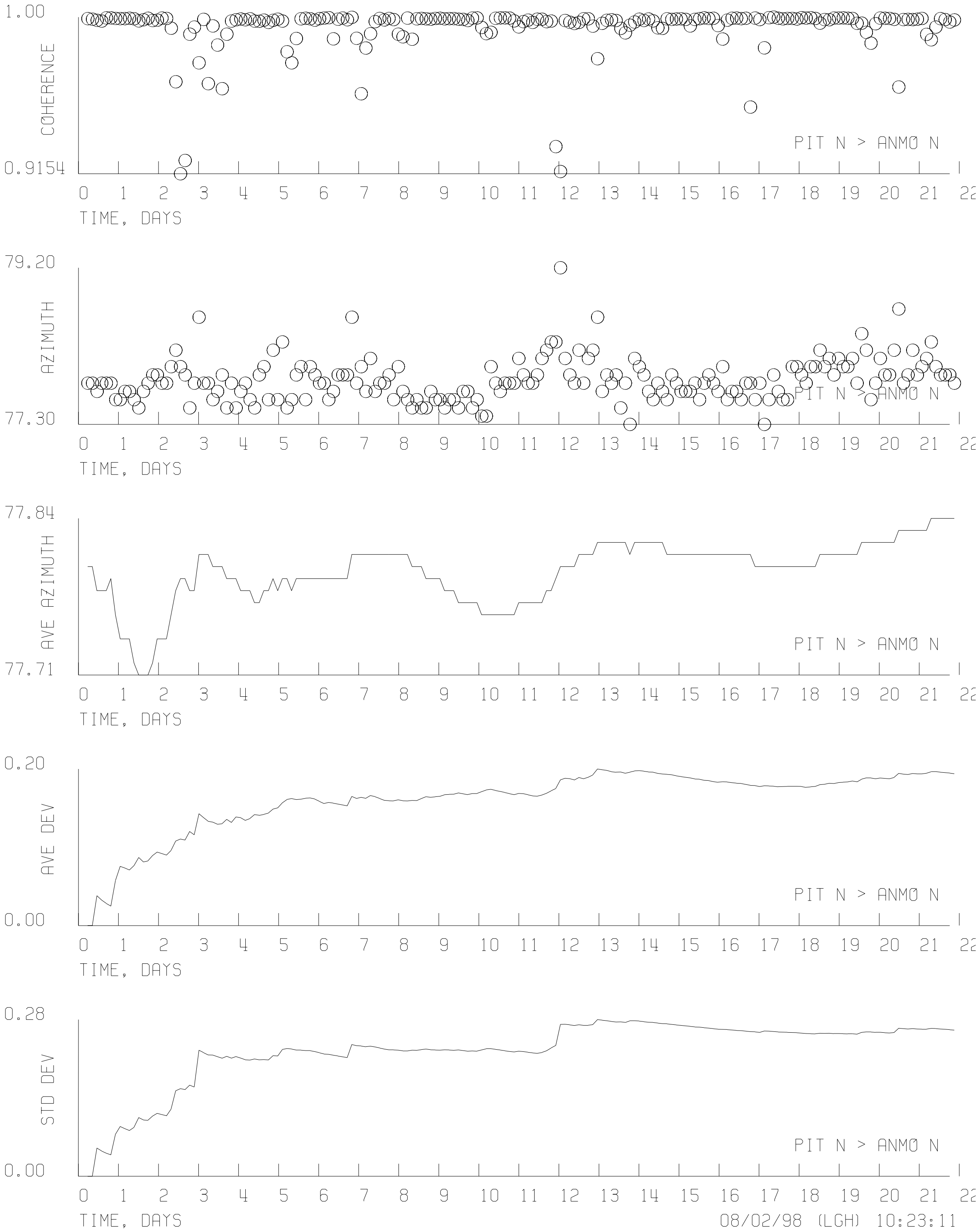

Figure 8.8 Time histories of the calculated coherence, the coherence derived relative azimuth, the average coherence derived azimuth, the average deviation of the coherence derived relative average, and the standard deviation of the coherence derived relative azimuth for the PIT N > ANMO N angle.

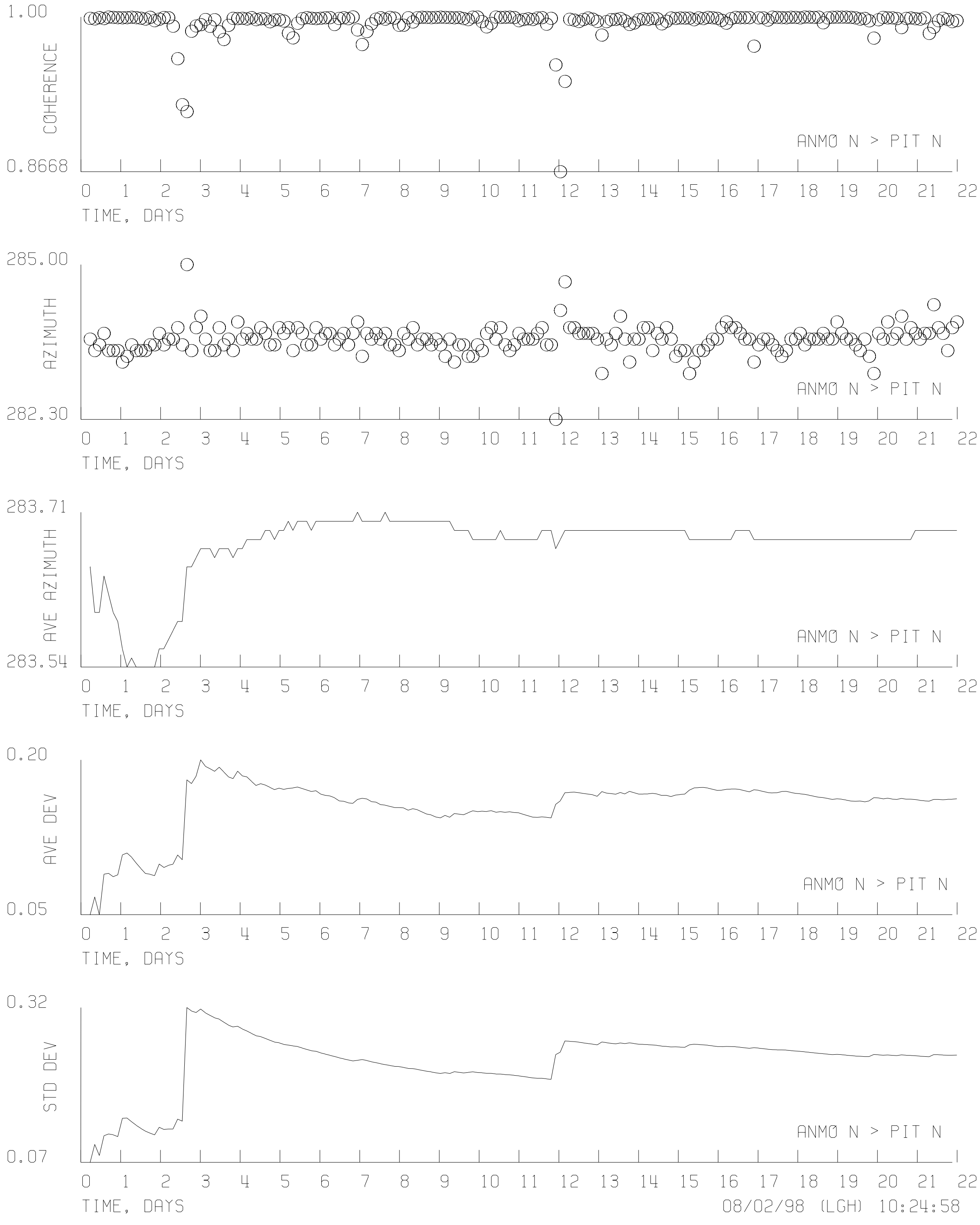

Figure 8.9 Time histories of the calculated coherence, the coherence derived relative azimuth, the average coherence derived azimuth, the average deviation of the coherence derived relative average, and the standard deviation of the coherence derived relative azimuth for the ANMO N > PIT N angle.

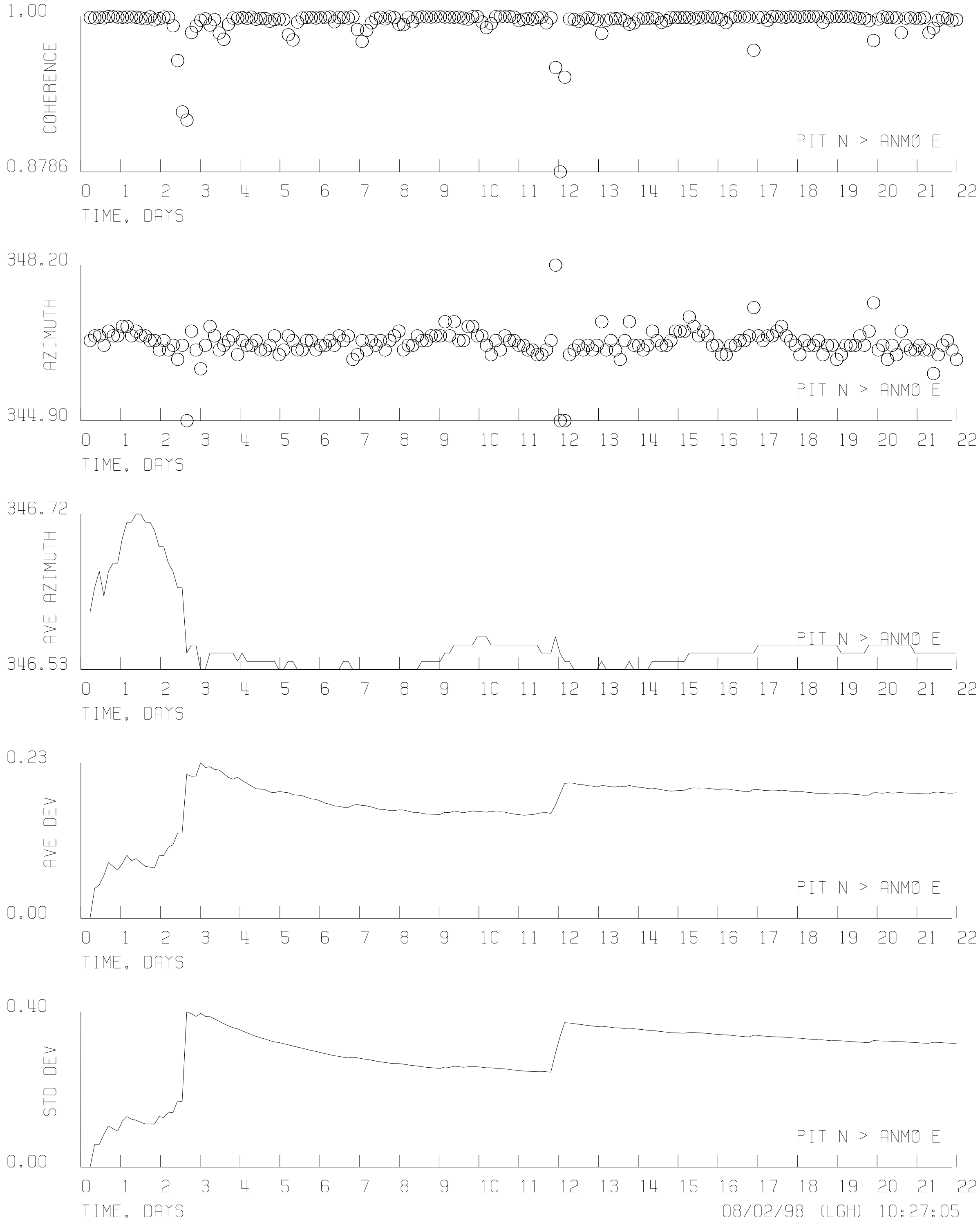

Figure 8.10 Time histories of the calculated coherence, the coherence derived relative azimuth, the average coherence derived azimuth, the average deviation of the coherence derived relative average, and the standard deviation of the coherence derived relative azimuth for the PIT N > HIGH E angle.

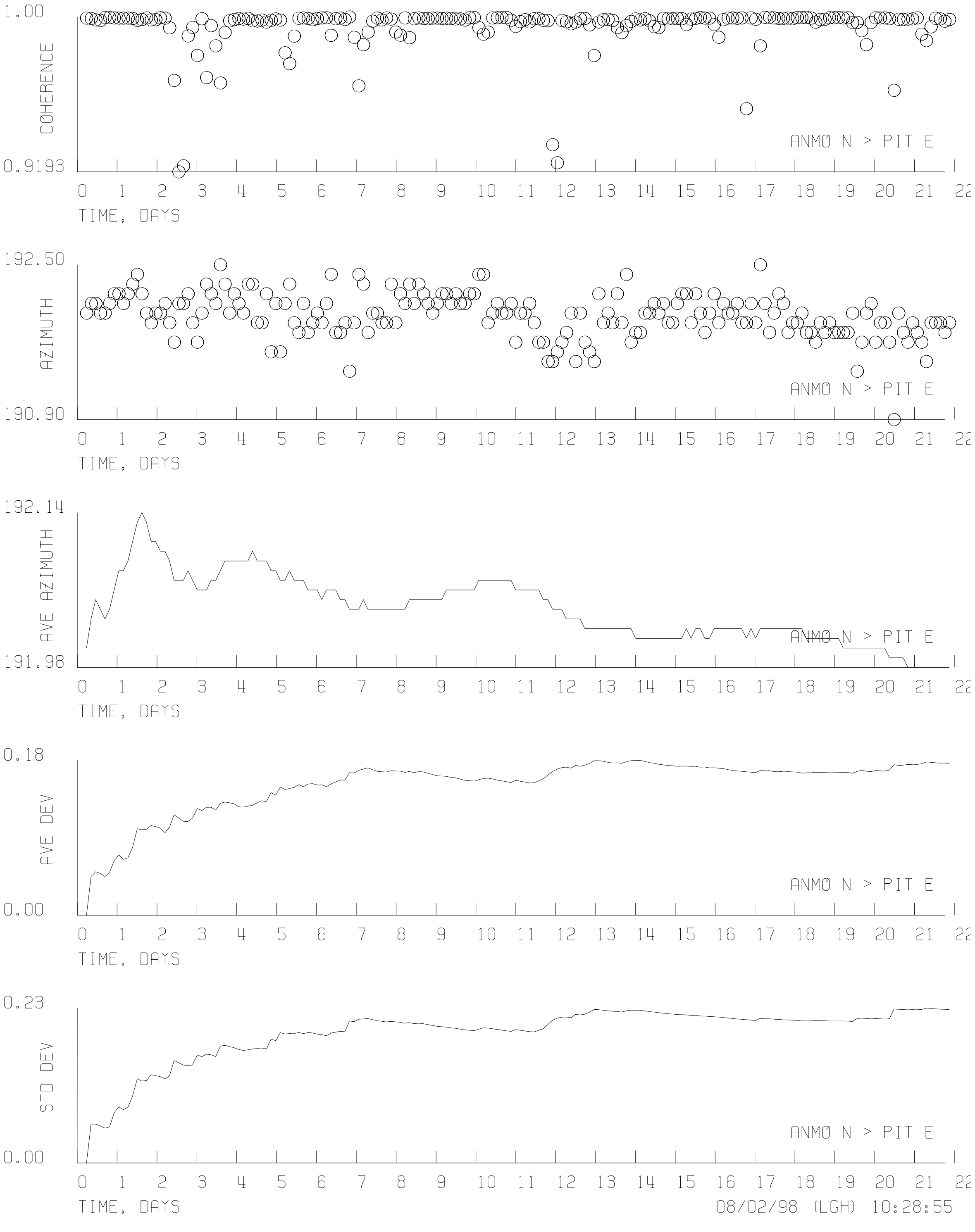

Figure 8.11 Time histories of the calculated coherence, the coherence derived relative azimuth, the average coherence derived azimuth, the average deviation of the coherence derived relative average, and the standard deviation of the coherence derived relative azimuth for the ANMO N > PIT E angle.

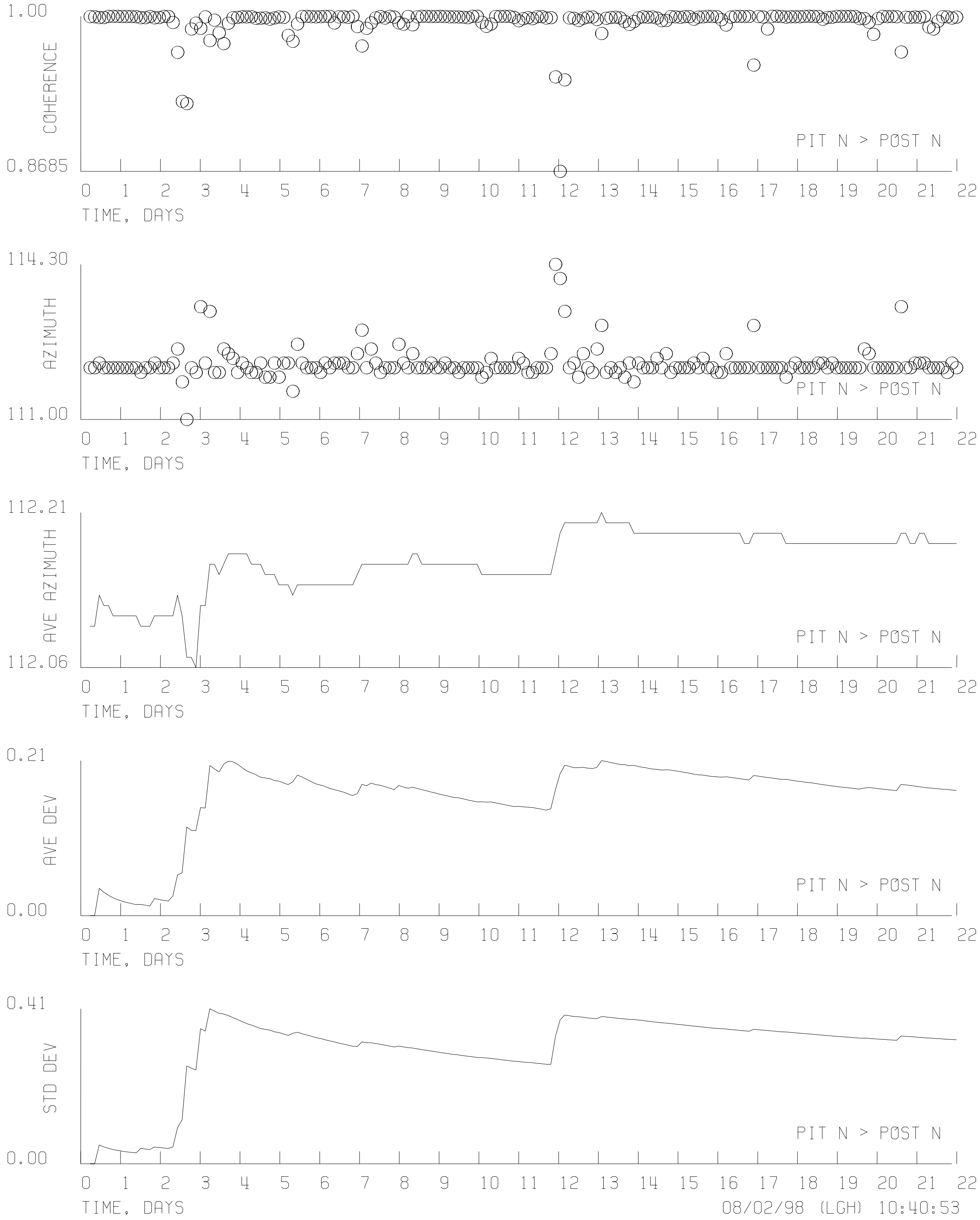

Figure 8.12 Time histories of the calculated coherence, the coherence derived relative azimuth, the average coherence derived azimuth, the average deviation of the coherence derived relative average, and the standard deviation of the coherence derived relative azimuth for the PIT N > POST N angle.

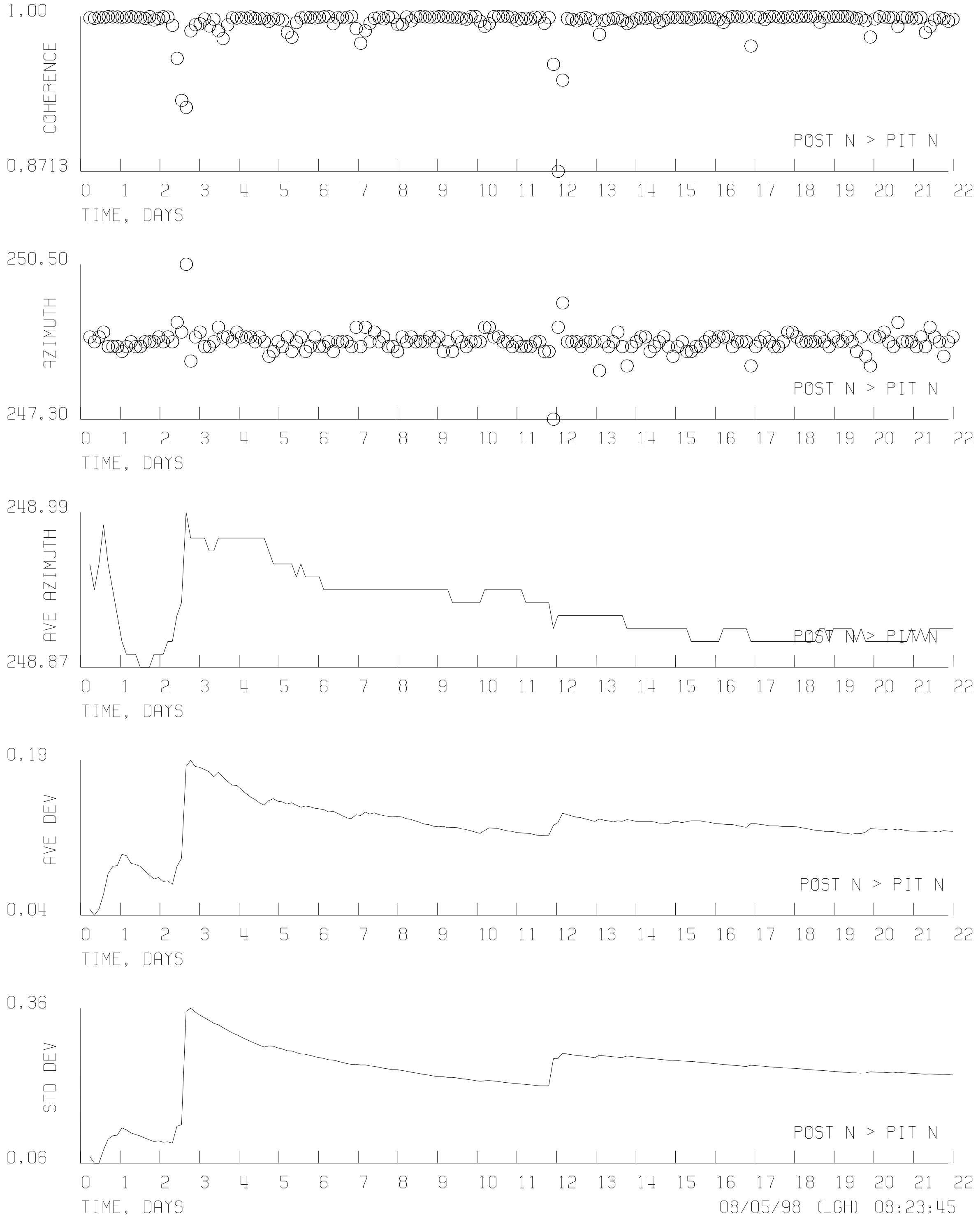

Figure 8.13 Time histories of the calculated coherence, the coherence derived relative azimuth, the average coherence derived azimuth, the average deviation of the coherence derived relative average, and the standard deviation of the coherence derived relative azimuth for the POST N > PIT N angle.

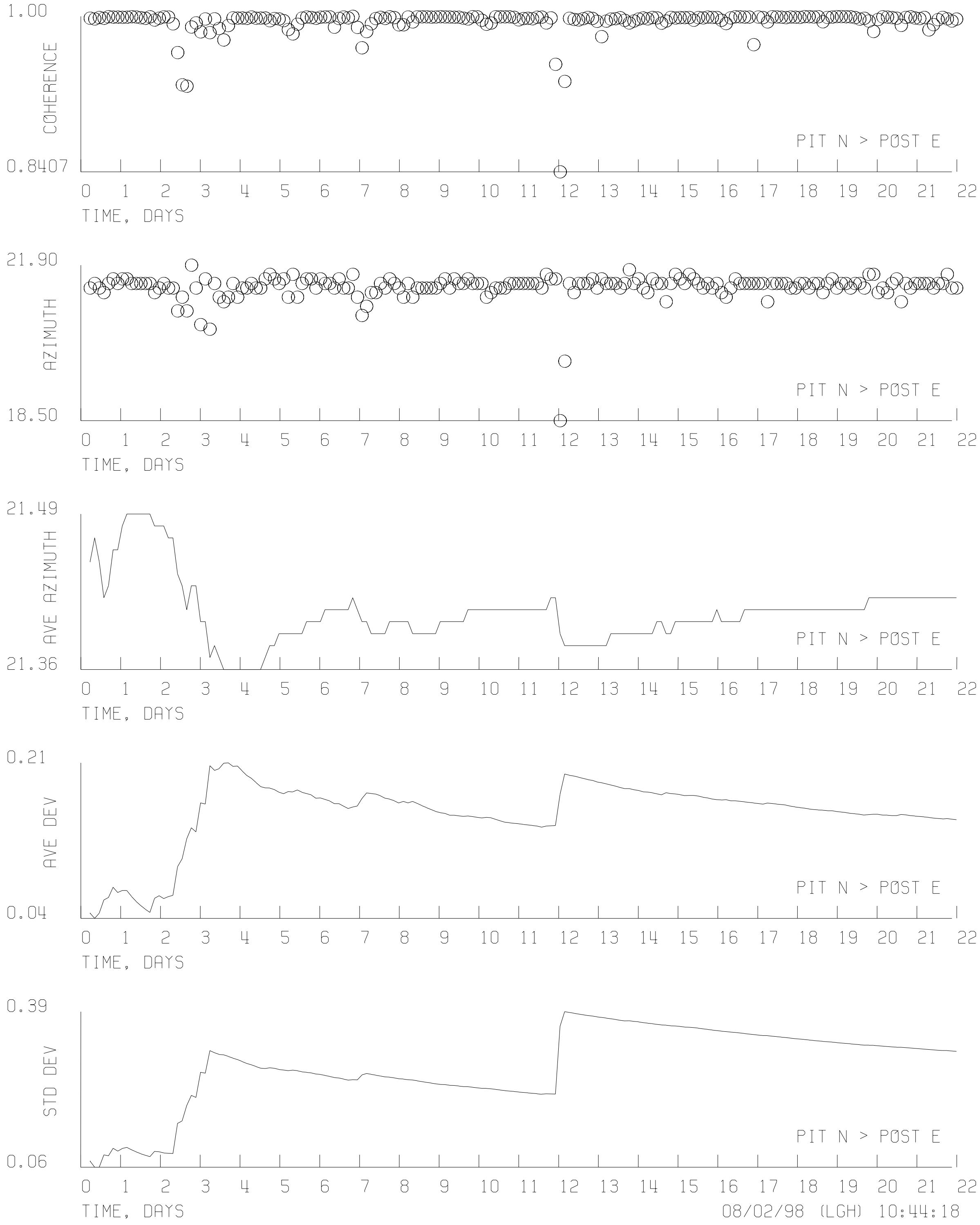

Figure 8.14 Time histories of the calculated coherence, the coherence derived relative azimuth, the average coherence derived azimuth, the average deviation of the coherence derived relative average, and the standard deviation of the coherence derived relative azimuth for the PIT N > POST E angle.

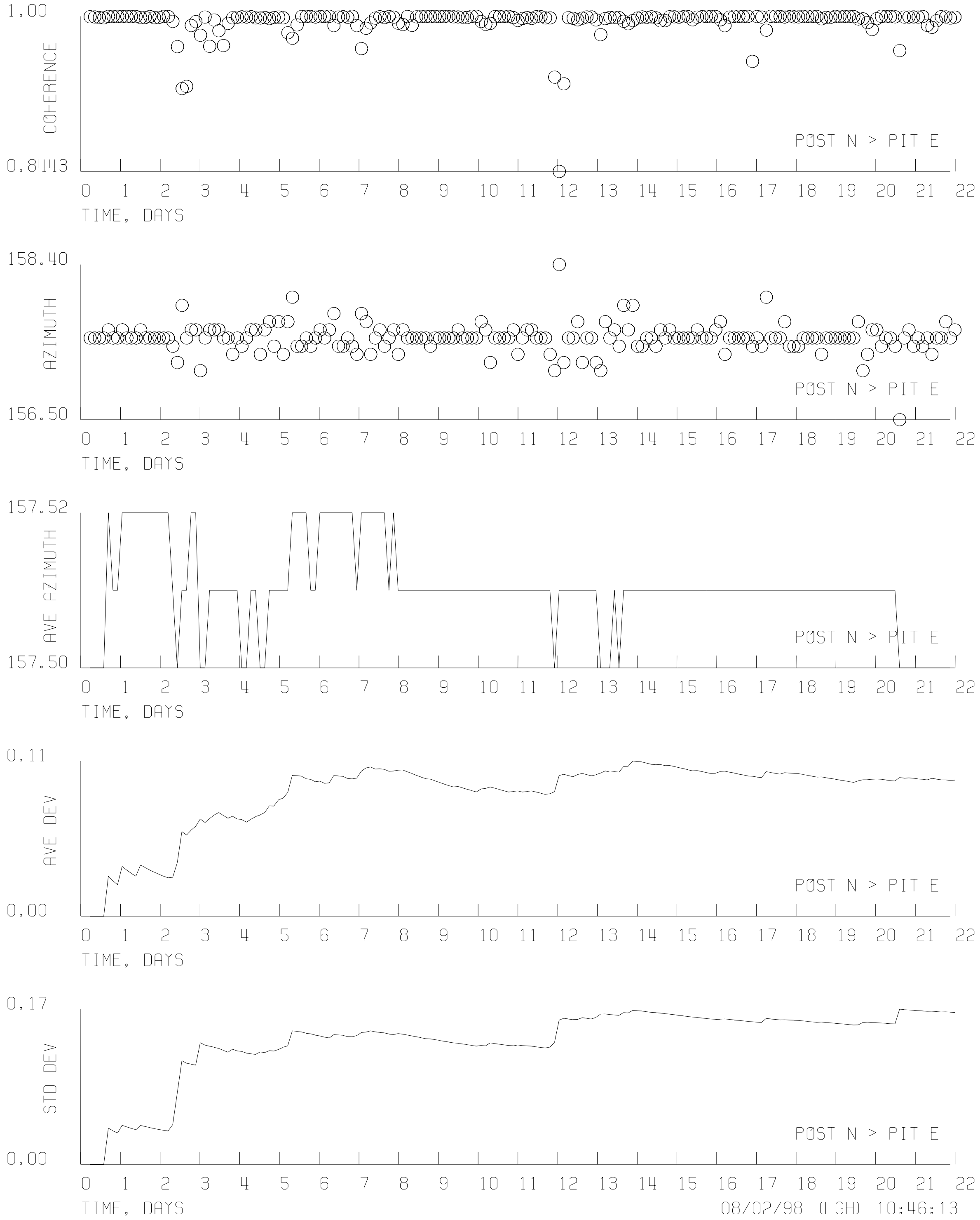

Figure 8. 15 Time histories of the calculated coherence, the coherence derived relative azimuth, the average coherence derived azimuth, the average deviation of the coherence derived relative average, and the standard deviation of the coherence derived relative azimuth for the POST N > PIT E angle.

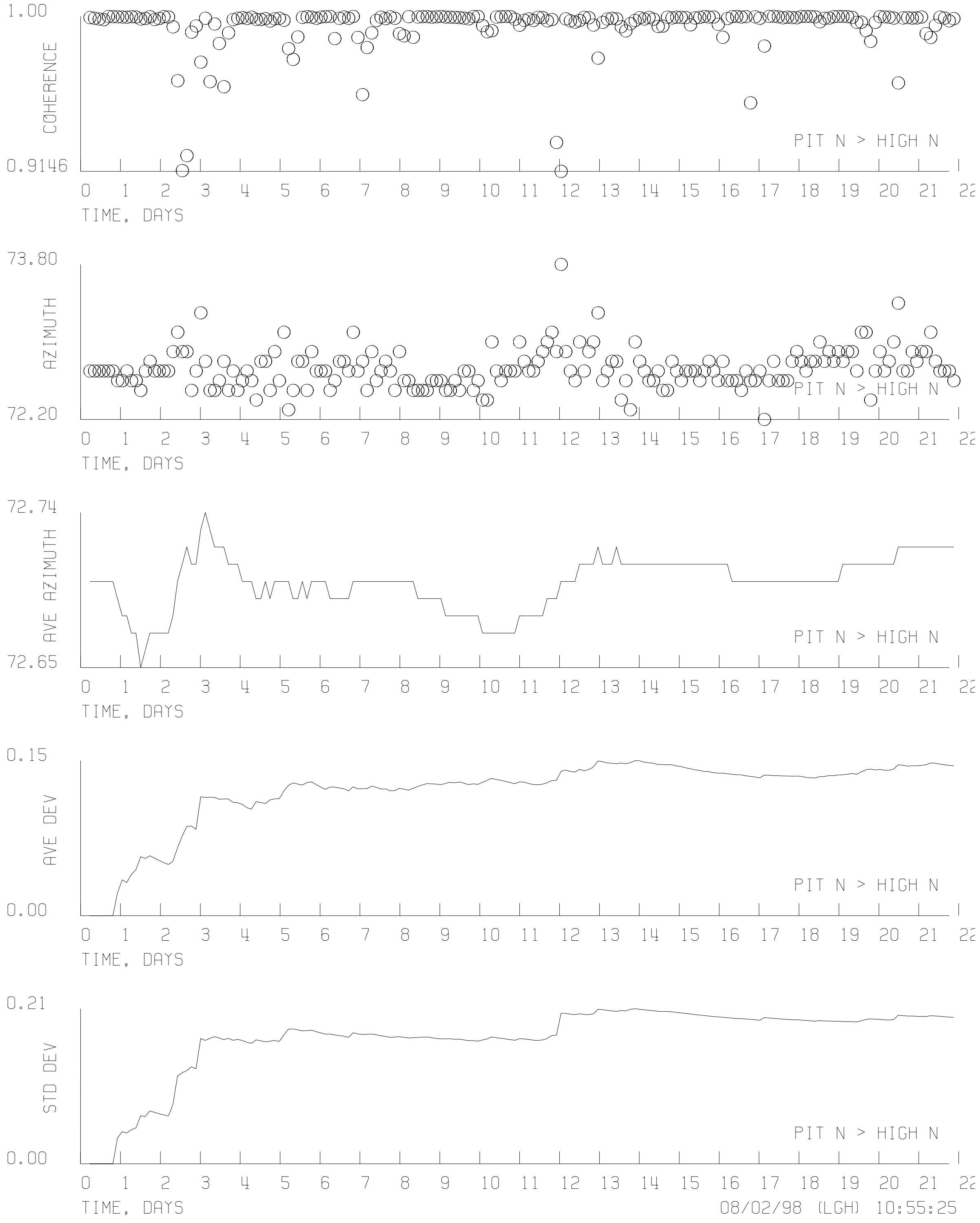

Figure 8.16 Time histories of the calculated coherence, the coherence derived relative azimuth, the average coherence derived azimuth, the average deviation of the coherence derived relative average, and the standard deviation of the coherence derived relative azimuth for the PIT N > HIGH N angle.

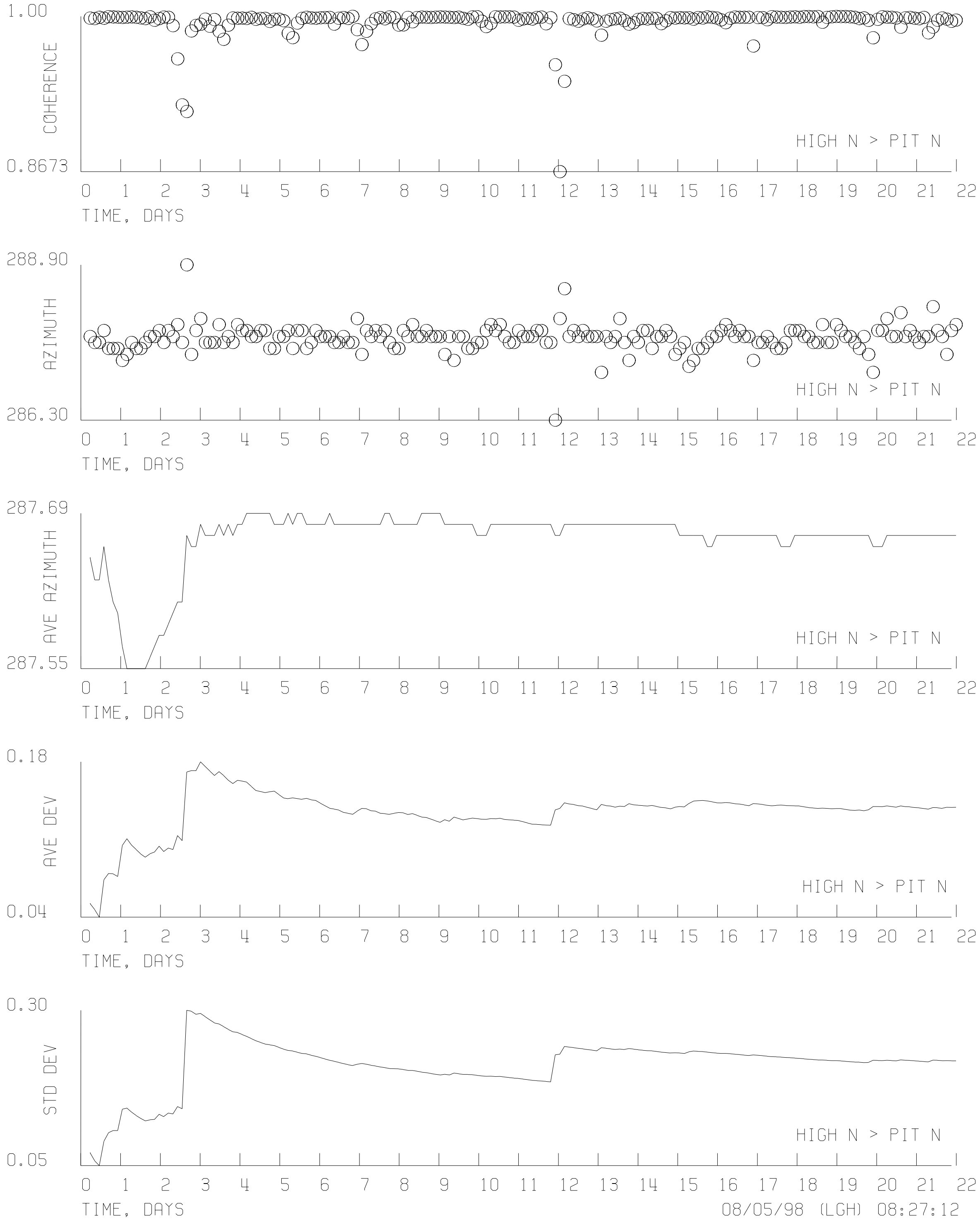

Figure 8.17 Time histories of the calculated coherence, the coherence derived relative azimuth, the average coherence derived azimuth, the average deviation of the coherence derived relative average, and the standard deviation of the coherence derived relative azimuth for the HIGH N > PIT N angle.

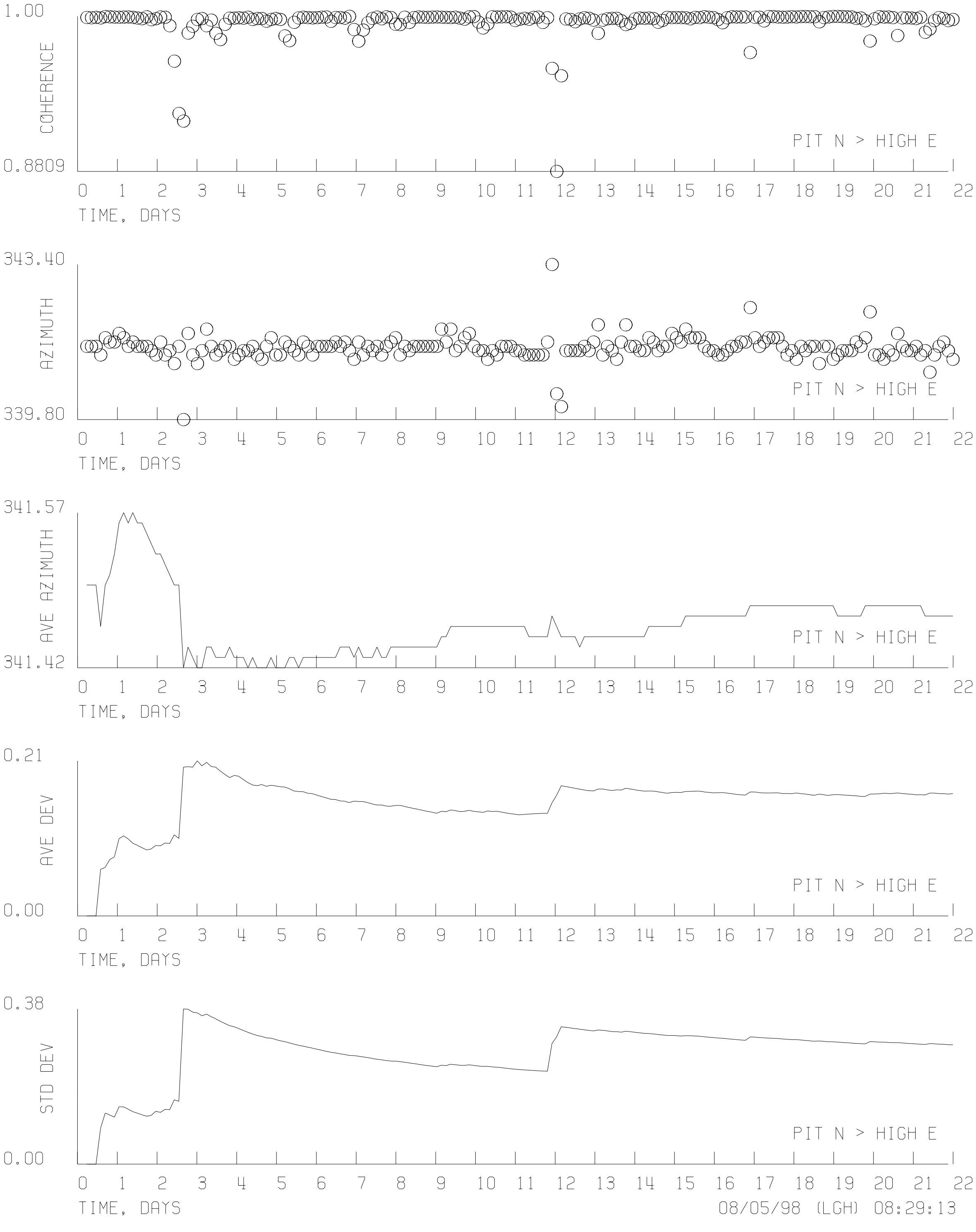

Figure 8.18 Time histories of the calculated coherence, the coherence derived relative azimuth, the average coherence derived azimuth, the average deviation of the coherence derived relative average, and the standard deviation of the coherence derived relative azimuth for the PIT N > HIGH E angle.

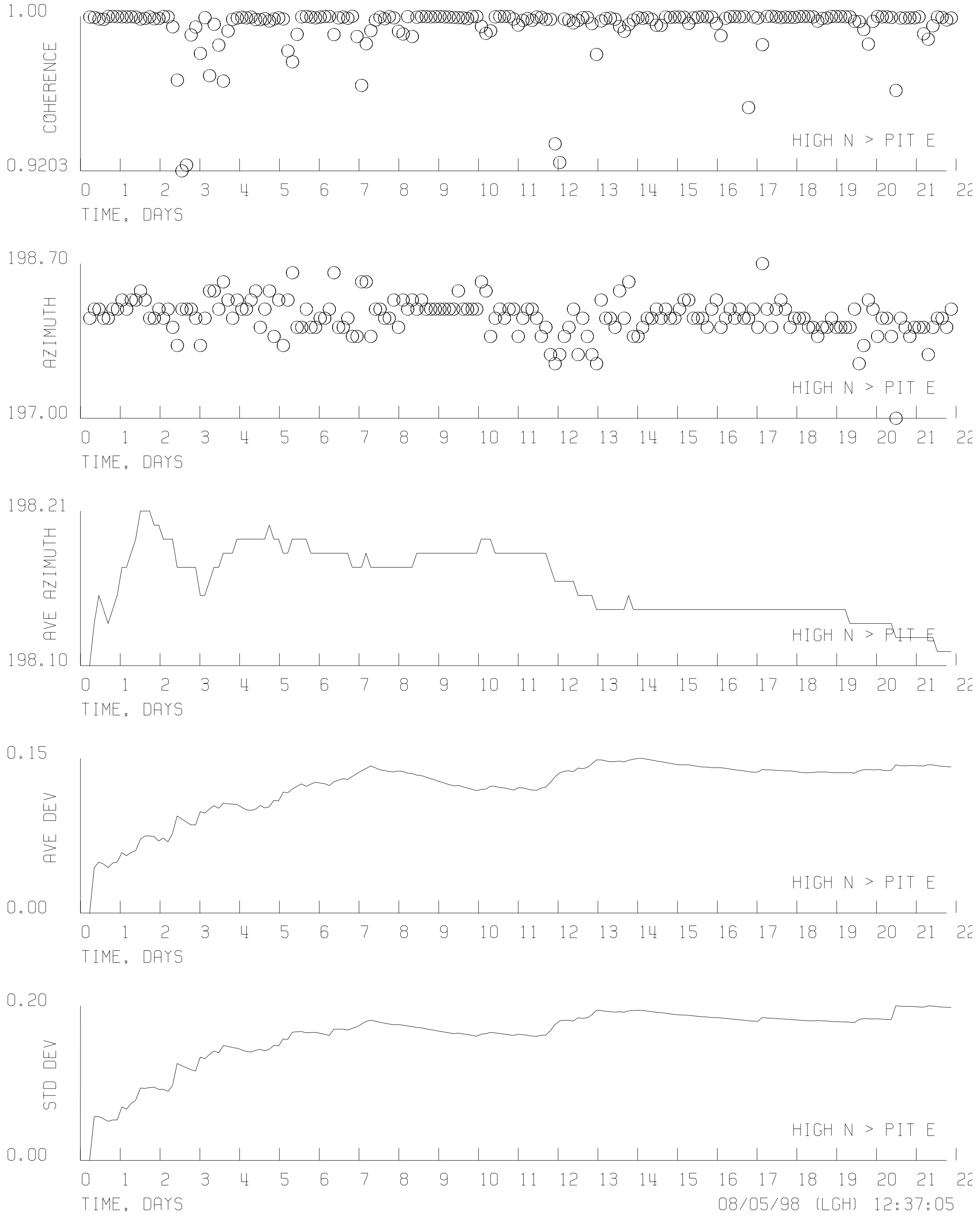

Figure 8.19 Time histories of the calculated coherence, the coherence derived relative azimuth, the average coherence derived azimuth, the average deviation of the coherence derived relative average, and the standard deviation of the coherence derived relative azimuth for the HIGH N > PIT E angle.

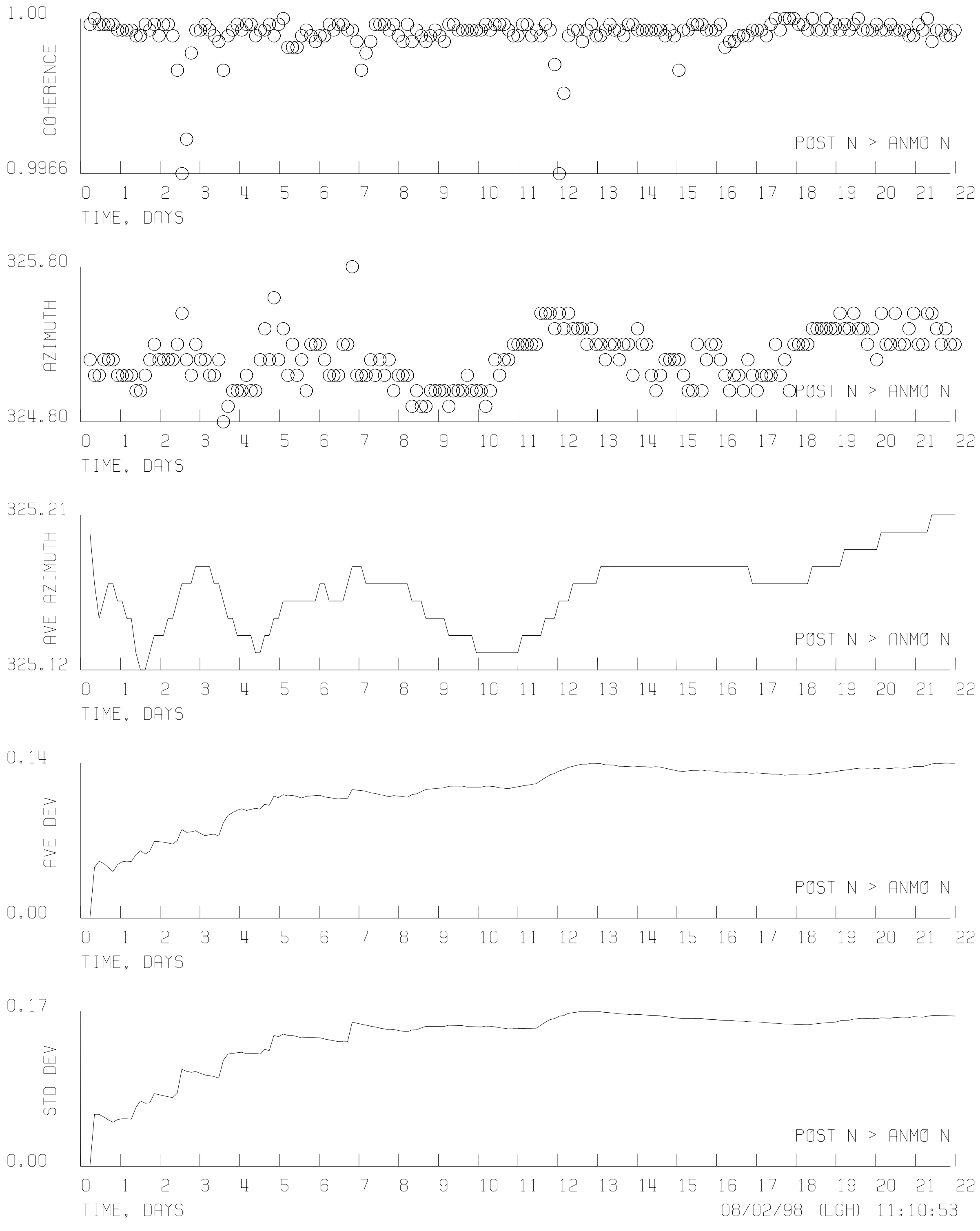

Figure 8.20 Time histories of the calculated coherence, the coherence derived relative azimuth, the average coherence derived azimuth, the average deviation of the coherence derived relative average, and the standard deviation of the coherence derived relative azimuth for the POST N > ANMO N angle.

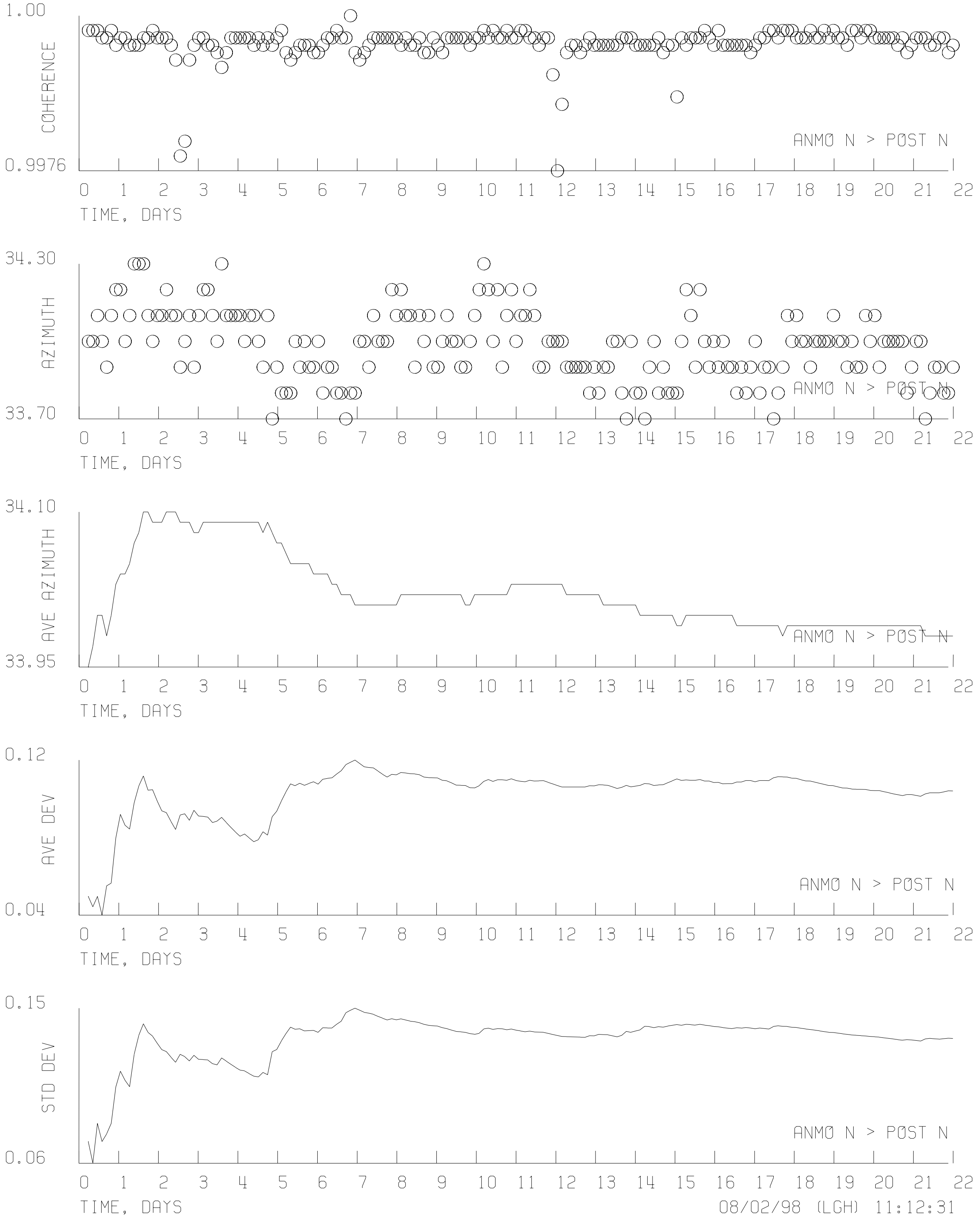

Figure 8.21 Time histories of the calculated coherence, the coherence derived relative azimuth, the average coherence derived azimuth, the average deviation of the coherence derived relative average, and the standard deviation of the coherence derived relative azimuth for the ANMO N > POST N angle.

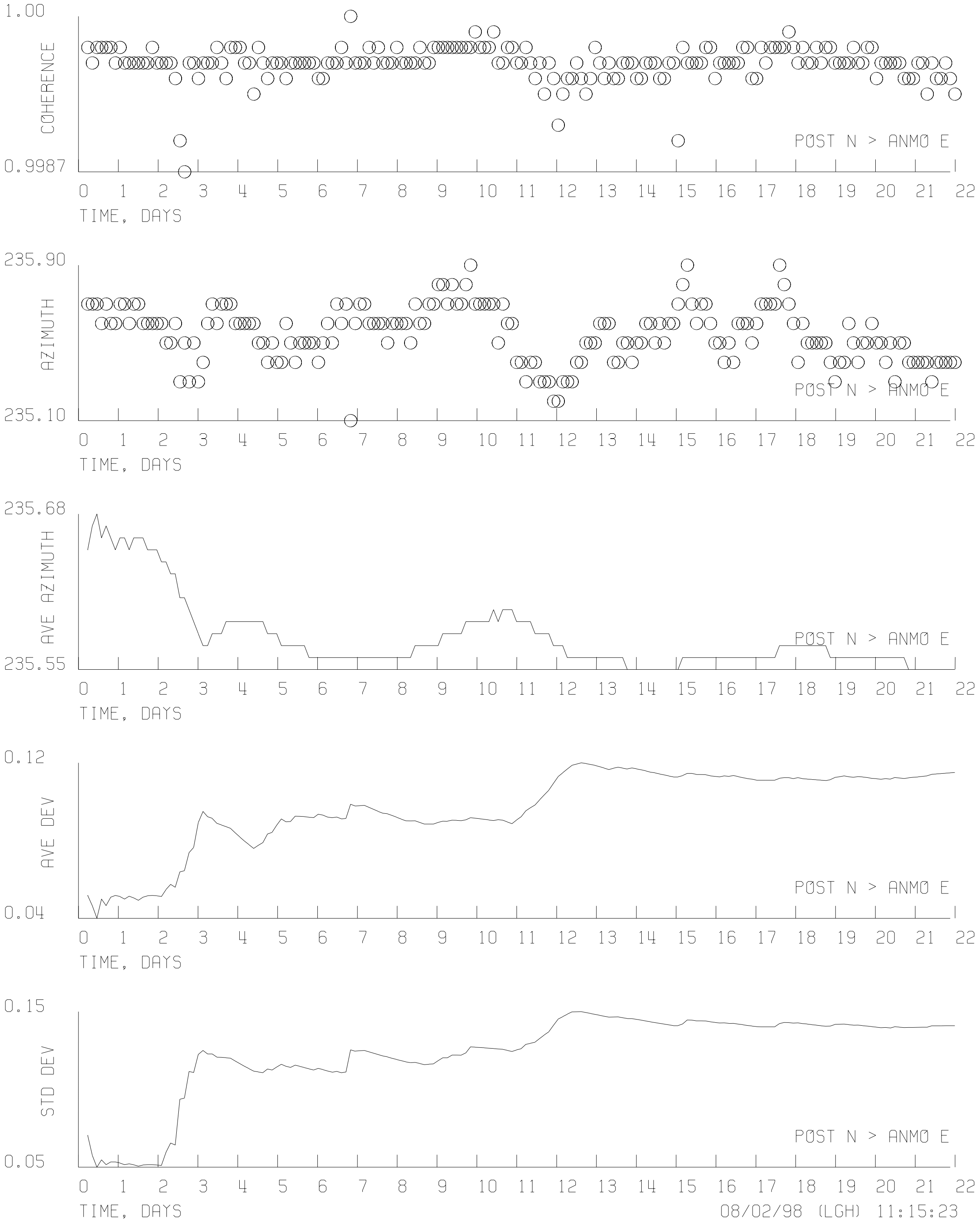

Figure 8.22 Time histories of the calculated coherence, the coherence derived relative azimuth, the average coherence derived azimuth, the average deviation of the coherence derived relative average, and the standard deviation of the coherence derived relative azimuth for the POST N > ANMO E angle.

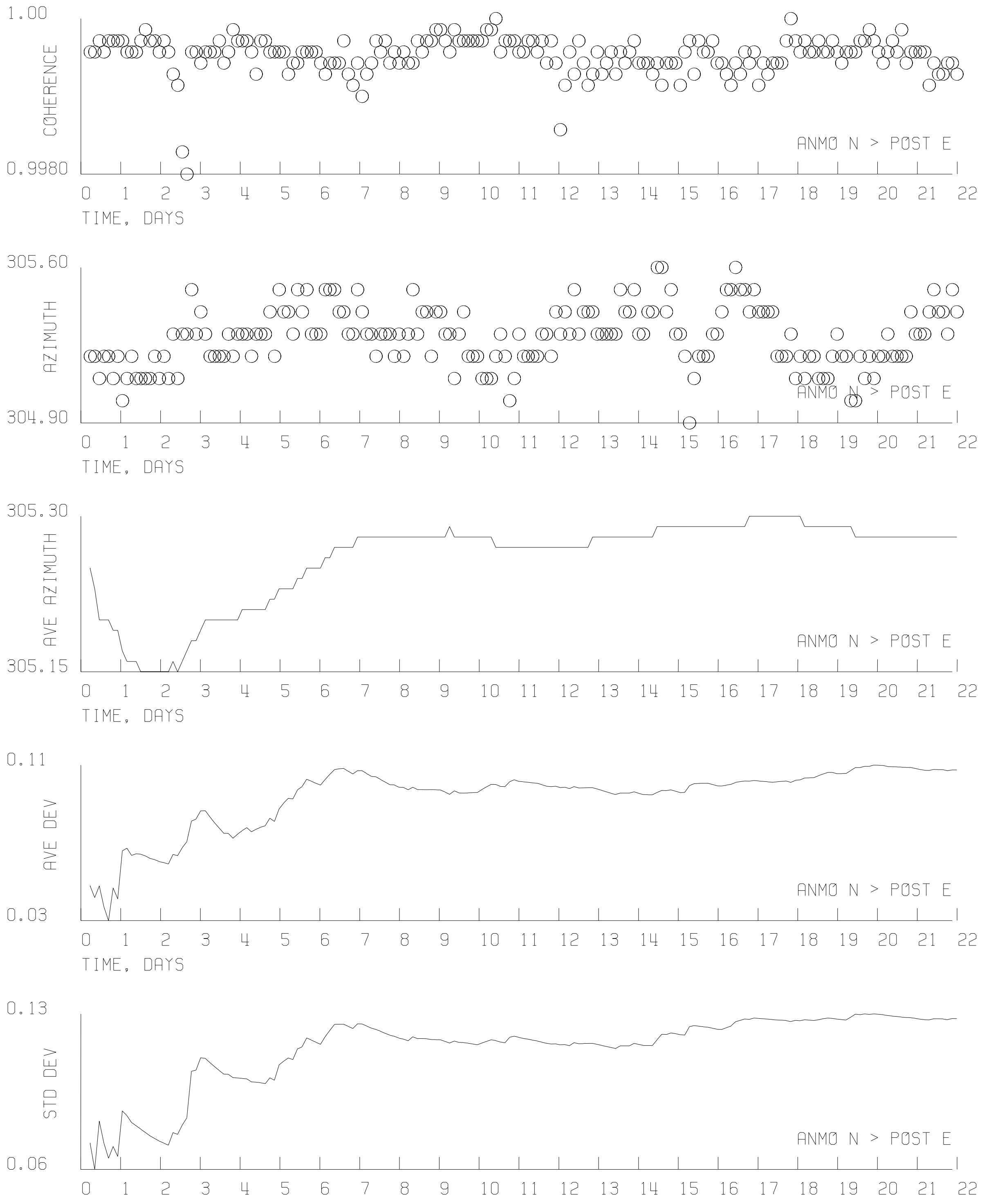

Figure 8.23 Time histories of the calculated coherence, the coherence derived relative azimuth, the average coherence derived azimuth, the average deviation of the coherence derived relative average, and the standard deviation of the coherence derived relative azimuth for the ANMO N > POST E angle.

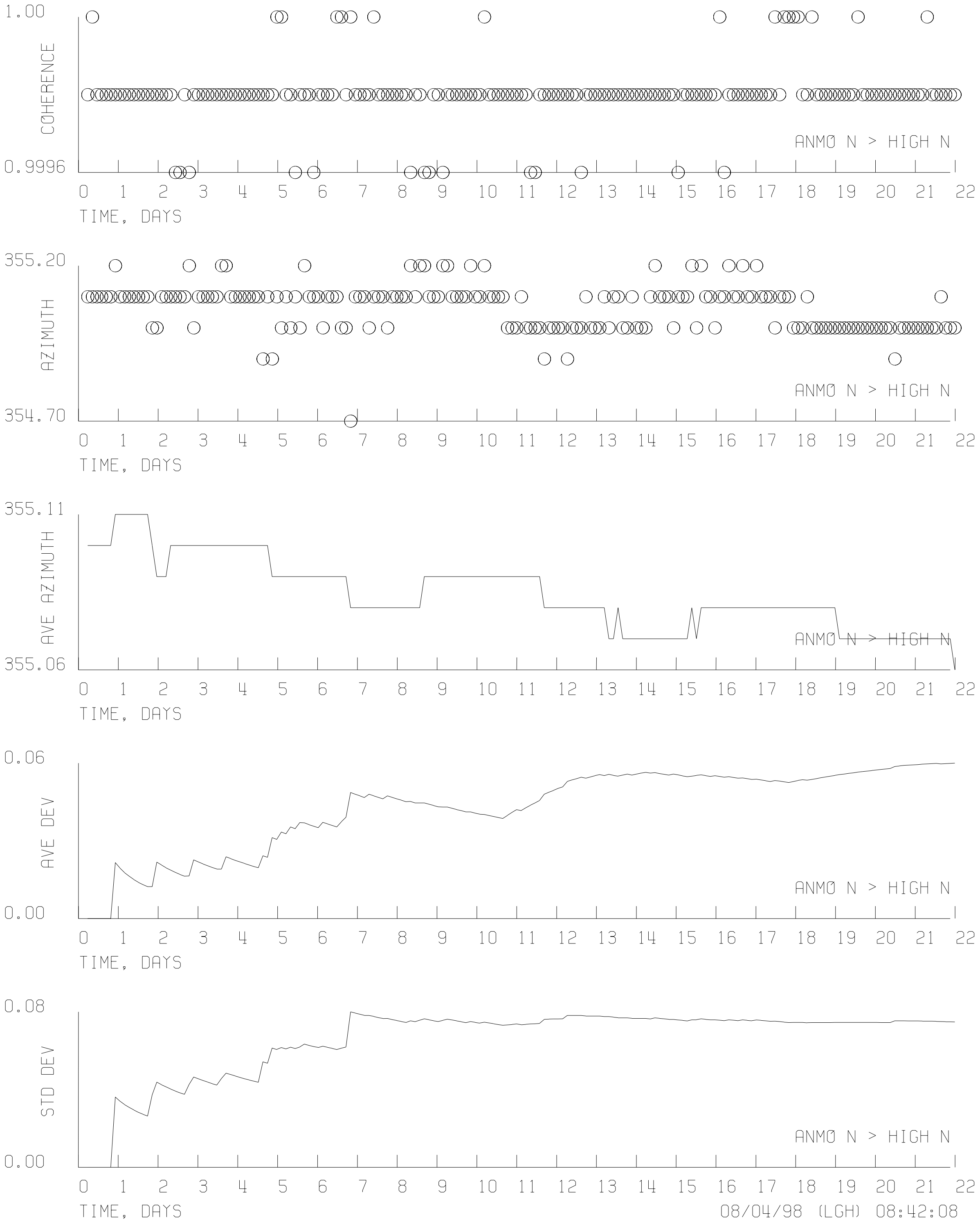

Figure 8.24 Time histories of the calculated coherence, the coherence derived relative azimuth, the average coherence derived azimuth, the average deviation of the coherence derived relative average, and the standard deviation of the coherence derived relative azimuth for the ANMO N > HIGH N angle.

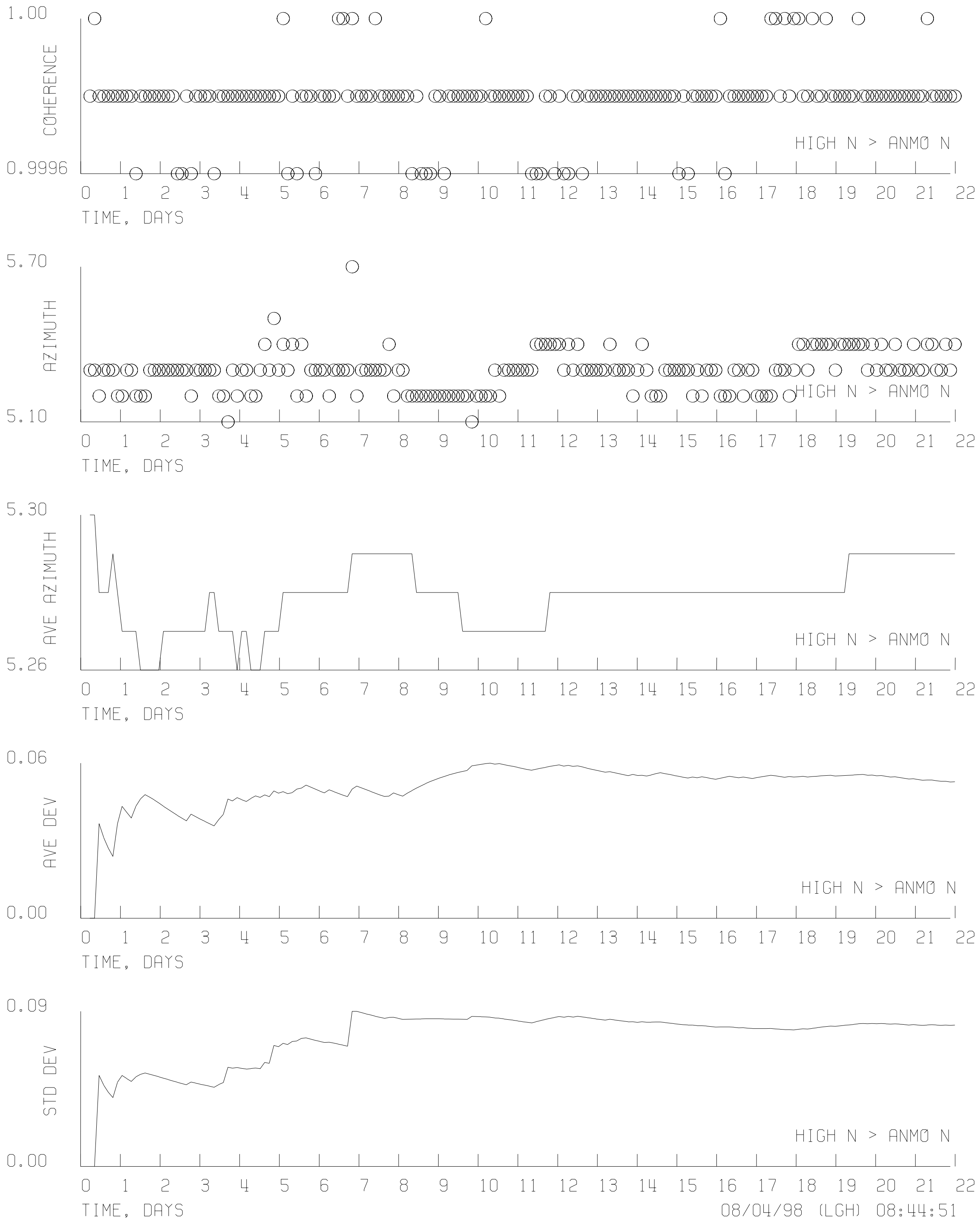

Figure 8.25 Time histories of the calculated coherence, the coherence derived relative azimuth, the average coherence derived azimuth, the average deviation of the coherence derived relative average, and the standard deviation of the coherence derived relative azimuth for the HIGH N > ANMO N angle.

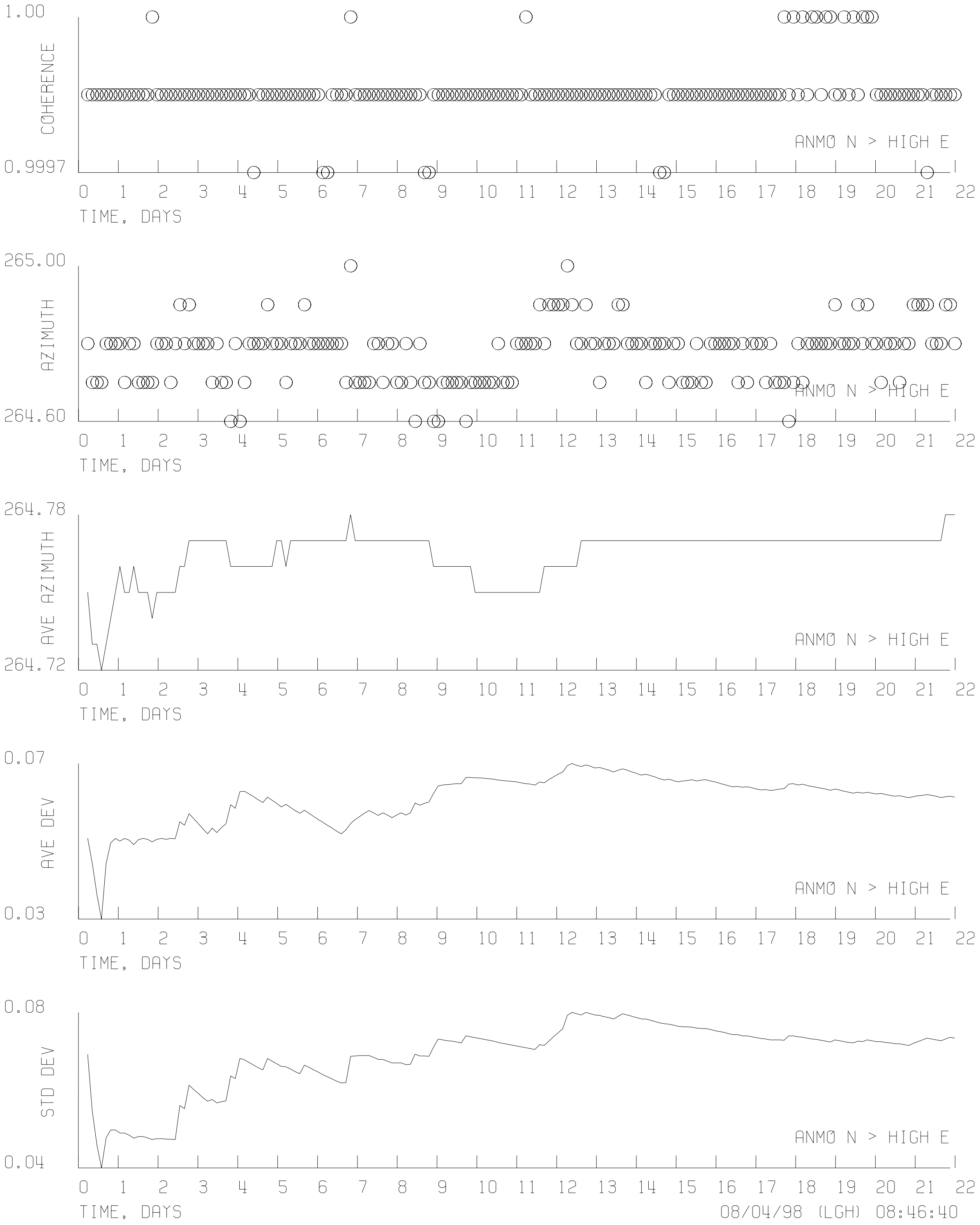

Figure 8.26 Time histories of the calculated coherence, the coherence derived relative azimuth, the average coherence derived azimuth, the average deviation of the coherence derived relative average, and the standard deviation of the coherence derived relative azimuth for the ANMO N > HIGH E angle.

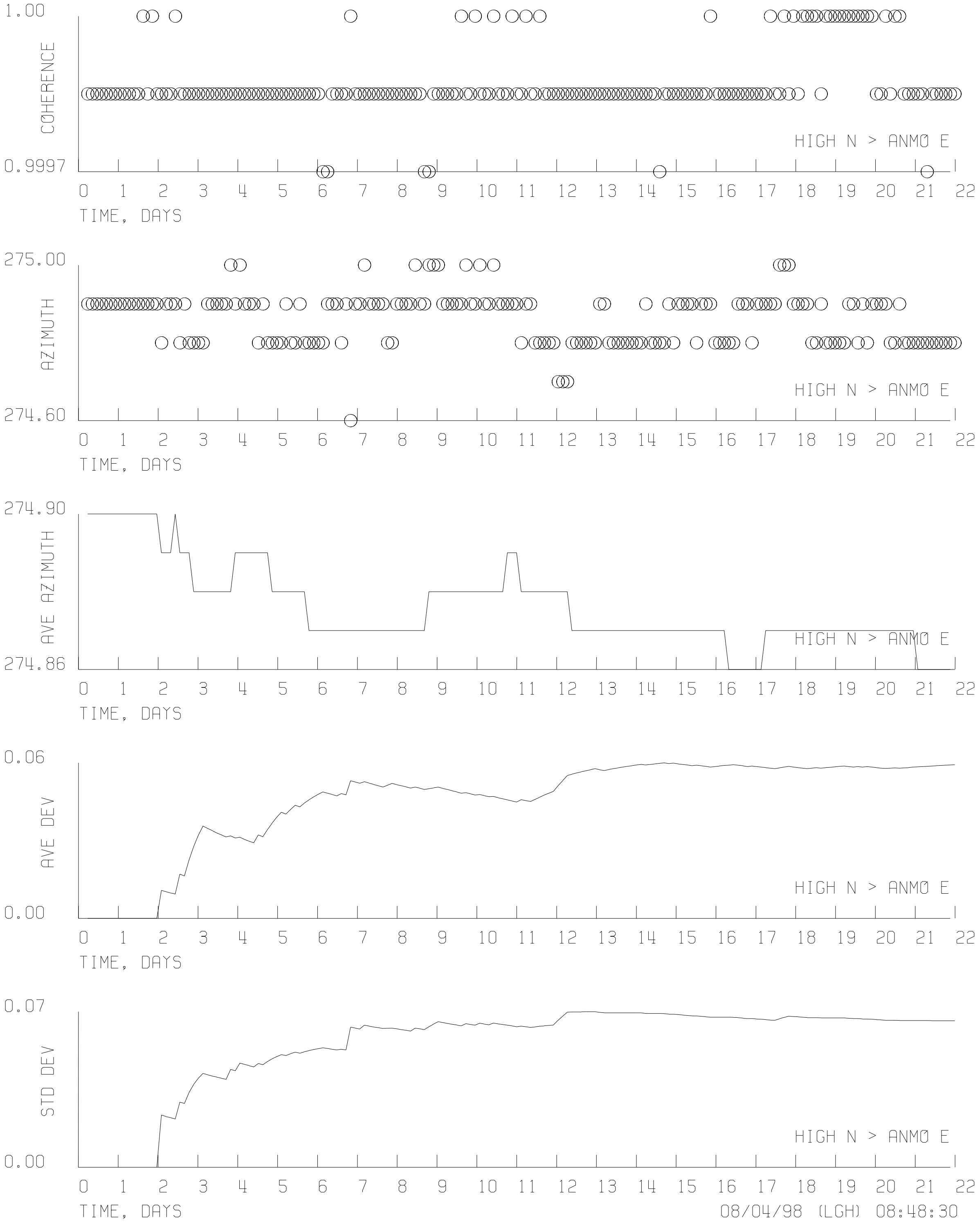

Figure 8.27 Time histories of the calculated coherence, the coherence derived relative azimuth, the average coherence derived azimuth, the average deviation of the coherence derived relative average, and the standard deviation of the coherence derived relative azimuth for the HIGH N > ANMO E angle.

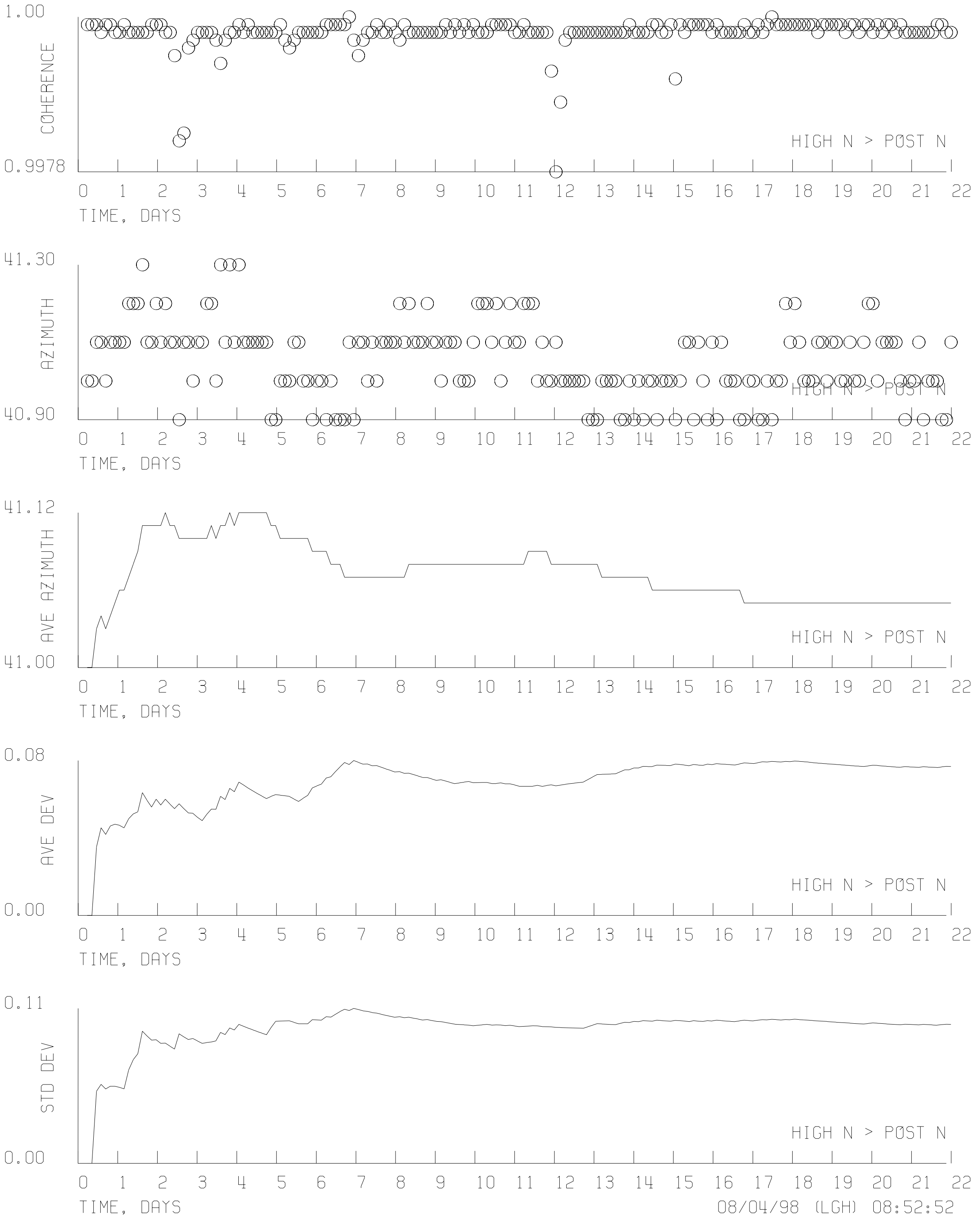

Figure 8.28 Time histories of the calculated coherence, the coherence derived relative azimuth, the average coherence derived azimuth, the average deviation of the coherence derived relative average, and the standard deviation of the coherence derived relative azimuth for the HIGH N > POST N angle.

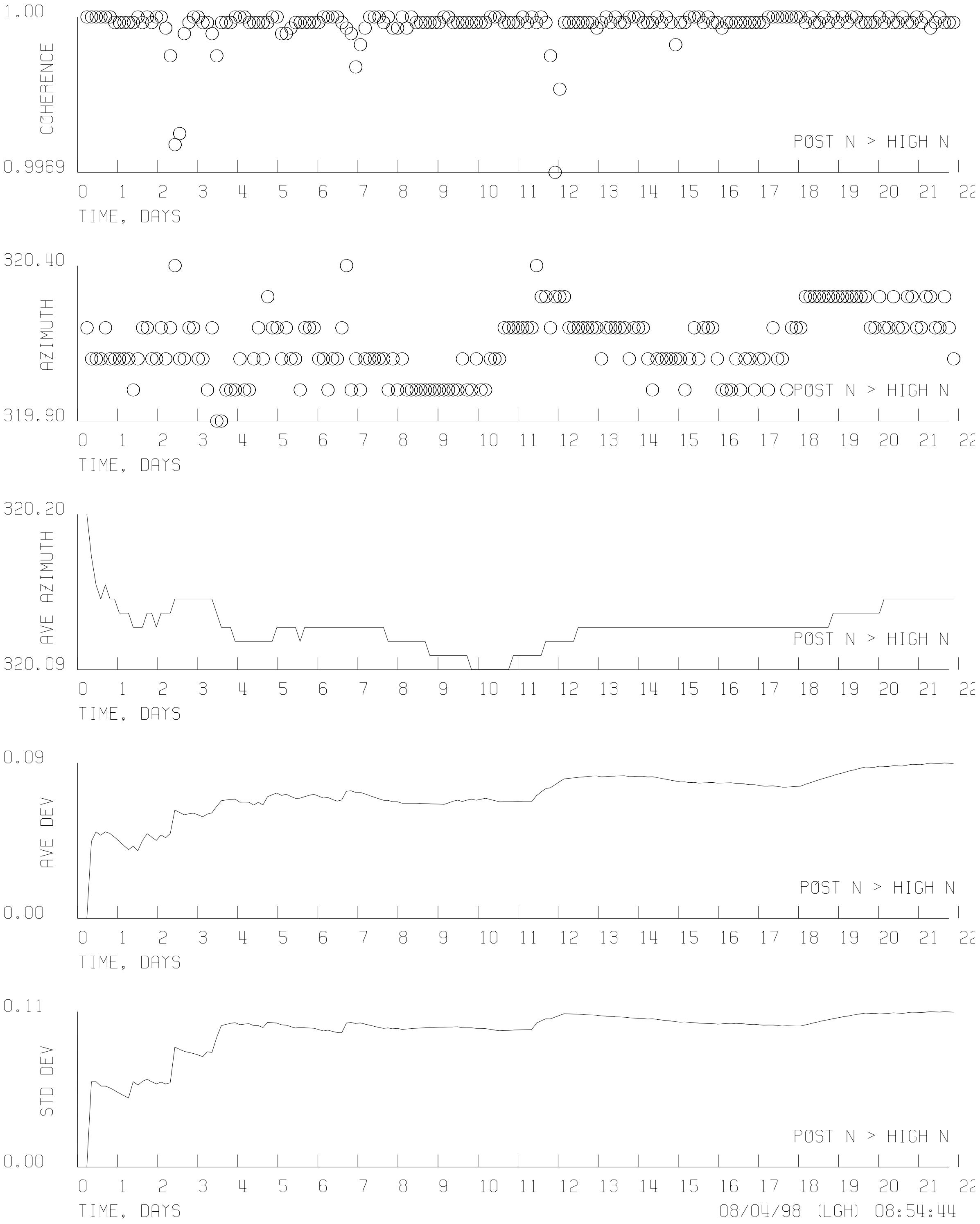

Figure 8.29 Time histories of the calculated coherence, the coherence derived relative azimuth, the average coherence derived azimuth, the average deviation of the coherence derived relative average, and the standard deviation of the coherence derived relative azimuth for the POST N > HIGH N angle.

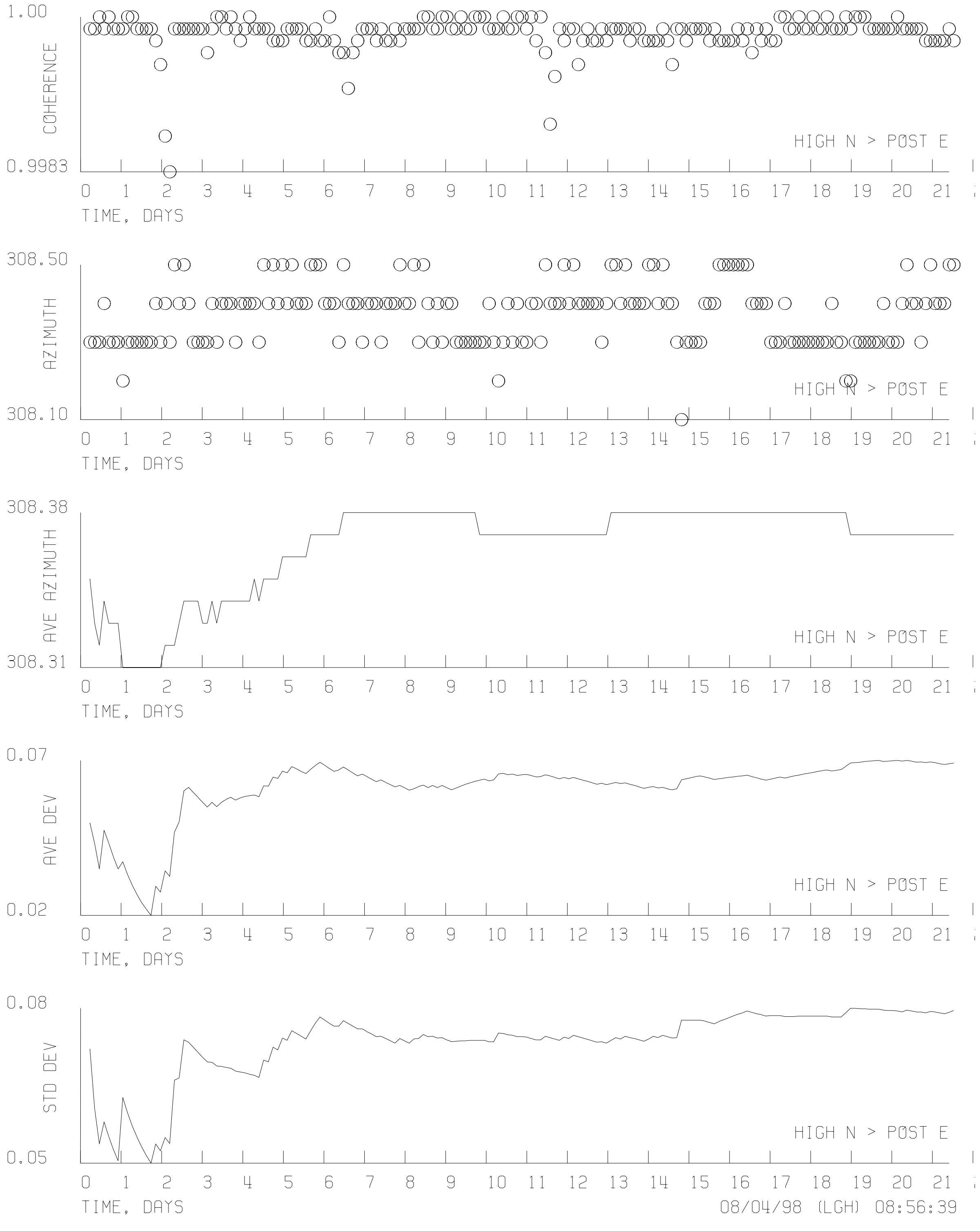

Figure 8.30 Time histories of the calculated coherence, the coherence derived relative azimuth, the average coherence derived azimuth, the average deviation of the coherence derived relative average, and the standard deviation of the coherence derived relative azimuth for the HIGH N > POST E angle.

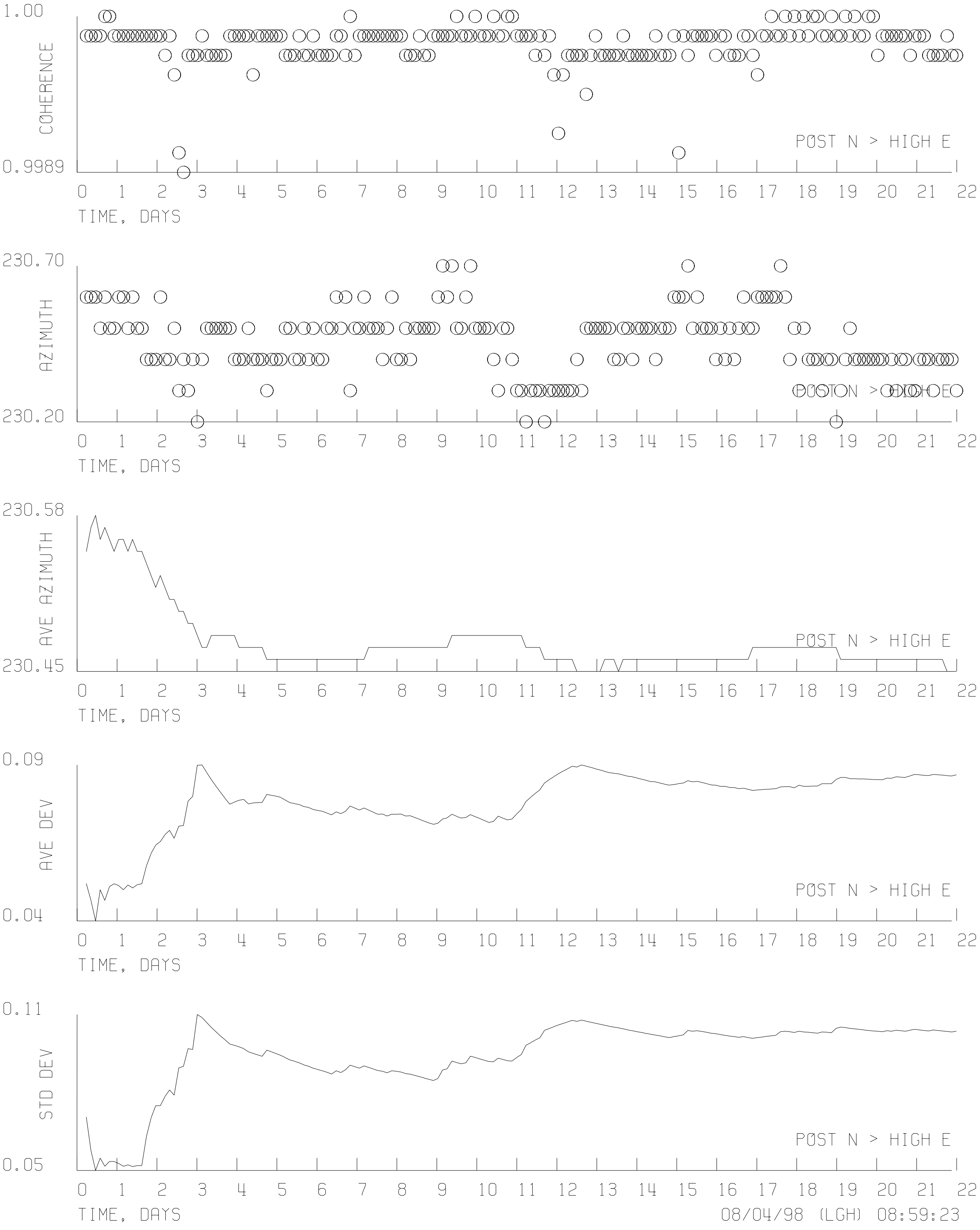

Figure 8.31 Time histories of the calculated coherence, the coherence derived relative azimuth, the average coherence derived azimuth, the average deviation of the coherence derived relative average, and the standard deviation of the coherence derived relative azimuth for the POST N > HIGH E angle.

8.8 PRELIMINARY THOUGHTS ON PROBABLE OVERALL ACCURACY

The problem of determining the overall accuracy of the relative azimuth measurements is a very difficult problem to directly address. The difficulty arises because there is no known independent means of determining the relative azimuth between two sensor systems separated by tens of feet with a greater known accuracy than the technique under investigation. This is particularly true if one or more of the sensors is installed in a borehole. Therefore, we will resort to some indirect observations to gain a feel for the overall potential accuracy of the process. First, some discrepancies in the current data set will be presented as evidence of possible inaccuracies in the azimuths determined in this experiment. Then a plausible explanation will be offered to explain these inaccuracies.

Two of the relative azimuths determined for each pair of sensors relate to the relative angular positions of the north components of the two sensors. These calculations are A N > B N and B N > A N (see the fourth paragraph of Section 8 for an explanation of this terminology). In Figure 8.2, these two angles are the two arcs indicated between the POST N and the PIT N (112.2°) and the PIT N and the POST N (248.9°). Obviously these two relative azimuths should add up to 360° but they don't do so; instead, their sum is 361.1° . The departures from 360° are summarized for all six sensor pair combinations in Table 8.25

SENSOR COMBINATION	SUM	ERROR FROM 360^{o}	SOURCE FIGURE NUMBER
PIT-POST	361.1	1.1	8.2
PIT-HIGH	360.4	0.4	8.3
PIT-ANMO	361.5	1.5	8.4
HIGH-POST	361.2	1.2	8.5
POST-ANMO	359.2	-0.8	8.6
ANMO-HIGH	360.4	0.4	8.7

Table 8.25 Relative north component azimuth sums and their departure from 360° for all six possible sensor combinations. All angles are in degrees. The raw data are plotted in the indicated figures.

These results are summarized in another format in Figures 8.32 through 8.35 in which a different sensor in each figure is considered to be the reference sensor (for convenience, the reference sensor in each figure is assumed to be oriented north) in each of the four figures and the relative positions of the north components of the remaining three sensors are plotted with respect to this reference sensor. Both the forward and reverse azimuths are plotted between each pair of north sensors. The reverse azimuth was calculated by subtracting the complementary forward azimuth from 360°. In the ideal world, these forward and reverse angles would be exactly equal. As the data in Figures 8.32 through 8.35 demonstrates, this is not true for the real world results obtained from this experiment. The disagreement in the two methods for determining the relative positions of the north components is 0.4° for the PIT and HIGH, 0.4° for the ANMO and HIGH, 0.8° for the POST and ANMO, 1.1° for the PIT and POST, 1.2° for the HIGH and POST, and 1.5° for the PIT and ANMO. The forward azimuth was calculated by rotating the north component of the first sensor system in the indicated pair combination until it was aligned with the north component of the second sensor system in the indicated pair combination. The reverse azimuth was calculated by rotating the north component of the second sensor system in the indicated pair combination until it was aligned with the north component of the first sensor system in the indicated pair combination. The same data set (data from exactly the same time period) was used to calculate both the forward and the reverse azimuths so a difference in the character of the input signal should not be the problem. There must be an explanation for the discrepancy.

The relative coherence derived azimuth measurements summarized in Tables 8.3, 8.7, 8.11, 8.15, 8.19, and 8.23 provide sufficient data for calculating the degree of orthogonality between the horizontal components in the four sets of sensors involved in the posthole experiment. There are two ways to calculate the orthogonality from the data on hand. The first method is provided by A N > B N measured azimuth and the A N > B E measured azimuth (see Section 8, the fourth paragraph for clarification of this terminology). Both of these azimuth angles are derived by rotating the north component of sensor A to align it first with the north component of sensor B (A N > B N), then with the east component of sensor B (A N > B E). This result will be referred to as a "direct" measure of the orthogonality because the rotation of one component of one sensor is involved in evaluating the orthogonality. The second estimate of the orthogonality is derived from the A N > B E measured azimuth combined with the B N > A N measured azimuth. Since this measurement involves the rotation of the north component of both sensor systems it will be referred to as an "indirect" measure of the orthogonality. The estimates of the orthogonality of all four sensor systems as calculated by the direct measurement are shown in Table 8.26 and those obtained via the indirect method are contained in Table 8.27.

PIT		POST		ANMO		HIGH	
ORTH	ERROR	ORTH	ERROR	ORTH	ERROR	ORTH	ERROR
91.7	1.7	90.8	0.8	91.3	1.3	90.9	0.9
91.4	1.4	88.7	-1.3	89.7	-0.3	90.3	0.3
89.6	-0.4	92.7	2.7	90.4	0.4	89.7	-0.3

Table 8.26 Experimentally calculated direct azimuths between the north and east horizontal components of the indicated sensors. The columns labeled error contain the departure from 90°. All angles are in degrees.

PIT		POST		ANMO		HIGH	
ORTH	ERROR	ORTH	ERROR	ORTH	ERROR	ORTH	ERROR
90.2	0.2	89.7	-0.3	89.8	-0.2	90.9	0.9
90.3	0.3	89.5	-0.5	92.5	2.5	98.9	0.1
89.2	-0.8	91.5	1.5	90.1	0.1	88.5	-1.5

Table 8.27 Experimentally calculated indirect azimuths between the north and east horizontal components of the indicated sensors (columns headed ORTH). The columns labeled ERROR contain the departure from the ideal case of 90°. All angles are in degrees.

All of the orthogonality azimuths in both tables are in the 90° vicinity but there are significant variations about 90°. The data seem to be inconsistent because one would expect the orthogonality of a given sensor to be nearly the same regardless of which other sensor was used to measure it. This is not the case. Each ORTH column in both of the tables contains three calculated orthogonality azimuths; each of these three angles was derived from one of the remaining three sensors. Yet, for a given sensor, they vary up to 1° or more. There must be an explanation for these discrepancies.

A potential source of error in both the coherence determined azimuths and in the orthogonality estimates is one of the very things we attempted to measure; the lack of perfect alignment of the two horizontal components within a given sensor may contribute to errors in relative angular measurements. The rotation algorithms utilized to process the data in this study assume that the two horizontal components in each sensor system are perfectly orthogonal with a 90° span between them. This assumption is probably not true very often in real world sensor systems. Seismometer manufacturers certainly attempt to build their instruments with orthogonal horizontals but in practice there will almost always be errors in mechanical alignment of the two systems. Manufacturers specifications on horizontal component alignment vary over a broad range. The Guralp Systems CMG-3T Broadband Seismometer Installation Manual says "The mounting accuracy of the horizontal sensors to each other and to the orientation pointers to indicate the orientation is better than 0.2 degrees.". The Streckeisen Portable Very-Broad-Band Triaxial Seismometer (STS-2) manual says "The orthogonal output signals are factoryadjusted to represent motions in the geometrical X, Y, and Z axis of the seismometer with an accuracy of 1 percent (0.6 degrees) at a period of 6 sec.". The Teledyne Brown Engineering (Geotech) manual for the Borehole Seismometer System Model 54000-0103 (KS-54000) says in the Operating Characteristics Section for the middle seismometer element is aligned North South $\pm 3^\circ$ and the bottom seismometer element is aligned East West $\pm 3^\circ$ (this specification is the same as that contained in the Teledyne Geotech manual for the KS-36000). Thus, the three manufacturers azimuth alignment specifications vary over a broad range of 'claimed' accuracy. None of these manufacturers mention how they arrived at their misalignment specifications so the author and readers will have to speculate about probable sources of this information. Therefore, the following two paragraphs contain the author's "best guess" concerning what the manufacturers specifications mean.

Acquiring data to fully substantiate the accuracy of the horizontal component alignment specification would require an extensive test series involving a 'representative' number of instruments and rather tedious set up, data acquisition, and data analysis procedures. The definition of representative is not known but the more the better. The author doubts that any of the manufacturers have actually performed the costly experiments necessary to validate their alignment claims. Instead, the author feels that, in the cases of the Guralp CMG-3T and the Streckeisn STS-2, the manufacturers may have measured the sensitivity axis misalignment in one or two or at most 'a few' of their preproduction sensor systems and then assumed that all their production units were assembled to the same accuracy. In the case of the Teledyne KS-36000 and the KS-54000, the author suspects that the sensitivity axis alignment was not measured at all; rather, the manufacturer probably first calculated the worst possible alignment from manufacturing mechanical drawings, then added an engineering safety margin to yield the alignment specification printed in the manual. This could explain the rather large $\pm 3^\circ$ alignment specification for the KS-36000 and the KS-54000.

If we take the manufacturers specifications at face value, they indicate that in the Guralp CMG-3T, the horizontal component orthogonality could depart from the perfect 90° by 0.4°, the horizontal components in a Streckeisen STS-2 could be off 90° by 1.2°, and the KS series horizontal orthogonality might range from 84° to 96°. It is the author's opinion that the CMG-3T specification is unrealistically tight and the KS specs are probably too broad. The Streckeisen specification seems to be the most reasonable of the three and it quite coincidentally is approximately the same magnitude as are the errors in the azimuth processing results derived from this experiment.

It is highly conceivable that deviations from true orthogonality of the horizontal sensitivity axis in the four sensors used in the posthole experiment are the source of much of the error in the relative derived azimuths and orthogonality data discussed earlier in this section. It is possible that the accuracy of the azimuth determination method is limited by the degree of orthogonality in the instrumentation. Regardless of the source of the error, it seems to make sense that it is useless to attempt to align the sensor systems with geographic north-south and east-west more accurately than they are constructed internally. To make such an attempt with a sensor with three components within one package is useless because even if one is successful in aligning the north component exactly north-south, it will then probably be impossible to simultaneously align the east component exactly east-west because the two components are probably not truly orthogonal. With the north component perfectly aligned north-south, the east component will remain out of perfect east-west alignment by the magnitude of the as originally manufactured orthogonality misalignment.

If greater accuracy in the azimuthal positions of the horizontal components of sensors is desired in the future, it will probably be necessary to custom measure the nonorthogonality of each pair of sensors within each sensor package and include this angle as part of the instrument calibration data. To date, we have not actually performed such a custom orthogonality measurement, but it should be possible to conduct an experiment to measure this angle using the techniques discussed in this paper and a pair of STS-1 horizontals, which can be carefully oriented orthogonally. Perfecting this technology could be the subject of a future report if there is sufficient interest.

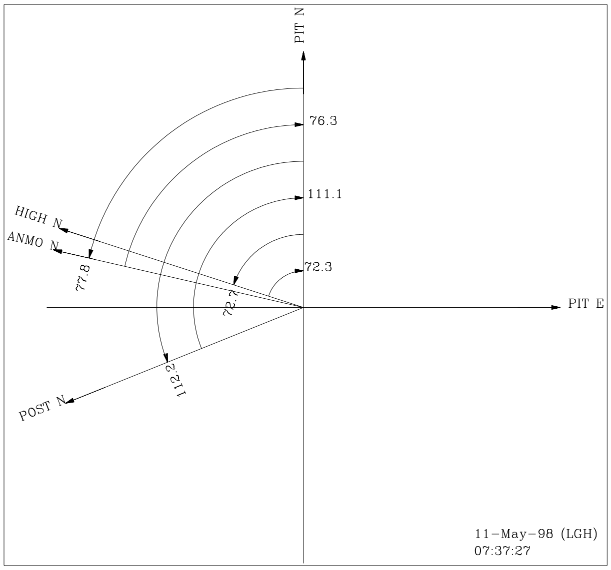

Figure 8.32 Relative azimuths of the ANMO, POST, and HIGH north components referred to the PIT north.

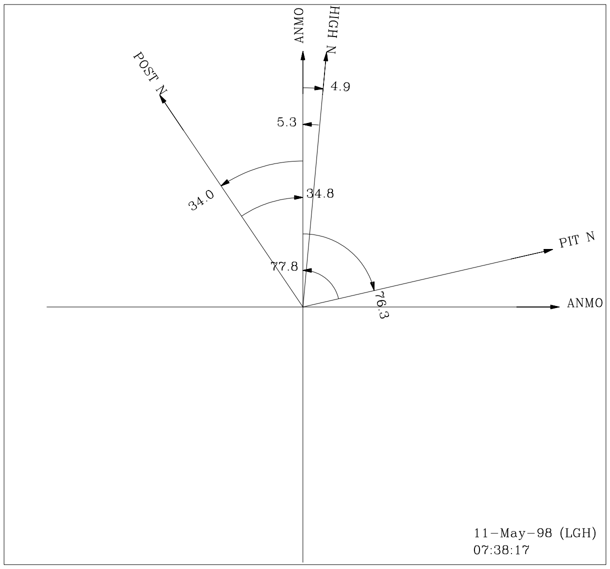

Figure 8.33 Relative azimuths of the PIT, POST, and HIGH north components referred to the ANMO north.

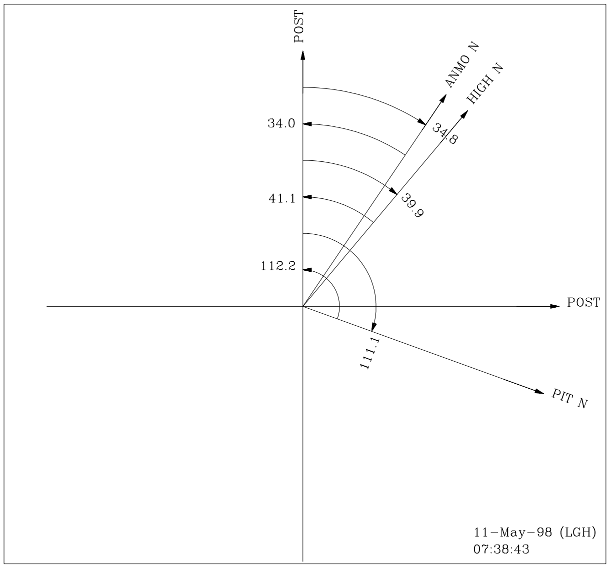

Figure 8.34 Relative azimuths of the PIT, ANMO, and HIGH north components referred to the POST north.

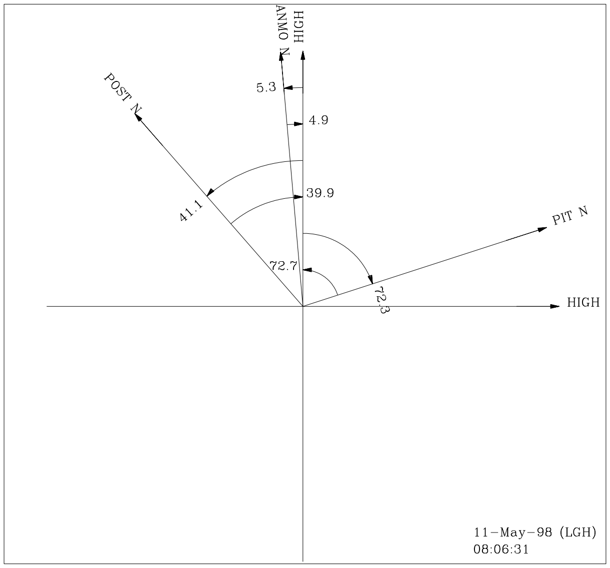

Figure 8.35 Relative azimuths of the PIT, ANMO, and POST north components referred to the HIGH north.

8.9 SUMMARY OF POSTHOLE EXPERIMENTAL RESULTS

Figure 8.36 is an attempt to summarize the statistical results obtained from this experiment. The figure depicts an approximately vertical planar view of the experimental layout (not nearly to scale) in which the distances between the four sensors are labeled. The six double ended arrows are labeled with the physical spacing between sensors; they also denote the six possible pairings for relative azimuth calculations. Labeled beside each double ended arrow are the overall coherence derived angle averaged statistics calculated from the experimental data for each unique pair of seismometers.

The averaged statistics for all three of the pairs involving the PIT sensor (PIT-POST, PIT-HIGH, and PIT-ANMO) are all approximately the same. All three angle standard deviations are about 0.3° and the average spans are in the 2° to 3° range. The coherence standard deviations are all three approximately 0.02 and the span in the coherence values are all about 0.11. This result indicates that the three sets of data are dominated by the characteristics of the PIT sensor and not by the spacing between the sensor systems. Since the PIT sensor is nearest the surface, surface noise in the PIT sensor data is the likely source that makes all three sets of statistics so nearly equal.

The statistics calculated from the POST-ANMO and POST-HIGH pairings are significantly better than those for the PIT pairings. The two angle standard deviations are about 0.1° and the span of the azimuths are both about 0.5°. The average coherences are higher with smaller standard deviations and smaller spans. These improved statistics are probably due to reduced surface noise in the POST sensor due to its 20 foot burial.

Finally by far the best statistics originate from the ANMO-HIGH pair of sensors both of which are installed at relatively large depths. Once again this result can be explained by noise reduction with depth.

The results from the posthole experiment reveal some important facts. When attempting to determine the orientation of a borehole sensor system using correlation and coherence calculations between the rotated borehole components and a reference surface instrument, it is important that the surface instrument be carefully installed to reduce potential noise sources in this sensor system. Separation distances up to the order of 500 vertical feet do not appear to degrade the precision of the calculated relative azimuth angle. Single data segment estimated azimuths may deviate from the many segment average azimuth by up to 1.5° depending on which segment is selected. Averaging over many segments increases the probability that the result is more precise.

The accuracy of coherence determined relative azimuth measurements appears to be limited by the relative alignment of the horizontal components within the three component sensor package. It makes sense that one will never be able to align such a package more accurately than the individual components are aligned within. Therefore, with current instrumentation, horizontal component alignment accuracy will be limited to somewhere in the ±0.5° to ±1.0° range regardless of the method chosen or the alignment procedure.

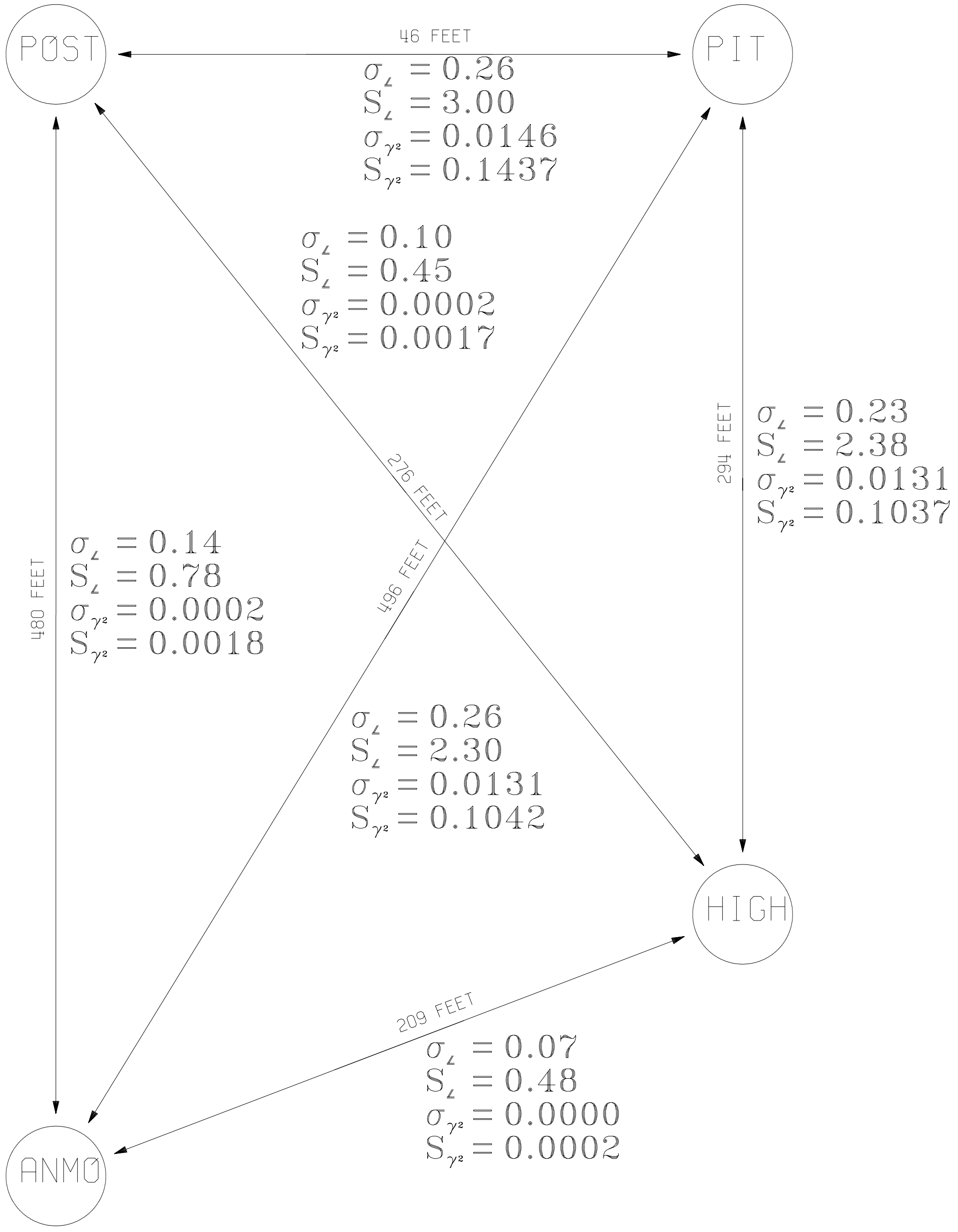

Figure 8.36 Compilation of the coherence derived azimuth statistics for all six possible combinations of sensor systems. The symbol $\sigma_\angle$ is the average of all four of the standard deviations of the angles in degrees between each pair of sensor systems, $S_\angle$ is the span of the estimated azimuths in degrees, σ_{γ^2} is the average of all four standard deviations of the coherence between each pair of sensor systems, and S_{γ^2} is the span of the calculated coherences. (Not to scale)

8.10 REFERENCE SEISMOMETER INSTALLATION PRECISION EXPERIMENT

The absolute accuracy of the coherence determined azimuth of the borehole seismometer depends on several independent factors in the alignment process. One of these factors is the accuracy with which the reference sensor can be aligned in a known direction. As currently envisioned, this operation usually first involves the drawing of a line, on the floor of the vault or on the seismometer pier, whose azimuth is known (usually this line is oriented geographic north-south). The sensitive axis of the sensor is then aligned with the line on the floor by lining up reference marks on the outside of the sensor housing parallel to the line on the floor or on the pier. Both the initial drawing of the line on the floor or pier and the alignment of the sensitive axis of the reference instrument parallel to that line are subject to errors. It is important that the approximate probable errors in these operations be estimated if the overall accuracy of the experimental technique is to be estimated.

The ASL posthole experiment arrangement provided the basis for conducting an experimental investigation into how repeatably a reference sensor could be installed parallel to a fixed reference line. The data processing results discussed in the previous subsections of Section 8 firmly establish the relative azimuthal positions of the horizontal components of the four sensors. Thus, if one of the sensors is physically rotated, we should be able to measure the degree of this rotation by calculating the new position relative to the remaining three sensors, which we assume to have not been moved.

An experiment in which several individuals installed the PIT sensor parallel to the same line was conducted to obtain an estimate of the angular spread in the azimuth alignment one might expect from more than one installation of the reference sensor. Each person installed the reference sensor once and attempted to align the sensor parallel to the same line. We should note that the installation operation was slightly more complicated than simply aligning the sensor over a line drawn on the floor immediately beneath the sensor. The reference line was drawn on opposite sides of the top of the pit on the pit rim whereas the sensor was installed on the bottom of the pit which was 5' below the rim. Therefore, each installer was left to his own devices to transfer the reference line from the rim of the pit to the site of the actual installation. A certain amount of innovation was required and the individuals involved utilized different methods for achieving the orientation. However, this situation is probably somewhat typical of real installation problems which will be encountered in the field; each field site is unique and innovation on the part of the field personnel is essential to achieving the final operating configuration.

The results of this experiment are summarized in Tables 8.28 and 8.29 in which the alphabetical column headings denote different installations by different people. The row titles in both tables denote different relative azimuths calculated between the horizontal components of the sensors (see the fourth paragraph of Section 8 for an explanation of the terminology). Table 8.28 contains the raw coherence calculated intercomponent azimuths for all 9 installations. If all of the installers had been successful in perfectly aligning the reference sensor with the reference line on the rim of the pit, and if none of the reference sensors have moved, and if the coherence based azimuth calculation algorithm were perfect, all of the azimuths in each row of the table would be exactly equal. Obviously, from the data in Table 8.28, either all of the installations were not exactly aligned with the line and/or the reference sensors somehow moved, and/or the coherence algorithm was not perfect. Note that, since only the PIT sensor was physically moved, only those azimuths involving a reference to the PIT sensor in Table 8.28 should have changed purely as a result of an alignment change by the installer. This is approximately true because all of the calculated relative azimuths not involving the PIT sensor (all of the azimuths below the double line in the middle of Table 8.28) are nearly equal. In contrast, the azimuths involving the PIT sensor (all of the azimuths contained in rows above the double line in the middle of Table 8.28) show a much greater variation between individual installers.

The relative changes in the azimuths from installation to installation are presented in Table 8.29. To derive the data in this table, the average of a particular azimuth over all 9 installations was utilized as a reference for calculating the deviation of a particular azimuth. Thus, from Table 8.29, the calculated relative azimuth between the PIT north and the POST north in installation A was $0.53°$ larger than the over all average azimuth for the 9 installations etc..

The changes in the various azimuths contained in Table 8.29 are much easier to visualize than the raw azimuths of Table 8.28 First a few words about the character of Table 8.29. If the three non PIT sensors have not moved (they were not knowingly moved during the experiment) and if the coherence azimuth calculation algorithm is perfect, all of the azimuth changes below the double lines in the middle of Table 8.29 should equal $0.00°$. Note that all of these changes are quite small (the largest calculated change is $0.46°$ and the average change is $0.08°$); this fact supports the assumption that the three sensors involved have not moved and that the algorithm produces quite reproducible values for all of the azimuths involved. Thus, the calculated changes in the relative azimuths between the three stationary sensors are as we should expect them to be: they are all small approaching zero.

The changes in azimuths involving the PIT sensor in any one installation (changes in any particular column above the double lines in the middle of Table 8.29) should be equal in magnitude but they should be opposite in sign as follows. Relative azimuth PIT N > POST N is the $112.18°$ angle in Figure 8.2 whereas relative azimuth POST N > PIT N is the $248.9°$ angle in the same figure. Now if the PIT sensor is moved a little bit clockwise in the figure, relative azimuth PIT N > POST N will increase and relative azimuth POST N > PIT N will decrease by the same amount. The same is true for relative azimuths PIT N > POST E and POST N > PIT E. Thus, the changes in azimuth in each column above the double lines in the middle of Table 8.43 should theoretically be equal in absolute value but of alternating sign as one reads up or down a particular column.

Note that the signs of the changes do alternate as expected for installations in which the azimuth deviates the most from the average value (installations C, H, and I). Installations A and E have one azimuth which violates the sign alteration ideal case. The azimuths for installations D, F, and G are so close to their corresponding average values that the deviations in their azimuths are equal to or less than errors in the calculated azimuth arising from the apparent inaccuracy in the azimuth calculating algorithm and/or noise fluctuations in the recorded data which contaminate the azimuth data results. These results indicate that the precision of the azimuth measurement technique is probably limited to $0.5°$ or so when applied to data from the PIT sensor (this is the noisiest of the four sensors).

The "AVE PIT DEV" row in Table 8.29 is the average deviation from the average azimuth for each of the installations. Each of these averages is derived by calculating the average value of the absolute value of all of the azimuth deviations in the column above each "AVE PIT DEV' result. This number is a best estimate of the magnitude of the deviation of the orientation of the sensor in a particular installation from the average orientation for all 9 installations.

The object of this experiment was to obtain an example of the spread in azimuths which might result from the attempted installation of a reference seismometer parallel to a common reference line by several individuals. The average changes in row "AVE PIT DEV" in Table 8.29 are the numbers we are seeking; they denote the accuracy of each installation with respect the artificially created true azimuth which we chose to be the average azimuth of all 9 installations. From the averages in the "AVE PIT DEV" row, the total span of the average deviations of the 9 installations is $2.60°$. This is true because the sense of the alternating signs in columns C and I are opposite; this means that the calculated azimuths in column C are in the opposite direction from average azimuths than are the calculated azimuths in column I. Therefore, the two average deviations in columns C and I add in calculating the span.

	A	B	C	D	E	F	G	H	I
PIT N → POST N	112.18	111.33	110.84	111.81	112.33	111.66	112.14	111.22	114.05
POST N → PIT N	248.90	249.68	249.92	249.00	249.50	249.48	249.00	1249.90	247.47
PIT N → POST E	21.42	20.71	20.52	21.45	21.93	21.87	21.32	20.42	22.64
POST N → PIT E	157.50	158.27	158.64	157.71	157.19	157.99	157.60	158.41	155.88
PIT N → HIGH N	72.72	72.05	71.71	72.46	73.26	72.39	72.65	72.02	74.40
HIGH N → PIT N	287.67	288.37	288.66	287.84	287.27	287.35	287.54	288.76	286.58
PIT N → HIGH E	341.47	340.59	340.29	341.22	341.67	341.72	341.54	340.09	342.85
HIGH N → PIT E	198.11	198.94	199.27	198.39	197.75	198.53	198.26	199.04	196.23
PIT N → ANMO N	77.84	77.16	76.83	77.55	78.37	77.60	77.74	77.19	79.74
ANMO N → PIT N	283.69	284.47	284.83	284.02	283.32	284.55	283.51	284.97	282.73
PIT N → ANMO E	346.55	345.70	345.38	346.24	246.77	345.67	346.73	345.07	347.65
ANMO N → PIT E	192.98	192.70	192.95	192.19	191.57	192.24	192.08	192.75	190.03
HIGH N → POST N	41.05	41.13	41.08	41.14	41.05	41.09	41.18	41.22	41.13
POST N → HIGH N	320.14	320.15	320.20	320.21	320.21	320.30	320.14	320.26	320.44
HIGH N → POST E	308.37	308.27	308.33	308.40	308.29	308.35	308.18	308.34	308.39
POST N → HIGH E	230.45	230.46	230.41	230.36	230.44	230.25	230.54	230.21	230.04
POST N → ANMO N	325.21	325.24	325.33	325.17	325.32	325.47	325.20	325.40	325.69
ANMO N → POST N	33.98	33.94	33.87	33.94	33.98	33.99	34.07	34.07	33.97
POST N → ANMO E	235.55	235.56	235.47	235.39	235.53	235.23	235.73	235.19	234.94
ANMO N → POST E	305.28	305.27	305.36	305.49	305.28	305.40	305.11	305.37	305.44
ANMO N → HIGH N	355.06	355.07	355.03	355.09	355.04	355.01	355.06	355.00	354.90
HIGH N → ANMO N	5.29	5.32	5.36	5.31	6.35	5.39	6.32	6.39	6.48
ANMO E → HIGH E	264.78	264.76	264.79	264.83	264.78	264.86	264.66	264.89	265.01
HIGH N → ANMO E	274.86	274.86	274.83	274.27	274.86	274.75	274.95	274.74	274.65

Table 8.28 Coherence derived relative azimuths of the horizontal components of the four posthole experiment sensors after 9 unique installations (A through I) of the PIT sensor system. The remaining three sensors were not moved. All azimuths are in degrees.

	A	B	C	D	E	F	G	H	I
PT N → POST N	0.23	-0.62	-1.11	0.14	0.38	-0.29	0.19	-0.73	2.10
POST N → PIT N	-0.31	0.47	0.71	-0.21	0.29	0.27	-0.21	0.69	-1.74
PIT N → POST E	0.06	-0.65	-0.84	0.09	0.57	0.51	-0.04	-0.94	1.28
POST N → PIT E	-0.19	0.58	0.95	0.02	-0.50	0.30	-0.09	0.72	-1.81
PIT N → HIGH N	0.09	-0.58	-0.92	-0.17	0.63	-0.24	0.02	-0.61	1.77
HIGH N → PIT N	-0.11	0.59	0.88	0.06	-0.51	-0.43	-0.24	0.98	-1.20
PIT N → HIGH E	0.20	-0.68	-0.98	-0.05	0.40	0.45	0.27	-1.18	1.58
HIGH N → PIT E	-0.17	0.66	0.99	0.11	-0.53	0.25	-0.02	0.76	-2.05
PIT N → ANMO N	0.06	-0.62	-0.95	-0.23	0.59	-0.18	-0.04	-0.59	1.96
ANMO N → PIT N	-0.32	0.46	0.82	0.01	-0.69	0.54	-0.50	0.96	-1.28
PIT N → ANMO E	0.35	-0.50	-0.82	0.04	0.57	-0.53	0.53	-1.13	1.45
ANMO N → PIT E	0.81	0.53	0.78	0.02	-0.60	0.07	-0.09	0.58	-2.14
AVE PIT DEV	0.24	0.58	0.90	0.10	0.52	0.34	0.19	0.82	1.70
HIGH N → POST N	-0.07	0.01	-0.04	0.0-2	-0.07	-0.03	0.06	0.10	0.01
POST N → HIGH N	-0.08	-0.07	-0.02	0.12	0.01	0.08	-0.08	0.04	0.22
HIGH → POST E	-0.05	-0.05	0.01	0.08	-0.03	0.03	-0.13	0.02	0.07
POST N → HIGH E	0.10	0.11	0.06	0.01	0.09	-0.10	0.19	-0.14	-0.31
POST N → ANMO N	-0.13	-0.10	0.01	-0.17	-0.02	0.13	-0.14	0.06	0.35
ANMO N → POST N	0.03	-0.01	-0.08	-0.01	-0.06	-0.04	0.04	0.12	0.02
POST N → ANMO E	0.15	0.16	0.07	-0.01	0.13	-0.17	0.33	-0.21	-0.46
ANMO N → POST E	-0.05	-0.06	0.03	0.16	-0.05	0.07	-0.22	0.04	0.11
ANMO N → HIGH N	0.03	0.04	0.00	0.06	0.01	-0.02	0.03	-0.03	-0.13
HIGH N → ANMO N	-0.07	-0.04	0.00	-0.05	-0.01	0.03	-0.04	0.03	0.12
ANMO N → HIGH E	-0.04	-0.06	-0.03	0.01	-0.04	0.04	-0.16	0.07	0.19
HIGH N → ANMO E	0.05	0.05	0.02	-0.02	0.05	-0.06	0.14	-0.07	-0.16
AVE NO PIT DEV	0.07	0.06	0.03	0.06	0.05	0.07	0.13	0.08	0.18

Table 8.29 Changes in the coherence derived relative azimuths of the horizontal components of the four posthole experiment sensors after 9 unique installations (A through I) of the PIT sensor system. The remaining three sensors were not moved. All changes in azimuth are in degrees.

	AVE	SPAN
PIT N > POST N	111.95	3.21
POST N > PIT N	249.21	2.54
PIT N > POST E	21.36	2.22
POST N > PIT E	157.69	2.76
PIT N > HIGH N	72.63	2.69
HIGH N > PIT N	287.78	2.82
PIT N > HIGH E	341.27	2.76
HIGH N > PIT E	198.28	3.04
PIT N > ANMO N	77.78	2.91
ANMO N > PIT N	284.01	2.24
PIT N > ANMO E	346.20	2.58
ANMO N > PIT E	192.16	2.94
HIGH N > POST N	41.12	0.17
POST N > HIGH N	320.22	0.34
HIGH N > POST E	308.32	0.22
POST N > HIGH E	230.35	0.50
POST N > ANMO N	325.34	0.52
ANMON > POST N	33.95	0.20
POST N > ANMO E	235.50	0.79
ANMO N > POST E	305.33	0.38
ANMO N > HIGH N	355.03	0.19
HIGH N > ANMO N	5.36	0.19
ANMO N > HIGH E	264.82	0.35
HIGH N > ANMO E	274.81	0.30

Table 8.30 Averages and spans of the 24 relative azimuths for all 9 installations. All angles are in degrees.

9 ON THE ABSOLUTE ACCURACY OF COHERENCE BASED AZIMUTH ESTIMATION

The absolute accuracy of the coherence based azimuth determination technique is difficult to determine because a standard is needed with which to compare. The coherence method appears to be fairly accurate so a very accurate standard is required if one is to quantitatively evaluate the accuracy of the coherence method. It is very difficult to establish an independent means of determining the relative azimuths of two instruments, which is more accurate than the method under evaluation, especially if the two instruments are separated by a significant distance. The only feasible approach appears to be to carefully physically position the two instruments in known orientations and then to compare the coherence derived relative azimuthal positions with the hopefully known azimuthal positions.

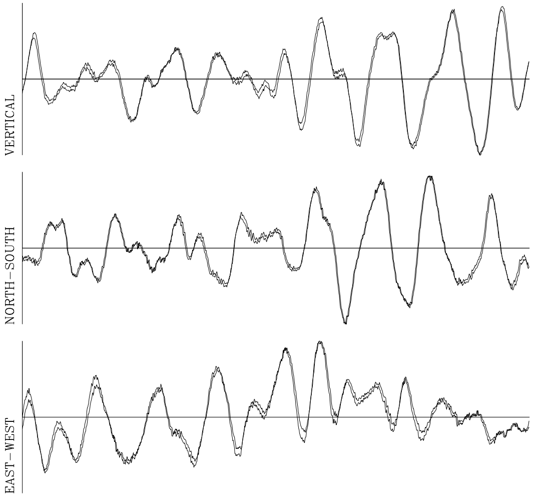

Figure 9.1 Overlays of one minute of the raw 20 sps time series data recorded with both STS-2 sensors installed in the vault with their horizontal components aligned in parallel.

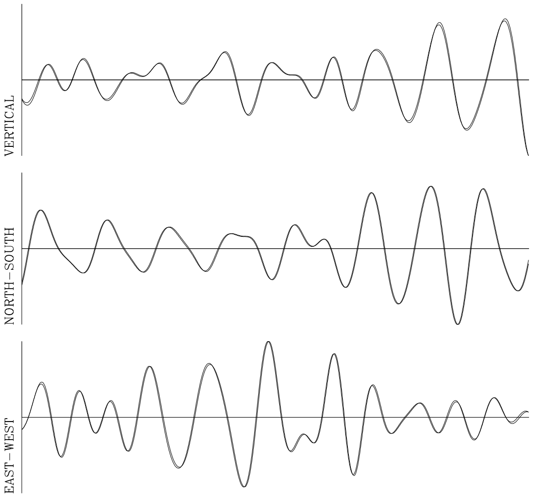

Figure 9.2 Overlays of one minute of the six second bandpass filtered 20 sps time series data recorded with both STS-2 sensors installed in the vault with their horizontal components aligned in parallel.

In the late summer of 1999, an experiment was conducted by Holcomb, Hutt, and Sandoval at ASL with the intent of demonstrating the accuracy of the coherence based azimuth determination technique when applied to a semi real world situation which approximated a simulated borehole installation. A line was established in the ASL subsurface vault using standard surveying techniques and a parallel line was transferred to a site near the crest of the ridge south of the ASL vault using the same technique. These two sites were approximately 372 horizontal feet and 200 vertical feet apart. A STS-2 sensor system was installed in the ASL subsurface vault and carefully oriented with respect to that line and another STS-2 sensor that was installed on top of the ridge in a shallow pit in the ground was also carefully oriented with respect to that line. This situation established two sensors whose relative orientation was known fairly precisely that were separated by 200 vertical feet as is approximately the case when the coherence azimuth determination technique is applied to a 100 meter deep borehole.

The installation in the vault was relatively straightforward. The STS-2 sensor (serial number 39911) was aligned with respect to the line drawn on the floor of the vault by carefully positioning two of the feet on the bottom of the seismometer so that they both rested exactly on the line. All three channels of data from the vault sensor was recorded on a Quanterra Q680 24 bit data recording system. This sensor will be referred to as the borehole sensor.

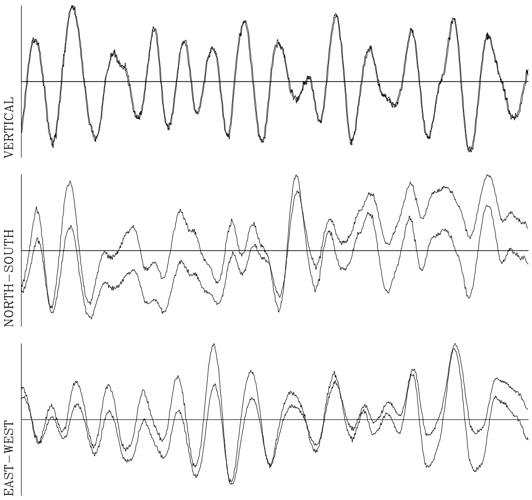

Figure 9.3 Overlays of one minute of the raw 20 sps time series data recorded with one of the STS-2 sensors installed in the vault and the other STS-2 sensor installed near the ridge crest with their horizontal components aligned in parallel.

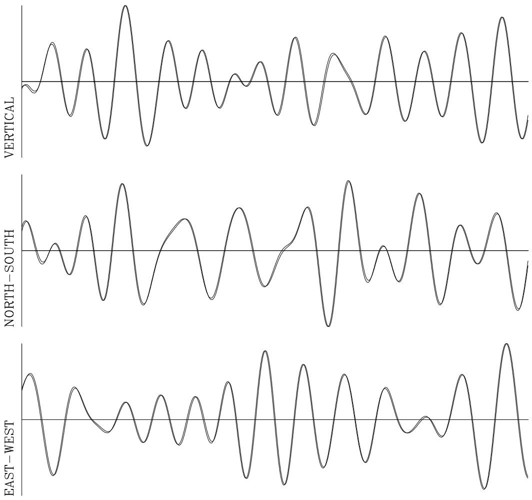

Figure 9.4 Overlays of one minute of the six second bandpass filtered 20 sps time series data recorded with one of the STS-2 sensors installed in the vault and the other STS-2 sensor installed near the ridge crest with their horizontal components aligned in parallel.

The pit near the ridge line was approximately 1 to 1.5 feet deep and only about 2 to 3 inches on the radius larger than the STS-2 diameter. It was dug in the gravely decomposed granite soil mixture in the vicinity (within 5 to 15 feet) of several bedrock outcrops; the depth to bedrock beneath the sensor was unknown. The bottom of the pit was leveled with loosely compacted fine gravel soil and a 1 inch thick, 10 inch diameter aluminum plate was placed on the bottom of the pit. The plate had 3 shallow indents 7.5 inches apart machined into the top surface which matched the foot pattern on the bottom of the STS-2. Two of the indents were very carefully aligned parallel with the line in the vault with the aid of a surveying transit and the STS-2 (serial number 39912) was then positioned to align its feet with the three indents. The pit was then covered with a plywood lid and the fine gravely decomposed granite soil mixture was piled on the lid to a depth ranging from 1 to 5 inches deep. This arrangement provided significant thermal isolation of the sensor and prevented noise generation by direct wind action on the sensor. The north component of this sensor will be referred to as the reference sensor. All three channels of data from the pit sensor were recorded on a Quanterra 4120 24 bit data recording system which was powered by a 110 ampere hour lead acid storage battery. This battery also powered the STS-2 sensor; battery capacity limited continuous data recording to about 30 hours per charge.

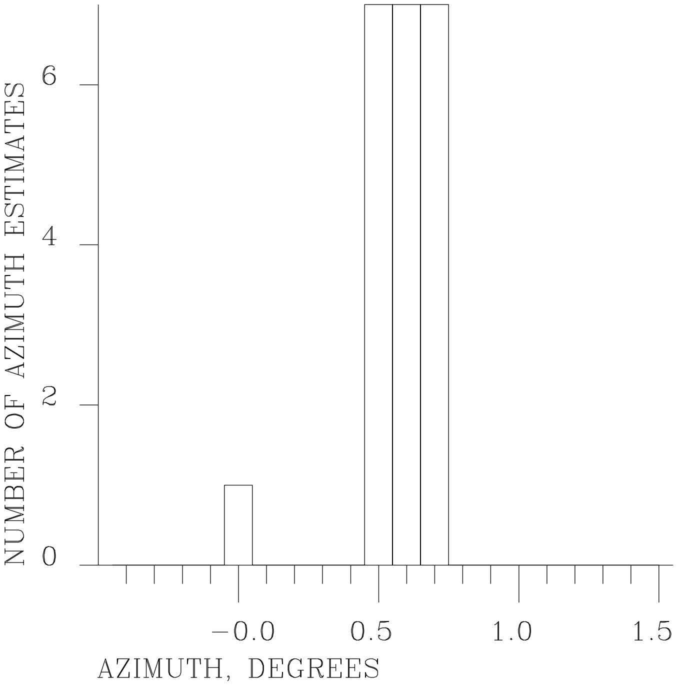

Figure 9.5 Histogram of the 22 azimuth estimates calculated from the vault installation with the borehole components physically lined up in space with the reference sensor.

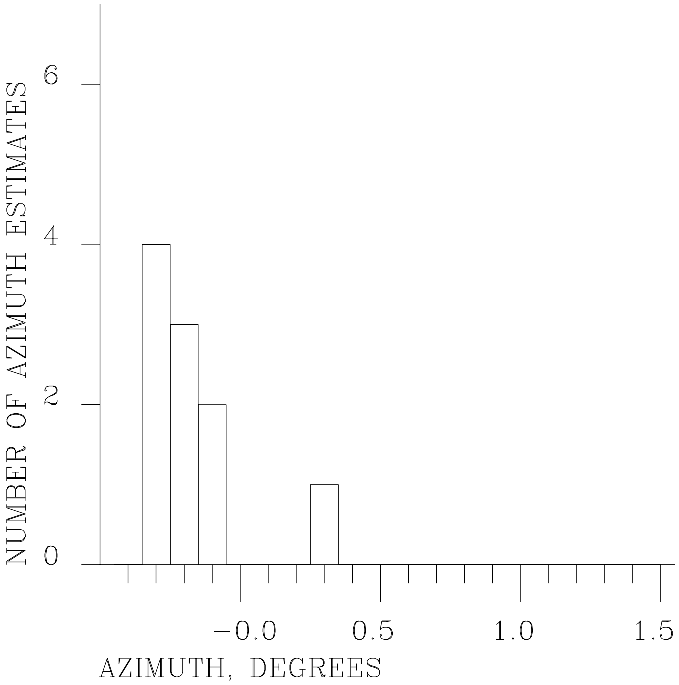

Figure 9.6 Histogram of the 12 azimuth estimates calculated from the ridge installation with the borehole components physically lined up in space with the reference sensor.

The experiment was conducted in four stages as follows.

First, both STS-2 sensors (serial numbers 39911 - the borehole sensor, and 39912 - the reference sensor) were installed very near to one another (about 2 feet spacing) in the vault and were carefully oriented with their horizontal axis aligned parallel with respect to the same straight line. Two days of data was recorded and processed to establish that all of the cabling and data recording software were working properly. Serial number 39911 was treated as the borehole sensor throughout the experiment

A short one minute long time series from the horizontal components from this installation is shown in Figure 9.1 as an example of the character of the data. The time series in this figure and all of the time series in figures in this section start at 0 hours GMT. In Figure 9.1, the time series for the vertical, north, and the east components from both instruments have been overlaid to facilitate comparison of the data. The six second microseisms dominate the plots with evidence of some longer period incoherent noise. Note that the appearance of the six second microseisms are very similar but not identical in the outputs of both instruments as one should expect because the components of the two instruments are aligned in parallel. Figure 9.2 contains a plot of the same data after applying a 4 to 10 second bandpass Bessel digital filter to the time series. On the scale in this figure, it is virtually impossible to discern any difference between the filtered outputs of the two instruments in this passband. Slight differences can be seen in the first negative cycle of the outputs of the two vertical channels and in the very last part of the east channel outputs. Thus, the six second microseism peak provides a source of a highly coherent input signal to both instruments if they are installed near one another

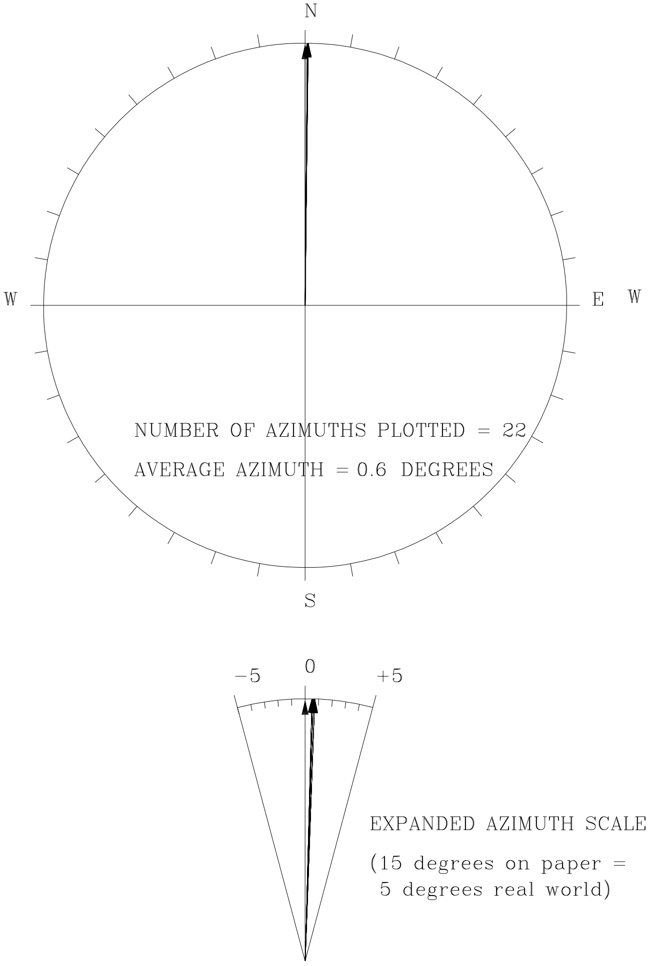

Figure 9.7 Relative azimuth estimates calculated from the vault installation with the borehole components physically lined up in space with the reference sensor.

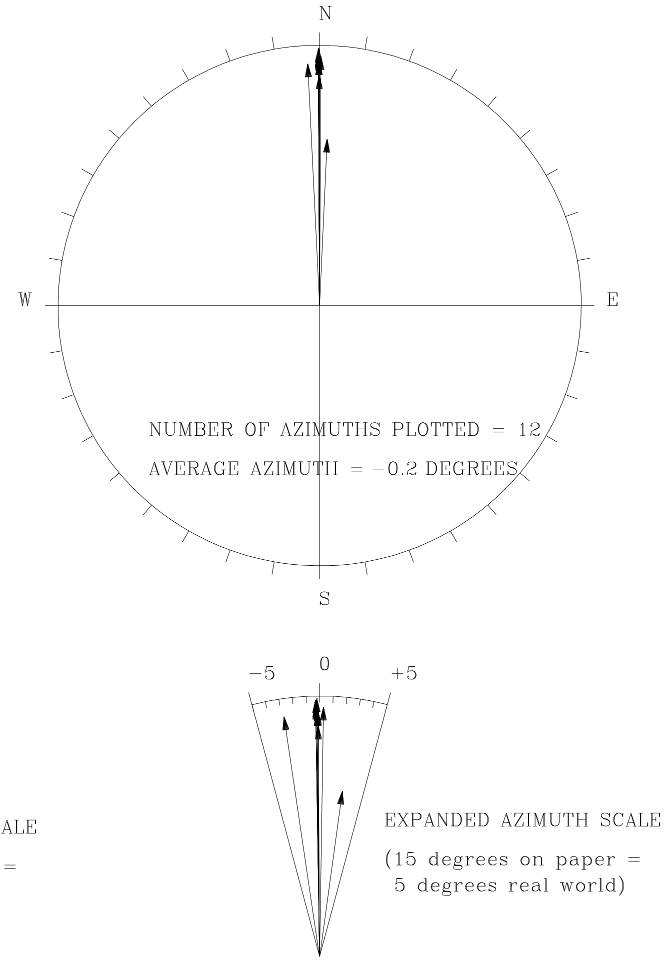

Figure 9.8 Relative azimuth estimates calculated from the ridge installation with the borehole components physically lined up in space with the reference sensor.

This configuration was operated over a weekend thereby providing a long time series for azimuth analysis. Azimuth estimates were calculated from twenty two 10,000 second long consecutive time segments and a histogram of the results is shown in Figure 9.5. Twenty one of the estimates are tightly grouped in the +0.5° to +0.7° range while there is one outlier at 0.0°. It is noteworthy that the outlier was calculated from a time segment during which the energy from an earthquake was dominating the time series. However, there is no known reason why energy from an earthquake should influence the azimuth results. The same coherence derived azimuth estimates are geometrically replotted in the upper part of Figure 9.7. All twenty two of the estimates are so close that they appear to be one arrow in the figure. Therefore, they are replotted in the bottom portion of Figure 9.7 in which the angular scale has been expanded by a factor of 3; that is, $1°$ of real azimuth equals $3°$ on the paper in Figure 9.7. On this scale, the outlier azimuth estimate is just barely visible. As indicated in the figure, the average of the twenty two azimuth estimates is $+0.6°$ clockwise looking down the borehole from the reference sensor.

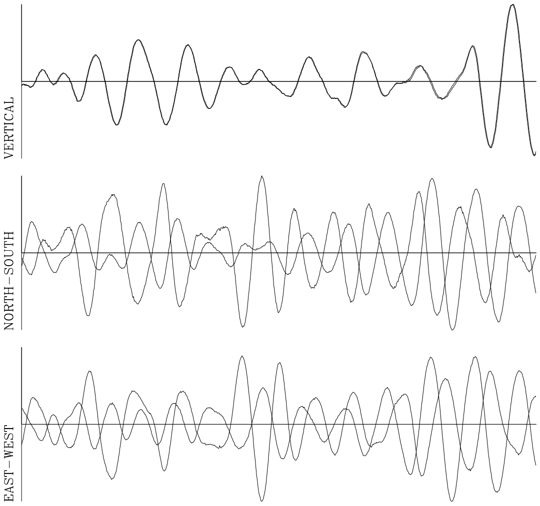

Figure 9.9 Overlays of one minute of the raw 20 sps time series data recorded with both STS-2 sensors installed in the vault with their horizontal components positioned 120^o apart.

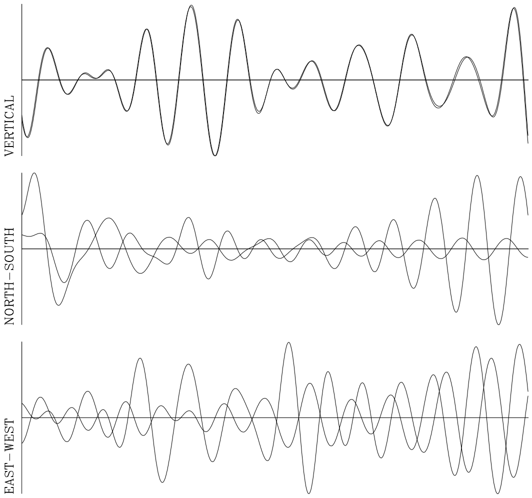

Figure 9.10 Overlays of one minute of the six second bandpass filtered 20 sps time series data recorded with both STS-2 sensors installed in the vault with their horizontal components positioned 120^o apart.

The second stage of the experiment was to remove one of the STS-2 instruments (serial number 39912 - the reference sensor) from the vault and reinstall it in the pit near the top of the ridge with its horizontal components aligned in parallel to the horizontal components of the other STS-2 (serial number 39911 - the borehole sensor) which remained installed in the vault.

A short one minute long time series from this installation is shown in Figure 9.9 as an example of the character of the data. The raw data produced by the vertical components of the two sensors are very similar and overlay quite well. As one might expect, there is quite noticeable long period noise evident in the two horizontal components of the instrument that was installed in the pit near the ridge crest. Applying the 4 to 10 second bandpass Bessel filter to the time series produces the time series shown in Figure 9.10. The long period noise has been removed and all of the component time traces overlay very nicely. Thus, the six second microseism peak provides a source of a highly coherent input signal to both instruments even if they are not installed immediately side-by-side one another.

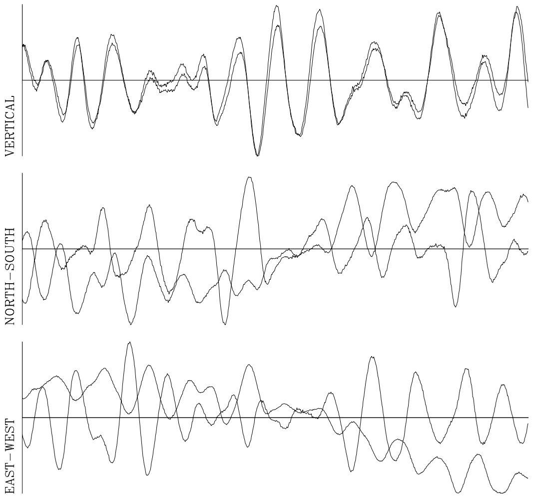

Figure 9.11 Overlays of one minute of the raw 20 sps time series data recorded with one of the STS-2 sensors installed in the vault and the other STS-2 sensor installed near the ridge crest with their horizontal components positioned 120^{o} apart.

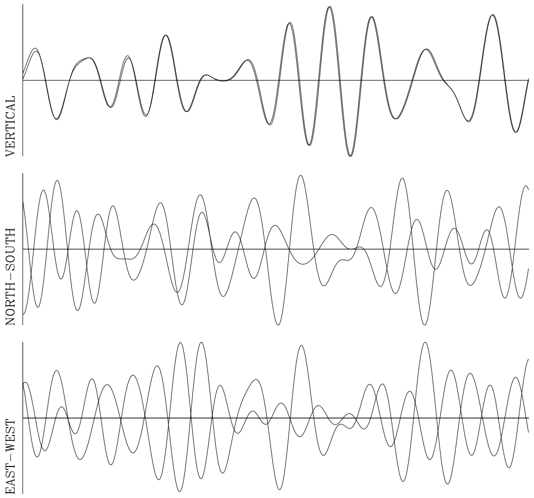

Figure 9.12 Overlays of one minute of the six second bandpass filtered 20 sps time series data recorded with one of the STS-2 sensors installed in the vault and the other STS-2 sensor installed near the ridge crest with their horizontal components positioned 120° apart.

Only twelve azimuth estimates could be calculated for this installation because the data recording time was limited by the amphour capacity of the battery that was used to power the ridge sensor and its data recording system. A histogram of ten of these estimates is shown in Figure 9.6. Two of the estimates significantly differed from those in Figure 9.6; they have not been plotted in the histogram to preserve the azimuth scale. It is significant to note that time segment used to calculate one of these outlier estimates contained energy from an earth quake just as was the case for the two sensors in the vault installation. The other outlier time segment did not contain any obvious anomalies. All twelve of the azimuth estimates have been geometrically plotted in the upper portion of Figure 9.8. In this figure, another feature of the geometric displays of the azimuth data becomes evident in this figure. The length of each arrow has been scaled by the value of the peak coherence calculated for that particular estimate; therefore, the lengths of each arrow ranges from 0 to 1. The same was true for the data that was presented in Figure 9.7, but in that figure all of the coherence values were so near to 1 for that data that all of the arrows appear to be the same length. The differences in arrow length are even more evident in the expanded azimuth scale display in the lower portion of Figure 9.8. Note that at least in this case, the lower coherence values for the two outliers could have been used as a criteria for discarding the outliers from the final averaged azimuth estimate if desired. The average of all twelve of the azimuth estimates was -0.2 degrees clockwise looking down the borehole from the reference sensor.

The third step of the experiment was to introduce an unknown (at least to the data analyst) azimuth in the borehole orientation. Hutt and Sandoval rotated the borehole sensor in the vault 120° clockwise looking down the borehole from its original orientation; the size of this rotation was not revealed to Holcomb who was to analyze the data from the experiment. This rotation was accomplished by simply aligning another pair of the STS-2 feet (the STS-2 has three feet that are located 120° apart) parallel to the same line in the vault. The new installation was first checked with another STS-2 reference sensor (serial number 39910) that was installed in the vault with its horizontal components aligned in the same direction as the original vault reference sensor (serial number 39912).

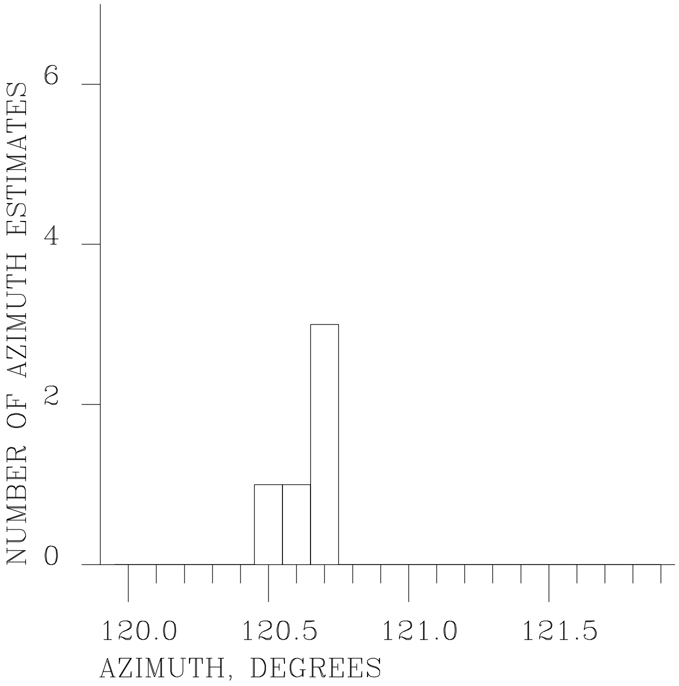

Figure 9.13 Histogram of the 5 azimuth estimates calculated from the vault installation with the borehole components rotated 120°clockwise looking down the borehole clockwise looking down the borehole from the reference sensor.

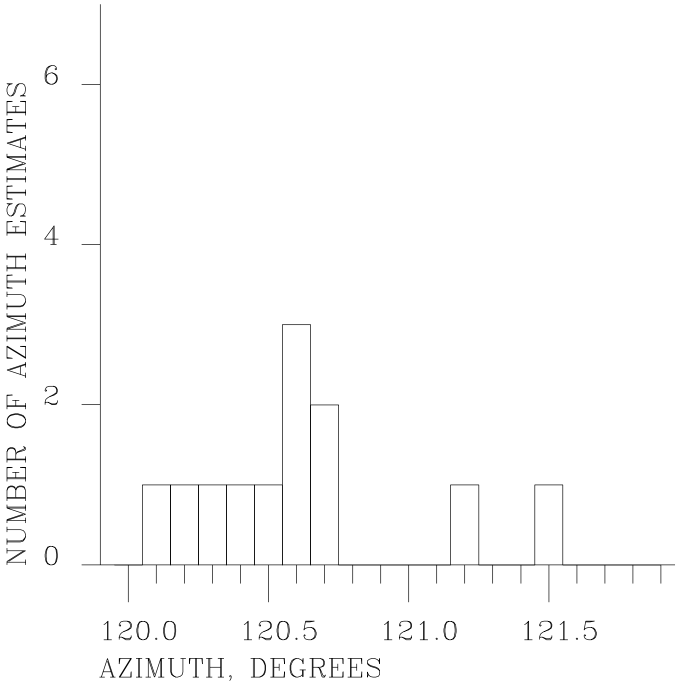

Figure 9.14 Histogram of the 12 azimuth estimates calculated from ridge installation with the borehole components rotated 120° clockwise looking down the borehole from the reference sensor.

Data was recorded overnight from this experimental configuration to provide a short time record for azimuth estimates. Figure 9.9 contains a component overlay plot example of the data recorded for this test. The vertical data overlays perfectly and there is considerable difference in the horizontal outputs of the two sensors as there should be because they are not aligned in space. The bandpass filtered overlays are shown in Figure 9.10 for completeness. The histogram of the estimated coherence derived relative azimuths is shown in Figure 9.13 and a geometric plot of the same data is contained in Figure 9.15. All five derived azimuths are tightly grouped near120° with an average value of 120.6° clockwise looking down the borehole from the reference sensor.

The fourth and final configuration of the experiment was to record data from the 120° rotated borehole STS-2 (serial number 39911) in the vault and the reference (serial number 39912) sensor in the pit near the ridge crest, which had been left undisturbed since it was installed in the pit in step two of this experiment.

A sample of the raw unfiltered 20 sps data recorded in this experiment is shown in the overlay plot of Figure 9.11 and the 4 to 10 second bandpass filtered overlay of the same data is in Figure 9.12. Horizontal long period noise is evident in the unfiltered data of Figure 9.11 and this noise is effectively removed by the filtering as shown in Figure 9.12. Twelve azimuth estimates were calculated from the recorded time series. Figure 9.14 contains a histogram of these estimates and Figure 9.16 presents the same data in a geometric azimuth plot. The average of the twelve calculated azimuths was 120.6° clockwise looking down the borehole from the reference sensor.

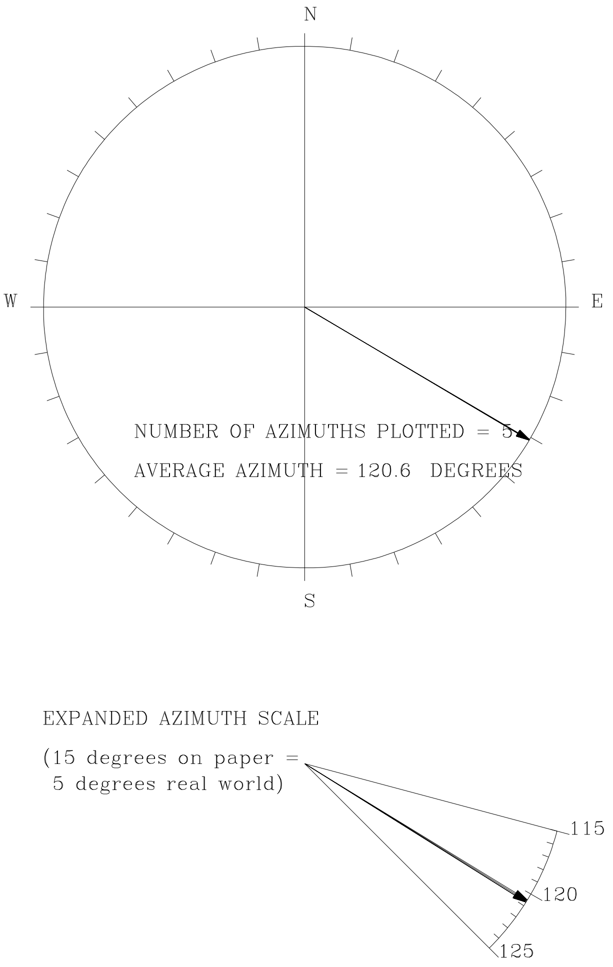

Figure 9.14 Relative azimuth estimates calculated from the vault installation with the borehole components rotated 120° clockwise looking down the borehole from the reference sensor.

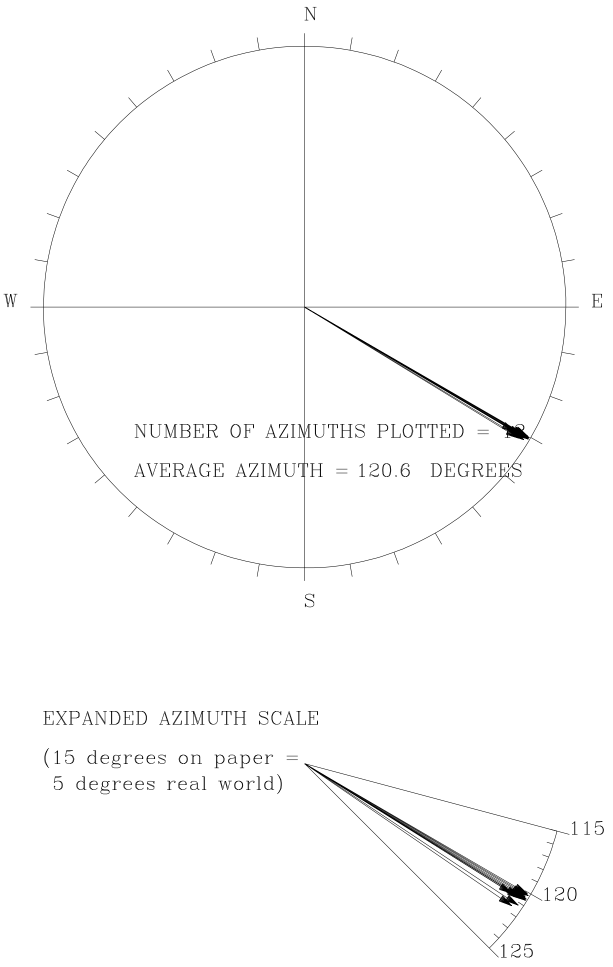

Figure 9.16 Relative azimuth estimates calculated from the ridge installation with the borehole components rotated 120° clockwise looking down the borehole from the reference sensor.

	TARGET RELATIVE AZIMUTH	MEASURED RELATIVE AZIMUTH	ERROR RELATIVE AZIMUTH
Experiment 1	0.0	0.6	0.6
Experiment 2	0.0	-0.2	-0.2
Experiment 3	120.0	120.6	0.6
Experiment 4	120.0	120.6	0.6

Table 9. 1 Summary of the results of the four relative azimuth experiments. The "TARGET RELATIVE AZIMUTH" is the relative azimuthal position that the experiment attempted to achieve by careful mechanical alignment of the two sensor systems. The "MEASURED RELATIVE AZIMUTH" is the experimentally derived relative azimuthal position of the two systems as derived by the coherence method. The "ERROR RELATIVE AZIMUTH" is the difference between the first two numbers.

Table 9.1 summarizes the results of the four experiments. In the table, the "TARGET RELATIVE AZIMUTH" is the relative azimuthal position to which we attempted to mechanically align the two sensors. We had no means of independently verifying the accuracy of this mechanical alignment in any of the four experiments. One might assume that the mechanical alignment in Experiments 1 and 3, in which the two sensors were aligned with respect to the same straight line drawn on the floor of the vault, would be nearly perfect. This is probably not true because of the finite width of the line on the floor, the finite width of the rounded tips of the feet on the bottom of the STS-2 sensors, and the difficulty of visually determining when the four feet are perfectly centered on the line. In addition, the true sensitive axis of the sensor is not necessarily perfectly aligned with the mechanical marks (in this case, the feet) on the outside of the sensor housing. Therefore, there was undoubtedly a finite unknown error in attempting to aligning the horizontal components of the two sensors absolutely parallel. The same sources of errors in the intended mechanical alignment were present in the other two experiments (experiments 2 and 4). In addition, there was a possible error in establishing the two hopefully parallel lines on the vault floor and in the bottom of the shallow pit near the ridge line.

In Table 9.1, "EXPERIMENT RELATIVE AZIMUTH" is the experimentally derived relative azimuth between the two systems in all four of the experiments and the "ERROR RELATIVE AZIMUTH" column in this table contains the difference between the intended relative azimuth and the coherence based measurement of the relative azimuth between the two systems. Note that although the numbers in this column are referred to as "ERROR", they do not necessarily represent errors that can be blamed solely on the coherence based relative azimuth determination method. Instead, they should be viewed as being representative of the summation of all of the possible errors in the experiment; they should be indicative of the overall accuracy with which the whole experiment was conducted.

This set of four experiments should be regarded as a singular example of how well the experiments can be performed. Many more experiments utilizing many different instruments and numerous independently established parallel lines under varying soil and rock types would be necessary to establish a firm statistical basis for the overall accuracy of these experiments. Even then, without an independent method for ascertaining the precise alignment of the widely separated sensors with significantly greater accuracy than the sought after accuracy of the coherence based azimuth estimates, it would be impossible to completely separate out the probable error due to the coherence based azimuth determination method from the other possible errors inherent in the experiments.

As summarized in Table 9.1, the results of the four experiments seem to promote the warm fuzzy feeling that the coherence derived azimuth method should yield azimuth estimates that are accurate to within less than a degree of the true relative azimuth between the borehole sensor and the reference sensor. This is well within the probable error of the mechanical alignment of the horizontal components of the sensors within their housings and quite adequate for ascertaining the azimuthal alignment of borehole sensors deployed in the field for modern data gathering purposes.

10 RMS SIGNAL LEVELS

While processing the azimuth data from the four experiments discussed in Section 9, it appeared that the amplitude of the six second microseisms had increased significantly between the aligned experiments and the experiments in which the sensors were 120° misaligned. Therefore, plots of the root mean square (RMS) signal levels in the six second band (4 to 10 seconds) were constructed for all four experimental periods of time in order that the relative six second amplitude could be studied. Each data point in these plots contains the RMS average of the signal over a fifteen minute interval sampled every fifteen minutes throughout the duration of each experiment.

Figure 10.1 contains plots of the RMS amplitude of the signals from both the borehole and reference sensors while they were both installed in the ASL vault with their horizontal components aligned in parallel in space. The curve labeled NS3X in the figure is the data from the borehole sensor (39911) and the curve labeled NS4X is the data from the reference sensor data (39912). The first thing to notice in this figure is that the two sensors appear to have different sensitivities. Investigations conducted as a result of this observation have subsequently revealed that the difference in signal levels is due to a difference in the sensitivity of the two Quanterra digital data recording systems (a Q680 and a Q4120) that were used to record the data from the two sensors. The relatively large time coincident increases in the RMS signal levels of all six components denote the arrival of event energy at the site. The relatively broad peak in increased RMS levels between about 1999,234,06:00:00 and about 1999,235,04:00:00 is probably due to an increase in the level of the six second microseism peak due to a source far removed from the site. Note that the RMS signals of the two vertical channels, the two north channels, and the two east channels track one another quite well throughout the test period; one should expect this to be the case because the two sensors were positioned very close together (about 1 foot apart) during this experiment.

To illustrate how closely the RMS signals from the three sets of components track one another, the ratios of the three sets of components are plotted in Figure 10.5. With the exception of an initial transient in the NS4X system, the ratios are essentially constant throughout the test duration with only small changes in the ratios the largest of which corresponds to the time period when event energy was highest. Note that the signal levels in both horizontal channels track one another about as well as the two vertical channels do as one would expect because the two sensors were installed so close together.

The RMS signal levels for the second experiment (borehole sensor in the ASL vault and reference on the ridge above the vault - horizontal components aligned in space) are shown in Figure 10.2. The presence of one large event during this time period is indicated by the high level RMS signal level on all six channels at about 1999,236,13:00:00. Once again, the difference in system sensitivity is evident (this discrepancy is due to a difference in the Quanterra digital data system gain). Note that the RMS signals for each pair of components do not track nearly as well as they did when both sensors were installed side-by-side in the vault. This fact is evident in Figure 10.2 and is enhanced in the RMS ratio plot in Figure 10.6. Note the much greater deviations in the RMS ratio plot in Figure 10.6 for the separated instrument installation as compared to the deviations in the RMS ratio plot for the adjacent instrument installation in Figure 10.5. One would logically argue that the lack of tracking in the signal levels in the separated instrument installation must be due the increased noise level in the ridge reference installation because the ridge installation lacks the superior environmental protection that the vault offers. However, the data does not support this argument as can be seen by comparing the RMS plots in Figure 10.2. Note that the RMS data from the vault installation exhibits larger fluctuations than does the same data from the ridge installation. This result is contrary to what is believed to be known about the probable sources of noise in the two types of installations. Rest assured that a painstaking search for errors in processing the data has been conducted in an effort to find an accidental swapping of the true sources of the data without success. We are left without an explanation for the inconsistency between the actual results and what we believe should be the case.

The RMS levels for the two sensors when they were installed in the vault with their horizontal components misaligned by 120° are plotted in Figure 10.3. Note that in Figures 10.3, 10.4, 10.7, and 10.8 the horizontal data from the borehole sensor (NS3X) has been rotated counterclockwise with software before calculating the RMS signal levels. The very large disturbance near the beginning of the time period was probably due to human activity in the vault. Here we encounter another anomaly because the gain of the north component of the reference sensor (NS4X) appears to be greatly reduced as compared with the gain of the other five components. A rough calculation indicates that the gain of the north-south channel is approximately a factor of 13.3 lower than it should be. Note that another sensor was used as the reference sensor for this part of the experiment (STS-2 serial number 39910); this was the only time that this sensor was used in this experiment. The gain of the north-south channel of serial number 39910 was checked at a later date and found to be within specifications. Therefore, the source of the apparent low gain indicated in Figure 10.3 remains unknown.

A comparison of the RMS signal levels in Figure 10.3 with those in Figures 10.1 and 10.2 indicates that the microseismic background at ASL did indeed increase significantly between the aligned and 120° misaligned portions of the experiment. The RMS levels in the 4 to 10 second band for the vertical component were about 2.6 times greater during the 120° experiment time period. The higher levels in the 6 second microseismic peak are probably due to the presence of hurricane Dennis that was hovering virtually stationary just off the east coast of North Carolina during this time period. The higher levels in the microseism peak means that the signal (the microseism peak is the signal in a coherence based azimuth measurement) was larger during the 120° misaligned portion of the experiment; this may be a possible explanation for the smaller spread in the azimuth estimates in the 120° misaligned measurements as compared with the aligned azimuth estimates. In other words, the signal-to-noise ratio was probably higher for the 120° misaligned experiment.

Another anomaly appears when the ratio of the RMS signals obtained from the 120° misaligned experiment while installed in the vault as shown in Figure 10.7. The rather large transient near the beginning of the recording time period is explainable because it was probably due to human activity in the vault. If this initial transient is ignored, the vertical and east-west RMS ratio data in Figure 10.7 is comparable to the corresponding RMS ratio data in Figure 10.5 as one would expect. However, the large deviations in the ratio of the RMS signals from the north-south component is in sharp contrast to the relatively constant ratios for the previous aligned vault data shown in Figure 10.5. Note that the vertical scale for the north-south RMS ratio in Figure 10.7 is about the same as that in the rest of the ratio plots (0.3 for the north-south component in Figure 10.7 as compared with 0.324 for the rest of the plots). Therefore, the variations in the north-south RMS ratio plot in Figure 10.7 are significantly larger than they are in the aligned vault data in Figure 10.5. These observations are contrary to what one would expect because the microseismic peak was higher during the time period shown in Figure 10.7; a higher signal should have generated a higher signal-to-noise ratio and corresponding smaller deviations in all of the RMS ratio plot. The low gain indicated in the north-south RMS level data in Figure 10.3 and the large variations in the north-south RMS ratio data of Figure 10.7 point to a possibly significant problem in the configuration of the experimental equipment for the 120° misaligned in the vault experiment. No reasonable explanation for the strange behaviors indicated in this data has been found. Suffice it to note that despite the anomalous behavior indicated in the RMS data, the azimuth estimates detailed in the previous section are very close to what was expected.

The RMS levels for the 120° misaligned ridge experiment are shown in Figure 10.4. Note that the RMS level in the 4 to 10 second band slowly decreases throughout the time period. The ratios of the RMS levels for this experiment are shown in Figure 10.8. All three of the RMS ratio plots compare favorably with the aligned ridge RMS ratio plots in Figure 10.6; in fact, the 120° misaligned ridge RMS signal levels seem to track each other slightly better than they did when the sensors were aligned.

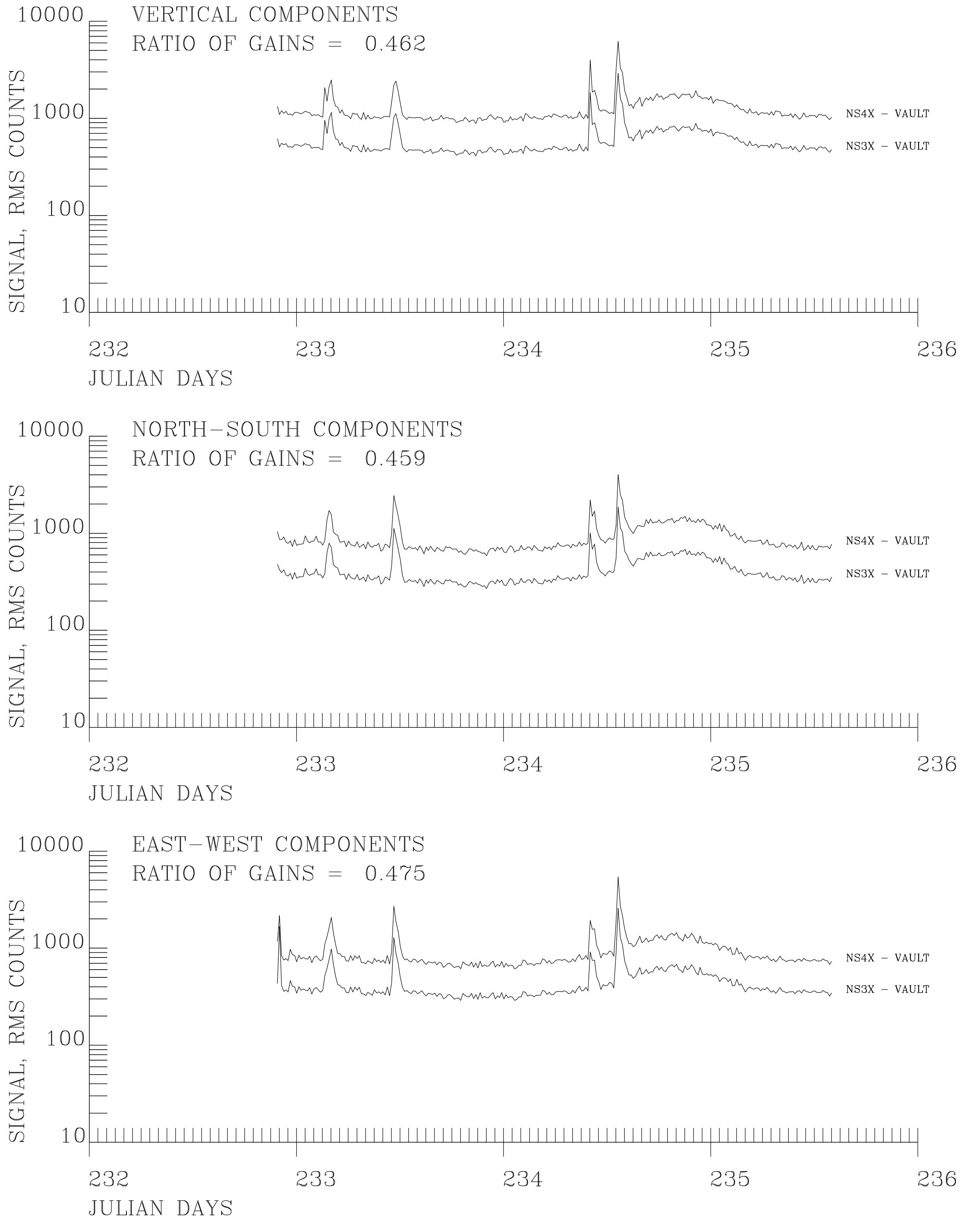

Figure 10.1 RMS signal levels in the 4 to 10 second band for both the borehole and reference sensors while they were both installed in the ASL vault with their horizontal components aligned parallel in space.

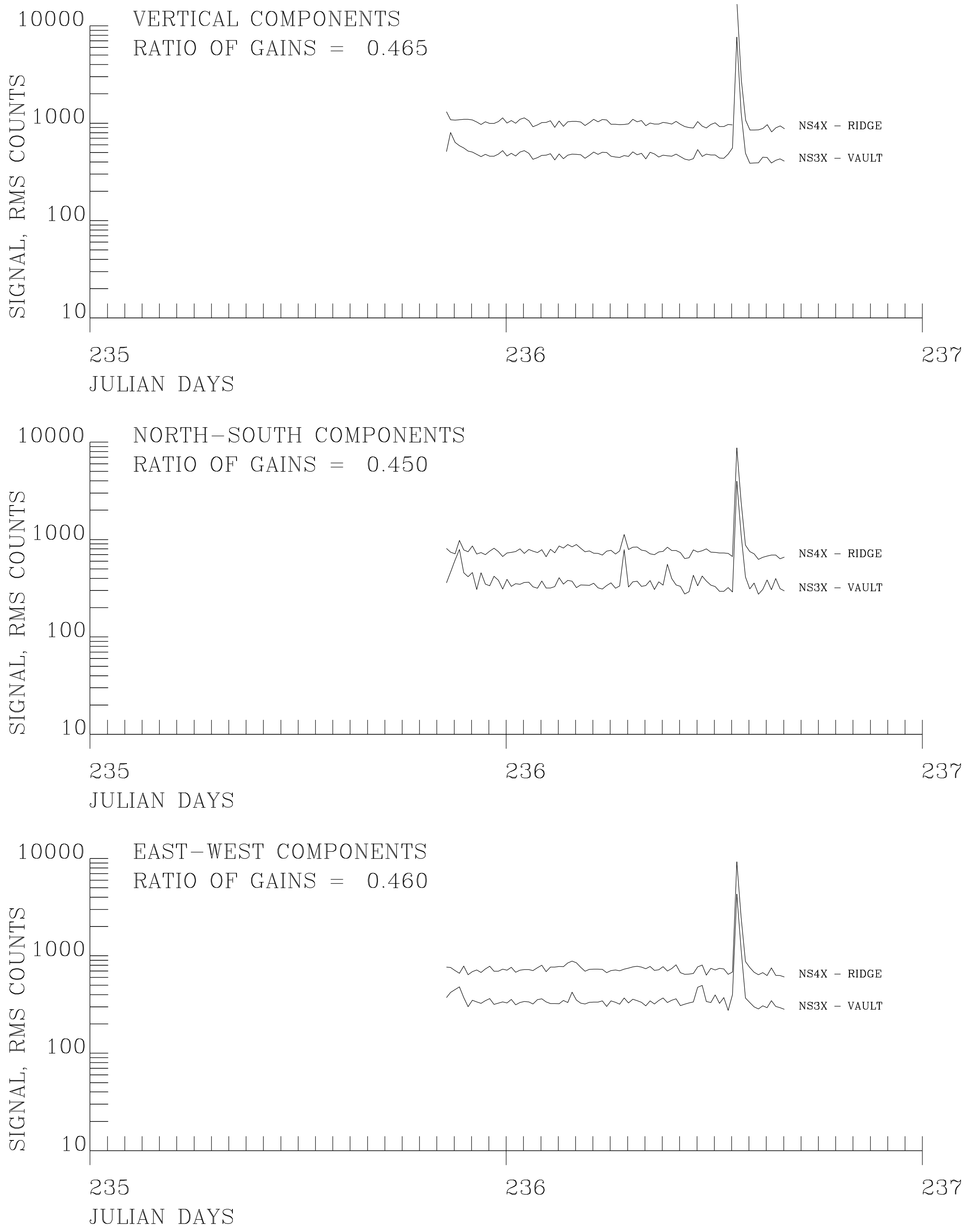

Figure 10.2 RMS signal levels in the 4 to 10 second band for both the borehole and reference sensors while the borehole sensor was installed in the ASL vault and the reference sensor was installed on the ridge above the vault with their horizontal components aligned parallel in space

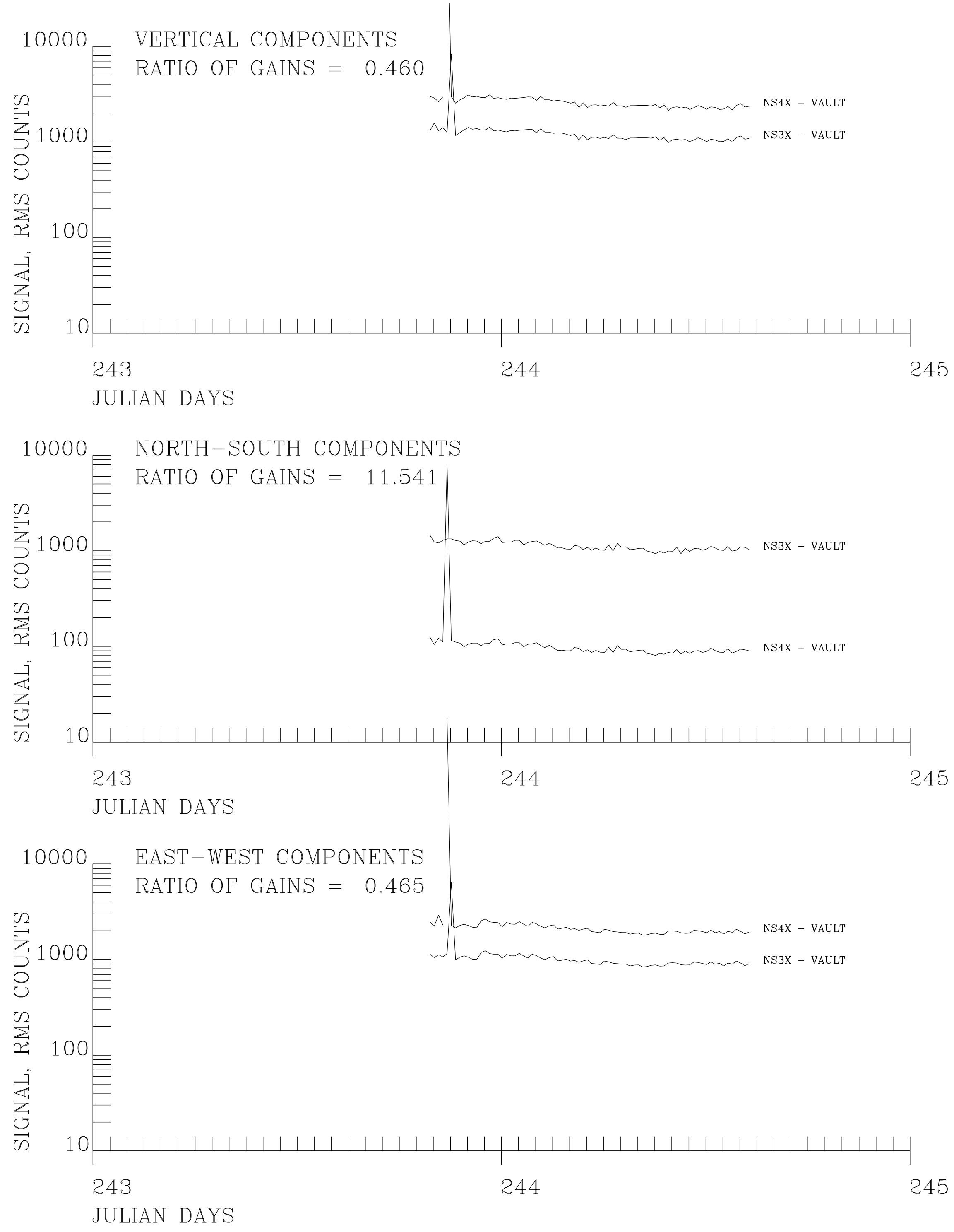

Figure 10. 3 RMS signal levels in the 4 to 10 second for both the borehole and reference sensors while they were both installed in the ASL vault with the horizontal components of the borehole sensor aligned 120^{o} clockwise from the reference sensor.

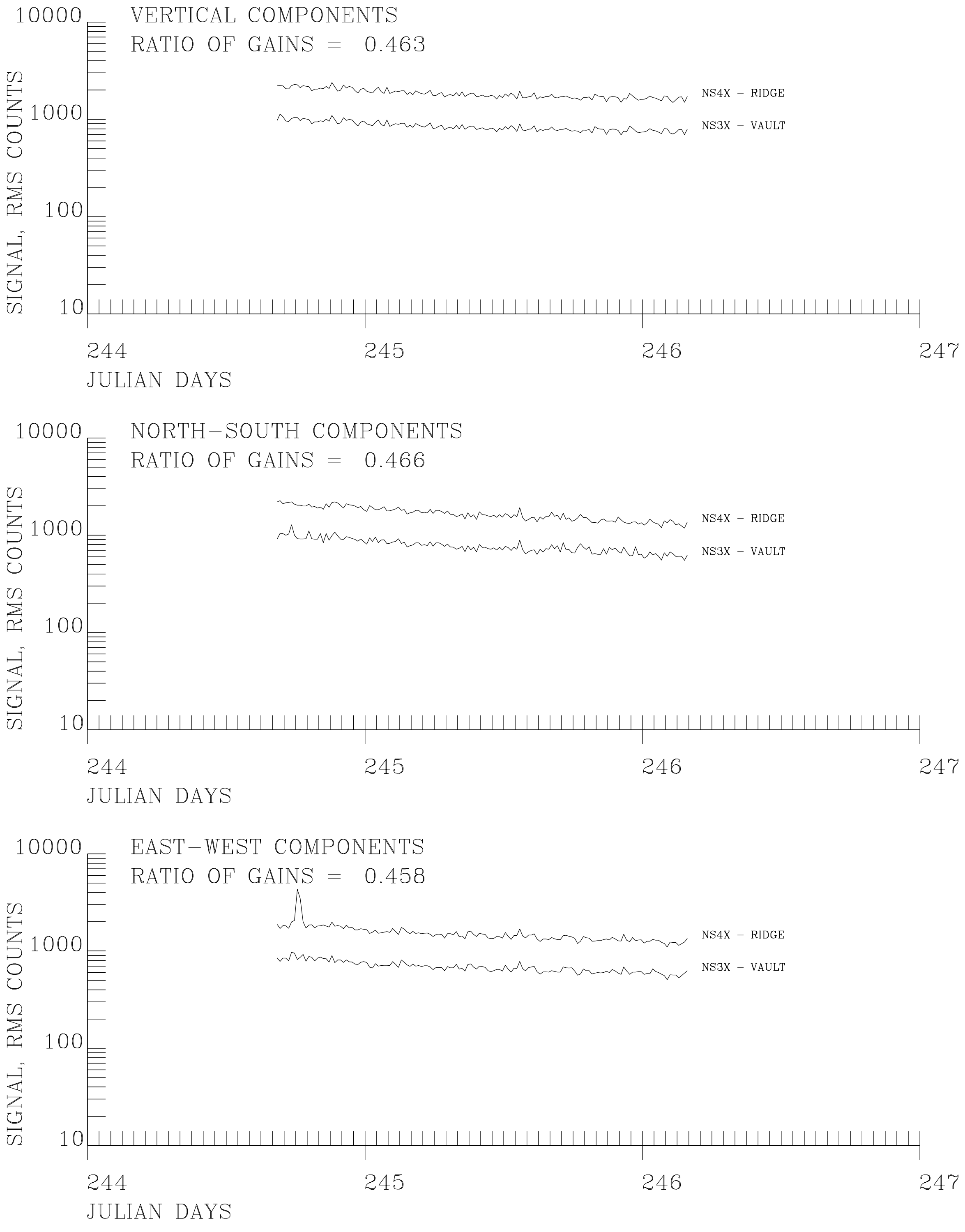

Figure 10.4 RMS signal levels in the 4 to 10 second band for both the borehole and reference sensors while the borehole sensor was installed in the ASL vault and the reference sensor was installed on the ridge above the vault with the horizontal components of the borehole sensor aligned 120° clockwise from the reference sensor.

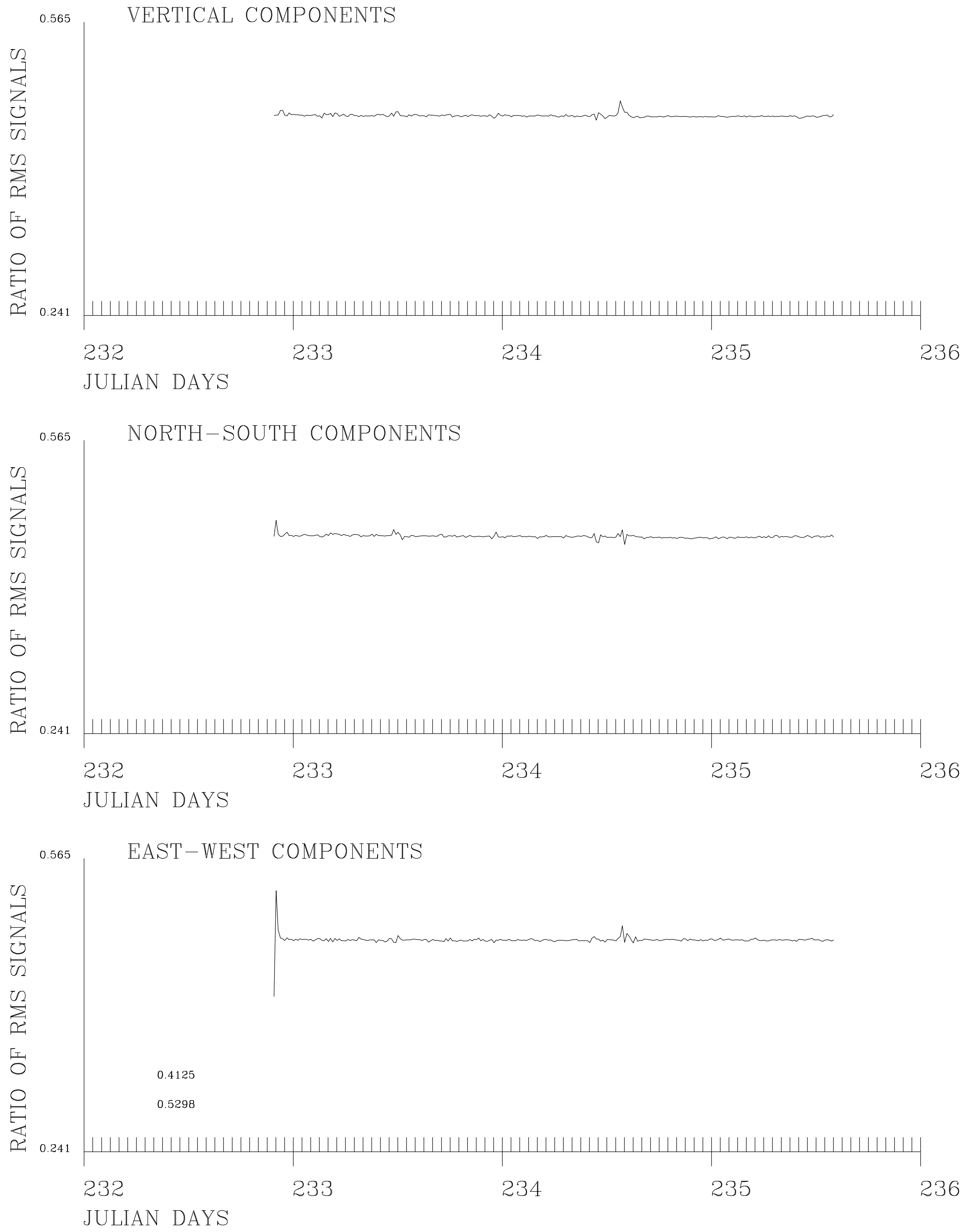

Figure 10.5 Ratio of the RMS signal levels in the 4 to 10 second band for the borehole and reference sensors while they were both installed in the ASL vault with their horizontal components aligned parallel in space.

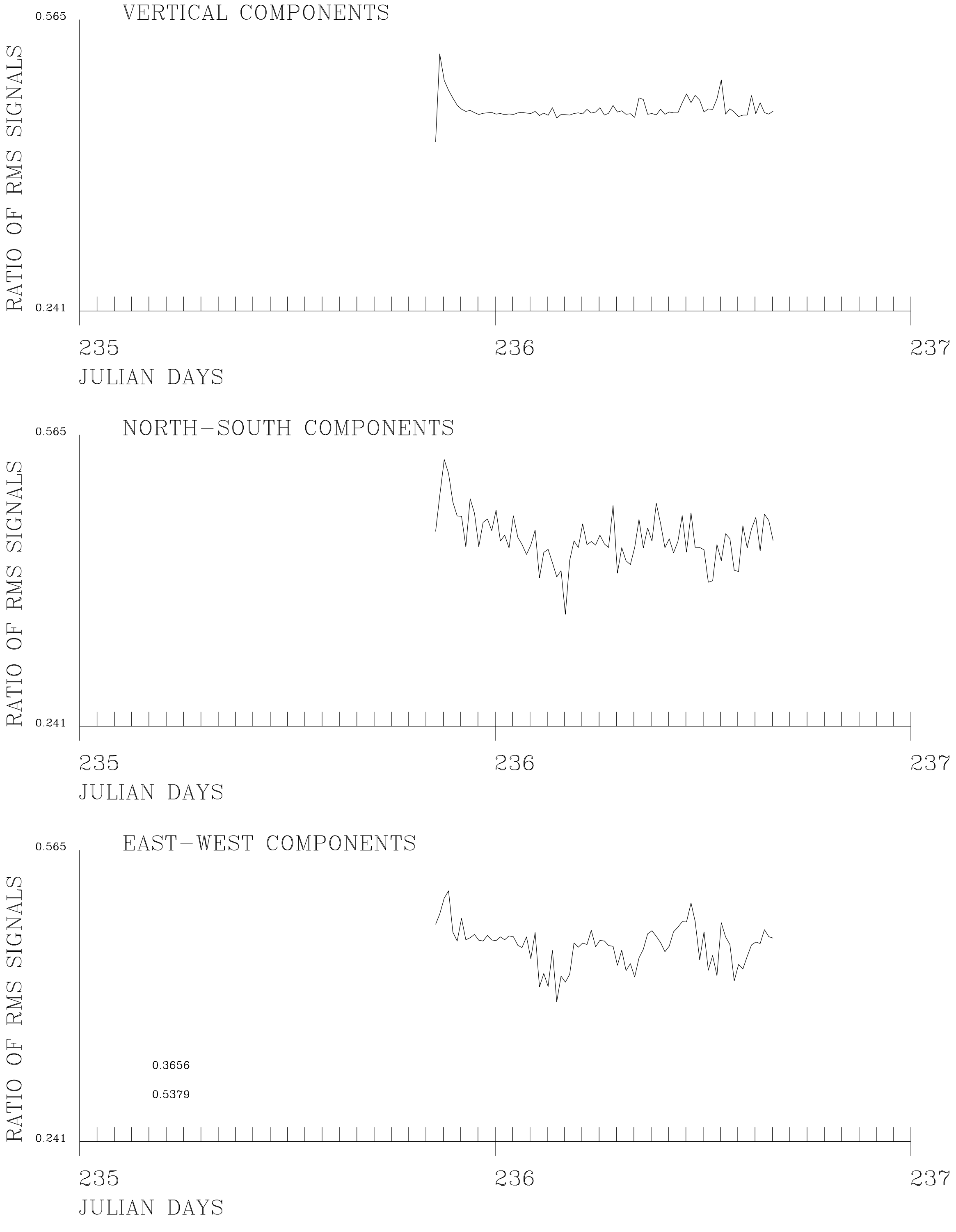

Figure 10.6 Ratio of the RMS signal levels in the 4 to 10 second band for the borehole and reference sensors while the borehole sensor was installed in the ASL vault and the reference sensor was installed on the ridge above the vault with their horizontal components aligned parallel in space.

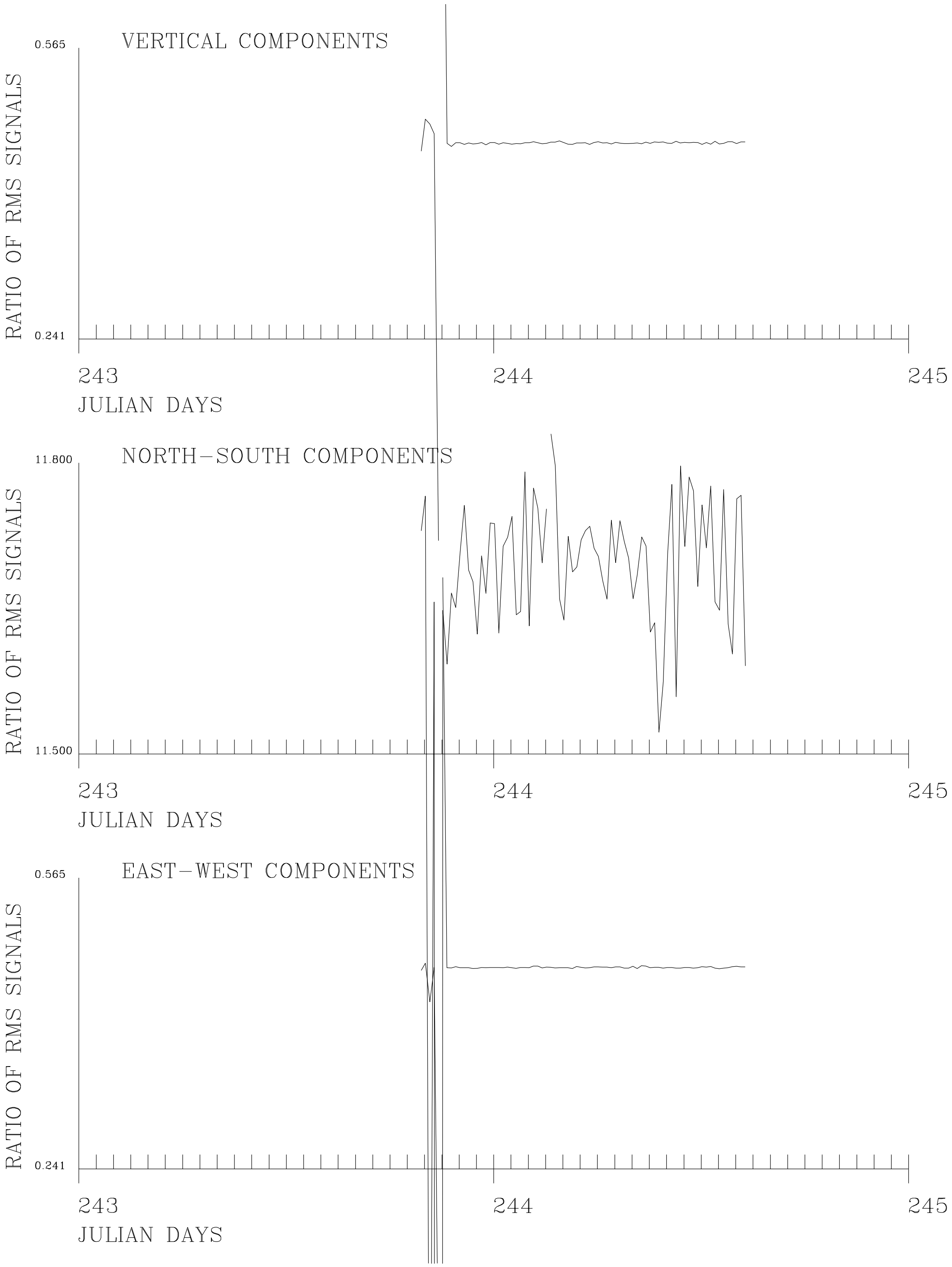

Figure 10.7 Ratio of the RMS signal levels in the 4 to 10 second band for the borehole and reference sensors while they were both installed in the ASL vault with the horizontal components of the borehole sensor aligned 120° clockwise from the reference sensor.

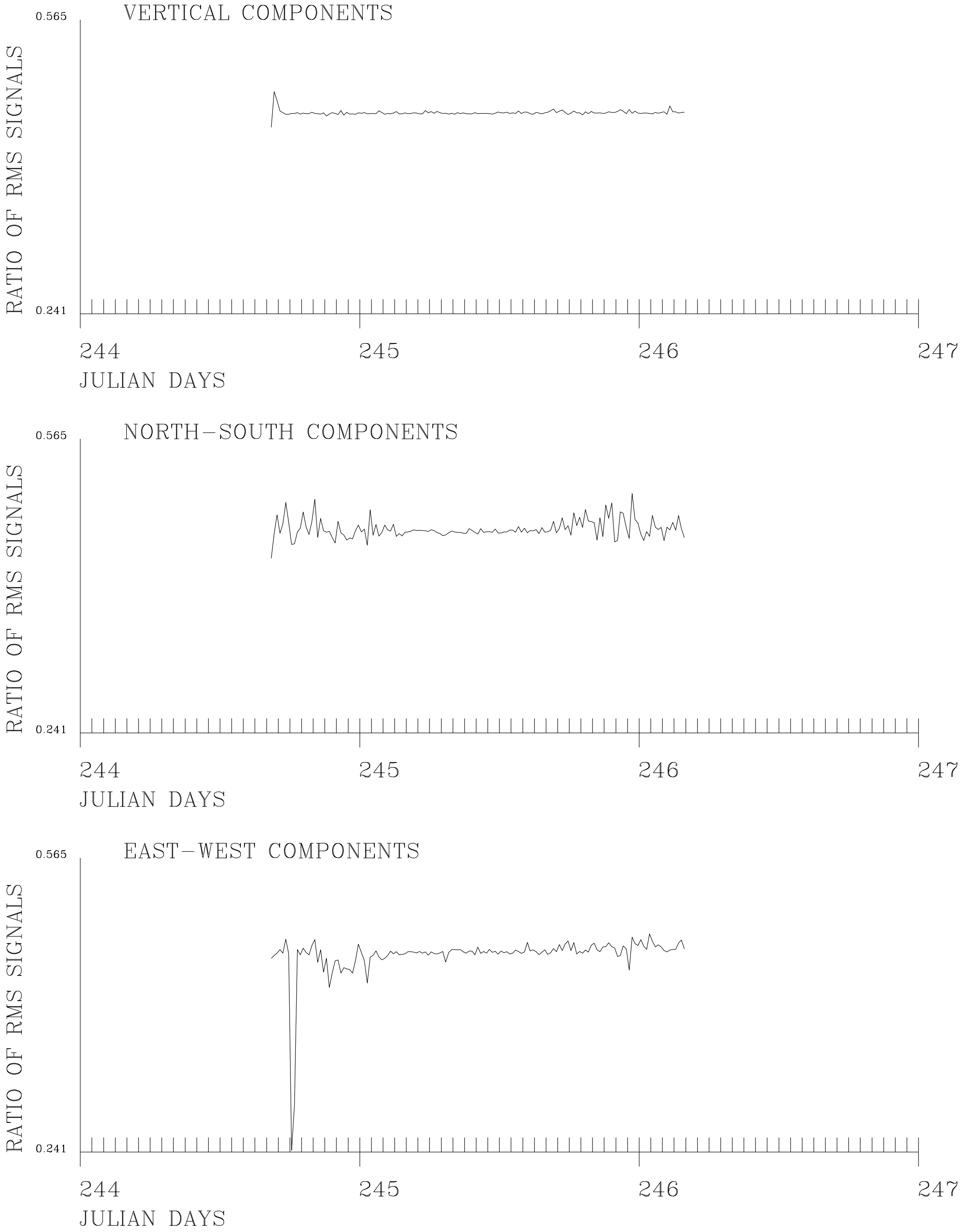

Figure 10.8 Ratio of the RMS signal levels in the 4 to 10 second band for the borehole and reference sensors while the borehole sensor was installed in the ASL vault and the reference sensor was installed on the ridge above the vault with the horizontal components of the borehole sensor aligned 120° clockwise from the reference sensor.

11 CHECKING FOR CORRECT REFERENCE SIGNAL POLARITY IN FIELD INSTALLATIONS

Obviously, all sensor channels must be wired with the correct polarity if the coherence based azimuth measurement procedure is to yield correct results. Fortunately, reversals in polarity should yield relatively large errors in the calculated azimuth that can be spotted by analyzing the arrival azimuth of a few events. However, it would be advantageous to have a method for checking that the wiring is correct in the field before analyzing azimuth data.

The installation of a KS-54000 at RSSD illustrates how polarity reversals can happen in the field. The borehole and reference sensors were wired with care and azimuth data was collected and analyzed. However when the results were compared with the arrival azimuth of a known earthquake, the two disagreed by about 180°. This can be best explained if the reference sensor signal line was somehow wired backwards. This event motivated a search for a method that could be used to verify the reference system wiring in the field.

Tilt was chosen as a possible means of inducing a signal with a known polarity into the closed loop sensor system. An experiment was conducted in the ASL vault in which a person approached the reference sensor (both an STS-2 and a CMG-3T were tested) and simply stood about 1 foot from the sensor first on the north side of the sensor then in turn on the remaining three sides. The expected outcome of standing north of the sensor was that the north-south signal should break downward due to the tilt induced in the vault floor by the added weight nearby. The expected polarity of the channel signal is predicted from the following argument. Adding weight on the north side of the sensor should bend the floor immediately under the north side of the sensor downward relative to the floor immediately under the south side of the sensor. This action should tilt the top end of the sensitive axis of the sensor to the north relative to the bottom end of the axis; the sensor mass should then react by moving toward north which corresponds to earth motion south. Standard polarity conventions require a positive going signal for earth motion in the up, north and east directions. The predicted equivalent earth motion in this experiment is south so the signal should break downward. Similar arguments predict the output of the north-south component signal should break upward if one stands south of the sensor. In addition, the east-west component of the sensor should break downwards if the weight is put east of the sensor and upwards if west of the sensor.

Figure 11.1 displays the results of conducting this experiment with a CMG-3T sensor. In center of the figure is depicted the top view of the sensor with the brass orientation pointer pointing north. Surrounding the sensor are plots of the signal outputs of the seismometer horizontal data channels that were obtained when a person stood near the sensor in the four indicated directions. The experiment was repeated twice for each component so there are two system responses in each plot. The time series in the plots are similar to but not exactly step responses of the sensor system. First, the weight could not be instantaneously added to the area near the sensor; it took a little bit of time to walk up to the spot near the sensor. In addition, the weight near the sensor was not left in place throughout the time period depicted in the figures. Instead the weight was removed when the sensor output peaked out in response to adding the weight (the weight was in place about 25 seconds). Therefore, a break is observable in each of the curves shortly after the system output response to the added weight peaks. We are interested in the direction that the system output breaks after the addition of the weight so the disturbance caused by removing the weight 25 seconds after it was added is not important.

Note that all eight of the signals in Figure 11.1 break in the directions predicted by the simple analysis presented earlier in this section. Since the predicted signals and experimental results agree we gain a warm fuzzy feeling that the experimental setup was wired correctly.

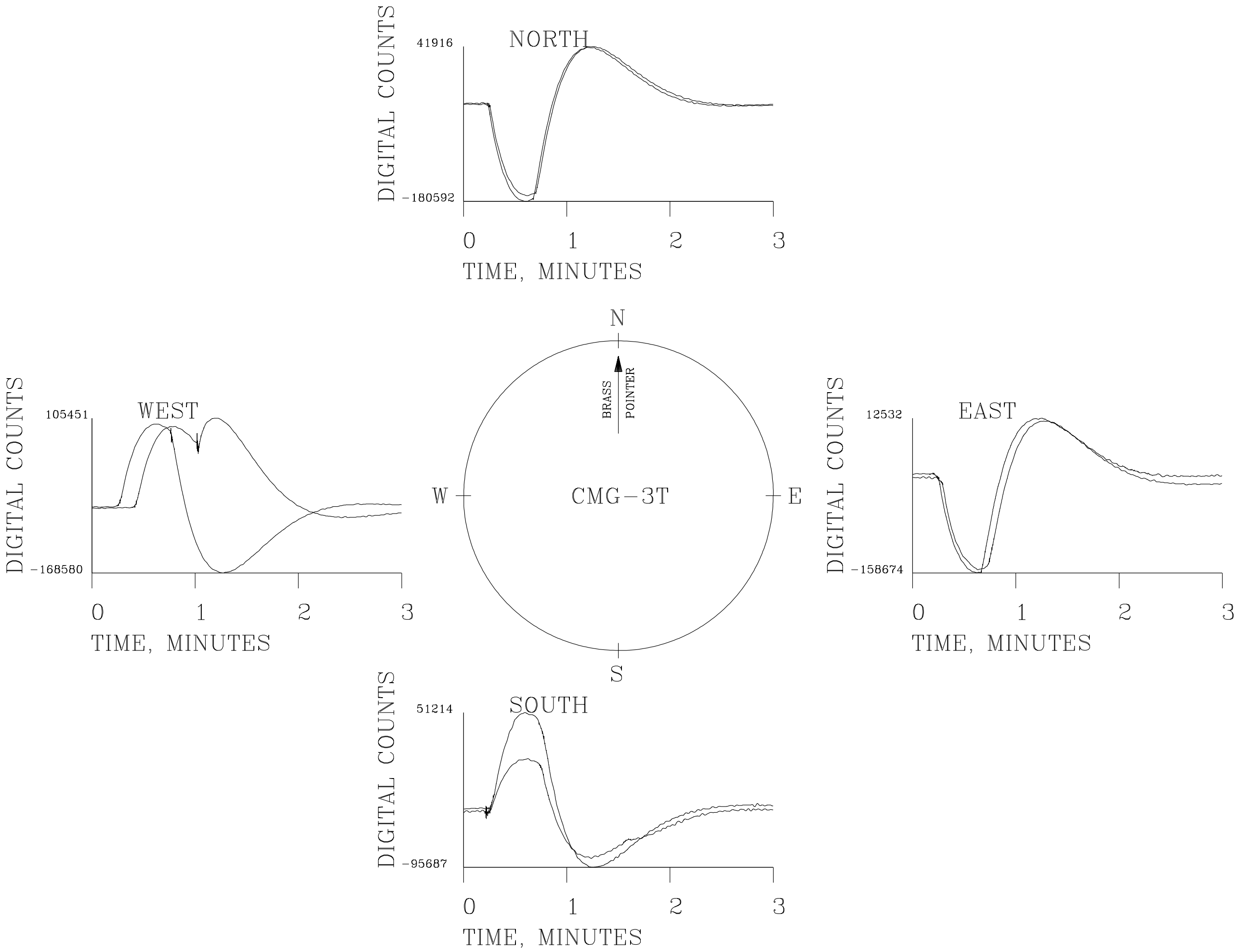

Figure 11.1 Examples of channel outputs if weight is placed on the vault floor near a CMG-3T sensor. Curves NORTH and SOUTH are the north-south channel outputs if weight is placed on the floor north and south of the CMG-3T respectively. Curves EAST and WEST are the east-west channel outputs if weight is placed on the floor east and west of the CMG-3T respectively.

The responses to addition of weight near the sensor are not identical even when weight is added near the same side of the sensor. This can probably be explained by the fact that it is difficult repeat the experiment exactly when the weight has the form of a person. Slight differences in the rate at which the person approaches the sensor and slight differences in the precise spot the person stands probably make a considerable difference in the amplitude of the response of the sensor to the addition of the weight. In Figure 11.1, the two responses to the addition of weight near the north and east components compare very well. However, the amplitude of the two south tests are quite different and obviously something different occurred when the weight was removed during one of the west tests. Fortunately, the goal in this experiment is limited to the sense of the first break in the response to the addition of the weight so we are not concerned about the details of the sensor output after the first break.

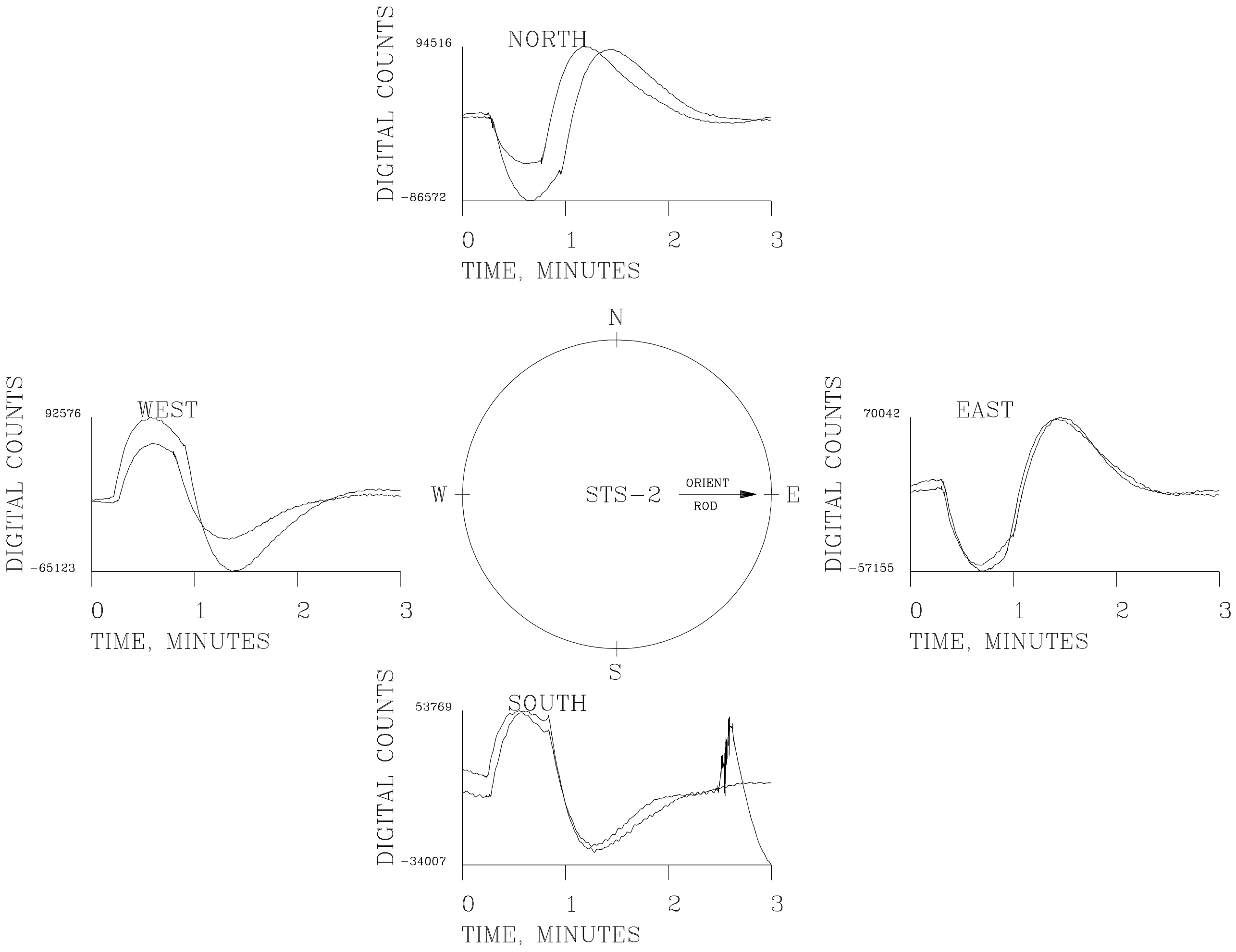

Figure 11.2 Examples of channel outputs if weight is placed on the vault floor near a STS-2 sensor. Curves NORTH and SOUTH are the north-south channel outputs if weight is placed on the floor north and south of the STS-2 respectively. Curves EAST and WEST are the east-west channel outputs if weight is placed on the floor east and west of the STS-2 respectively.

Figure 11.2 contains the results of repeating the experiment while using a STS-2 sensor. In the middle of this figure is the top view of the STS-2 with the orienting rod direction indicated in the figure. Remember that the orienting rod on a STS-2 points east when the sensor is oriented in the conventional north-south east-west directions. Once again the fact that the outputs of the STS-2 respond to the addition of the weight as predicted by the simple analysis indicates that the STS-2 sensor and the data recording system were wired correctly.

The data in Figures 11.1 and 11.2 establishes that adding weight to the vicinity of the sensor works successfully in determining the correct polarity response of a sensor after it is completely installed under ideal conditions - on a concrete floor poured on granite in a quiet vault. However, reference sensors in the field will usually be installed in much more primitive conditions. Therefore, the two experiments were repeated by installing the two sensors one at a time in the small shallow pit vault near the ANMO pad. This pit has a thin concrete floor that is poured on alluvial fill that is composed of gravel and dirt with concrete block walls; it is about 20 inches deep and is about 26 inches by 26 inches square and it has a 0.5 inch thick plywood lid.

Figure 11.3 contains the results of adding weight near the sensor while is was installed in the small shallow pit vault near the ANMO pad. A quick glance at this data reveals that the sense of the first break of the output signal after adding the weight is the same as it was when the sensor was installed in the vault. Similarly, the first breaks shown in Figure 11.4 for the STS-2 when it was installed in the small shallow pit vault near the ANMO pad all have the same sense.

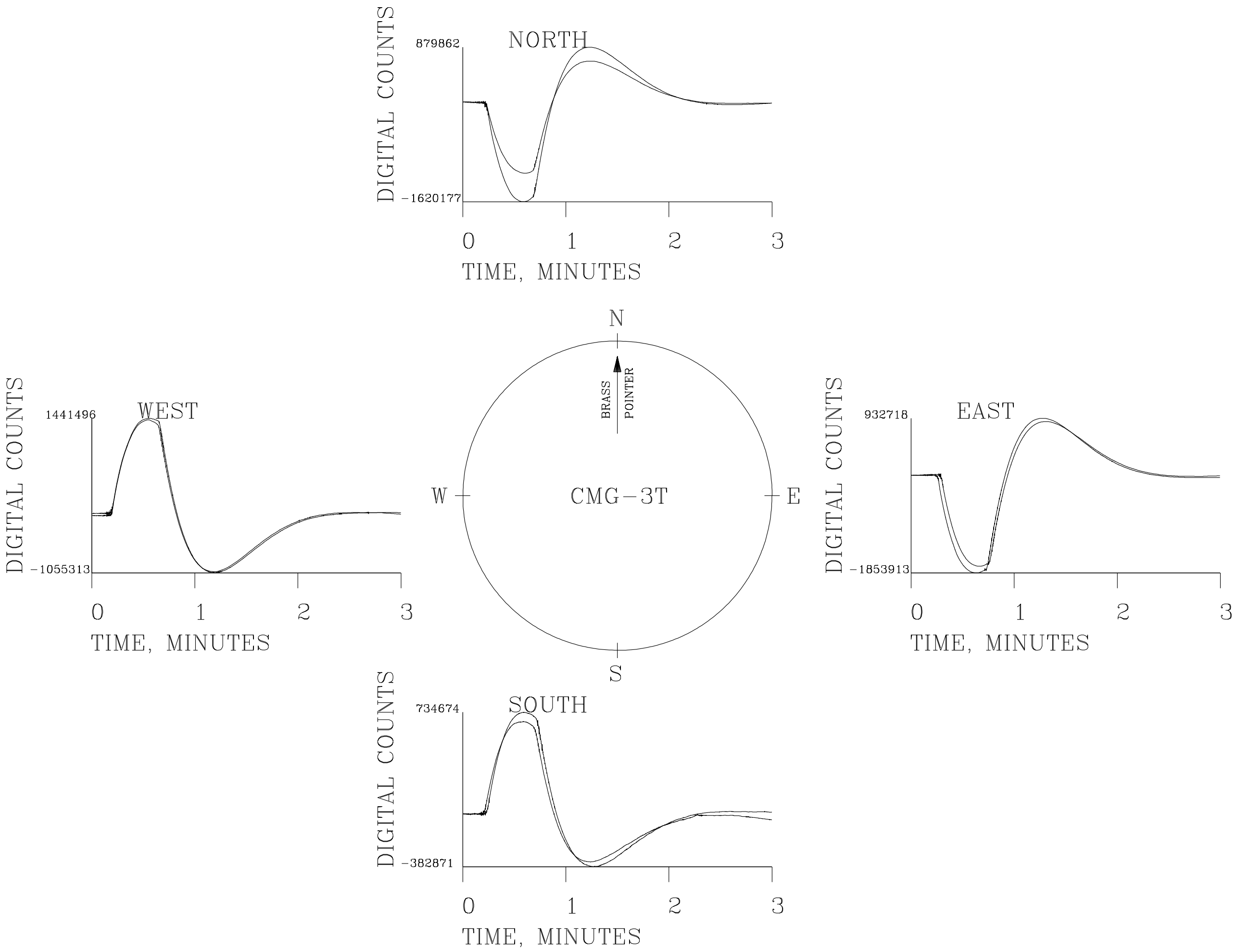

Figure 11.3 Examples of channel outputs if weight is placed on the surface near a CMG-3T sensor installed in a shallow concrete pit vault in the ground. Curves NORTH and SOUTH are the north-south channel outputs if weight is placed on the surface north and south of the CMG-3T respectively. Curves EAST and WEST are the east-west channel outputs if weight is placed on the surface east and west of the CMG-3T respectively.

As a worst case example of anticipated field installations, both of the sensors were installed one at a time in a freshly dug hole in the alluvial fill near the ASL Snake Pit. This hole was barely large enough in diameter and deep enough to accommodate the sensors and to facilitate leveling and instrumentation cable attachment. A 1 inch thick disk of aluminum was placed in the bottom of the hole and was roughly leveled to provide a firm surface for the seismometer feet to rest on. The sensor was installed, mechanically leveled, and then a 0.5 inch thick plywood lid was put over the sensor. The lid was then covered with 2 to 4 inches of dirt.

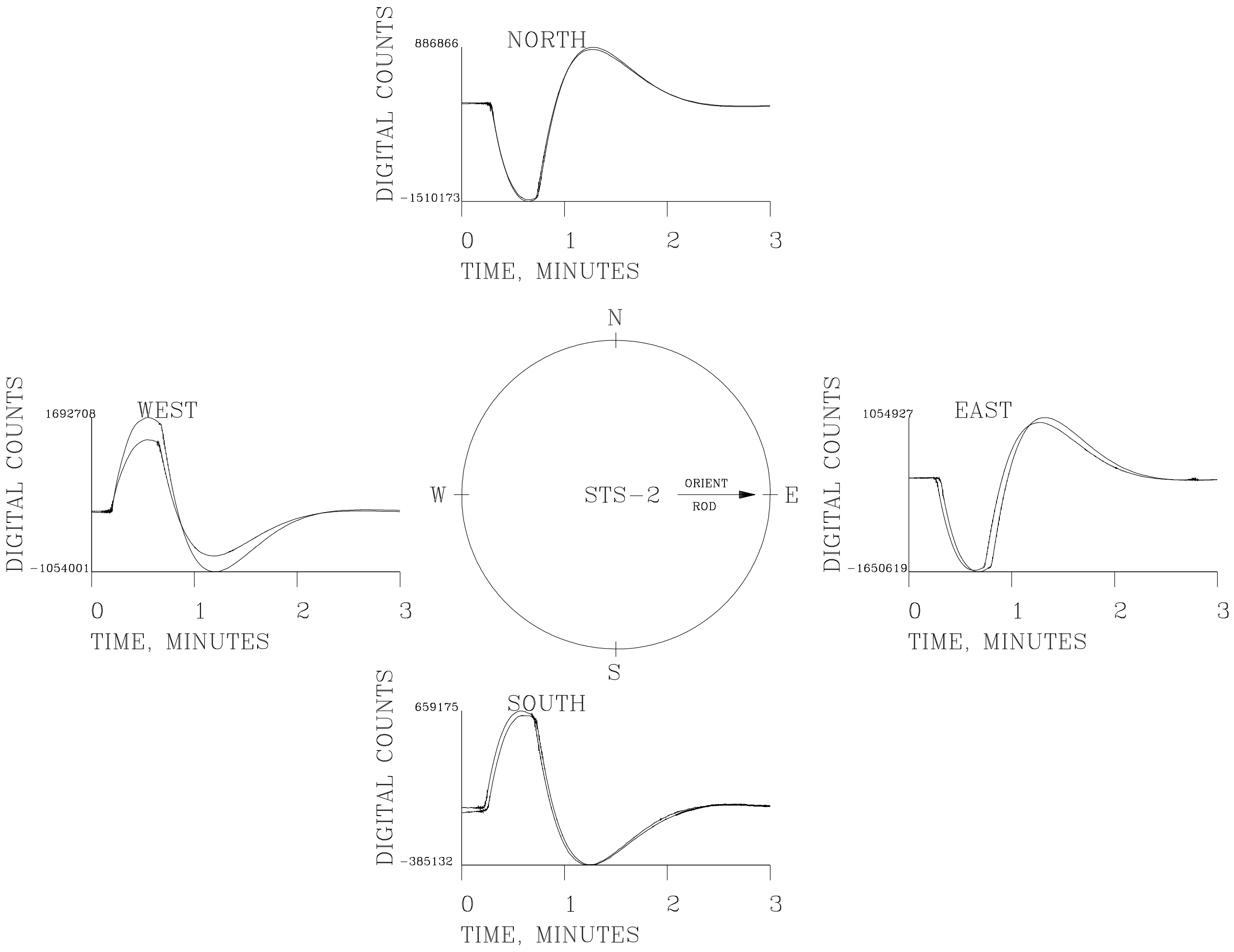

Figure 11.4 Examples of channel outputs if weight is placed on the surface near a STS-2 sensor installed in a shallow concrete pit vault in the ground. Curves NORTH and SOUTH are the north-south channel outputs if weight is placed on the surface north and south of the STS-2 respectively. Curves EAST and WEST are the east-west channel outputs if weight is placed on the surface east and west of the STS-2 respectively.

The results of conducting the adding weight experiment for both sensors when they were installed in this hole are shown in Figures 11.5 and 11.6. The sense of the signal breaks caused by the addition of weight near the hole in the four directions are consistent with the results of both the vault and pit installations.

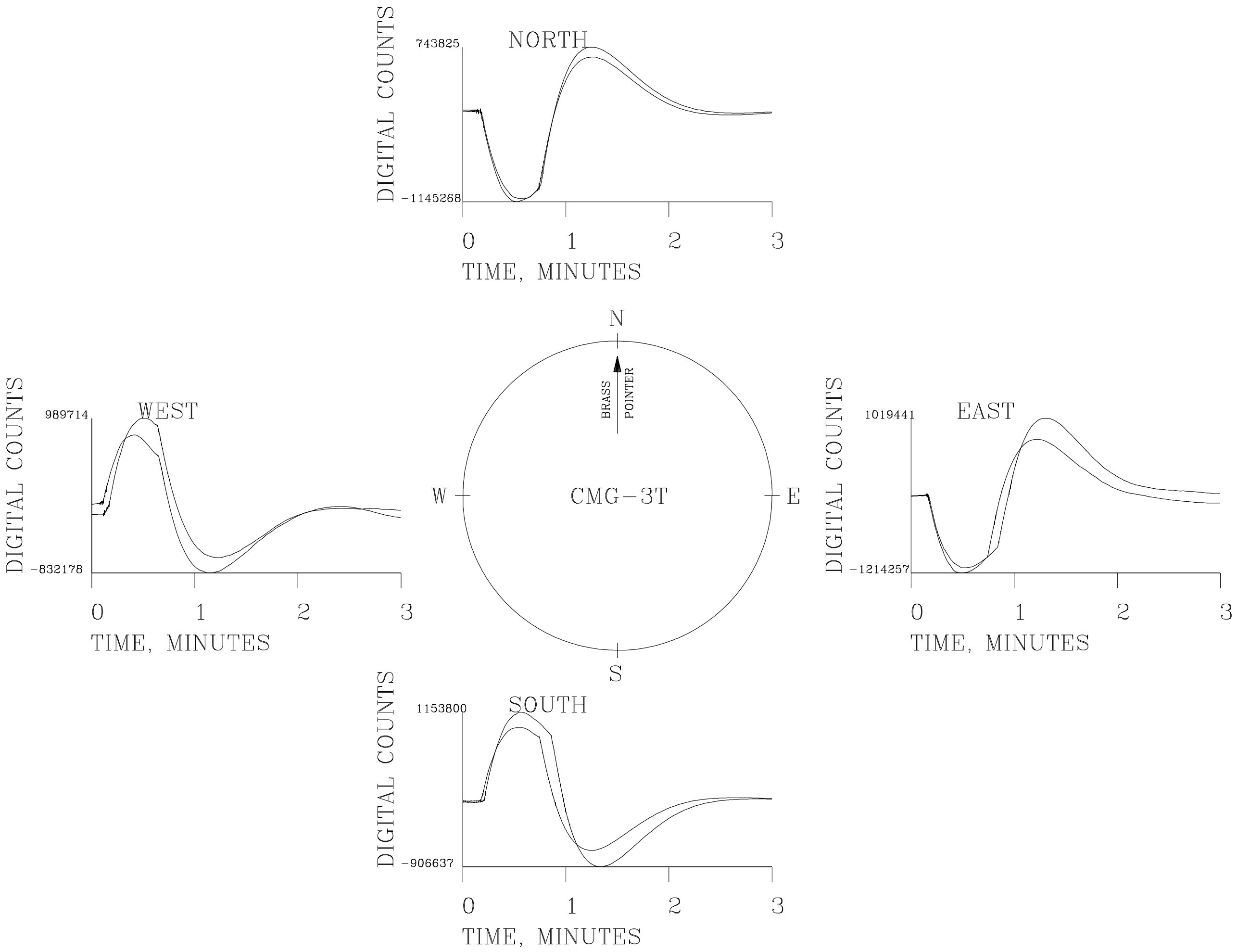

Figure 11.5 Examples of channel outputs if weight is placed on the surface near a CMG-3T sensor installed in a shallow hole in the ground. Curves NORTH and SOUTH are the north-south channel outputs if weight is placed on the surface north and south of the CMG-3T respectively. Curves EAST and WEST are the east-west channel outputs if weight is placed on the surface east and west of the STS-2 respectively.

Regardless of the type of installation (vault, pit or hole), if weight is added near the sensor on the north side, the north-south signal breaks down. Similarly, if weight is added near the sensor on the east side, the east-west signal breaks down, if weight is added near the sensor on the south side, the north-south signal breaks up, and if weight is added near the sensor on the west side, the east-west signal breaks up. The sense of the first breaks are identical in all three installations and it is very easy to determine the sense of the first break. Thus, adding weight near the sensor and noting the sense of the first break of the sensor output produced by the added weight should serve as a reliable quick check of reference sensor polarity correctness in the field.

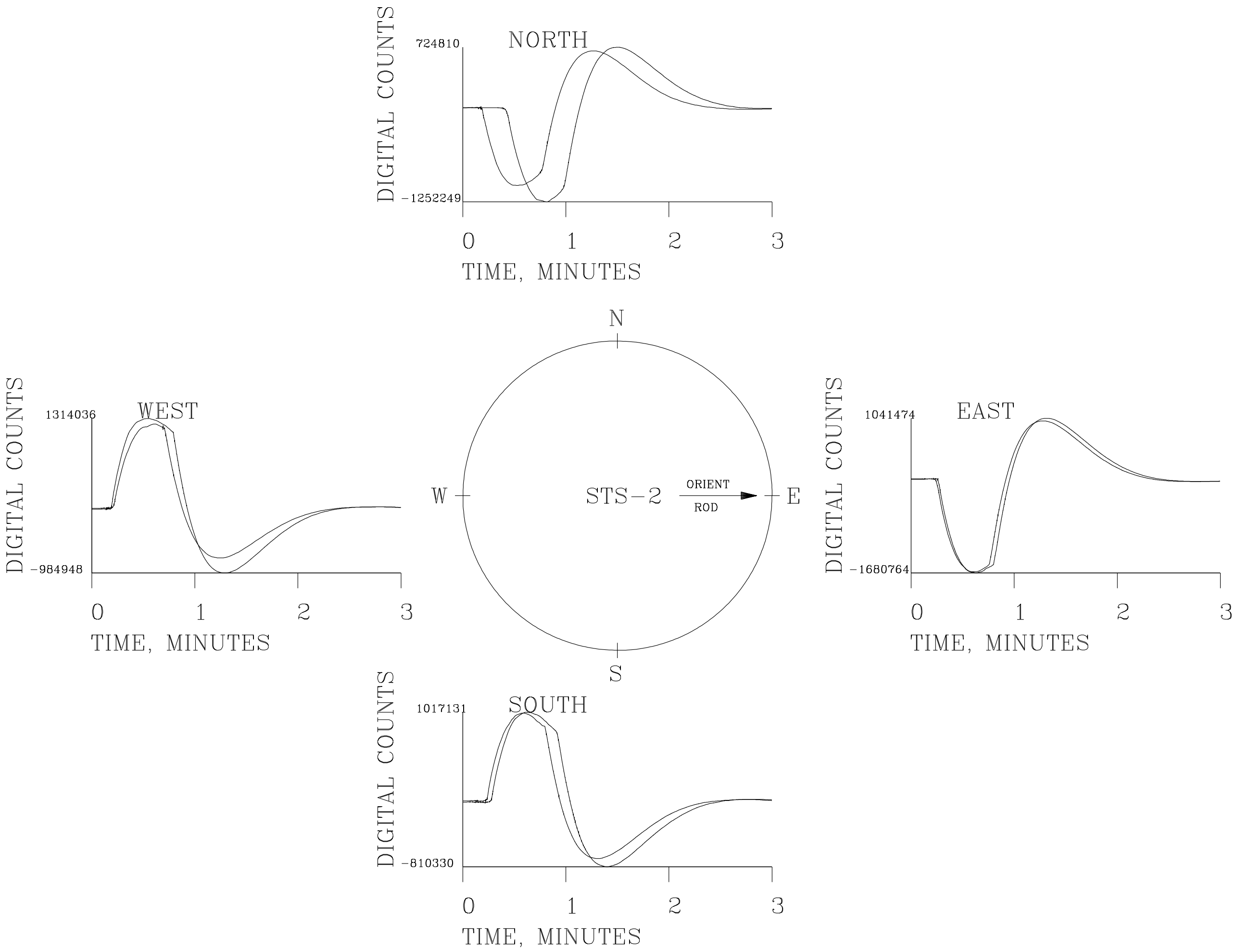

Figure 11.6 Examples of channel outputs if weight is placed on the surface near a STS-2 sensor installed in a shallow hole in the ground. Curves NORTH and SOUTH are the north-south channel outputs if weight is placed on the surface north and south of the STS-2 respectively. Curves EAST and WEST are the east-west channel outputs if weight is placed on the surface east and west of the STS-2 respectively.

SUGGESTED FIELD PROCEDURE FOR REFERENCE SENSOR POLARITY CHECK

1. Assemble all hardware (sensors, data recording system and connect all associated cabling). Unlock sensor and center masses. Start the data recording system.

2. Terminate all activity in the vicinity of the reference sensor (both human and vehicular).

3. Approach the reference sensor (preferably from the north) and stand still near (within 2 feet) the north side of the instrument for at least 25 seconds.

4. Leave the vicinity of the instrument.

5. Observe the sense of the signal break at the time the instrument was approached. If the signal breaks down, the polarity is correct. If the signal breaks up, check all wiring, check for a polarity reversal in the software, correct, and return to step 1.

CMG-3T	NORTH	EAST	SOUTH	WEST
VAULT	222,508	171,206	146,901	274,031
PIT	2,500,039	2,786,631	1,117,545	2,496,809
HOLE	1,889,093	1,316,201	2,060,437	1,821,892

Table 11.1 Maximum peak-to-peak channel responses to the addition of weight near the CMG-3T sensor on the indicated four sides of the sensor while installed in the vault, pit, and hole.

Although not specifically designed to do so, this experiment yields some additional information about the relative stiffness of the mediums surrounding the installations. Tables 11.1 and 11.2 contain the peak-to-peak amplitudes of the sensor responses to the addition of the weight for the CMG-3T and the STS-2 respectively. The numbers in these two tables are the vertical scale ranges for the plots in Figures 11.1 through 11.6. Note that the peak-to-peak responses for both the CMG-3T and the STS-2 sensors are reduced by about a factor of 10 when installed on the concrete over granite floor of the vault as compared with both the pit and hole installations. The primary reason for smaller responses in the vault is probably that the vault floor is much stiffer; adding a given weight to the concrete floor poured on granite bedrock probably induces much less tilt into the sensor than does adding the same weight to alluvial fill. There is also a considerable difference in the relative responses of the CMG-3T and the STS-2 while installed in the vault. This is probably primarily due to the fact that the two instruments were not installed in the same location in the vault; instead, they were installed about 6 feet apart. Evidently, the vault floor was stiffer under the STS-2 installation site than it was under the CMG-3T site because the STS-2 response to the application of the same weight was less than the CMG-3T. Stiffness is also evident in the data obtained from the shallow pit vault near the ANMO pad. The pit is located immediately adjacent to the north side of the concrete pad at ANMO; it is so close to the edge of the pad that it is not possible to stand on the south side of the vault without standing on the ANMO pad. This fact is evident in the responses of both of the sensors as shown in Tables 11.1 and 11. Note that the peak-to-peak response to placing weight south of the pit vault is about half the amplitude of the peak-to-peak response to placing weight on the north, east, and west sides of the vault. This is probably due to the fact that the rigid concrete ANMO pad distributes the weight over a wider area thereby resulting in less tilt being induced into the sensor in the pit vault.

STS-2	NORTH	EAST	SOUTH	WEST
VAULT	181,088	97127,1	87,776	157,699
PIT	2,397,039	2,705,546	1,044,307	2,737,015
HOLE	1,977,059	2,722,238	1,827,461	2,298,984

Table 11.2 Maximum peak-to-peak channel responses to the addition of weight near the STS-2 sensor on the indicated four sides of the sensor while installed in the vault, pit, and hole.

12 LONGRANGE AZIMUTH ESTIMATES

In the latter half of April 2001, an STS-2 seismometer and a portable Quanterra Q4120 digital recording system were deployed at the Star File Optical Range One Mile Site on Kirtland Air Force Base to acquire data for assessing the ambient background seismic noise level at the One Mile Site. Initially, this data was gathered for use in determining the suitability of the site for the possible construction of a new seismic vault test facility for the Albuquerque Seismological Laboratory.

However, this data also provides an opportunity to gain some insight into the answer to the question of how far can a reference sensor be installed from the borehole without degrading coherence derived azimuth estimates. The One Mile Site is approximately 1.4 miles from the Sandia National Laboratories Facilities Acceptance, Certification, and Test (FACT) site at which ANMO has been installed since October of 2000. The results of treating the FACT installed ANMO borehole sensors (a KS-54000 and a CMG-3TB) as sensors whose orientation are unknown and the north component of the One Mile Site installed STS-2 as the orientation sensor were remarkable as will be illustrated below.

The One Mile Site is an abandoned target area that was used for testing high power carbon dioxide laser weapons by the US Air Force several years ago. It consists of a right angle notch excavated in the side of a solid rock hillside. The horizontal floor of this notch is bedrock (Precambrian granite) and the vertical side of the notch is a solid rock cliff about 50 feet high. The STS-2 sensor was installed by first hand digging a shallow (about 1 foot deep) hole in the alluvial backfill overlying the bedrock at the site. The surface of the bedrock was then carefully cleaned by prying and chipping away the loose rock pieces on the bedrock and by brushing and vacuuming the surface to remove all small pieces of dirt and dust. A thin (about 0.5 to 2 inch thick) layer of cement was then poured in the bottom of the hole and allowed to cure. The STS-2 sensor was installed on the cement and the hole was covered with a plywood sheet and the plywood was in turn covered with about a foot of decomposed granite for thermal isolation. No effort was made to determine the orientation of the sensor although it was noted that it was roughly oriented north-south east-west by “eyeballing” the surrounding topography. Several days of data were recorded at the site in an effort to obtain a significant amount of data during which the wind was not blowing.

The fact that the clock in the Quanterra Q4120 that was used to record the data at the One Mile Site was not locked to satellite timing made the intersite calculations a little harder than usual. Comparing the data recorded at the One Mile Site with the data recorded at ANMO indicated that, to the nearest second, the clock in the Q4120 at the One Mile Site was running 26 seconds slower than the clock at ANMO which was synced to satellite time. Therefore, 26 samples of the 1 sample per second data was manually edited from the ANMO data to bring the data from the two sites into time alignment.

Data from day 116, 2001 was chosen for analysis because that day was relatively wind free and no large earthquakes were present during that time period. Table 12.1 contains the azimuth estimates obtained from the analysis of several (six in most cases) consecutive 10000 second long segments of data from day 116. The data from the ANMO CMG-3TB sensor was contaminated by maintenance activities at ANMO starting at about 18:45 GMT on day 116 thereby limiting the number of segments available for calculations that utilized CMG-3TB data to 6. Data from the ANMO KS-54000 and the One Mile Site STS-2 was not affected so 8 segments of data were analyzed for that combination. Table 12.2 summarizes the corresponding coherences calculated between the individual sensor signal outputs for each of the 10000 second long segments.

The ANMO FACT intrasite coherences (KS→CMG and CMG→KS) shown in Table 12.2 are all quite high as one should expect based on the extensive data already presented in earlier sections of this report because the KS-54000 and the CMG-3TB sensors at ANMO FACT are positioned quite near one another (the boreholes are approximately 25 feet apart at the surface and the sensors are both installed at a 100 meter depth). Sensors operated in bedrock this close together should be highly coherent especially at higher signal levels such as in the six second microseism portion of the spectrum. The intersite coherences (CMG→STS and KS→STS) shown in Table 12.2 are also remarkably high if one considers the approximate 1.4 mile separation between the ANMO FACT borehole sensors and the reference STS-2 installed at the One Mile Site and the additional noise that is probably present in the STS-2 data as a result of its installation on the surface.

The results of calculating the relative azimuths of the ANMO KS-54000 north and the ANMO CMG-3TB north with respect to the north component of the One Mile Site installed STS-2 are shown in Figure 12.1. The data indicates that the ANMO KS-54000 north component is 46.3° (46.3° is the average of the 8 azimuth estimates shown in the KS→STS row of Table 12.1) clockwise from the north component of the One Mile Site STS-2 and the ANMO CMG-3TB north component is 280.9° (280.9° is the average of the 6 azimuth estimates shown in the CMG→STS row of Table 12.1) clockwise from the north component of the One Mile Site STS-2. Combining these two numbers yields the fact that the ANMO KS-54000 north must be 125.4° clockwise from the ANMO CMG-3TB north as indicated in Figure 12.1.

Figure 12.2 presents the sensor orientation data that was obtained shortly after ANMO FACT was installed in October 2000. This orientation data was obtained by Neil Ziegelman and Juan Nieto by installing a CMG-3T sensor on the surface with a known orientation (geographic north) and processing recorded data from this sensor and both of the borehole sensors to obtain the true geographic orientation of both borehole sensors. Their measurements indicated that the north component of the ANMO KS-54000 was 89° clockwise from the reference sensor and that the north component of the ANMO CMG-3TB was 323° clockwise from the reference sensor. Combining these two numbers yields the fact that the ANMO KS-54000 north must be 126° clockwise from the ANMO CMG-3TB as is indicated in Figure 12.2.

At this point, we should note that the original ANMO orientation calculations were made with 1° increments in azimuth whereas the calculations between ANMO FACT and the One Mile Site were made with 0.1° azimuth increments. Therefore, the azimuth estimates in Figure 12.1 are shown to 0.1° while those in Figure 12.2 are to the nearest 1°.

It is quite remarkable that the two independent measurements of the azimuth angle between the north components of the two ANMO FACT borehole sensors agree so closely. The 126° measurement obtained by Ziegelman and Nieto (Figure 12.2) were based on data from a reference sensor that was installed within 20 feet or so of both of the ANMO FACT boreholes. The 125.4° measurement obtained from the One Mile Site data (Figure 12.1) was based on data from a reference sensor that was installed approximately 1.4 miles away from the boreholes. The fact that the two sets of measurements yield essentially the same results indicates that utilizing data from a reference sensor that is installed at a considerable distance from the unknown orientation borehole sensor should yield accurate estimates of the orientation of the borehole sensor if the reference sensor installation is a fairly high quality installation on bedrock.

Two more estimates of the relative azimuth between the ANMO KS-54000 and the ANMO CMG-3TB can be calculated by directly calculating the relative positions of the two instruments without using an intermediatory reference instrument. Figure 12.3 (row CMG→KS of Table 12.1) presents the results of treating the ANMO CMG-3TB north component as the reference instrument and calculating the relative azimuth of the ANMO KS-54000 north with respect to it and Figure 12.4 (row KS→CMG of Table 12.1) shows the result of the interchanging the function of the two instruments in this calculation. Thus, we now have four measurements of the azimuth between the north components of the two borehole instruments installed at ANMO FACT. They are 125.4° (based on the One Mile Site reference STS-2), 126° (based on a reference sensor installed near the ANMO FACT boreholes), 125.2° (based on treating the ANMO CMG-3TB north as a reference sensor), and 124.0° (based on treating the ANMO KS-54000 north as a reference sensor. All four azimuth estimates are quite consistent and they are within the possible horizontal component orthogonal alignment errors discussed earlier in this report.

In summary, the data presented in this section indicates that the reference sensor does not necessarily need to be installed in the immediate vicinity of the borehole containing the sensor whose orientation is to be determined. An installation considerably removed from the borehole can yield reliable azimuth estimates if the installation is on bedrock and is done with care.

	SEG 1	SEG 2	SEG 3	SEG 4	SEG 5	SEG 6	SEG 7	SEG 8
CMG→STS	281.1	281.1	280.4	281.6	280.4	280.6		
KS→STS	46.5	46.5	45.6	46.8	45.6	45.8	47.2	46.5
KS→CMG	125.2	125.2	125.3	125.3	125.2	125.1		
CMG→KS	235.9	236.0	236.0	235.9	236.0	236.1		

Table 12. 1 Summary of the calculated azimuth estimates between sensors located at the One Mile Site and ANMO FACT and between the two borehole sensors at ANMO FACT for several data segments on day 116, 2001. All angles are in degrees.

	SEG 1	SEG 2	SEG 3	SEG 4	SEG 5	SEG 6	SEG 7	SEG 8
CMG→STS	0.9290	0.9251	0.9291	0.9446	0.9276	0.9250		
KS→STS	0.9264	0.9227	0.9263	0.9427	0.9253	0.9218	0.9735	0.9609
KS→CMG	0.9998	0.9998	0.9998	0.9998	0.9998	0.9987		
CMG→KS	0.9998	0.9998	0.9998	0.9998	0.9999	0.9996		

Table 12. 2 Summary of the calculated coherence estimates between sensors located at the One Mile Site and ANMO FACT and between the two borehole sensors at ANMO FACT for several data segments on day 116, 2001.

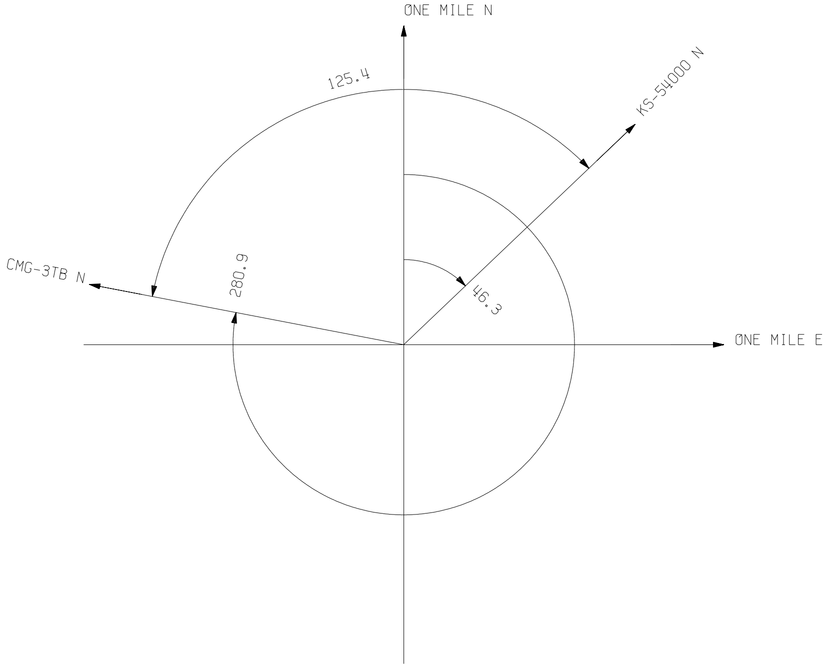

Figure 12. 1 Relative azimuths of the ANMO KS-54000 and ANMO CMG-3TB north components as determined by processing azimuth data between the two sensors and the north component of the STS-2 sensor installed at the One Mile Site. The north component of the STS-2 is assumed to be oriented north.

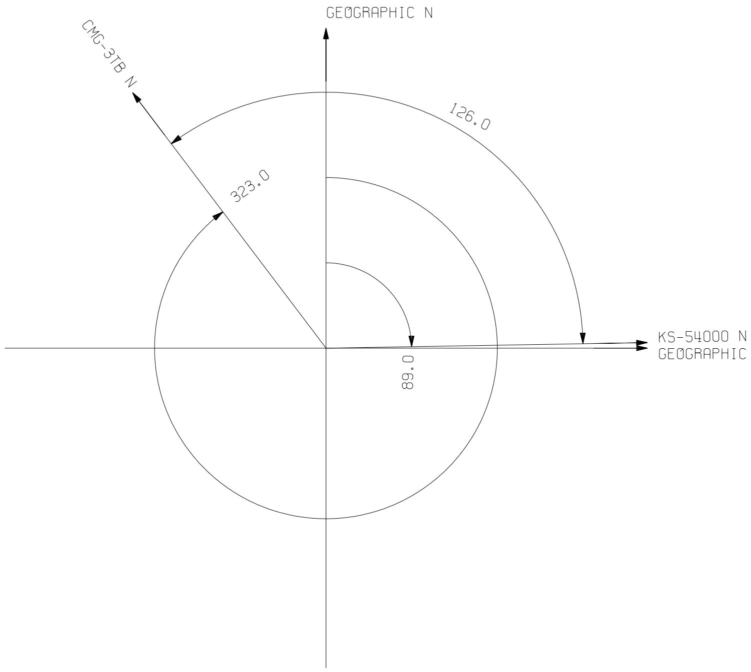

Figure 12. 2 Relative orientation azimuths of the north components of the AMMO sensors located at the Sandia National Laboratories FACT site. All azimuths are with respect to true geographic north. These orientations were obtained by Neil Ziegleman and Juan Nieto.

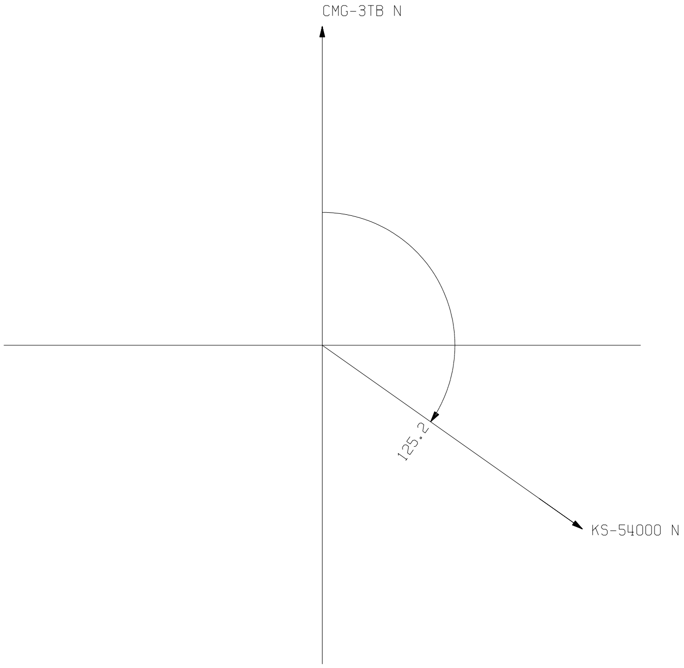

Figure 12. 3 Relative positions of the ANMO KS-54000 and the ANMO CMG-3TB as calculated by treating the north component of the CMG-3TB as the reference sensor and the KS-54000 as the unknown orientation borehole sensor. The CMG-3TB north component is assumed to be oriented north.

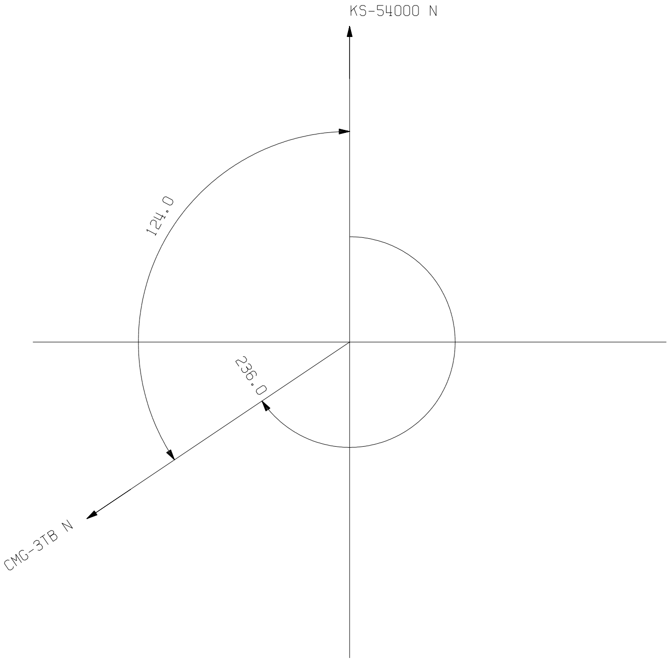

Figure 12. 4 Relative positions of the ANMO KS-54000 and the ANMO CMG-3TB as calculated by treating the north component of the KS-54000 as the reference sensor and the CMG-3TB as the unknown orientation borehole sensor. The KS-54000 north component is assumed to be oriented north.

13 REFERENCES

Bendat, J.L., and Piersol, A.G., Random Data: Analysis and Measurement Procedures, Second Edition, Wiley-Interscience, New York, 1986

Press, W.H., Flannery, B.P., Teukolsky, S.A, and Vettering, W.T., Numerical Recipes – the Art of Scientific computing, Cambridge University Press, Cambridge, 1986